May 2020

Seasonality in a changing climate: Insights from the modern ocean with application to the Eocene Epoch

Emily J. Judd
Syracuse University

Recommended Citation

Judd, Emily J., "Seasonality in a changing climate: Insights from the modern ocean with application to the Eocene Epoch" (2020). *Dissertations - ALL*. 1157.
https://surface.syr.edu/etd/1157

ABSTRACT

Climate change is arguably the most important issue facing modern society. One of the best tools we have for constraining future climate conditions comes from looking at warm and transitional intervals in Earth's geologic past, such as the Eocene Epoch (~56-34 Ma). The Eocene Epoch was a time of large-scale global climate change, bookended by both the warmest temperatures of the Cenozoic (i.e., the Paleocene-Eocene Thermal Maximum) and the onset of southern hemisphere glaciation (i.e., the Eocene-Oligocene Transition). While mean global climatic conditions across the Eocene, inferred from a compilation of oxygen isotopes of benthic foraminifera, are well constrained and document a clear cooling trend, the few and geographically disparate records of local sea surface temperature (SST) from this interval are often conflicting and difficult to reproduce with climate models. Likewise, multi-proxy studies from the same location frequently yield diverging SST estimates.

These inconsistencies within the climate record inhibit our ability to identify the mechanisms responsible for late Eocene cooling, and call into question our understanding of fundamental aspects of climate dynamics and the underlying assumptions guiding our interpretation of proxy data. Further, they highlight one of the dominant shortcomings of paleoclimate studies; namely the propensity to express climate variability in terms of global or latitudinal averages, while overlooking local and regional scale climate heterogeneity. Distilling global climate to single numbers (e.g., the 2^{o}C global warming threshold) or metrics (e.g., meridional temperature gradients) is appealing, as it allows for direct comparison of different climate states, however oversimplifying conditions by ignoring natural spatial heterogeneity may lead to erroneous paleoclimate interpretations and contribute to the frequent need to set unrealistic boundary conditions in climate modelling studies. In fact, inspection of modern SST data reveal abundant

variability along individual latitudinal bands. This contradicts the simplifying assumption of homogenous zonal paleotemperatures and suggests that improving our understanding on the controls on modern SSTs may hold the key to better understanding ancient climate systems.

The ultimate goal of my dissertation is to provide the tools to facilitate a more robust evaluation of ancient climate dynamics, and thereby improve the fidelity of proxy-based paleoclimate reconstructions and future climate predictions. In Chapter 2, I use analyses of modern SST data to identify sampling biases in the paleo record and propose a new framework within which to more meaningfully interpret annually- and seasonally-resolved SST proxy data. In Chapter 3, I develop a bivalve growth rate model, which accounts for variable intra-annual growth rates and facilitates the temporal alignment of serially-sampled geochemical proxy data, increasing the reliability and applicability of paleo-seasonality interpretations. In Chapters 4 and 5, I apply these approaches to reconstruct seasonal changes in nearshore waters off the eastern margin of the Antarctic Peninsula between the middle and late Eocene. Proxy data are evaluated using climate models and modern analog analyses, supplemented with seasonal precipitation data, and contextualized with existing SST data from the Eocene Southern Ocean, resulting in a holistic assessment of climatic conditions during this critical time interval.

The findings of these studies: 1) demonstrate the utility of seasonal data in distinguishing between the mechanisms responsible for large-scale climate change and identifying seasonal biases in other SST proxy data, 2) suggest that initial late Eocene Antarctic cooling was driven by changes in ocean circulation, rather than pCO_2, 3) reveal how sampling location biases can generate spurious climate interpretations, and 4) illustrate that recognition of and correction for these biases can allow for a more comprehensive and accurate understanding of ancient climate dynamics conditions.

Seasonality in a changing climate: Insights from the modern ocean with application to the Eocene Epoch

by
Emily J. Judd
B.S., Utah Valley University, 2013

Dissertation
Submitted in partial fulfillment of the requirements for the degree of
Doctor of Philosophy in *Earth Sciences*

Syracuse University

May 2020

ACKNOWLEDGEMENTS

It feels wrong to have only my name on this dissertation. The work presented here was truly a team effort and could not have been accomplished without the academic guidance and personal support of many. I am finding it difficult to properly express the enormous gratitude I have for the long list of mentors, colleagues, and friends that I have gained over the course of my PhD.

To my committee members, I sincerely appreciate your guidance and feedback at varying stages of this process. Tripti, I'm so grateful that you came to Syracuse University. You are a powerhouse researcher, a well-rounded academic, and an amazing role model and mentor. Thank you for being the person I look to for advice and support. I look forward to continued collaboration and friendship. Chris, thank you for opening your lab to me and for insightful discussion. Zunli (and Wanyi), thank you for assistance with trace element analyses. Rob, thank you for putting up with my relentless MATLAB questions. I'm amazed that after five years, you still keep your office door open. Scott, the (many) classes I took from you were an absolute delight, and although we still have yet to generate any strontium data, I know we will.

A huge thank you to my lab mates, past and present – I have learned so much from all of you. David, I so valued our afternoon conversations over Bud Light. You kept me grounded and always challenged me to think deeper and work harder. Marie, your effervescence brightened up the lab even on the dreariest Syracuse days and I would never have made it through historical without you. To the larger PaleoX collective, thank you for providing a platform to critically discuss research and for tolerating my relentless questions and comments. Thursdays at 11am were often the highlight of my week.

We all need a good sounding board to pull us out of the weeds of dissertation work. Dan Curewitz, you have been this for me. Much of the work presented here has benefited from our (often lively and lengthy) discussions, and your friendship, insight, and encouragement have been invaluable.

Lindsay Moon, you are a rock star. Mentoring you has been one of the highpoints of my PhD. I sincerely appreciate your hard work, patience, and willingness to go along with all of my half-baked ideas. Thank you (!!) for all your help – I could not have generated a fraction of these data without your assistance. You have taught me so much and been an irreplaceable asset throughout this process. Wherever I end up, you will also have a home in my lab.

Over the course of my PhD, I have been given several opportunities to expand my research network and learn from the leaders in my field. To my external collaborators, Drs. Rob DeConto and Martin Ziegler, thank you for welcoming me into your universities and labs. Ruthie, thank you for your friendship, encouragement, and masterful wordsmithing. You are an amazing scientist and person. Attending the Urbino Summer School in Paleoclimatology was an incredible learning experience, and introduced me to a cohort of fantastic young scientist, with whom I have no doubt will result in countless future collaborations and continued friendships.

To my friends, Siobhan, Mattie, Sarah, Kristy, Kara, Robin, Lachlan, Daniel, Sebastian, Lexi, Ben, Rachel, Kyle, and Jess (and others who I have rudely neglected to list), thank you for being there during the lows, celebrating during the highs, and keeping me sane throughout this process.

Bruce, you saw my potential as a scientist well before I ever did. At every point during my PhD, you have challenged me to question conventional paradigm and encouraged me to be a better scientist. Our frequently colorful, but (almost) always intellectually-engaging debates continually reinvigorated my passion for the Earth Sciences. Though I hate to admit it, I think you may be right about a lot of stuff (but I still don’t like the term ‘memory’). Thank you for changing the way I see the world and approach science.

Linda, in the fall of 2013, I attended my first GSA meeting with one goal: to meet you. Your body of work was not only prolific, but also thoughtful, innovative, and fun to read. Before we had ever talked in person, I knew that I wanted to work with you. Under your mentorship, I have grown as a scientist and a person. You allowed me the freedom to develop my own research questions and explore my scientific identity, provided me with every opportunity to succeed, and kept me focused and grounded. Any accolade or accomplishment that I have received is much more a reflection on you than me. Thank you for taking a chance on a young woman from a no-name school in Utah who really loves the Eocene.

James, thank you for your unwavering companionship and support. You taught me the importance of first-order thinking and for that I am a far better scientist. You have been my biggest cheerleader and your constant encouragement kept me going, even when I didn’t want to. Daily reminder, and whatnot.

Dissertation research was supported by NSF-PLR-1543031 (LCI), a Summer Dissertation Fellowship from the Graduate School of Syracuse University (EJJ), and by grants from Sigma Xi and GSA and the SU Department of Earth Sciences (EJJ). Samples were originally collected during fieldwork funded by OPP-9908828 to Richard Aronson and OPP-9908856 to Daniel Blake; specimens are housed at Syracuse University and supplemented by gracious loans from Florida Museum of Natural History. I thank Lora Wingate at the University of Michigan Stable Isotope Lab and David Dettman at the University of Arizona Environmental Isotope Laboratory for performing the conventional stable isotope analyses and Edward Berry at the State University of New York—Upstate for assisting with X-Ray diffraction analyses.

“The most erroneous stories are those we think we know best – and therefore never scrutinize or question.”

-Stephen Jay Gould, *Full House: The Spread of Excellence from Plato to Darwin* (1996)

TABLE OF CONTENTS

LIST OF FIGURES

List of tables

Chapter 1:

Introduction, overview, and summary of key findings

1.1 Introduction

As atmospheric CO_2 levels rise well-beyond the range of values typical of an interglacial (Lüthi et al., 2008) and global temperatures continue on an upward trajectory (Hansen et al., 2006), extreme weather events, such as heat waves, draughts, and floods, have become more common (Hansen et al., 2012). Ringing in the dawn of a new geologic epoch defined by human impact on the Earth system (Ruddiman, 2013), we face the seemingly unknown. More and more, the climate community has turned to the deep time record to understand how the Earth system operated during warm and transitional intervals in its past, searching for insight into future conditions. A recent study found that under a high emission scenario (RCP 8.5), by the year 2150 our climate would most closely resemble that of the greenhouse warmth of the Eocene Epoch (~56-34 Ma; Burke et al., 2018). Accurate paleo-reconstruction of the Eocene climate may therefore hold the key to understanding future change.

Despite the wealth of studies dedicated to understanding Eocene climate, there are still several fundamental unanswered questions regarding Earth surface conditions during this societally important time interval. In some places, proxy data from similar latitudes yield diverging temperature estimates (e.g., Bijl et al., 2009; Douglas et al., 2014; Hines et al., 2017), as do multi-proxy studies from the same location (e.g., Douglas et al., 2014). Further, proxy-model mismatches are abundant (e.g., Huber and Caballero, 2011; Lunt et al., 2012), suggesting we may be neglecting important aspects of climate dynamics and underlying assumptions guiding our interpretation of proxy data. Studies utilizing novel techniques focused on resolving these discrepancies are therefore required to understand not just Eocene paleotemperatures, but the global-scale paleoclimate dynamics that drove climate change in the past, with implications for future climate predictions.

The work presented in this dissertation is focused on improving the accuracy of proxy-based paleoclimate reconstructions by developing new methods and approaches for combating observable biases in the climate record and limitations of proxy application. In the sections that follow I outline some of these key biases, uncertainties, and limitations, particularly with respect to seasonal SST data. I summarize how my dissertation work has provided advancement in these areas, both by creating a framework to more meaningfully contextualize proxy data and by developing methods to maximize the fidelity of proxy data (Chapters 2 and 3). I then apply these new approaches to reconstruct seasonal changes in nearshore waters off the eastern margin of the Antarctic Peninsula between the middle and late Eocene (Chapters 4 and 5).

1.2 Toward identifying sampling location biases and improving paleoclimate reconstructions

Ultimately, the overarching goals of the paleoclimate community are to generate a high-fidelity record of mean global temperature and latitudinal temperature gradients under different climatic regimes across the Phanerozoic. Integral to these goals are proxy-derived SST data, which are used both to estimate these metrics and benchmark climate modeling studies. However, sampling locations for proxy materials are inherently unevenly distributed, favoring coastal settings (in the Cretaceous through Cenozoic) and epeiric seas (in the Paleozoic through Jurassic).

SSTs are controlled, to a first-order, by intra-annual and meridional differences in solar insolation, and thus should correlate with latitude; however, modern data (Hirahara et al., 2014) reveal large and systematic zonal variability, qualitatively associated with atmospheric and oceanic circulation patterns. Moreover, the magnitude of zonal variability is proportional to the ratio of land to ocean, with significant SST deviations along coastlines and within shallow semirestricted seas. As proxy-based paleo-SST estimates dominantly come from these environments, this finding has profound implications for reconstructing ancient climates and may help explain many of the proxy-model mismatches in paleoclimatic studies.

In **Chapter 2** (Judd et al., *submitted*), I explore global patterns in the zonal heterogeneity of modern SSTs, with a specific focus on shallow continental seas (i.e., epeiric sea analogs) and nearshore marine settings to demonstrate how sampling location bias impedes straightforward interpretation of proxy-derived paleotemperatures. SST data from these environments are not representative of the zonal mean temperature, but instead exhibit geographic, process-driven offsets, providing insight into how paleoclimate inferences drawn from these data might skew paleoclimate interpretations.

I demonstrate that modern epeiric sea analogs (e.g., the Baltic and Red seas) are almost always warmer and more seasonal than open ocean values from the same latitude. Oxygen isotope values of carbonate ($\delta^{18}O_{carb}$), used to infer SST, are generally more depleted in the Paleozoic, which is often attributed to either diagenesis or a secular evolution of seawater chemistry (e.g., Veizer and Prokoph, 2015). However, nearly all of these data come from epeiric seas. Therefore, these data should not be interpreted in the context of the global open ocean signal, but rather likely reflect the true local conditions of sparsely sampled warm shallow seas.

Analysis of modern nearshore environments reveal similar systematic offsets in both the mean annual temperature (MAT) and mean annual range of temperatures (MART) from zonal mean values. These deviations correlate with meridional advection (along western boundaries) and coastal upwelling patterns (along eastern boundaries), associated with gyre circulation. Using the location of sampling sites from which there are early Eocene proxy-SST data (Hollis et al., 2019), I demonstrate how preferential sampling of coastal environments can generate spurious estimates of the latitudinal temperature gradient, even in the modern world. Finally, I show that historical climate model simulations (HadCM3, CCSM4, and CESM) struggle to reproduce the observed patterns of zonal variability in SST, particularly at sites of large-scale eddy shedding and coasting upwelling, likely contributing to many proxy-model mismatches.

Despite these environment-specific SST deviations, first-order patterns are systematic and therefore predictable in deep time based on paleogeography and assumptions regarding gyre circulations. By understanding the processes controlling these deviations, we can apply a qualitative correction to account for sampling biases, enabling a more accurate interpretation of paleoclimate conditions in Earth's past. This work challenges the assumption of zonal uniformity in SST frequently invoked in paleoclimatic and paleoceanographic studies and provides a new framework within which to more meaningfully contextualize and interpret the deep time climate record.

1.3 Toward improving the interpretation of seasonally-resolved proxy data

Seasonally-resolved data are a powerful and underutilized tool for understanding the evolution of Earth's climate. The analyses of Chapter 2 highlight the utility of seasonally-resolved proxy records in reconstructing ancient climate dynamics and identifying seasonal biases in other proxy data (e.g., TEX_{86}). Further, understanding how seasonal extremes vary through time is critical to accurately forecasting regional biotic responses to global warming, and to identifying the mechanisms responsible for past climate change. Yet, seasonal data are rare in paleoclimatic studies, largely due to the dearth of materials that accumulate continuously throughout the year. Fossil bivalves, which growth through accretion, are one of the most useful materials, as the geochemical signature (e.g., stable oxygen isotopes) preserved within their shells can provide a seasonally-resolved record of SST. However, bivalves grow at variable rates throughout the year, which can convolute the seasonal signal and obfuscate the full seasonal amplitude. Therefore, to robustly interpret isotope profiles in a climatic context requires transforming data from their original sampling distance values into the time domain.

In **Chapter 3** (Judd et al., 2017), I present a computational bivalve growth rate model, which facilitates the temporal alignment of high-resolution serially-sampled oxygen isotope data from accretionary organisms. The MATLAB® script derives seasonal growth rate and temperature functions using only serially-sampled $\delta^{18}O_{carb}$ data and associated sampling distance values. By assuming that water temperature varies sinusoidally throughout the year and that growth rates can be described using skewed-clipped sinusoids, the program iteratively generates synthetic isotope profiles by varying the parameters of the growth rate and temperature functions. A final solution is reached by minimizing the difference between the synthetic and observed isotope profiles. This model improves our ability to recover the full seasonal amplitude of temperature variability in deep time, improving reconstructions of both seasonal and mean annual SSTs.

In addition to its paleoclimate utility, this procedure also has several (paleo-)ecological applications. In environments where temperatures can be directly measured or constrained using other methods, the temperature function can be *a priori* parameterized with these values. The resulting growth rate functions can then be used, with high fidelity, to compare seasonal growth patterns both within and across populations of accretionary organisms, through space and time.

1.4 Toward reconciling diverging climate records in the Eocene Southern Ocean

Austral high-latitude paleoclimate data from the Eocene are integral to understanding climatic conditions during greenhouse intervals and the evolution of Earth's climate into an icehouse. Two mechanisms have been proposed to explain late Eocene cooling, culminating in the inception of a Southern Hemisphere ice sheet: 1) the thermal isolation of Antarctica as a result of tectonic reconfiguration of ocean gateways and initiation of the Antarctic Circumpolar Current (ACC; Kennett, 1977), and 2) a decrease in atmospheric CO_2 levels, driving global cooling (Anagnostou et al., 2016; Deconto and Pollard, 2003; Raymo and Ruddiman, 1992). Earlier modelling studies demonstrated the importance of pCO_2 in providing a threshold for glaciation (Deconto and Pollard, 2003; Huber and Nof, 2006). However, recent evidence of ephemeral glaciation (e.g., Carter et al., 2017; Gulick et al., 2017; Scher et al., 2014) preceding significant decreases in pCO_2 (e.g., Pagani et al., 2011; Zhang et al., 2013) and discrepancies in model-specific pCO_2 glaciation thresholds (e.g., Gasson et al., 2014) have led to renewed debate.

Seasonally-resolved proxy data from Antarctica during the Eocene can provide unique insight, helping to answer several fundamental questions regarding Earth's climate during this transition. First, as the inception and expansion of ice sheets is largely dependent on summer temperatures, seasonal temperature data can help constrain the timing of the incipient Antarctic Ice Sheet. Second, as changes in ocean circulation should result in a different change to the annual cycle than decreasing pCO_2, these data can help distinguish between the two proposed cooling mechanisms. Finally, seasonal precipitation data from the warm middle Eocene can address open questions regarding the potential for high latitude monsoons during times of greenhouse warmth (e.g., Jacques et al., 2014; Schubert et al., 2012; West et al., 2015).

In **Chapters 4 and 5**, I assess climatic conditions along the eastern margin of the Antarctic Peninsula during the middle (~42 Ma) and late (~38 Ma) Eocene, using accretionary bioarchives from the La Meseta Formation, Seymour Island, Antarctica. Oxygen isotope profiles, sampled across the ontogeny of bivalves and processed with the growth model of Chapter 3 (Judd et al., 2017), reveal the annual temperature cycle in nearshore Antarctic waters and organic carbon isotope analyses across tree rings of driftwood provide insights into the seasonal phasing of precipitation. These results are compared to other existing proxy records from the Southern Ocean, and contextualized using climate models and insights gained from the analyses of the modern ocean in Chapter 2.

I find evidence of a warm and seasonal temperature regime during the middle Eocene, with subequal precipitation in winters and summers, with a closest modern analog to coastal Argentinian waters. Even under a high obliquity, and thus high seasonality, scenario, I am unable to reproduce the seasonal amplitude inferred from the proxy data with climate model simulations. Given that that the model is parameterized with a computationally-efficient slab ocean, these results suggest that surface ocean circulation is most likely responsible for the high seasonal conditions. I propose that nearshore eastern peninsular waters were situated at the confluence of two currents: the cool western boundary of the proto-Weddell Gyre and a warmer current extending either extending across a shallow Drake Passage or branching from the South Atlantic Gyre. Similar to the Brazil-Malvinas Confluence of the modern analog location, the position of the currents would oscillate seasonally, creating warmer winters, cooler summers, and overall more seasonal conditions.

Comparison of middle Eocene proxy data with other high-austral locations (e.g., Bijl et al., 2009; Hollis et al., 2012) indicate warmer conditions in the South Pacific reach of the Southern Ocean than in the South Atlantic Sector. In Chapter 2, I identify strong hemispheric asymmetries in the zonal variability of SSTs, which relate to differences in tectonic configuration. Meridional advection in noncontiguous ocean basins, such as those in the modern boreal high latitudes, increase the zonal variability in both annual and seasonal SSTs. In contrast, the powerful zonal flow of the Antarctic Circumpolar Current (ACC) in the Southern Hemisphere homogenizes SSTs. However, in the absence of an open Drake and Tasman passages, as was the case in the middle Eocene (e.g., Pfuhl and McCave, 2005; Scher and Martin, 2006; Stickley et al., 2004), the Southern Hemisphere high latitudes would have had a tectonic configuration that more closely resembles the modern Artic region. Therefore, increased zonal heterogeneity should be the expectation, reflecting the effect of latitudinal heat transport within subpolar gyres, a hypothesis consistent with existing SST and precipitation proxy data.

The late Eocene temporally-aligned oxygen-isotope derived SSTs are cooler and less seasonal than the middle Eocene data. Remarkably, the ~2 ºC cooling in MAT between the two intervals is manifest entirely by a reduction in summertime temperatures. Similar to the model results from the middle Eocene, we were unable to reproduce the low amplitude annual cycle with climate models, even when parameterized with low eccentricity, high eccentricity, and a July perihelion (i.e., the lowest seasonality orbital configuration in the Southern Hemisphere). Additionally, we observe no change in seasonality with changing pCO_2. These findings, again, suggest that the pattern is controlled by ocean circulation. The trend is best explained by the opening of the Drake Passage (Scher and Martin, 2006) and the initiation of a (weak) circum-global current, deflecting the warm equatorial-derived current hypothesized to reach the Antarctic Peninsula during middle Eocene summers. This proposed model is consistent with other Southern Ocean proxy data, which record a cooling trend in at the East Tasman Plateau (i.e., within the reach of a circum-global current; Bijl et al., 2009) and a warming trend at the lower-latitude New Zealand sites (i.e., outside of the reach of a circum-global current; Hines et al., 2017). These findings, therefore support the hypothesis that tectonically-driven changes in ocean circulation, rather than pCO_2, was likely responsible for initial late Eocene cooling, preconditioning the continent for large scale glaciation at the close of the epoch.

A comparison of existing SST proxy data from the La Meseta Formation yields good agreement between the data presented here and MAT estimates from clumped isotope analyses of fossil bivalves. However, SST estimates from the organic biomarker, TEX_{86}, are consistently warmer, and the cooling trend observed between the middle and late Eocene approximates the pattern observed in the reduction of summertime temperatures. TEX_{86} is postulated to have a seasonal (generally summertime) bias (e.g., Hollis et al., 2012; Sluijs et al., 2011, 2006). The multi-proxy comparison presented here provide direct evidence of this bias, at least in the high latitude nearshore setting of the La Meseta Formation, demonstrating the necessity and utility of seasonally-resolved proxy data in reconstructing ancient climates.

References

Anagnostou, E., John, E.H., Edgar, K.M., Foster, G.L., Ridgwell, A., Inglis, G.N., Pancost, R.D., Lunt, D.J., Pearson, P.N., 2016. Changing atmospheric CO 2 concentration was the primary driver of early Cenozoic climate. Nature 533, 380–384. doi:10.1038/nature17423

Bijl, P.K., Schouten, S., Sluijs, A., Reichart, G.-J., Zachos, J.C., Brinkhuis, H., 2009. Early Palaeogene temperature evolution of the southwest Pacific Ocean. Nature 461, 776–779. doi:10.1038/nature08399

Burke, K.D., Williams, J.W., Chandler, M.A., Haywood, A.M., Lunt, D.J., Otto-Bliesner, B.L., 2018. Pliocene and Eocene provide best analogs for near-future climates. Proc. Natl. Acad.

Sci. 115, 201809600. doi:10.1073/pnas.1809600115

Carter, A., Riley, T.R., Hillenbrand, C.D., Rittner, M., 2017. Widespread Antarctic glaciation during the Late Eocene. Earth Planet. Sci. Lett. 458, 49–57. doi:10.1016/j.epsl.2016.10.045

Deconto, R.M., Pollard, D., 2003. Rapid Cenozoic glaciation of Antarctica induced by declining atmospheric CO2. Nature 421, 245–249.

Douglas, P.M.J., Affek, H.P., Ivany, L.C., Houben, A.J.P., Sijp, W.P., Sluijs, A., Schouten, S., Pagani, M., 2014. Pronounced zonal heterogeneity in Eocene southern high-latitude sea surface temperatures. Proc. Natl. Acad. Sci. U. S. A. 111, 1–6. doi:10.1073/pnas.1321441111

Gasson, E., Lunt, D.J., Deconto, R., Goldner, A., Heinemann, M., Huber, M., Legrande, A.N., Pollard, D., Sagoo, N., Siddall, M., Winguth, A., Valdes, P.J., 2014. Uncertainties in the modelled CO2 threshold for Antarctic glaciation. Clim. Past 10, 451–466. doi:10.5194/cp-10-451-2014

Gulick, S.P.S., Shevenell, A.E., Montelli, A., Fernandez, R., Smith, C., Warny, S., Bohaty, S.M., Sjunneskog, C., Leventer, A., Frederick, B., Blankenship, D.D., 2017. Initiation and long-term instability of the East Antarctic Ice Sheet. Nature 552, 225–229. doi:10.1038/nature25026

Hansen, J., Sato, M., Ruedy, R., 2012. Perception of climate change. Proc. Natl. Acad. Sci. 109, E2415–E2423. doi:10.1073/pnas.1205276109

Hansen, J., Sato, M., Ruedy, R., Lo, K., Lea, D.W., Medina-Elizade, M., 2006. Global temperature change. Proc. Natl. Acad. Sci. U. S. A. 103, 14288–14293. doi:10.1073/pnas.0606291103

Hines, B.R., Hollis, C.J., Atkins, C.B., Baker, J.A., Morgans, H.E.G., Strong, P.C., 2017.

Reduction of oceanic temperature gradients in the early Eocene Southwest Pacific Ocean. Palaeogeogr. Palaeoclimatol. Palaeoecol. 475, 41–54. doi:10.1016/j.palaeo.2017.02.037

Hirahara, S., Ishii, M., Fukuda, Y., 2014. Centennial-scale sea surface temperature analysis and its uncertainty. J. Clim. 27, 57–75. doi:10.1175/JCLI-D-12-00837.1

Hollis, C.J., Dunkley Jones, T., Anagnostou, E., Bijl, P.K., Cramwinckel, M.J., Cui, Y., Dickens, G.R., Edgar, K.M., Eley, Y., Evans, D., Foster, G.L., Frieling, J., Inglis, G.N., Kennedy, E.M., Kozdon, R., Lauretano, V., Lear, C.H., Littler, K., Lourens, L., Meckler, A.N., Naafs, B.D.A., Pälike, H., Pancost, R.D., Pearson, P.N., Röhl, U., Royer, D.L., Salzmann, U., Schubert, B.A., Seebeck, H., Sluijs, A., Speijer, R.P., Stassen, P., Tierney, J., Tripati, A., Wade, B., Westerhold, T., Witkowski, C., Zachos, J.C., Zhang, Y.G., Huber, M., Lunt, D.J., 2019. The DeepMIP contribution to PMIP4: methodologies for selection, compilation and analysis of latest Paleocene and early Eocene climate proxy data, incorporating version 0.1 of the DeepMIP database. Geosci. Model Dev. 12, 3149–3206. doi:10.5194/gmd-12-3149-2019

Hollis, C.J., Taylor, K.W.R., Handley, L., Pancost, R.D., Huber, M., Creech, J.B., Hines, B.R., Crouch, E.M., Morgans, H.E.G., Crampton, J.S., Gibbs, S., Pearson, P.N., Zachos, J.C., 2012. Early Paleogene temperature history of the Southwest Pacific Ocean: Reconciling proxies and models. Earth Planet. Sci. Lett. 349–350, 53–66. doi:10.1016/j.epsl.2012.06.024

Huber, M., Caballero, R., 2011. The early Eocene equable climate problem revisited. Clim. Past 7, 603–633. doi:10.5194/cp-7-603-2011

Huber, M., Nof, D., 2006. The ocean circulation in the southern hemisphere and its climatic impacts in the Eocene. Palaeogeogr. Palaeoclimatol. Palaeoecol. 231, 9–28.

doi:10.1016/j.palaeo.2005.07.037

Jacques, F.M.B., Shi, G., Li, H., Wang, W., 2014. An early-middle Eocene Antarctic summer monsoon: Evidence of “fossil climates.” Gondwana Res. 25, 1422–1428. doi:10.1016/j.gr.2012.08.007

Judd, E.J., Wilkinson, B.H., Ivany, L.C., 2017. The life and time of clams: Derivation of intra-annual growth rates from high-resolution oxygen isotope profiles. Palaeogeogr. Palaeoclimatol. Palaeoecol. 490, 70–83. doi:10.1016/j.palaeo.2017.09.034

Kennett, J.P., 1977. Cenozoic evolution of Antarctic glaciation, the circum-Antarctic Ocean, and their impact on global paleoceanography. J. Geophys. Res. 82, 3843–3860. doi:10.1029/JC082i027p03843

Lunt, D.J., Jones, T.D., Heinemann, M., Huber, M., LeGrande, A., Winguth, A., Loptson, C., Marotzke, J., Roberts, C.D., Tindall, J., Valdes, P., Winguth, C., 2012. A model-data comparison for a multi-model ensemble of early Eocene atmosphere-ocean simulations: EoMIP. Clim. Past 8, 1717–1736. doi:10.5194/cp-8-1717-2012

Lüthi, D., Le Floch, M., Bereiter, B., Blunier, T., Barnola, J.M., Siegenthaler, U., Raynaud, D., Jouzel, J., Fischer, H., Kawamura, K., Stocker, T.F., 2008. High-resolution carbon dioxide concentration record 650,000-800,000 years before present. Nature 453, 379–382. doi:10.1038/nature06949

Pagani, M., Huber, M., Liu, Z., Bohaty, S.M., Henderiks, J., Sijp, W., Krishnan, S., DeConto, R.M., 2011. The role of carbon dioxide during the onset of antarctic glaciation. Science (80-.). 334, 1261–1264. doi:10.1126/science.1203909

Pfuhl, H.A., McCave, I.N., 2005. Evidence for late Oligocene establishment of the Antarctic Circumpolar Current. Earth Planet. Sci. Lett. 235, 715–728. doi:10.1016/j.epsl.2005.04.025

Raymo, M.E., Ruddiman, W.F., 1992. Tectonic forcing of late Cenozoic climate. Nature 359, 117–122. doi:10.1038/359117a0

Ruddiman, W.F., 2013. The Anthropocene. Annu. Rev. Earth Planet. Sci. 41, 45–68. doi:10.1146/annurev-earth-050212-123944

Scher, H.D., Bohaty, S.M., Smith, B.W., Munn, G.H., 2014. Isotopic interrogation of a suspected late Eocene glaciation. Paleoceanography 29, 628–644. doi:10.1002/2014PA002648

Scher, H.D., Martin, E.E., 2006. Timing and climatic consequences of the opening of Drake Passage. Science (80-.). 312, 428–430. doi:10.1126/science.1120044

Schubert, B.A., Jahren, A.H., Eberle, J.J., Sternberg, L.S.L., Eberth, D.A., 2012. A summertime rainy season in the Arctic forests of the Eocene. Geology 40, 523–526. doi:10.1130/G32856.1

Sluijs, A., Bijl, P.K., Schouten, S., Röhl, U., Reichart, G.J., Brinkhuis, H., 2011. Southern ocean warming, sea level and hydrological change during the Paleocene-Eocene thermal maximum. Clim. Past 7, 47–61. doi:10.5194/cp-7-47-2011

Sluijs, A., Schouten, S., Pagani, M., Woltering, M., Brinkhuis, H., Sinninghe Damsté, J.S., Dickens, G.R., Huber, M., Reichart, G.-J., Stein, R., Matthiessen, J., Lourens, L.J., Pedentchouk, N., Backman, J., Moran, K., the Expedition, S., 2006. Subtropical Arctic Ocean temperatures during the Palaeocene/Eocene thermal maximum. Nature 441, 610–613. doi:10.1038/nature04668

Stickley, C.E., Brinkhuis, H., Schellenberg, S.A., Sluijs, A., Röhl, U., Fuller, M., Grauert, M., Huber, M., Warnaar, J., Williams, G.L., 2004. Timing and nature of the deepening of the Tasmanian Gateway. Paleoceanography 19, 1–18. doi:10.1029/2004PA001022

Veizer, J., Prokoph, A., 2015. Temperatures and oxygen isotopic composition of Phanerozoic oceans. Earth-Science Rev. 146, 92–104. doi:10.1016/j.earscirev.2015.03.008

West, C.K., Greenwood, D.R., Basinger, J.F., 2015. Was the Arctic Eocene “rainforest” monsoonal? Estimates of seasonal precipitation from early Eocene megafloras from Ellesmere Island, Nunavut. Earth Planet. Sci. Lett. 427, 18–30. doi:10.1016/j.epsl.2015.06.036

Zhang, Y.G., Pagani, M., Liu, Z., Bohaty, S.M., Deconto, R., 2013. A 40-million-year history of atmospheric CO 2. Phil Trans R Soc A A 40-million-year history of atmospheric CO 2. doi:10.1098/rsta.2013.0096

Chapter 2:

A dynamical framework for interpreting ancient sea surface temperatures

Chapter 2 is submitted for publication as:

Judd, E.J., Bhattacharya, T., and Ivany, L.C. A dynamical framework for interpreting ancient sea surface temperatures.

2.1 Abstract

Proxy-derived sea-surface temperature (SST) estimates are integral to understanding ancient climate systems, benchmarking climate models, and informing future climate predictions. However, efforts to estimate past global mean temperature and latitudinal gradients must contend with spatial heterogeneity in ocean temperatures. Here, we use modern SST data to show that the environments from which most paleoclimatic data are drawn, shallow epeiric seas and continental margins, are systematically offset from zonal mean temperatures. Epeiric seas are nearly always warmer and more seasonal than open-ocean values from the same latitudes. SSTs along continental margins exhibit consistent deviations from open ocean temperatures that are directly related to gyre circulation. These insights have profound implications for paleoclimate reconstruction. The warm temperatures inferred from Paleozoic proxy data may largely reflect the fact that data derive almost entirely from epeiric sea environments. Moreover, even in shallower time under-sampling of the full range of dynamical environments associated with ocean gyre circulation can result in spurious estimates of latitudinal temperature gradients. A pseudoproxy analysis based on existing Paleogene sampling localities demonstrates how a proxy record biased toward these nearshore environments can artificially attenuate inferred paleo-SST gradients. However, recognition of these global patterns allows for a predictive framework within which to more robustly interpret existing and new proxy data, test and improve Earth system model fidelity, and reconstruct ancient dynamic regimes.

2.2 Introduction

Substantial attention within the paleoclimate community focuses on quantifying key climate metrics, such as average global temperature, climate sensitivity, and the latitudinal temperature gradient (Caballero and Huber, 2013; Cramwinckel et al., 2018; Evans et al., 2018; Hollis et al., 2019; Zhu et al., 2019). These parameters are relatively easy to calculate in today's well-instrumented world, but efforts to characterize them in deep time present the unique challenge of inferring broad, zonal averages from a sparsely sampled world. The majority of SST data, even for relatively well-studied time intervals, come primarily from continental margins (Dowsett et al., 2013; Hollis et al., 2019) (Fig. 1). This problem of under-sampling the open ocean further intensifies prior to 200 Ma, as nearly all paleo-SST data are restricted to epeiric seas due to recycling of the ocean floor and alteration during orogenesis along continental margins (Veizer and Prokoph, 2015). The specialized environments from which proxy data derive calls into question whether these data can be used to estimate global mean climate parameters, or whether they reflect primarily local dynamical processes. In many cases, local-scale dynamics are invoked post-hoc to explain proxy data disagreement (Hollis et al., 2012), but to date no study has presented a systematic and global analysis of the dynamical processes that influence offsets between proxy locations and global mean climate parameters.

Here, through analysis of modern globally-gridded SSTs, we show that zonal heterogeneity of modern SSTs is significant, but first-order patterns are systematic and therefore predictable in deep time based on paleogeography and its impacts on ocean dynamics (e.g. gyre circulations). We consider the extent to which Earth System Models (ESMs) capture these patterns, and present a framework with which these data can be used to reconstruct past ocean dynamics.

2.3 Zonal heterogeneity and tectonic configurations

We investigate spatial patterns in the modern distribution of SSTs, in terms of both the mean annual temperature (MAT) and mean annual range of temperatures (MART), using globally-gridded modern climatological reanalysis data from the modern ocean (Hirahara et al., 2014). In order to identify patterns related to the direction and magnitude of a given location's deviation from the zonal mean, we introduce two new parameters: the zonal MAT anomaly (δ_{MAT}) and the zonal MART anomaly (δ_{MART}). Positive δ_{MAT} values reflect locations warmer than anticipated for their given latitude, while negative values are associated with locations cooler than zonal MAT. Similarly, positive and negative δ_{MART} values demarcate locations that are more or less seasonal than the zonal mean MART, respectively.

Global maps of δ_{MAT} and δ_{MART} reveal large-scale systematic heterogeneity along latitudinal bands, qualitatively reflecting processes associated with the wind-driven ocean circulation (Figs. 2A,B). Though the modern zonally-averaged pole-to-equator temperature gradient is ~30ºC, 70% of discrete latitudinal bands exhibit more than 5ºC variability in MAT, and 14% of latitudes exhibit more than 10ºC variability (Fig. 2C). Similar variability can also be observed in the paleo record, where, for example, during greenhouse intervals with suppressed latitudinal gradients, longitudinal variability in proxy temperature estimates within narrow latitudinal bins can even exceed the inferred latitudinal temperature gradient (Evans et al., 2018; Hollis et al., 2019). While some of the spread of paleo-SST estimates within these bins may be due to uncertainty in proxy calibration, time averaging, or analytical error, much of the longitudinal variation could alternatively reflect true spatial heterogeneity arising from ocean dynamics.

The majority of latitudes exhibit a broad range of MAT and MART values, but the magnitude and trend of the variability is hemispherically asymmetric (Fig. 2C,D). The variance of both MAT and MART across latitudes exhibits a statistically significant positive relationship with the amount of land cover (Fig. S1), suggesting this pattern is largely driven by tectonic configuration and can thus be predicted even in the past. This is best exemplified in the high latitudes where the range of both MAT and MART in the Southern Hemisphere begins rapidly decreasing at

~55°S, yet boreal ranges remains high up to ~70°N. With no landmasses to divert zonal flow, the modern Antarctic Circumpolar Current homogenizes high-austral SSTs, while meridional flow within subpolar gyres in the noncontiguous high-boreal ocean basins amplifies the zonal heterogeneity of SSTs (Judd et al., 2019). This observation implies that the presence or absence and latitudinal position of circum-global currents should be considered when evaluating paleo-SSTs to determine meridional temperature gradients. It also suggests that large landmasses inflate zonal variability, and highlights that past changes in tectonic configuration exert an important influence on regional SST patterns.

2.4 Environment specific variability in SSTs

Two types of geologic settings produce the vast majority of marine paleotemperature proxy data: epeiric seas and continental margins (e.g., Fig. 1). To visualize the offsets related to these environments, we cross plot of δ_{MART} and δ_{MAT}. Locations emblematic of zonal mean climate will plot near the origin; indeed, over 40% of modern SST data fall within ±1°C of the zonal mean for both variables. However, a disproportionate number of data from epicontinental seas and continental margins exhibit greater than 1°C deviation from the zonal mean. These deviations are non-random and driven by the particular dynamics in each of these environments.

2.4.1 Epeiric seas and semi-enclosed basins

Subduction has recycled nearly all oceanic crust and accompanying sediment older than about 180 Ma (Müller et al., 1997), and many materials used to reconstruct SST (e.g., organic biomarkers and most microplankton) are unavailable until the late Mesozoic or early Cenozoic (Brassell, 2014; Schouten et al., 2004; Tappan and Loeblich, 1973). By necessity therefore, nearly all Paleozoic and many Mesozoic SST reconstructions rely instead on the geochemistry of skeletal macrofossils preserved within marine successions deposited on the continents and recovered in outcrop. Given the prevalence of and reliance on these pre-Cenozoic epeiric SST records, our ability to reconstruct ancient climate systems hinges on how representative these environments are of global climate conditions at any given time.

Today, there are few true epeiric seas. However, we identify ten semi-enclosed and marginal seas from across a range of latitudes to use as modern analogs (Fig. 3A). On a cross-plot of δ_{MART} and δ_{MAT}, 75% of the data from epeiric sea analog locations plot in the upper righthand quadrant, indicating warmer and more seasonal conditions than the zonal mean (Fig. 3B, Table S1). In total, 81% of epeiric sea analog data are warmer (i.e., $+\delta_{MAT}$) and 92% more seasonal (i.e., $+\delta_{MART}$) than zonally anticipated. Further, across the entire global dataset (N = 43,723 ocean grid cells), only 141 cells have δ_{MART} and δ_{MAT} values both exceeding $+2.5^{o}$C, and remarkably, 114 (~80%) of these come from epeiric seas.

This analysis demonstrates that semi-enclosed basins are unusually warm and seasonal compared to the vast majority of open ocean locations situated at the same latitudes. These bodies of water are smaller and shallower, and often seasonally stratified, allowing surface waters to change temperature more rapidly than larger, deeper open ocean basins. The surface of ice-free epicontinental seas may heat up more strongly with the development of a strong thermocline in the summer. Seasonal runoff with strong temperature variability may also contribute to an amplified seasonal cycle in many semi-enclosed basins. This result has important, broad-reaching implications for paleoclimate studies: SST records older than the Cretaceous very likely overestimate zonal, and therefore global, temperatures.

The oxygen isotope record of skeletal carbonate and apatite over the Phanerozoic exhibits a secular depletion trend with increasing age, interpreted to reflect: 1) the oxygen isotopic evolution of seawater ($\delta^{18}O_{sw}$) through geologic time, 2) a true temperature signal from a much warmer Paleozoic world, or 3) the increased influence of diagenetic alteration with age (Jaffrés et al., 2007; Veizer and Prokoph, 2015). While thorough screening for altered materials has removed some of the most suspect values (Grossman, 2012), broadly, the trend holds true. However, mounting evidence suggests that epeiric seas are chemically and dynamically decoupled from the open ocean. Several authors have demonstrated geochemical differences between coeval open ocean and epeiric sea water masses (Brand et al., 2009; Holmden et al., 1998). Intra-basinal trends in isotope values that suggest epeiric seas have non-marine seawater compositions (Brand et al., 2009; Jimenez et al., 2019; Montañez et al., 2018; Roark et al., 2017) ($\delta^{18}O_{sw}$), and observations of $\delta^{18}O_{sw}$ from modern epeiric sea analogs corroborate this hypothesis (LeGrande and Schmidt, 2006). Given the finding here, we propose that low skeletal $\delta^{18}O$ values in the Paleozoic can be in part explained by distinctive non-marine $\delta^{18}O_{sw}$ values combined with the fact that these environments were likely warmer and more seasonal than their open ocean counterparts. A secular trend in $\delta^{18}O$-inferred temperature may therefore instead reflect changes in the proportional representation of environments from which samples are drawn over time.

2.4.2 Gyre circulation

While most geochemically-derived paleotemperature data from the Paleozoic are relegated to epeiric sea settings where sedimentary rocks are still present and are less likely to have been deformed, many later Mesozoic and Cenozoic SST data come from settings in proximity to a continental margin, where both sedimentation rate and preservation potential are higher than in the deep sea (Gregor, 1985). For example, in both the Eocene and Pliocene, epochs of particular interest for studies that attempt to constrain climate sensitivity and latitudinal temperature gradients in the future using analogs from the past (Burke et al., 2018), more than half of all sampling localities are found within 500 km of a coastline (Cramwinckel et al., 2018; Dowsett et al., 2013; Evans et al., 2018; Hollis et al., 2019; Lunt et al., 2012; Zhu et al., 2019) (Fig. 1). SSTs in these environments are significantly offset from the zonal mean as a result of large-scale features of the wind-driven surface ocean circulation.

Eastern and western ocean margins each feature deviations in both δ_{MART} and δ_{MAT} related to patterns of wind-driven surface ocean circulation (Forget et al., 2015; Fukumori et al., 2017). Along western margins, 88% of grid cells with poleward flow are warmer than the zonal mean (Fig. 4A), reflecting advection of warm water by the fast-moving western boundary currents of subtropical gyres. 79% of data from the western margins are also more seasonal than the zonal mean, reflecting the strong seasonality in the meridional advection of warm water[29]. This pattern reverses in the higher latitudes of the noncontiguous northern hemisphere ocean basins (>40^{o}N), where equatorward flow from the subpolar gyres generates anomalously cold δ_{MAT} values (Fig. 4B,S2,S3, Table S1). On eastern ocean margins, 90% of lower-latitude westward flowing locations have negative δ_{MAT} values, highlighting the role of upwelling and radiative cooling in generating cold temperatures in subtropical eastern margins (Seager et al., 2003) (Fig. 4B, Table S1). The majority of data from eastern margins are much less seasonal than the zonal mean or western margins (Table S1), and poleward of 40^{o}N/S, eastward advection of warm waters from western ocean margins generates anomalously warm δ_{MAT} values (Fig. 4B).

The paleoclimatic implications of these systematic patterns of δ_{MART} and δ_{MAT} are broad and often overlooked. For time intervals where paleoclimatic data preferentially sample eastern or western ocean boundaries, estimates of latitudinal temperature gradients may be significantly steepened or attenuated simply as a result of sampling bias (Fig. 4B). We explore this further by using a pseudoproxy approach to test the extent to which the modern latitudinal temperature gradient can be approximated from SSTs derived only from locations for which there are paleo-SST estimates. Sampling localities were drawn from the DeepMIP compilation, representing three time intervals within the Paleogene: the late Paleocene, the Paleocene Eocene Thermal Maximum, and the Early Eocene Climactic Optimum (Hollis et al., 2019) (Methods, Table S2). A second order polynomial fit through all zonal mean values produces a gradient of 26.2°C between 55°N/S; however, in all three subsets of Paleogene data, this gradient is reduced to 19.8, 19.5, and 21.7°C, respectively, comparable to published estimates for this interval based on proxy data (Cramwinckel et al., 2018) (Fig. 4C). This measurable attenuation reflects a strong sampling bias toward North Atlantic western boundary sites within the subtropical gyre, and eastern boundary sites from higher latitudes and epeiric seas (Fig. S6), all of which culminates in compounding warmer-than-anticipated SSTs, flattening the inferred gradient. The steeper (albeit still reduced) gradient of the Early Eocene Climatic Optimum is due to the addition of several high latitude South Pacific western boundary locations. In the modern ocean, these sites help anchor the high latitudes, however given the noncontiguous nature of the Eocene Southern Ocean, it is unlikely to have had the same effect in deep time. Incidentally, shallower gradients are inferred throughout much of the Paleogene (Cramwinckel et al., 2018; Evans et al., 2018). While it is expected that greenhouse climates exhibit reduced the pole-to-equator temperature gradients, it is yet unclear the magnitude of this reduction. This example demonstrates the ease with which these gradients can be artificially suppressed or inflated when using sparse and unevenly distributed data.

2.5 Comparison with historical ESMs

Many efforts to assess climate sensitivity and latitudinal temperature gradients in deep time have focused on intercomparisons of Earth System Model (ESM) simulations and proxy data (Caballero and Huber, 2013; Haywood et al., 2016; Hollis et al., 2019). In many cases, model simulations require unrealistic boundary conditions (e.g. extremely high pCO_2) to capture patterns present in proxy data (Huber and Caballero, 2011; Lunt et al., 2012). In addition, many ESMs diverge dramatically in their predictions of the seasonal temperature cycle (Gasson et al., 2014). Recently, paleoclimatic data assimilation efforts have shown promise for characterizing past latitudinal temperature gradients (Tierney et al., *in review*). Below, we assess the extent to which models successfully capture observed offsets in δ_{MAT} and δ_{MART} that we have shown strongly influence the localities from which proxy data derive.

Comparisons among three ESMs - CCSM4 (Danabasoglu et al., 2012), CESM (Kay et al., 2015), and HadCM3 (Johns et al., 2003) - suggest that models reasonably simulate zonally heterogeneous SST patterns, with some key exceptions (Fig. 5). Within western boundaries, the models, particularly CESM and CCSM4, show regions that are much warmer than observations, especially at confluence regions with strong eddy heat transports (e.g., where the Gulf Stream diverges from the North American coastline, or the Brazil-Malvinas Confluence) (Fig. 5, Fig. S4). Coarse resolution ocean models, which do not resolve mesoscale processes, are unlikely to capture the correct magnitude of temperature in these regions (Kwon et al., 2010; Ma et al., 2016). For similar reasons, all three models substantially underestimate seasonality along the frontal regions of the North Atlantic and Pacific western boundaries, although this pattern is not consistently manifest across all western boundaries. Furthermore, the models differ in their performance along eastern margins. Model MAT and δ_{MAT} tend to exceed observed values, with the most dramatic offsets at locations of upwelling. CESM, which features an atmospheric model with updates to the cloud parameterization scheme resulting in a less negative shortwave cloud feedback (Gettelman et al., 2012), is more consistent with observed values.

The ESMs also show substantial spread in their estimates of temperature seasonality. Interestingly, while HadCM3 routinely overestimates the seasonality of temperature over land (Gasson et al., 2014), in the ocean MART and δ_{MART} are more consistently underestimated, particularly in highly seasonal (e.g., MART >10°C) northern hemisphere locations (Fig. S4). Conversely, CCSM4 and CESM preferentially overestimate seasonality in the southern hemisphere. However, these two models do not exhibit substantial biases in simulated mean annual temperature or seasonality in modern semi-enclosed basins, our closest epeiric sea analogs (e.g. the Mediterranean). This suggests that these models may more successfully capture offsets between ancient epicontinental seas and zonal mean temperatures.

Overall, models generally perform well but struggle to capture patterns of mean and seasonal temperature variability in specific dynamical environments. In particular, the deviation from observed values of model nearshore MAT and MART outputs, especially in confluence regions, suggests that unresolved coastal dynamical processes in ESMs could be partially responsible for many proxy-model mismatches in paleoclimatic modeling studies.

2.6 Lessons for interpreting paleo-SST data

The analyses presented here demonstrate that proxy-based SST records are unevenly distributed across global paleo-oceans, and that comparable settings in the modern ocean exhibit consistent, geographically systematic offsets from zonal mean values that are not always captured in coarse resolution ESMs. However, incorporating these insights can result in a more dynamically rigorous interpretation of ancient ocean temperature data that can help resolve proxy-model mismatches. We outline three specific lessons below.

First, researchers must use caution when evaluating data drawn from epicontinental seas, as these values are nearly always warmer and more seasonal than the zonal means. Efforts to explicitly model epicontinental seawater oxygen isotopic composition and temperature will be especially useful, particularly when using models that are known to effectively capture the seasonality and temperature of modern semi-enclosed ocean basins.

Second, time intervals where proxy data are only available for certain sides of ocean basins will preferentially reflect certain dynamical regimes that are systematically offset from the zonal mean. Extreme caution should be used when attempting to infer latitudinal temperature gradients from these datasets. Data assimilation methods may be helpful, provided that the models used in these efforts capture zonal heterogeneity in temperature. In addition, data from certain environments, especially regions of intense eddy heat transports, are unlikely to represent zonal mean conditions nor are they likely to be captured by models. A corollary of this lesson is that future sampling efforts for Cenozoic paleoclimate should focus on capturing signals from under-sampled dynamical regimes (e.g. under-sampled ocean margins).

Finally, our work highlights the critical importance of reconstructions of seasonality for constraining the dynamical regimes from which proxy data are drawn. Western and eastern boundary current environments are most reliably differentiated based on their δ_{MART} values (Fig. 4), suggesting that paired measurements of mean annual temperature and seasonal range of temperature can help us constrain the particular dynamical regime they represent. Paleoseasonal deviations also have implications for interpreting proxy-derived MAT, as many proxies are postulated to have seasonal biases in certain environments (Fraile et al., 2009; Hollis et al., 2009; Malevich et al., 2019; Sluijs et al., 2009). Our results suggest that these seasonal biases may play a larger role along western ocean boundaries and epeiric seas, where MART is inflated.

Targeted generation of proxy data from undersampled dynamical regimes and paired measurements of mean temperature and seasonality will allow for better resolution of patterns in, and reasons for, zonal heterogeneity in observed paleotemperatures. A dynamical perspective of this heterogeneity based on the modern ocean allows for improved estimates of global MAT, latitudinal temperature gradients, and climate sensitivity, and could even provide insights relative to shifts in the strength and position of gyre circulation. Ultimately, capitalizing on the framework laid out above provides a way forward, where disagreements among proxy data are no longer impediments to an understanding of ancient temperatures, but rather offer greater clarity about past thermal gradients and ocean dynamics.

2.7 Methods

2.7.1 IODP locations and Eocene and Pliocene SST sites

Coordinates for all IODP drill holes were extracted from the Drill Hole File from the IODP website (http://www.iodp.org/resources/maps-and-kml-tools; n = 3,886). Because this dataset includes all drill hole, rather than individual legs or expeditions, latitudes and longitudes of the sites were rounded to one decimal and duplicate coordinates were removed (n = 1,356). The distance between each location and the nearest coastline was calculated using the dist_from_coast function found on the MATLAB file exchange.

Coordinates of the sites of Pliocene SST data dominantly come from the PRISM4 compilation (Dowsett et al., 2013) and are supplemented with additional locations from the literature. Sites of

Eocene SST data dominantly come from the DeepMIP PMIP4 (Hollis et al., 2012) and similar compilations (Evans et al., 2018), and are supplemented with additional locations from the literature. Duplicate locations were removed from the datasets and distance to the nearest coastline was calculated as with the IODP dataset.

2.7.2 SST data

SST data come from the Japan Meteorological Agency Centennial *in situ* Observation Based Estimates of SST, version 2 (COBE-SST2) (Hirahara et al., 2014). This globally-gridded reanalysis dataset is averaged between 1981 and 2010, providing a climatological mean and eliminating secular trends related to ongoing global warming and quasi-decadal scale climate oscillations (e.g., El Niño Southern Oscillation). The data have a mean monthly temporal resolution and a 1^o x 1^o spatial resolution (N = 43,723 ocean grid cells). These data were used to calculate a suite of climate parameters, including MART, MAT, and their respective zonal anomalies (δ_{MART}, δ_{MAT}).

Calculation of MAT and MART. MAT was calculated by taking the arithmetic mean of the mean monthly temperatures for each ocean grid cell and MART was calculated by taking the difference in temperature between the warmest and coldest month for each ocean grid cell. This accounts for the fact that the timing of the warmest and coldest month might differ in different oceanographic settings. In addition, it also follows the convention for calculating seasonal temperature ranges in sclerochronological proxy data. Overall, individual profiles of mean monthly temperatures at a given location exhibit sinusoidal oscillations, consistent with the theoretical prediction based on intra-annual variability in solar insolation at a given latitude (Haney and Davies, 1976). This pattern breaks down slightly in the high latitude (70 – 90^oN/S), where winter SSTs are constrained by the freezing point of salt water, and in equatorial regions of deep convection (Fig. S5). Averaged across all latitudes, the time between seasonal extremes is approximately 6 months (5.6 ± 1.3 months (1σ)).

Calculation of δ_{MAT} *and* δ_{MART}. To investigate spatial patterns in the direction and magnitude of deviations from zonal means, we introduce two new parameters: the zonal MAT anomaly (δ_{MAT}), or deviation from the zonal mean of a given site's mean annual temperature, and the zonal MART anomaly (δ_{MART}), the deviation from the zonal mean of a site's seasonal range of temperature. These parameters were calculated by averaging all ocean grid cells within a latitudinal band and subtracting the zonal mean from each individual value within that latitudinal band. The units of both of these parameters are $^{\circ}$C, indicating the absolute magnitude of the deviation.

Environment-specific data subdivisions. We investigate spatial patterns within epeiric seas, by identifying ten semi-enclosed or marginal seas to use as modern analogs and extracting the data from all ocean grid cells within these basins. To avoid conflating coastal processes with epeiric sea patterns, we intentionally avoided selecting marginal seas with strong connections to powerful boundary currents, such as the Sea of Japan in the northwest Pacific and the Argentine Sea in the southwest Atlantic. Additionally, we subdivided the data into eight separate datasets representing the eastern and western boundaries of the northern and southern Atlantic and Pacific Ocean basins. These datasets consist of all ocean grid cells that fall within 500 km of coastline, are between $\pm 15^{\circ}$ N/S and $\pm 55^{\circ}$ N/S, and are not already previously categorized as belonging to an epeiric sea modern analog (Fig. S2).

2.7.3 Surface circulation data

Surface current vector data come from the non-linear inverse model ECCO V4r3, which estimates the time-mean ocean circulation using available ocean data and the MITgcm (Forget et al., 2015; Fukumori et al., 2017). Mean monthly data were averaged between 1992 and 2015, to minimize variability from quasi-decadal scale climate oscillations, and were regridded from a 0.5^{o} x 0.5^{o} resolution to a 1^{o} x 1^{o} spatial resolution to match the observations SST data. Mean annual flow direction and 1σ standard deviations were calculated using the CircStat MATLAB Toolbox (Berens, 2009).

2.7.4 Pseudoproxy approach

The modern coordinates for proxy-derived SST data from the Late Paleocene (LP), Paleocene-Eocene Thermal Maximum (PETM), and the Early Eocene Climatic Optimum (EECO) come from the DeepMIP compilation (Hollis et al., 2019). Sites from high latitudes (>55^{o}N/S), the Indian Ocean, and those with no obvious modern analog (e.g., Well 10, West Siberia) were removed from the compilation, resulting in 15 LP, 18 PETM, and 14 EECO pseudoproxy sampling locations. Each site was assigned a representative basin and environment (Table S2) and a sampling swath was established by extracting all grid cells from that environment within $\pm 5^{o}$ of the modern latitude. For example, Lodo Gulch, located in California, USA (36.59^{o}N, 120.64^{o}W) was assigned to the Pacific Ocean eastern boundary; its sampling swath, therefore, includes all Pacific Ocean eastern boundary (i.e., <500 km from the coastline) grid cells between 31.59^{o}N and 41.59^{o}N.

For each time interval, a latitudinal SST gradient was estimated by extracting one modern SST from each of the sampling swaths and fitting the data with a second order polynomial. The exercise was repeated 1000 times, allowing for determination of the mean and standard deviation of the pseudoproxy-inferred latitudinal temperature gradient (Fig. 4C). The exercise was repeated using the same latitudinal bands but extending the sampling swaths across all longitudes. Using this approach, we found no statistically significant reduction to the modern gradient, confirming that the observed reduction to the latitudinal temperature gradient from the first approach (Fig. 4C) was a direct result of environment-specific sampling biases, as opposed to over or under sampling of specific latitudes irrespective of environment.

2.7.5 ESM simulations

We compare observed spatial patterns in SST with historical GCM simulations from CCSM4 (Danabasoglu et al., 2012), CESM (Kay et al., 2015), and HadCM3 (Johns et al., 2003). CCSM4 and HadCM3 were included in the Fifth Climate Model Intercomparison Project (CMIP5), which included PMIP3, while CESM1.2 is a newer version of the NCAR Earth System model, with an updated version of the atmospheric model (CAM5 in CESM1.2 vs. CAM4 in CCSM4). For consistency with our calculation of historical climatology from the COBE SST data product, modeled mean monthly SSTs were regridded from each models' native ocean grid to a 1° x 1° spatial resolution, and averaged over 1976 to 2005 (i.e., the last 30 years of the model simulation). Using similar time intervals for observed and modeled data avoids any offsets that could be related to anthropogenic forcing (e.g., compared pre-industrial model SST to a late 20th century climatology, which could have a strong fingerprint of warming).

Figures

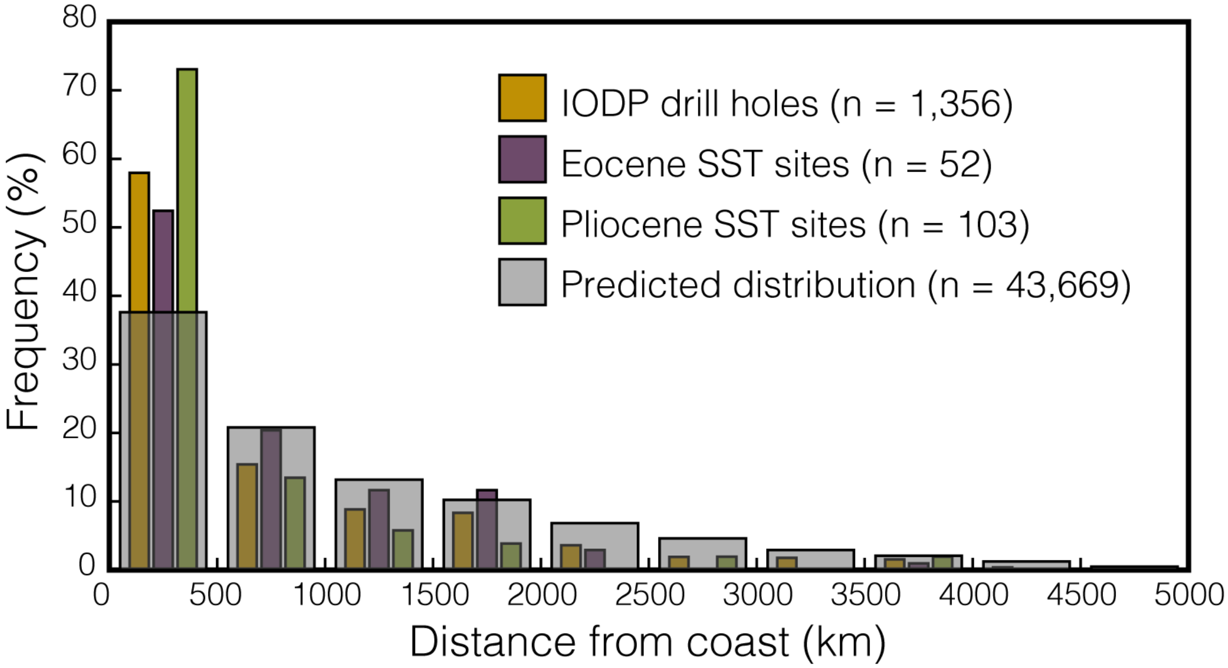

Figure 2.1. Sampling locations are biased toward nearshore environments. Distributions of the proximity to a modern coastline of all IODP associated drill holes (orange) and sampling locations from which there are Eocene (purple) and Pliocene (green) SST estimates, compared to the predicted distribution if the ocean were evenly sampled (gray).

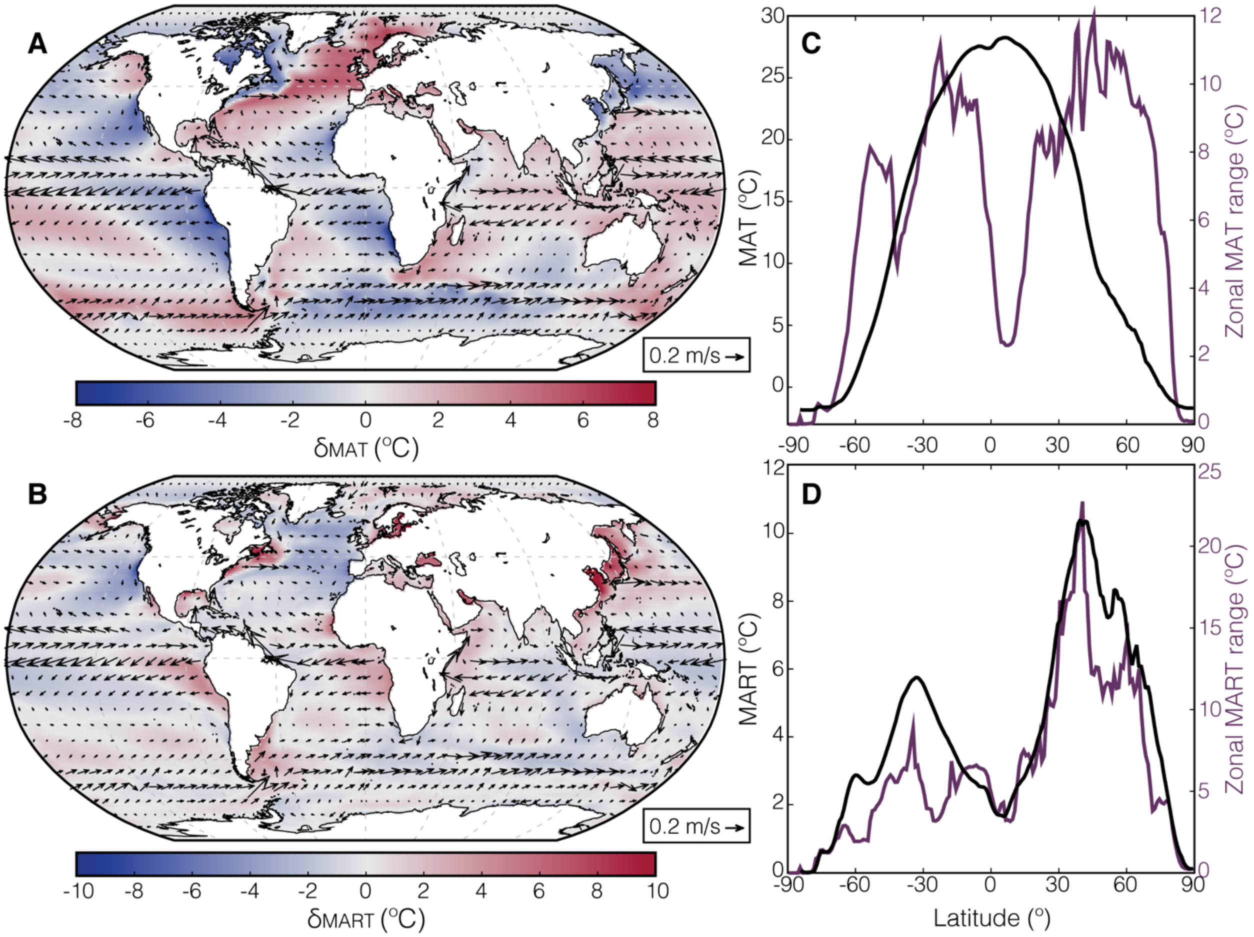

Figure 2.2. Zonal variability of modern SSTs (Hirahara et al., 2014). **A**. δ_{MAT}, with mean surface circulation (Forget et al., 2015; Fukumori et al., 2017) overlain. Positive (red) and negative (blue) shading represent locations warmer or colder than the zonal mean, respectively. **B**. δ_{MART}. Positive (red) and negative (blue) shading denotes locations more or less seasonal than the zonal mean, respectively. **C**. Meridional gradient of MAT (black line) based on zonal means compared with the range of MATs within that latitudinal band. **D**. Same as **C** but for MART.

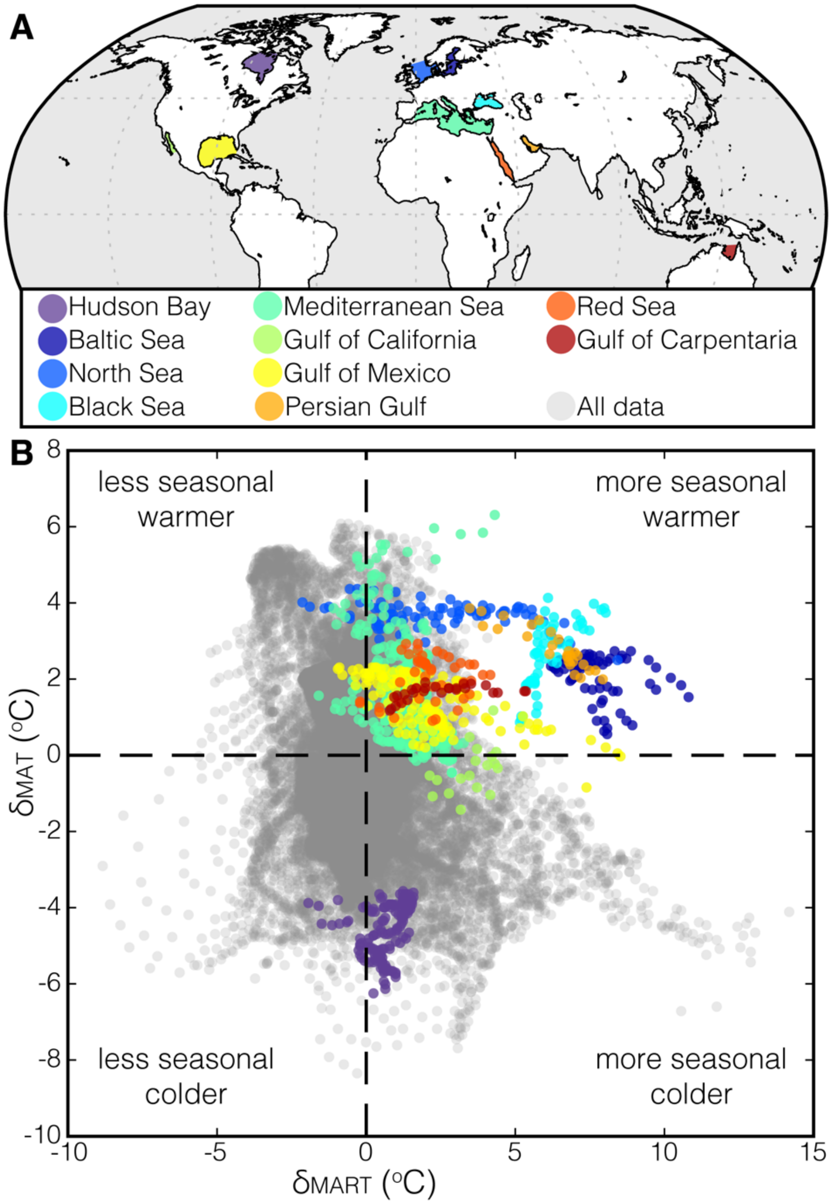

Figure 2.3. Zonal MAT and MART deviations in modern epeiric sea analogs. **A**. The ten sites selected to serve as modern epeiric sea analogs. **B**. Cross-plot of δ_{MART} and δ_{MAT} values from all ocean data (gray points) compared with modern epeiric sea analogs (colored points). Nearly all epeiric sea analog data plot in the upper righthand quadrant, indicating they are warmer and more seasonal than their respective zonal means.

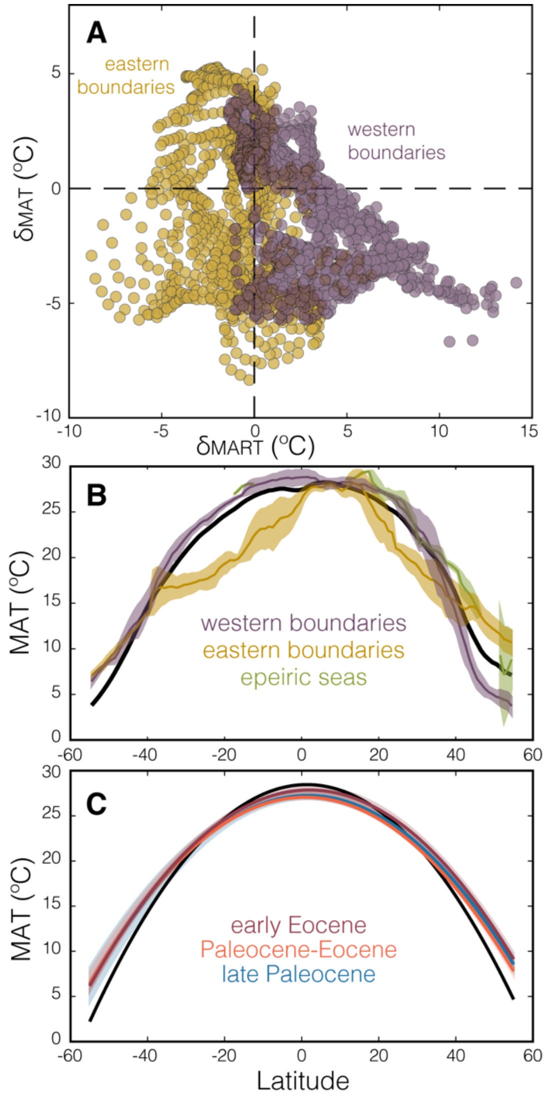

Figure 2.4. Zonal MAT and MART deviations in nearshore environments (<500 km from the shoreline). **A.** Cross-plot of modern coastal δ_{MART} and δ_{MAT} values, separated by western (purple) and eastern (yellow) boundaries. **B.** The latitudinal gradient (±1σ) of western (purple) and eastern (yellow) boundaries, and epeiric sea analogs (green), compared to the observed latitudinal temperature gradient (thick black line). **C**. Pseudoproxy analysis to establish the extent to which modern SSTs from Paleogene sampling localities (Hollis et al., 2019) are able to reproduce the known latitudinal temperature gradient (second order polynomial fit; thick black line).

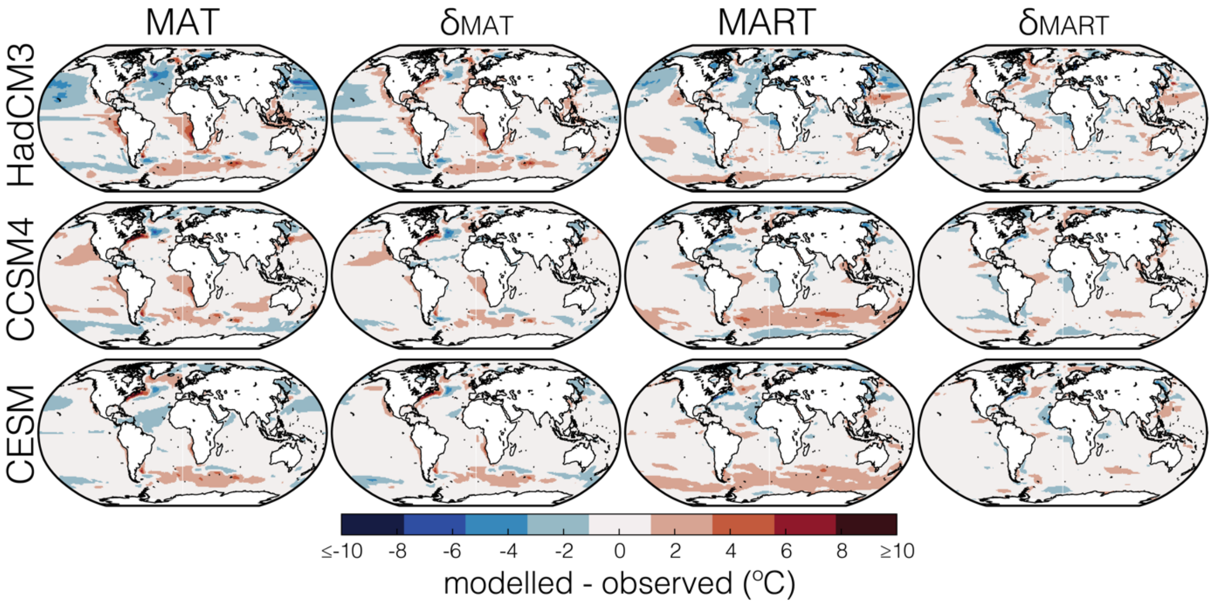

Figure 2.5. Comparison of modelled and observed temperature parameters for three climatologically-average historical ESM simulations. Positive (red) and negative (blue) indicate regions where ESMs over- or underestimate the temperature parameters, respectively.

Supporting information

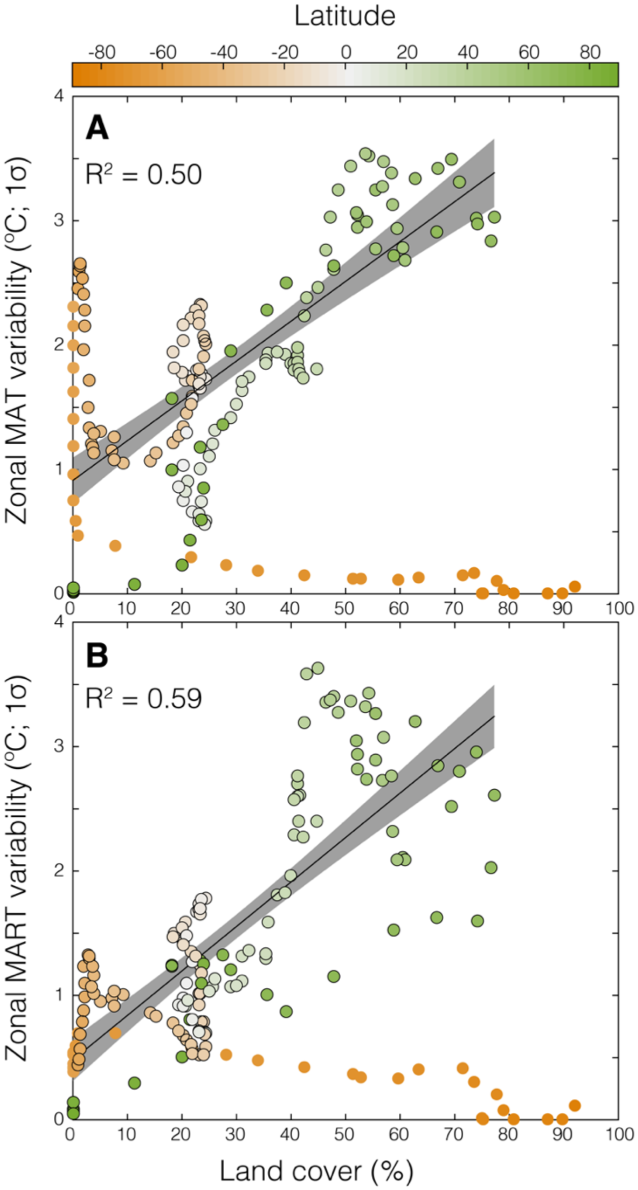

Figure S1. Summary of the statistically significant (p-value ≪ 0.0001) relationship between land cover and zonal variability. **A**. 1σ standard deviation of zonal MAT variability, plotted as a function of the percent of land (versus ocean) grid cells, and color coded by latitude. Regression line represents the linear relationship between the two parameters between 55°S and 90°N (i.e., those latitude outside the reach of the Antarctic Circumpolar Current). **B**. Same as **A**, but for the 1σ standard deviation of zonal MART variability.

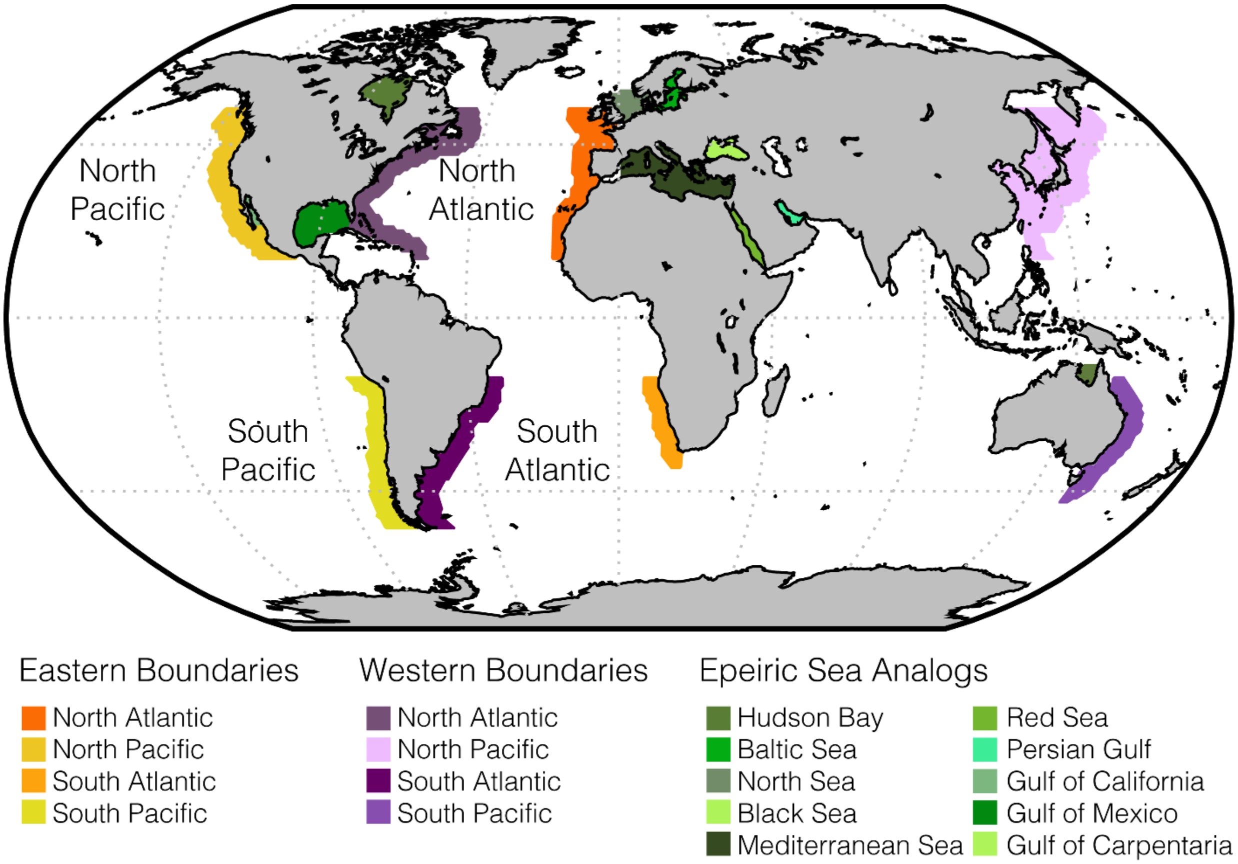

Figure S2. Environment-specific subdivisions of data.

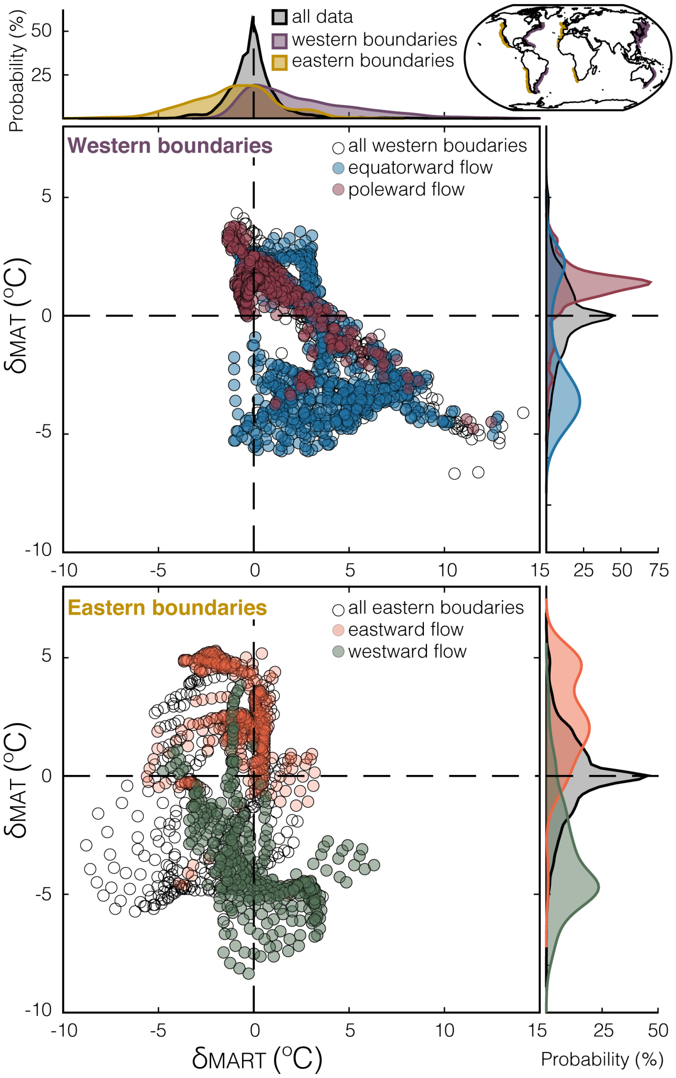

Figure S3. Summary of data from eastern and western boundaries. Within each, data are subdivided by mean flow direction. In western boundaries, flow is dominantly meridional and data are categorized as either equatorward (between -22.5 and -157.5° in the Northern Hemisphere) or as poleward (between 22.5 and 157.5° in the Northern Hemisphere; vice versa for the Southern Hemisphere). Unfilled points represent data with zonal flow that did not fit these criteria. Along eastern boundaries, flow has a more zonal component, so data are categorized as either eastward (between -67.5 and 67.5°) or as westward (between ±111.5 and ±180°). Unfilled points represent data with meridional flow that did not fit these criteria.

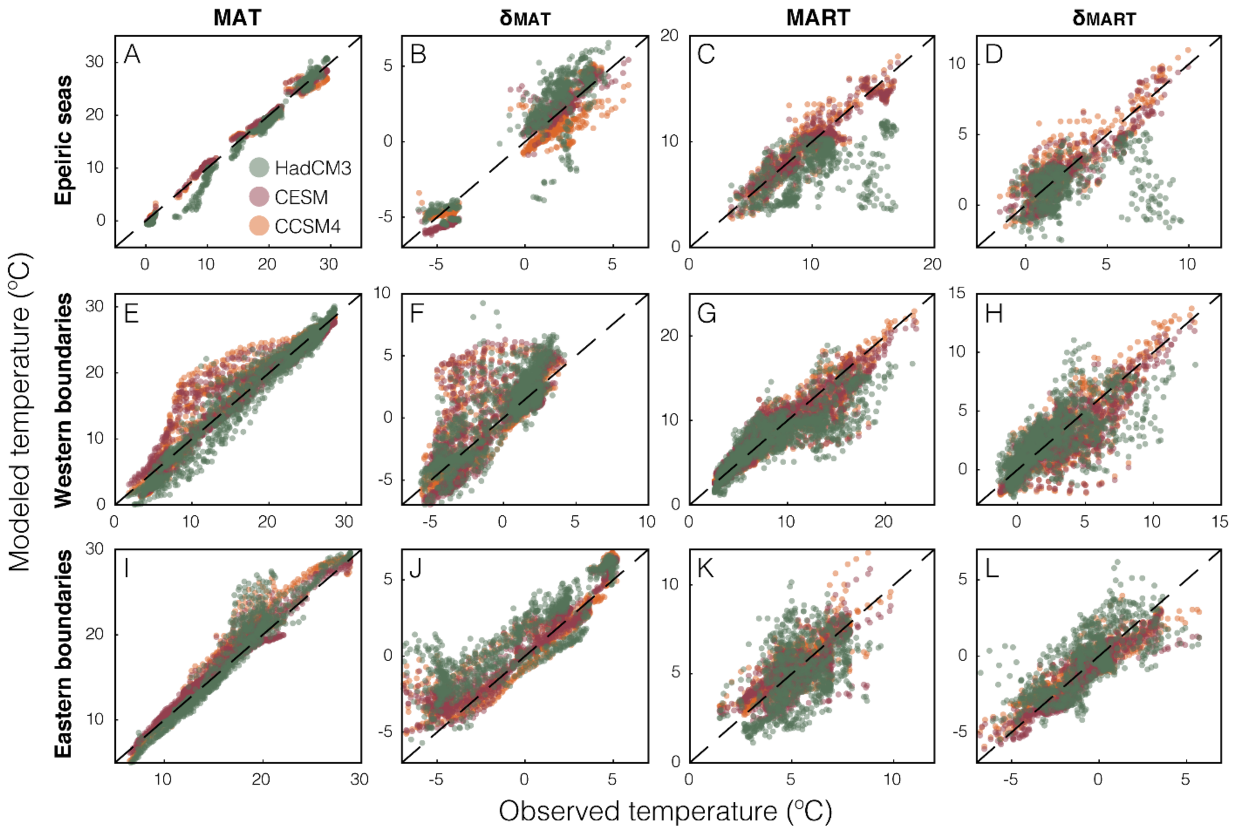

Figure S4. Summary of observed versus modelled temperature values for each of the specific environments explored within the text.

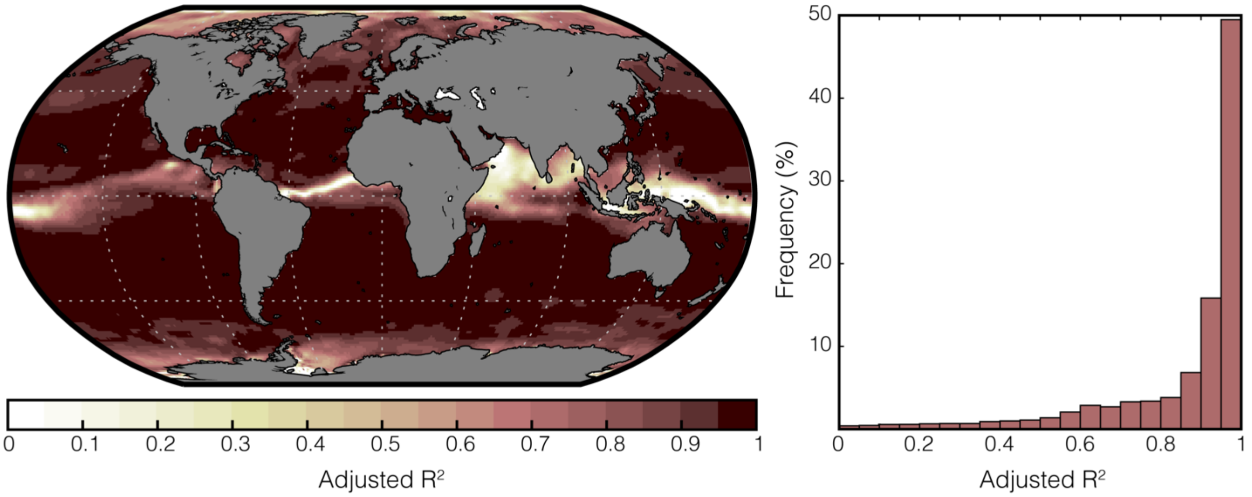

Figure S5. Map and histogram summarizing the adjusted R^2 value of the fit between mean monthly profiles from each ocean grid cell and a sine function with a fixed period of 12 months.

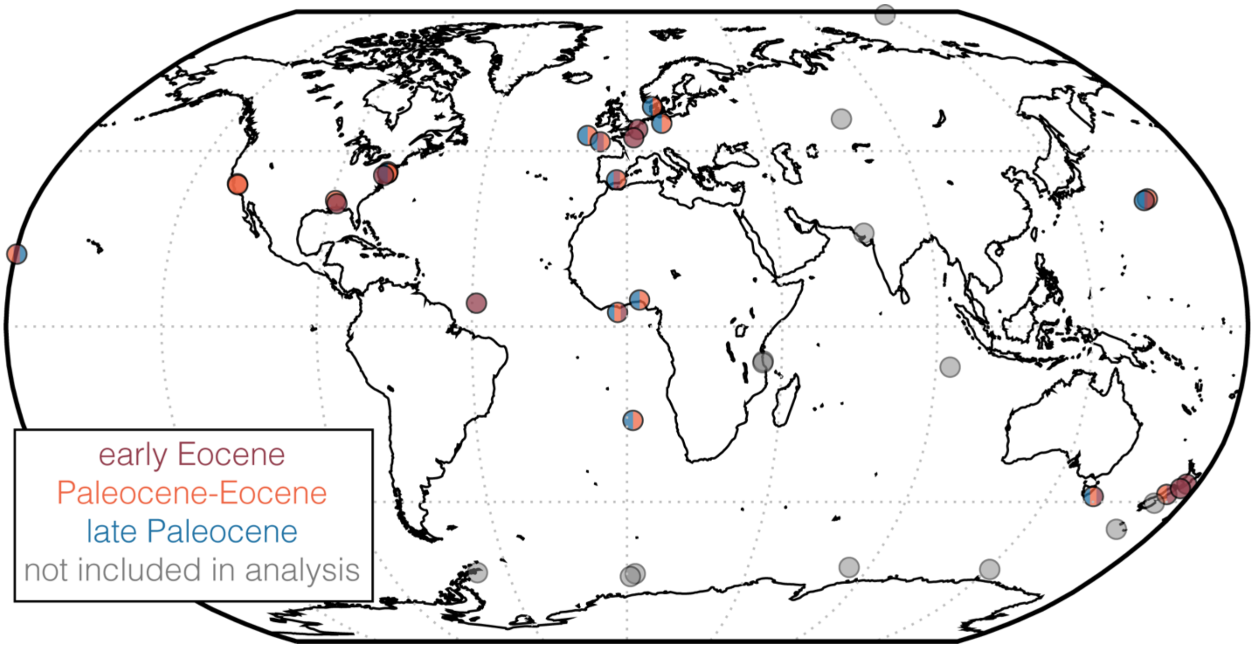

Figure S6. Spatial distribution of sampling locations used in the pseudoproxy analysis. Coordinates of sampling sites from which there are Paleogene SST data come from the DeepMIP compilation (Hollis et al., 2019).

Table S1. Summary of the distribution of δ_{MART} and δ_{MAT} values across all data and from specific environments. Number of grid cells per environment are provided in parentheticals. Poleward, equatorward, eastward, and westward flow are defined in figure caption of Fig. S3. High variability and low variability flow are defined as locations with an intra-annual standard deviation (1σ) greater than or equal to and less than 22.5^{o}, respectively. Q1 through Q4 refers to the percent of data plotting in each quadrant of a cross-plot of δ_{MART} vs. δ_{MAT}.

	Q1 (%)	**Q2 (%)**	**Q3 (%)**	**Q4 (%)**	**more seasonal**	**less seasonal**	**warmer**	**cooler**
All Data (43723)	26%	25%	29%	20%	46%	54%	51%	49%
Epeiric Seas (872)	75%	6%	2%	17%	92%	8%	81%	19%
Western Boundaries (1631)	34%	20%	1%	45%	79%	21%	54%	46%
Poleward flow (607)	46%	42%	0%	12%	58%	42%	88%	12%
Equatorward flow (695)	21%	7%	3%	69%	90%	10%	28%	72%
High variability flow (937)	21%	14%	1%	65%	86%	14%	35%	65%
Low variability flow (658)	44%	25%	2%	29%	73%	27%	69%	31%
North Atlantic (437)	11%	39%	2%	48%	59%	41%	50%	50%
North Pacific (675)	28%	2%	2%	68%	96%	4%	30%	70%
South Atlantic (312)	58%	23%	0%	19%	77%	23%	81%	19%
South Pacific (207)	66%	34%	0%	0%	66%	34%	100%	0%
Eastern Boundaries (1028)	14%	31%	35%	20%	34%	66%	45%	55%
Eastward flow (392)	33%	54%	7%	6%	39%	61%	87%	13%
Westward flow (364)	0%	10%	49%	41%	41%	59%	10%	90%
High variability flow (344)	12%	49%	23%	16%	28%	72%	61%	39%
Low variability flow (658)	14%	22%	41%	22%	37%	63%	37%	63%
North Atlantic (302)	3%	56%	34%	8%	10%	90%	58%	42%
North Pacific (322)	10%	38%	37%	14%	25%	75%	48%	52%
South Atlantic (135)	0%	19%	48%	33%	33%	67%	19%	81%
South Pacific (269)	38%	1%	26%	35%	73%	27%	39%	61%

Table S2. Summary of locations used in the pseudoproxy analysis. SSTs were extracted from the modern coordinates of locations between 55°N/S for which there are Paleogene proxy-derived SST estimates[1] (Fig. S6) to test the extent to which the modern latitudinal gradient can be estimated using a distribution of data similar to that used in paleo studies. Sites marked N/A were excluded from the analysis, either because 1) their latitude exceeds 55°N/S, 2) they come from an ocean basin not considered in this study (i.e., the Indian Ocean) or 3) there is no suitable modern analog location (e.g., Well 10, West Siberia).

Sites/Section	Leg or Country	Lat	Lon	Late Paleocene	Paleocene-Eocene	Early Eocene	Modern analog location	
							Basin/Region	Environment
IODP Site M004	Leg 302	87.87	136.18	✓	✓	✓	N/A	
Fur	Denmark	56.84	8.99	✓	✓		Europe	epeiric sea
Well 10	West Siberia	53.50	73.52	✓	✓	✓	N/A	
Store Baelt	Denmark	52.35	11.80	✓	✓		Europe	epeiric sea
North Sea	Belgium	50.70	3.60			✓	Europe	epeiric sea
DSDP Site 549	Leg 80	49.09	-13.10	✓	✓		North Atlantic	eastern boundary
Paris Basin	France	48.50	2.20			✓	Europe	epeiric sea
DSDP Site 401	Leg 48	47.43	-8.81	✓	✓	✓	North Atlantic	eastern boundary
Wilson Lake	USA	39.66	-75.04	✓	✓		North Atlantic	western boundary
Bass River	USA	39.61	-74.44	✓	✓		North Atlantic	western boundary
Millvile	USA	39.24	-75.05	✓	✓		North Atlantic	western boundary
South Dover Bridge	USA	38.7	-76.1			✓	North Atlantic	western boundary
Alamedilla	Spain	37.58	-3.24	✓	✓	✓	Europe	epeiric sea
Lodo Gulch	USA	36.59	-120.64		✓		North Pacific	eastern boundary
Turney Gulch	USA	36.32	-120.38		✓		North Pacific	eastern boundary
ODP Site 1209	Leg 198	32.68	158.60	✓	✓		North Pacific	open ocean
DSDP Site 577	Leg 86	32.26	157.43	✓		✓	North Pacific	open ocean
Harrell Core	USA	32.25	-88.72		✓		North Atlantic	western boundary
Hatchetigbee	USA	31.45	-88.05			✓	North Atlantic	western boundary
Kutch	India	23.90	70.40			✓	N/A	
ODP Site 865	Leg 143	18.55	-179.65	✓	✓	✓	North Pacific	open ocean

Dahomey Basin	Nigeria	6.80	3.63	✓	✓		Equatorial Atlantic	eastern boundary
ODP Site 929	Leg 154	5.98	-43.74			✓	Equatorial Atlantic	open ocean
ODP Site 959	Leg 159	3.63	-2.74	✓	✓	✓	Equatorial Atlantic	eastern boundary
TDP3	Tanzania	-8.85	39.63			✓	N/A	
TDP14	Tanzania	-9.28	39.51	✓	✓		N/A	
DSDP Site 213	Leg 22	-10.40	94.10		✓		N/A	
DSDP Site 527	Leg 74	-24.04	1.76	✓	✓		South Atlantic	open ocean
Tawanui	New Zealand	-40.38	176.38			✓	South Pacific	western boundary
Tora	New Zealand	-41.52	175.48			✓	South Pacific	western boundary
Mid-Waipara River	New Zealand	-43.06	172.61		✓	✓	South Pacific	western boundary
ODP Site 1172	Leg 189	-43.58	149.56	✓	✓	✓	South Pacific	western boundary
Hampden Beach	New Zealand	-45.32	170.83			✓	N/A	
DSDP Site 277	Leg 29	-52.22	166.19	✓	✓	✓	N/A	
ODP Site 738	Leg 119	-62.72	82.79	✓	✓	✓	N/A	
IODP Site U1356	Leg 318	-63.31	136			✓	N/A	
Seymour Island	Antarctic Pen.	-64.23	-56.63				N/A	
ODP Site 689	Leg 113	-64.52	3.10	✓	✓		N/A	
ODP Site 690	Leg 113	-65.33	1.28	✓	✓	✓	N/A	

References

Brand, U., Tazawa, J.I., Sano, H., Azmy, K., Lee, X., 2009. Is mid-late Paleozoic ocean-water chemistry coupled with epeiric seawater isotope records? Geology 37, 823–826. doi:10.1130/G30038A.1

Berens, P., 2009. CircStat : A MATLAB Toolbox for Circular Statistics. J. Stat. Softw. 31. doi:10.18637/jss.v031.i10

Brassell, S.C., 2014. Climatic influences on the Paleogene evolution of alkenones. Paleoceanography 29, 255–272. doi:10.1002/2013PA002576

Burke, K.D., Williams, J.W., Chandler, M.A., Haywood, A.M., Lunt, D.J., Otto-Bliesner, B.L., 2018. Pliocene and Eocene provide best analogs for near-future climates. Proc. Natl. Acad. Sci. 115, 201809600. doi:10.1073/pnas.1809600115

Caballero, R., Huber, M., 2013. State-dependent climate sensitivity in past warm climates and its implications for future climate projections. Proc. Natl. Acad. Sci. U. S. A. 110, 14162–14167. doi:10.1073/pnas.1303365110

Cramwinckel, M.J., Huber, M., Kocken, I.J., Agnini, C., Bijl, P.K., Bohaty, S.M., Frieling, J., Goldner, A., Hilgen, F.J., Kip, E.L., Peterse, F., Van Der Ploeg, R., Röhl, U., Schouten, S., Sluijs, A., 2018. Synchronous tropical and polar temperature evolution in the Eocene letter. Nature 559, 382–386. doi:10.1038/s41586-018-0272-2

Danabasoglu, G., Bates, S.C., Briegleb, B.P., Jayne, S.R., Jochum, M., Large, W.G., Peacock, S., Yeager, S.G., 2012. The CCSM4 Ocean Component. J. Clim. 25, 1361–1389. doi:10.1175/JCLI-D-11-00091.1

Dowsett, H.J., Foley, K.M., Stoll, D.K., Chandler, M.A., Sohl, L.E., Bentsen, M., Otto-Bliesner, B.L., Bragg, F.J., Chan, W.-L., Contoux, C., Dolan, A.M., Haywood, A.M., Jonas, J.A., Jost, A., Kamae, Y., Lohmann, G., Lunt, D.J., Nisancioglu, K.H., Abe-Ouchi, A., Ramstein, G., Riesselman, C.R., Robinson, M.M., Rosenbloom, N.A., Salzmann, U., Stepanek, C., Strother, S.L., Ueda, H., Yan, Q., Zhang, Z., 2013. Sea Surface Temperature of the mid-Piacenzian Ocean: A Data-Model Comparison. Sci. Rep. 3, 2013.

Evans, D., Sagoo, N., Renema, W., Cotton, L.J., Müller, W., Todd, J.A., Saraswati, P.K., Stassen, P., Ziegler, M., Pearson, P.N., Valdes, P.J., Affek, H.P., 2018. Eocene greenhouse climate revealed by coupled clumped isotope-Mg/Ca thermometry. Proc. Natl. Acad. Sci. 115, 1174–1179. doi:10.1073/pnas.1714744115

Forget, G., Campin, J.-M., Heimbach, P., Hill, C.N., Ponte, R.M., Wunsch, C., 2015. ECCO version 4: an integrated framework for non-linear inverse modeling and global ocean state estimation. Geosci. Model Dev. 8, 3071–3104. doi:10.5194/gmd-8-3071-2015

Fraile, I., Mulitza, S., Schulz, M., 2009. Modeling planktonic foraminiferal seasonality: Implications for sea-surface temperature reconstructions. Mar. Micropaleontol. 72, 1–9. doi:10.1016/j.marmicro.2009.01.003

Fukumori, I., Wang, O., Fenty, I., Forget, G., Heimbach, P., Ponte, R.M., 2017. ECCO Version 4 Release 3. doi:1721.1/110380

Gasson, E., Lunt, D.J., Deconto, R., Goldner, A., Heinemann, M., Huber, M., Legrande, A.N., Pollard, D., Sagoo, N., Siddall, M., Winguth, A., Valdes, P.J., 2014. Uncertainties in the modelled CO2 threshold for Antarctic glaciation. Clim. Past 10, 451–466. doi:10.5194/cp-10-451-2014

Gettelman, A., Kay, J.E., Shell, K.M., 2012. The Evolution of Climate Sensitivity and Climate

Feedbacks in the Community Atmosphere Model. J. Clim. 25, 1453–1469. doi:10.1175/JCLI-D-11-00197.1

Gregor, C.B., 1985. The mass-age distribution of Phanerozoic sediments. Geol. Soc. London, Mem. 10, 284–289. doi:10.1144/GSL.MEM.1985.010.01.22

Grossman, E.L., 2012. Applying Oxygen Isotope Paleothermometry in Deep Time, in: Ivany, L.C., Huber, B.T. (Eds.), Reconstructing Earth's Deep-Time Climate—The State of the Art in 2012. The Paleontological Society Papers, pp. 39–67.

Haney, R.L., Davies, R.W., 1976. The Role of Surface Mixing in the Seasonal Variation of the Ocean Thermal Structure. J. Phys. Oceanogr. 6, 504–510. doi:10.1175/1520-0485(1976)006<0504:TROSMI>2.0.CO;2

Haywood, A.M., Dowsett, H.J., Dolan, A.M., Rowley, D., Abe-Ouchi, A., Otto-Bliesner, B., Chandler, M.A., Hunter, S.J., Lunt, D.J., Pound, M., Salzmann, U., 2016. The Pliocene Model Intercomparison Project (PlioMIP) Phase 2: scientific objectives and experimental design. Clim. Past 12, 663–675. doi:10.5194/cp-12-663-2016

Hirahara, S., Ishii, M., Fukuda, Y., 2014. Centennial-scale sea surface temperature analysis and its uncertainty. J. Clim. 27, 57–75. doi:10.1175/JCLI-D-12-00837.1

Hollis, C.J., Dunkley Jones, T., Anagnostou, E., Bijl, P.K., Cramwinckel, M.J., Cui, Y., Dickens, G.R., Edgar, K.M., Eley, Y., Evans, D., Foster, G.L., Frieling, J., Inglis, G.N., Kennedy, E.M., Kozdon, R., Lauretano, V., Lear, C.H., Littler, K., Lourens, L., Meckler, A.N., Naafs, B.D.A., Pälike, H., Pancost, R.D., Pearson, P.N., Röhl, U., Royer, D.L., Salzmann, U., Schubert, B.A., Seebeck, H., Sluijs, A., Speijer, R.P., Stassen, P., Tierney, J., Tripati, A., Wade, B., Westerhold, T., Witkowski, C., Zachos, J.C., Zhang, Y.G., Huber, M., Lunt, D.J.,

2019. The DeepMIP contribution to PMIP4: methodologies for selection, compilation and analysis of latest Paleocene and early Eocene climate proxy data, incorporating version 0.1 of the DeepMIP database. Geosci. Model Dev. 12, 3149–3206. doi:10.5194/gmd-12-3149-2019

Hollis, C.J., Handley, L., Crouch, E.M., Morgans, H.E.G., Baker, J.A., Creech, J., Collins, K.S., Gibbs, S.J., Huber, M., Schouten, S., Zachos, J.C., Pancost, R.D., 2009. Tropical sea temperatures in the high-latitude South Pacific during the Eocene. Geology 37, 99–102. doi:10.1130/G25200A.1

Hollis, C.J., Taylor, K.W.R., Handley, L., Pancost, R.D., Huber, M., Creech, J.B., Hines, B.R., Crouch, E.M., Morgans, H.E.G., Crampton, J.S., Gibbs, S., Pearson, P.N., Zachos, J.C., 2012. Early Paleogene temperature history of the Southwest Pacific Ocean: Reconciling proxies and models. Earth Planet. Sci. Lett. 349–350, 53–66. doi:10.1016/j.epsl.2012.06.024

Holmden, C., Creaser, R.A., Muehlenbachs, K., Leslie, S.A., Bergström, S.M., 1998. Isotopic evidence for geochemical decoupling between ancient epeiric seas and bordering oceans: implications for secular curves. Geology 26, 567–570. doi:10.1130/0091-7613(1998)026<0567:IEFGDB>2.3.CO;2

Huber, M., Caballero, R., 2011. The early Eocene equable climate problem revisited. Clim. Past 7, 603–633. doi:10.5194/cp-7-603-2011

Jaffrés, J.B.D., Shields, G.A., Wallmann, K., 2007. The oxygen isotope evolution of seawater: A critical review of a long-standing controversy and an improved geological water cycle model for the past 3.4 billion years. Earth-Science Rev. 83, 83–122.

doi:10.1016/j.earscirev.2007.04.002

Jimenez, M.Y., Ivany, L.C., Judd, E.J., Henkes, G., 2019. Low and seasonally variable salinity in the Pennsylvanian equatorial Appalachian Basin. Earth Planet. Sci. Lett. 519, 182–191. doi:10.1016/j.epsl.2019.04.051

Johns, T.C., Gregory, J.M., Ingram, W.J., Johnson, C.E., Jones, A., Lowe, J.A., Mitchell, J.F.B., Roberts, D.L., Sexton, D.M.H., Stevenson, D.S., Tett, S.F.B., Woodage, M.J., 2003. Anthropogenic climate change for 1860 to 2100 simulated with the HadCM3 model under updated emissions scenarios. Clim. Dyn. 20, 583–612. doi:10.1007/s00382-002-0296-y

Judd, E.J., Ivany, L.C., DeConto, R.M., Halberstadt, A.R.W., Miklus, N.M., Junium, C.K., Uveges, B.T., 2019. Seasonally resolved proxy data from the Antarctic Peninsula support a heterogeneous middle Eocene Southern Ocean. Paleoceanogr. Paleoclimatology 2019PA003581. doi:10.1029/2019PA003581

Kay, J.E., Deser, C., Phillips, A., Mai, A., Hannay, C., Strand, G., Arblaster, J.M., Bates, S.C., Danabasoglu, G., Edwards, J., Holland, M., Kushner, P., Lamarque, J.-F., Lawrence, D., Lindsay, K., Middleton, A., Munoz, E., Neale, R., Oleson, K., Polvani, L., Vertenstein, M., 2015. The Community Earth System Model (CESM) Large Ensemble Project: A Community Resource for Studying Climate Change in the Presence of Internal Climate Variability. Bull. Am. Meteorol. Soc. 96, 1333–1349. doi:10.1175/BAMS-D-13-00255.1

Kwon, Y.O., Alexander, M.A., Bond, N.A., Frankignoul, C., Nakamura, H., Qiu, B., Thompson, L.A., 2010. Role of the gulf Stream and Kuroshio-Oyashio systems in large-scale atmosphere-ocean interaction: A review. J. Clim. 23, 3249–3281. doi:10.1175/2010JCLI3343.1

LeGrande, A.N., Schmidt, G.A., 2006. Global gridded data set of the oxygen isotopic composition in seawater. Geophys. Res. Lett. 33, L12604. doi:10.1029/2006GL026011

Lunt, D.J., Jones, T.D., Heinemann, M., Huber, M., LeGrande, A., Winguth, A., Loptson, C., Marotzke, J., Roberts, C.D., Tindall, J., Valdes, P., Winguth, C., 2012. A model-data comparison for a multi-model ensemble of early Eocene atmosphere-ocean simulations: EoMIP. Clim. Past 8, 1717–1736. doi:10.5194/cp-8-1717-2012

Ma, X., Jing, Z., Chang, P., Liu, X., Montuoro, R., Small, R.J., Bryan, F.O., Greatbatch, R.J., Brandt, P., Wu, D., Lin, X., Wu, L., 2016. Western boundary currents regulated by interaction between ocean eddies and the atmosphere. Nature 535, 533.

Malevich, S.B., Vetter, L., Tierney, J.E., 2019. Global core-top calibration of δ^{18}O in planktic foraminifera to sea-surface temperature. Paleoceanogr. Paleoclimatology 2019PA003576. doi:10.1029/2019PA003576

Montañez, I.P., Osleger, D.J., Chen, J., Wortham, B.E., Stamm, R.G., Nemyrovska, T.I., Griffin, J.M., Poletaev, V.I., Wardlaw, B.R., 2018. Carboniferous climate teleconnections archived in coupled bioapatite δ 18 O PO 4 and 87 Sr/ 86 Sr records from the epicontinental Donets Basin, Ukraine. Earth Planet. Sci. Lett. 492, 89–101. doi:10.1016/j.epsl.2018.03.051

Müller, R.D., Roest, W.R., Royer, J.-Y., Gahagan, L.M., Sclater, J.G., 1997. Digital isochrons of the world's ocean floor. J. Geophys. Res. Solid Earth 102, 3211–3214. doi:10.1029/96jb01781

Roark, A., Flake, R., Grossman, E.L., Olszewski, T., Lebold, J., Thomas, D., Marcantonio, F., Miller, B., Raymond, A., Yancey, T., 2017. Brachiopod geochemical records from across the Carboniferous seas of North America: Evidence for salinity gradients, stratification, and circulation patterns. Palaeogeogr. Palaeoclimatol. Palaeoecol. 485, 136–153. doi:10.1016/j.palaeo.2017.06.009

Schouten, S., Hopmans, E.C., Sinninghe Damsté, J.S., 2004. The effect of maturity and depositional redox conditions on archaeal tetraether lipid palaeothermometry. Org. Geochem. 35, 567–571. doi:10.1016/j.orggeochem.2004.01.012

Seager, R., Murtugudde, R., Naik, N., Clement, A., Gordon, N., Miller, J., 2003. Air–Sea Interaction and the Seasonal Cycle of the Subtropical Anticyclones*. J. Clim. 16, 1948–1966. doi:10.1175/1520-0442(2003)016<1948:AIATSC>2.0.CO;2

Sluijs, A., Schouten, S., Donders, T.H., Schoon, P.L., Röhl, U., Reichart, G.-J., Sangiorgi, F., Kim, J.-H., Sinninghe Damsté, J.S., Brinkhuis, H., 2009. Warm and wet conditions in the Arctic region during Eocene Thermal Maximum 2. Nat. Geosci. 2, 777.

Tappan, H., Loeblich, A.R., 1973. Evolution of the oceanic plankton. Earth-Science Rev. 9, 207–240. doi:10.1016/0012-8252(73)90092-5

Tierney, J.E., Ivany, L.C., Bhattacharya, T., Huber, B.T., n.d. The future of past climate: review summary. Science (80-.).

Veizer, J., Prokoph, A., 2015. Temperatures and oxygen isotopic composition of Phanerozoic oceans. Earth-Science Rev. 146, 92–104. doi:10.1016/j.earscirev.2015.03.008

Zhu, J., Poulsen, C.J., Tierney, J.E., 2019. Simulation of Eocene extreme warmth and high climate sensitivity through cloud feedbacks. Sci. Adv. 5, 1–10. doi:10.1126/sciadv.aax1874

Chapter 3:

The life and time of clams: Derivation of intra-annual growth rates from high-resolution oxygen isotope profiles

Chapter 3 is published as:

Judd, E. J., Wilkinson, B. H., Ivany, L. C., 2018. The life and time of clams: Derivation of intra-annual growth rates from high-resolution oxygen isotope profiles. Palaeogeography, palaeoclimatology, palaeoecology 490, 70-83.

3.1 Abstract

The paired analysis of subannual microincrements and serially-sampled oxygen isotope data affords insights into the physiological and environmental conditions controlling bivalve growth. However, daily microincrements are faint or absent in many taxa, difficult or ambiguous to count under the best conditions, and are often constrained to the earliest years of ontogeny, limiting the practicality of intra-annual comparisons between growth rate and environmental parameters. We present a computational approach to derive growth rates using only serially-sampled oxygen isotope data, thereby allowing for broader application of bivalve growth rate studies. Variation in the isotopic composition of shell carbonate along an ontogenetic sampling profile reflects temporal variation in ambient water temperatures, while variation in the position of isotope values in the distance domain reflects intra-annual variation in rates of shell accretion. Thus, the shape of the isotope profile in distance space over a given year records the concomitant influence of subannual variation in temperature (y-axis) and growth rate (x-axis). Presumption that annual variation in temperature is sinusoidal allows for the determination of an intra-annual growth rate function that best approximates observed $\delta^{18}O_{carb}$ data. The fidelity of the approach is affirmed using synthetically generated isotope datasets and previously published isotope profiles. The method offers a variety of applications to sclerochronologic studies. Using only oxygen isotope values determined along an ontogenetic trajectory, the approach can be used to quantify spatial and temporal patterns of intra-annual accretion within populations. Additionally, the model can be applied to long time series such that year-to-year variations in the growth profiles can be used to identify ontogenetic and climatic trends. While we focus here on isotope-distance records from bivalve shell carbonate, this method is equally applicable to similar data from other accretionary biogenic skeletal materials.

3.2 Introduction

Subannual growth increments in the skeletons of organisms that grow by accretion can be used to constrain both environmental and physiological conditions during ontogeny (Barker, 1964; Davenport, 1938; Rhoads and Lutz, 1980). Microincrements form on a variety of time scales, but most commonly reflect circatidal (e.g., Schöne et al., 2002a), circalunidian (e.g., Miyaji et al., 2010), or circadian (e.g., Chauvaud et al., 1998) rhythms. Growth increment widths and counts reveal the timing of growth line formation, duration of the growing season, and growth rate (e.g., Hallmann et al., 2009). Furthermore, comparison of growth rate profiles from multiple years along an ontogenetic trajectory, or between spatially or temporally disparate populations can elucidate the parameters controlling growth rate. For example, increment width profiles have been used to identify latitudinal trends in the number of growing days per year (Tanabe and Oba, 1988) and assess paleotidal regimes via the observed magnitude of diurnal inequality (Ohno, 1989).

High-resolution stable oxygen ($\delta^{18}O_{carb}$) and carbon ($\delta^{13}C_{carb}$) isotope analyses are frequently employed in sclerochronologic studies and, when coupled with microincrement analyses, reveal the effects of environmental conditions such as temperature and nutrient availability on growth rate (e.g., Schöne et al., 2003a). Additionally, they can provide valuable information on taxon-specific physiological parameters, such as thermal thresholds (i.e., temperatures above or below which the organism is too stressed to precipitate carbonate) and seasons of maximum and minimum growth (e.g., Weidman et al., 1994). Such coupled studies show that intra-annual shell growth often correlates with seasonal temperature variations (e.g., Cardoso et al., 2013; Jones and Quitmyer, 1996), but can also vary with a range of other parameters including productivity and nutrient availability (e.g., Witbaard et al., 2001), salinity (e.g., Koike, 1980), monsoons and typhoons (e.g., Schöne et al., 2003b), tidal cycles (e.g., Ohno, 1989), ontogenetic age (e.g., Tanabe, 1988), and the timing of reproduction (e.g., Sato, 1995), as well as quasi-decadal oscillations in one or more of these parameters (e.g., Lazareth et al., 2006).

Investigation of growth rates has practical applications that extend beyond the scope of traditional sclerochronologic studies. Knowledge of environmental parameters that yield faster or more continuous growth can provide valuable information to commercial fisheries, resulting in better, more targeted management practices. Yearly-resolved chronologies based on widths of annual bands are leading indicators of the long-term dynamics of climate change and associated anthropogenic effects across a range of temporal and spatial scales (e.g., Black et al., 2016). Growth rate data can also provide fundamental information to the emerging field of conservation paleobiology (e.g., Dietl et al., 2015). By comparing increment width profiles from modern and fossil taxa from the same species and setting, baseline growth rates can be established and environmental changes that serve to either inhibit or promote the growth of organisms can be identified (e.g., Steinhardt et al., 2016). Furthermore, inter-annual growth rate data have the potential to shed light on environmental conditions in shallow and deep time paleoclimate studies, such as the presence of quasi-periodic oscillations in paleocirculation or paleotemperature (e.g., Ivany et al., 2011; Schöne, 2013; Wanamaker et al., 2008). Lastly, such data afford insights into physiological conditions in paleontological studies, such as the onset of maturity or senescence via ontogenetic shifts in annual growth rate (e.g., Alvarez and Pérez, 2016).

While it is clear that subannual increment width analyses provide useful information not readily obtained by geochemical data alone, such analyses are time-consuming, often involve the use of toxic chemicals, and require fine-scale measurements that are interpretive and prone to human error (Karney et al., 2010; Wanamaker et al., 2009). Additionally, subannual bands are faint or absent in many taxa, inhibiting the ubiquitous application of microincrement analyses. Therefore, the reconstruction of subannual variation in growth rate from oxygen isotope profiles alone would offer a significant advantage to those studying relationships between bivalve growth and environment, theoretically producing more consistent and reliable constraints on the environmental conditions and physiological processes that prevailed during shell growth.

Several intra-annual growth functions have arisen predominantly as secondary aspects of models developed to address conversion of geochemical data from the distance domain into a continuous time series (e.g., De Ridder et al., 2007; Goodwin et al., 2003; Müller et al., 2015; Wilkinson and Ivany, 2002). Additionally, attempts have been made to extrapolate intra-annual accretion rates by temporally aligning isotope data to instrumental data (e.g., Yan et al., 2014). Currently, however, the Mollusc Growth Function Generator (MoGroFunGen; Goodwin et al., 2009) is the only growth model whose primary purpose is to mathematically quantify intra-annual growth rate in accretionary organisms using sequential isotope data. The model fits temperature-resolved oxygen isotopic data with a monotonic cubic spline, the first derivative of which results in a daily growth function. This sophisticated approach reliably reconstructs daily increment widths with high resolution, precision, and accuracy. However, the alignment of isotope data into the time domain is dependent on high-resolution temperature measurements, limiting its applicability to studies of modern specimens where such data are available. Additionally, the accuracy achieved by using a complex high-order polynomial yields growth rate functions with parameters that offer little interpretive utility.

Here, we present a new approach for quantifying subannual variation in the growth rate of accretionary organisms that is based on deviations in the shape of oxygen isotope profiles

($\delta^{18}O_{carb}$ versus distance along a sampling transect) from the predicted sinusoidal variation in temperature with the annual cycle. Although availability of temporally-resolved temperature data allows for the alignment of growth rates in an absolute timeframe, the method does not require these data, and can thus be applied to deep-time studies. Our approach generates an annually-resolved growth rate function that defines the timing, duration, rate, and temperatures of growth. Moreover, temporal alignment of isotope data is a secondary output of the model, transforming data from the distance domain into time space and providing insight into the climatological regime.

3.3 A model for bivalve shell growth derived from oxygen isotope data

The theoretical premise of the approach is based on the observation that qualitative aspects of the shape of oxygen isotope profiles reflect the interplay between the timing and magnitude of changes in both temperature and growth rate (e.g., Goodwin et al., 2003; Müller et al., 2015). Subannual variation in ambient water temperature controls the oxygen isotope composition of accreted carbonate in the time domain, while subannual variation in accretion rate serves to translate that pattern of compositional variation into the distance domain. Thus, deviations of $\delta^{18}O_{carb}$ data from a predicted sinusoidal temperature curve, when plotted versus distance, reflect growth rate (Fig. 1). For example, the oxygen isotope profile in the distance domain for a bivalve with a constant growth rate should be sinusoidal (Fig 1A, 1B). If, however, the bivalve grew faster in winter than summer, the oxygen isotope profile would tend toward cuspate (Fig. 1I, 1J) due to the greater amount of carbonate accreted during that season of growth. Provided that numerical functions can adequately describe first-order annual variations in temperature and growth rate, patterns of isotope variation along a well-sampled transect can be used to determine the metrics of those equations, thus resulting in a growth rate function.

3.3.1 Governing assumptions and equations

The approach we employ here is to iteratively optimize agreement between measured and modelled $\delta^{18}O_{carb}$ values along a distance transect, where the latter is generated using a set of input functions that describe annual variation in temperature and growth. In order to apply this approach, it is necessary to demonstrate that the majority of inter-annual variation in temperature and growth can be described with simple numerical functions.

Temperature function. – One of the primary assumptions of the growth model is that annual temperature variations, and thus annual $\delta^{18}O_{carb}$ variations, are sinusoidal. Wilkinson and Ivany (2002) describe several examples where observed annual variations in both air and ocean temperatures are well defined using a sinusoid and demonstrate that short-term deviations from this signal (residuals) typically comprise Gaussian noise. Furthermore, sinusoidal temperature variation is a theoretical expectation given that changes in ambient air and water temperature are primarily driven by variations in solar insolation, which sinusoidally oscillate throughout the year (e.g., Haney and Davies, 1976; Lando and Lando, 1977; Stine et al., 2009). There are some settings in which seasonal temperature variations deviate from the predicted sinusoid; however, they generally reflect unique oceanographic conditions. For example, temperature records from regions of coastal upwelling can exhibit a left-skew (e.g., Breaker, 2005), while shallow seasonal thermoclines in semi-enclosed basins can generate cuspate intra-annual temperature cycles (e.g., Schöne et al., 2005b). However, such instances appear to be the exception rather than the rule, and should not inhibit the application of this method to bivalves from most marine environments (e.g., Kubota et al., 2017; Richaud et al., 2016; Yan et al., 2012).

The parameters used to constrain the sine function (T_{sine}; Table 1) are amplitude (T_{amp}), period (T_{per}), temporal phase (T_{pha}), and vertical position (T_{pos}). Amplitude is equivalent to the annual range of temperatures and position is analogous to the mean annual temperature (MAT). While a record that includes shorter term temperature fluctuations superimposed on the annual cycle might be better described by a higher order polynomial (e.g., Goodwin et al., 2009), the parameters constraining such a fit are not based on climatological principles and can inadvertently fit the model to Gaussian noise. Therefore, the decreased goodness-of-fit when using a sinusoid (as compared to a high order polynomial) is offset by decreased model complexity, increased utility, and greater intuitive significance of parameters; hence, a sinusoidal function can constrain first-order temperature conditions with greater confidence. For example, the best-fit sinusoid to weekly resolved, interpolated sea surface temperature data from the coast of Mauritania, NW Africa (Müller et al., 2015; Reynolds et al., 2002) accounts for 83% of observed temperature variations over the seven-year-long time series (Fig. 2A); residual data consist of Gaussian noise with a standard deviation of ~1 °C (Fig. 2B).

Growth function. – In addition to describing sinusoidal seasonal change in temperature, a similar understanding of variation in growth over the year is needed to estimate absolute growth rates from stable isotope data arrayed in the distance domain. Inspection of several high-resolution increment width profiles (Fig. 3, black lines; Goodwin et al., 2003, 2001; Hallmann et al., 2009; Lorrain et al., 2004; Schöne et al., 2003b) provides insight into the factors controlling daily accretion rates and the parameters required to quantitatively constrain such variation with a single function. Collectively, these data suggest that: (1) Daily rates of shell growth are highly variable. Most short-term variations are related to diurnal and fortnightly tidal cycles, but can also include differences in growth rate related to ephemeral changes in temperature and salinity.

While any single growth function will likely be unable to capture this high frequency variation, these short-term differences in growth impart only a small fraction of the annual variance in growth rate. (2) Many bivalves do not grow their shells continuously throughout the year. Biochecks (*sensu* Hall et al., 1974), or cessations in growth, which are interpreted as the result of environmental and/or reproductive stress, are associated with the development of prominent macroscopic growth bands. Thus, a growth rate function must be able to account for an extended interval of zero growth. (3) Records of shell growth can exhibit patterns that are strongly skewed. In some instances (e.g., Fig. 3E), increases in growth rate are more protracted in time than decreases, while others (e.g., Fig. 3A, 3F, 3G) exhibit the opposite pattern. In order to constrain this asymmetry, the growth function must incorporate a skewness parameter. (4) Despite these caveats, most intra-annual growth rate data exhibit broadly similar patterns, though the timing, duration, and intensity of seasonal growth and growth cessation vary considerably with environmental setting and stage of ontogenetic development (Fig. 3). This suggests that, in most cases, a single function can be used to describe the general pattern of accretion throughout the year.

Such seasonal changes in accretion rate can also be mathematically characterized using a sinusoidal function. Here, the defining parameters (G_{sine}; Table 1) are seasonal range of growth rates (amplitude, G_{amp}), duration of growth variation (period, G_{per}), day of fastest growth within the year (phase, G_{pha}), and mean annual growth rate (position, G_{pos}). Additionally, because specimens can exhibit symmetrical growth over the season of accretion (e.g., Fig. 3D), or display positive or negative skewness in growth rates about some maximum rate (e.g., Fig. 3E), the growth rate sinusoid includes a skewness parameter (G_{skw}) that imposes differing degrees of asymmetry on the growth curve. Because growth rate cannot be negative, any negative growth values are assumed to be zero, thereby accommodating the necessity for intervals of complete growth cessation.

A skewed sinusoidal growth function cannot account for higher-frequency variation imposed by tides, storms, or other environmental perturbations; however, average day-to-day differences in band widths relative to the best-fit sinusoid generally comprise Gaussian noise. Though such an approach serves to average shorter-term growth rate variations, it does capture first-order growth attributes, such as maximum growth rate and number of growing days during any record of annual accretion (Fig. 3, gray curves).

3.3.2 Model inputs

The required input values for the model are serially-sampled $\delta^{18}O_{carb}$ data and their associated distances along the sampling (ontogenetic) trajectory. In the following examples, we convert oxygen isotope values into temperatures using the empirically derived aragonite paleotemperature equation of Grossman and Ku (1986), as later modified by Dettman et al. (1999). Because $\delta^{18}O_{carb}$ is dependent upon both the temperature and the oxygen isotopic composition of the seawater ($\delta^{18}O_w$) from which the carbonate is precipitated (Urey, 1948), calculation of temperature requires knowledge or an assumption of $\delta^{18}O_w$. In all examples considered here, we assume average normal marine conditions ($\delta^{18}O_w = 0‰$) unless otherwise stated. The approach is only applicable to datasets where $\delta^{18}O_w$ is known, can be reasonably assumed, or is presumed to be invariant over the year.

Optimal datasets should have a high sampling density, accurate distance measurements, and come from taxa that grow over large portions of the year. Ideally, the spatial distribution of samples should span nearly the full year of accreted growth, and the temperatures inferred from oxygen isotope values should capture a large portion of the observed seasonality (see below). For accurate distance measurements, sampling should be conducted on a MicroMill or comparable digital sampling platform that provides precise XY coordinates for each sample; however, distances can also be determined *a posteriori* from a digital image of any set of visually distinct sample traces using software such as ImageJ (Schneider et al., 2012). The need for distance data (or the knowledge that all samples are equally spaced) in order to apply this approach supports a call to authors to publish such information accompanying their sequential isotope analyses.

3.3.3 Iteration procedure to yield a best-fit solution

The presumption of sinusoidal variation allows us to determine, from a stable isotope profile collected in the distance domain, the parameters of the temperature (position, amplitude, and phase) and growth sinusoids (position, amplitude, phase, and asymmetry) that best approximate that isotope record in the time domain. The approach works by iteratively generating modeled isotope profiles and then comparing those profiles with input $\delta^{18}O_{carb}$ values and distance measurements. Here, we use the shuffled complex evolution method (Duan et al., 1992), an iterative global optimization program, in order to converge upon the set of parameters that minimizes the difference between the measured and modeled isotope profiles.

Temperature and growth sinusoid solutions are determined by holding T_{per} and G_{per} fixed at 365 days, T_{pha} aligned with the known or presumed date of maximum temperature, and iteratively varying all other T_{sine} and G_{sine} parameters. T_{sine} relates time and temperature (and thus $\delta^{18}O_{carb}$), while G_{sine} relates time and growth rate, which can be summed to yield the full sampled transect distance. Modeled isotope datasets are iteratively generated by extracting temperature values from the T_{sine} curve (which are converted to $\delta^{18}O_{carb}$ values) at the same distance values as the input dataset. Optimal solutions are determined by minimizing, by least squares, the differences between input and modelled isotope profiles. If the oxygen isotope profile spans multiple years of growth, then each year is fit separately. Supplemental File 1 is a static Excel file that includes the mathematical functions; MATLAB code to perform the above procedures is provided in Supplemental File 2.

3.4 Synthetic systems

Before applying the model to measured isotope data from natural systems, we first validate the approach and test its efficacy using simplified synthetic datasets where temperatures, growth rates, and coeval isotope compositions are known. We then use these synthetic datasets to assess the sensitivity of the model to the duration and timing of the growing season.

3.4.1 Validating the model

We begin by generating synthetic isotope profiles for bivalve shells grown at prescribed, sinusoidally varying temperatures and skewed sinusoidal growth rates in order to investigate the ability of the approach to recover known input parameters from idealized isotope transects. Figure 4 illustrates two such examples, one of which (Fig. 4D, 4E, 4F) also incorporates Gaussian noise into both input functions and a fortnightly (i.e., tidal) cycle into the growth rate function to better simulate some of the noise inherent to real world data. In both cases, oxygen isotope values are calculated at fixed intervals in the distance domain over a single year of growth to yield synthetic sampled transects (Fig. 4A, 4D) from known input functions (Fig 4B, 4E). Outputs from both synthetic datasets yield estimates of intra-annual variation in temperature and growth rate arrayed in time (Fig. 4C, 4F) that are virtually identical to those values employed in the generation of the original synthetic isotope profiles (Fig. 4B, 4E, Table 2). Particularly useful descriptors of the growth function derived from the output sine parameters include the number of growing days and the maximum growth rate.

These examples demonstrate that this technique is able to recover input parameters from synthetic sampled transects, but under what range of input conditions is this likely to remain true? In order to assess model performance over a wide range of conditions, we create and model 1,000 synthetic oxygen isotope profiles and then compare output solutions to input parameters in the same manner illustrated above. Profiles were generated by randomly selecting from a wide range of values for each of the T_{sine} and G_{sine} parameters, resulting in a suite of 1,000 unique combinations of growth and temperature input functions. The only constraint on synthetic datasets is that they all come from input functions that simulate growth for at least 60% of the year. Each synthetic isotope profile consists of 15 equally spaced samples in the distance domain. Because the goal here is to identify those parameters most vulnerable to error, no noise was introduced into the synthetic datasets.

When input values are plotted against modeled values, most comparisons fall on or very close to the 1:1 line, indicating that the model is generally able to reproduce input functions over a wide range of T_{sine} and G_{sine} parameters (Fig. 5). For temperature parameters, underestimation of T_{amp} is the most frequent cause of mismatch (Fig. 5A), while the skewness term for growth becomes increasingly unreliable toward endmember values (Fig 5D). Maximum growth rate is robust under nearly all circumstances (Fig. 5F), however the duration of the growing season is particularly difficult to recover (Fig. 5E), being overestimated by more than one month in 10% of model runs. The duration of the growing season is ultimately controlled by the value of the output seasonal amplitude, suggesting that T_{amp} has a substantial impact on the fidelity of model results. If the seasonal range of temperatures is underestimated, growth is forced to occur over longer portions of the year, thus overestimating the total number of growing days. In every case where duration of the growing season is overestimated, T_{amp} is also underestimated. While qualitative aspects of the growth function (e.g., timing of maximum growth) are still recovered under these circumstances, the erroneous extension of the growing season can lead to spurious interpretations of physiological parameters (e.g., threshold temperatures). Notwithstanding this issue, the generally exceptional agreement between input and modeled values over a range of conditions suggests that our approach can recover reliable information about intra-annual variation in temperature and growth from isotope profiles provided that: 1) the presumption of sinusoidal variation in temperature and growth rate holds true, and 2) that isotope data capture most of the actual seasonal range of temperatures.

3.4.2 Model sensitivity: The impact of T_{amp}

Results from the exercise above indicate that the duration of the growing season can be difficult to constrain with confidence, with the degree of uncertainty dependent upon the accuracy of modeled seasonal amplitude. The ability to recover T_{amp} relates to the range of temperatures captured by shell growth during the year, which itself is determined by the relationship between the timing of maximum temperature and maximum growth rates. Here we explore how these variables interact and the conditions under which they are most likely to lead to error in model outputs. The objective is to illustrate the potential for bias under the most idealized conditions so as to bring to light the circumstances in which the model underperforms, and to offer some strategies for circumventing problems where possible.

Output T_{amp} values are largely dependent upon the range of isotope values preserved within the sample transect, which in turn is primarily a function of the duration of the growing season and the temporal phase shift of the growth function with respect to the temperature function. When accretion occurs over large portions of the year, isotope datasets capture the majority of the annual variation in temperature (Fig. 6). However, as the duration of the growing season decreases, isotope-derived temperatures can increasingly underestimate the amplitude of seasonality. This underestimation can be amplified or dampened depending on the temporal phase shift of the growth function in comparison to the temperature function (i.e., the time difference between the dates of maximum temperature and maximum growth rate; Fig. 6). Over the same duration of growth, bivalves that experience growth cessations during a seasonal extreme (i.e., a temporal phase shift of the growth function of 0 or |6| months) will consistently record lower seasonal amplitudes than those with growth cessations during the fall or spring (i.e., temporal phase shift of the growth function of -3 or 3 months, respectively; Fig 6).

Further exploration into this issue using synthetic datasets generated under constant input temperatures parameters but variable G_{pha} and G_{amp} (which simulates accretion over varying fractions of the year) values indicates that the probability of underestimating T_{amp} and overestimating the duration of the growing season increases when the range of isotope-derived temperatures accounts for less than 75% of the input seasonal amplitude. Note, however, that these results stem from simplified and idealized datasets. In these synthetic examples, there is no uncertainty in distance measurements nor in isotope values, and the isotope transects are not subject to noise, time averaging, or other sampling biases intrinsic to real world data. Thus, it is possible that in natural systems, T_{amp} could still be underestimated even if the isotope-derived temperatures account for well over 75% of the known seasonal range.

In cases where the isotope-derived amplitude of seasonality deviates significantly from the known seasonal range, the model-data mismatch can be minimized by constraining the range of potential T_{amp} and/or T_{pos} values. Setting a minimum value for T_{amp} limits the range of potential output values over which the model will iterate and forces the model to incorporate a growth cessation long enough to account for discrepancies between isotope-derived temperatures and the known temperature range. Similarly, independent MAT data can be used to set bounds on the potential values of T_{pos}. So long as growth captures at least one seasonal extreme, artificially constraining the range of potential T_{pos} solutions will force the model to account for the missing seasonal extreme, and thus increase the value of T_{amp}. When the range of temperature variation is accurately constrained, our approach fully captures subannual variation in the rates of shell accretion regardless of the relation between phases of temperature and growth rate.

In light of these insights, the range of isotope-derived temperatures within any sample transect should be compared with available oceanographic/climatological data prior to the application of the approach. In studies of Recent taxa, the range of temperatures derived from isotope data can be compared with measured or interpolated temperature data, and if the former underestimates the latter, a lower boundary on the possible solutions of T_{amp} can be set. Datasets reporting sea surface temperatures (SST) and temperature at a variety of ocean depths are widely available (e.g., Boyer et al., 2013) and useful in this regard. Whenever the temperature is unknown, mean temperature inferred from the isotope values can be compared with MAT data from an independent proxy (e.g., Mg/Ca, TEX_{86}, clumped isotopes) or climate model. If proxy or model-based MAT values are significantly different from isotope-derived mean temperatures, they can be used to set upper and lower limits on T_{pos}. When the range of temperature variation and/or mean temperature values are constrained, the model can capture subannual variation in rates of shell accretion regardless of relations between phases of temperature and growth rate variation.

3.5 Testing the model in natural systems

In order to test the fidelity of the approach in natural systems, we consider two published examples in which isotope compositions from Recent bivalves are accompanied by both coeval measured temperatures and growth rate data derived from measured microincrement widths (Goodwin et al., 2001; Hallmann et al., 2009).

3.5.1 Natural system 1: Chione cortezi *from the Gulf of California*

The first dataset comes from the shallow, infaunal bivalve *Chione cortezi* (Goodwin et al., 2009, 2001; Schöne et al., 2002b). Specimen IM11-A1L was live-collected in February of 2000 from the margin of the Colorado River Delta in the Gulf of California (31°40'N, 114°41'W). Fifteen $\delta^{18}O_{carb}$ values arrayed in distance space constrain the last year of growth (February 1999 – February 2000; Fig. 7A). Measured circalunidian increment widths, which indicate that growth is restricted to the summer months, provide an excellent record of growth in time against which to compare model results (Fig. 7B, thin black line). A sine curve fit to filtered mean temperatures averaged from bihourly temperature logger data (Fig. 7B, dark gray curve) yield an environmental MAT of 19.9 °C and a seasonal range of 18.0 °C, while isotope-derived temperatures indicate a MAT of 23.55 °C and a seasonal range of 10.1 °C. Because the isotope-derived temperatures clearly overestimate measured MAT while underestimating seasonal range, indicating growth over only a portion of the year, we set a lower bound on T_{amp} of 16 °C. Based on the best-fit sinusoid to observed temperature data, growth and temperature functions were assigned Julian dates by presuming that maximum temperatures were reached on August 1.

Modeled temperature and growth functions of the *C. cortezi* specimen are in excellent agreement with observed curves (Fig. 7B, 7C). Output values from the growth function are consistent with measured data at key growth intervals throughout the year (Table 3), particularly with respect to the timing and duration of the growing season. Agreement between the model growth function and the best-fit sinusoid through the measured increment width data (Table 3) suggests that discrepancies in the timing and magnitude of maximum growth rate are likely a function of the high-amplitude, high-frequency variations in the observed increment width data. An observed late summer ephemeral growth check (arrow in Fig. 7B) is not accounted for by our approach. Consequently, growth rate is slightly overestimated in the weeks immediately preceding the check and slightly underestimated in the weeks immediately following. However, these differences are minor and do not inhibit the interpretation of overall environmental and physiological parameters controlling intra-annual growth.

3.5.2 Natural system 2: Saxidomus gigantean *from Little Takli Island, Alaska*

The second dataset comes from the intertidal butter clam *Saxidomus gigantea* (Hallmann et al., 2009). Specimen GI1-LTI0907-A2L was live-collected on September 9, 2007 from Little Takli Island, Alaska (58°03'N, 154°26'W). Twelve isotope samples constrain the third year of growth (2005; Fig. 8A) and are accompanied by contemporaneous increment width measurements and sea surface temperatures from the NOAA World Ocean Databas (Boyer et al., 2013; Fig. 8B). We used a $\delta^{18}O_w$ value of -3.0‰ to account for observed freshwater influx (Hallmann et al., 2009) and allow for a more direct comparison between the measured temperature values and the modeled temperature function. Results were temporally aligned by presuming that maximum temperatures occurred on July 26. In this example, we consider the growing season to occur when growth rates rise above 10 μm/day, the lowest reported growth rate from Hallmann et al. (2009).

The growth curve derived from the oxygen isotope profile of *S. gigantea* is again in good agreement with both the observed growth increments and the best-fit sinusoid to those increments (Fig. 8C, Table 3), confirming the reliability of the approach. Results indicate that growth began in the spring and increased rapidly before reaching a maximum in late spring-early summer. Growth then gradually decreased into the fall before stopping in late November, for a total of ~230 growing days. Growth occurred when temperatures exceeded ~6 °C. Maximum growth rates were achieved approximately two months prior to maximum temperatures.

3.6 Applications of the model

Growth rates estimated from stable isotope profiles are in good agreement with those determined from numbers and widths of ciraclunidian increments (Fig. 7, 8). The reliability of this approach in both synthetic and natural systems suggests that the model can confidently be applied to recover estimates of intra-annual variation in growth in cases where isotope data are all that exist with which to constrain them. Below, we explore some of the many potential applications and insights afforded by this approach.

3.6.1 Temporal alignment of temperature and growth rate

Notwithstanding the numerous advantages of increment width studies, their primary limitation is the inherent disconnect between observed temperatures and growth profiles. While both temperature and increment widths can be measured, it is difficult to accurately align the two datasets, particularly when growth is not continuous throughout the year. In such cases, calendar assignments of increment width measurements are often based on assumptions of physiological characteristics. For example, Schöne et al. (2003b) temporally align observed increment widths by phase shifting the profile such that temperatures are the same on the first and last day of growth. While the assumption that temperature is the primary control on the initiation or cessation of growth is often fair, employing such an assumption to the temporal alignment of the increment width profile presupposes the existence of a constant temperature threshold. In doing so, any further attempt to link temperature and growth becomes circular.

In contrast, the model presented here incorporates phase as a parameter of both the temperature and growth functions. As a result, temporal alignment of the growth profile with respect to the temperature sinusoid is an output, not an assumption. Because the model independently relates temperature and growth, it can serve as an objective test for the existence of temperature-based physiologic constraints on growth. Application of the model, in tandem with increment width analysis, can help facilitate accurate temporal alignment of growth profiles, allowing for a more robust comparison between observed temperature and growth parameters.

3.6.2 Environmental influences on spatial/geographic patterns of intra-annual shell growth

Data on widths and numbers of lunar daily growth increments demonstrate that many bivalves exhibit pronounced intra-annual variation in rates of shell accretion, often including intervals of complete growth cessation. Following intervals of no growth, increment widths typically increase, reach some seasonal maxima, and then decrease until the next interval of dormancy (Fig. 3). Skewed sinusoids fit to increment width profiles typically account for 70-80% of observed variation in growth rate, and their parameters quantify the net duration, maximum rate, and asymmetry of growth (Table 4). Sinusoids fit directly to increment width data produce a quantitative understanding of the parameters that control changes in annual accretion and illustrate how this approach, when applied to isotope profiles alone, can yield quantitative assessments of growth as arrayed in time or space. For an example, the three ontogenetic series in Fig. 3 (E-G, each comprising four years of growth) all exhibit a decrease in the net amount of shell accreted with age, but the degree to which that decrease is due to lower rates or shorter growing seasons is not apparent on the basis of visual inspection alone. However, a best-fit sinusoid to the growth profile clearly shows that the decrease in annual increment widths of *S. gigantea* (Fig. 3E) is almost entirely due to a reduction in accretion rate over a nearly constant number of growing days per year, while in the case of *C. cortezi*, the decrease in annual increment width is equally related to reductions in growth rates and annual durations (Table 4).

Quantitative assessment of the parameters responsible for differences in annual shell growth applied to populations arrayed in space enables attribution to correlated environmental variables. Sato (1997), for example, reports variation in daily increment formation during the third year of growth for 18 specimens of *Phacosoma japonicum* off the coast of northern and southern Japan (Fig. 9). Visual inspection is sufficient to show that shells in the northern population grew rapidly in late spring and summer while those from the two southern populations grew more slowly over more of the year. Differing skewness between the records has been related to seasonal changes in phytoplankton abundance (Sato, 1997). Determination of best-fit sinusoids to these data allows for a quantification of these generalizations. Although the widths of the third annual growth increment are similar across all three sites (Fig. 10A), the similarity is brought about by a pronounced inverse relationship between the duration of shell accretion and the widths of microincrements within the year (Fig. 10B). Moving south from northern Hakodate Bay (41.8 °N) to Ariake (33.0 °N) and Kagoshima (31.4 °N) Bays, the duration of intra-annual accretion progressively increases and the widths of microincrements progressively decrease. These changes correlate with latitudinal variations in MAT and the annual range of temperatures (Fig. 10C). While this example does not explicitly apply the model to stable isotope data, we include it to illustrate how mathematical quantification of intra-annual shell growth using sinusoidal functions allows for a more direct comparison of the timing and magnitude of growth rate variations between individuals and across populations. Thus, application of this model to serially sampled isotope datasets can answer first-order questions about the primary controls on subannual growth rate even in taxa where daily growth increments are absent or unavailable.

3.6.3 Examination of intra-annual growth patterns through ontogeny

Many authors have discussed the value of long time series of isotope data for revealing temporal patterns in climate variables at a given location (e.g., Wanamaker et al., 2011). Derivation of intra-annual growth parameters from those same stable isotope profiles would allow for a rigorous numerical analysis of the timing, rate, and duration of growth over time, as well as how growth parameters relate to associated temperature variables. Those variables can then be related back to environmental factors and interpreted in the context of physiology. Furthermore, modeling several successive years of growth can be used to determine whether those variables remain stationary, change through ontogeny, or vary with prescribed periodicities (e.g., El Niño Southern Oscillation, North Atlantic Oscillation).

As an illustration, we apply the approach to the longest and most complete isotope transect yet obtained from any bivalve, a 374-year-old specimen of the long-lived North Atlantic bivalve *Arctica islandica* (Schöne et al., 2005a). The 'Methuselah clam' was live-collected in July of 1868 from shallow (<30 m) marine water off the coast of Iceland. Ontogenetic years 3 through

40 were sampled, resulting in 1,051 stable isotope analyses spanning 38 complete years of growth from 1495 to 1532 CE (Fig. 11A; Schöne et al., 2005a). As noted by Schöne et al. (2005a), isotope profiles over each annual cycle are similar in form, defined by a saw-tooth-shaped profile that shifts abruptly from depleted (summer) values to more enriched (winter) values, then moves gradually to the next depleted value. The strongly skewed shape of the annual $\delta^{18}O$ profiles and the observation that growth bands typically occur within the cooling limb rather than at isotopic extremes (Fig. 11A) suggests that the shell grew slowly or not at all during the fall and most rapidly during the spring, and that growth captures both seasonal extremes.

We model temperature and growth rates for the 38 years of published stable isotope data. Years were delineated by successive isotopic extremes and the dataset was modeled twice - once with years demarcated by the most depleted values (Fig. 11A, open circles) and once with the years demarcated at the most enriched values (Fig. 11A, filled circles), resulting in 75 unique sets of output functions. Results were temporally aligned by assuming that maximum temperatures were reached on September 1. The modeled temperature functions yield a mean annual temperature of 6.3 ± 0.4 °C (Fig. 12A), virtually identical to the average isotope-derived temperature (6.3 °C), though cooler than the measured MAT in the region (7.4 ± 0.2 °C; Boyer et al., 2013; Smith and Reynolds, 2003). Mean seasonal temperature range is 1.6 ± 0.5 °C (Fig. 12B), similar to the range of values captured in the isotope data but somewhat underestimating the average SST range of 4.4 °C as reconstructed by Smith and Reynolds (2003). However, the attenuation of seasonal amplitude with increasing water depth (Wilkinson and Ivany, 2002) predicts that seasonal variation where this shell grew was reduced in comparison to that at the surface, particularly with respect to summer temperatures. In fact, temperature measurements over a range of depths for sites off the coast of Iceland exhibit a 3.5 °C average decrease in amplitude from the sea surface to a depth of 30 m (Boyer et al., 2013). The reduced seasonal range and somewhat lower MAT at depth in comparison to the surface are therefore predicted by oceanographic data, reflected in shell isotope data, and fully captured by modeled results.

Growth parameters for each of the 75 model runs reveal similar patterns of accretion (e.g., Fig. 11B, 11C). Growth begins in late February or early March and ceases sometime between late November and mid-December, for an average of 318 days of growth. Maximum growth rates are achieved between June and July, with a mean date of maximum growth of June 19 ± 68 days (Fig. 12C). These results are in excellent agreement with observed patterns of the timing and duration of intra-annual growth in modern North Atlantic *A. islandica* specimens (Ballesta et al., 2017). Analysis of yearly statistics through time can be used to identify temporal trends in growth parameters, in this case illustrating that the timing, rate, and duration of annual growth are consistent through this portion of ontogeny (Fig 12D). Furthermore, provided a long enough time series, Fast Fourier Transform (FFT) analysis can be used to identify potential periodic variations in growth parameters themselves, similar to that conducted by Schöne and colleagues (2005a) on seasonal extremes in isotope values in the Methuselah dataset.

Finally, relating growth parameters to environmental and annual increment width data can provide additional insights into the causes of changes in inter-annual growth rate through ontogeny. Schöne et al. (2005a) found a statistically significant correlation between maximum annual isotope-derived temperatures and residual annual increment width in the Methuselah clam, a finding we can reproduce with the model-derived seasonal range ($R^2 = 0.27$; $p < 0.001$). Because annual increment widths are determined by some combination of the duration and rate of shell accretion over the growing season, both of which are estimated by this approach, model outputs are able to deconvolve these two influences, something that Schöne and colleagues were unable to address in their original work. In this case, annual increment widths positively correlate with maximum annual growth rates ($R^2 = 0.81$; $p \ll 0.001$), but are unrelated to the number of growing days in the year ($R^2 = 0.04$; $p = 0.09$), indicating that year-to-year variations in annual increment width are brought about by changes in the rate, not the duration, of intra-annual growth. Pinpointing the mechanisms responsible for deviations in annual increment widths further illustrates how this approach can enrich studies of variation in growth over time.

3.7 Conclusions

We present a new model for quantifying intra-annual variations in accretion rate of bivalve shells based solely on oxygen isotope profiles arrayed in space. Comparison of output temperature and growth functions with a variety of synthetic and natural datasets confirm the fidelity of the approach. Veracity of results is optimized when constraints on the minimum amplitude of seasonality are set prior to running the model, particularly when one of the seasonal extremes is absent from the isotope profile. This methodology has a variety of practical applications, including quantifying differences in patterns of intra-annual growth over geographic regions and throughout ontogeny. When applied in tandem with increment width measurements, model results can be used to facilitate accurate calendar alignment of the observed increment widths. Furthermore, the approach can be applied to long time series in which increment width measurement would be impractical or infeasible to attain; temporal variations in the growth profiles can be used to identify ontogenetic trends and/or short-term climate oscillations. Additionally, though all of the model applications presented here utilize data from bivalves, the method is equally applicable to isotope profiles from other accretionary organisms, such as fish otoliths, corals, or other mollusks. This model offers a number of advantages over previous approaches to assess intra-annual variation in bivalve shell growth. Its application to new and existing stable isotope profiles in the distance domain will allow for a more sophisticated and nuanced evaluation of the patterns in and controls on shell growth in space and through time.

Figures

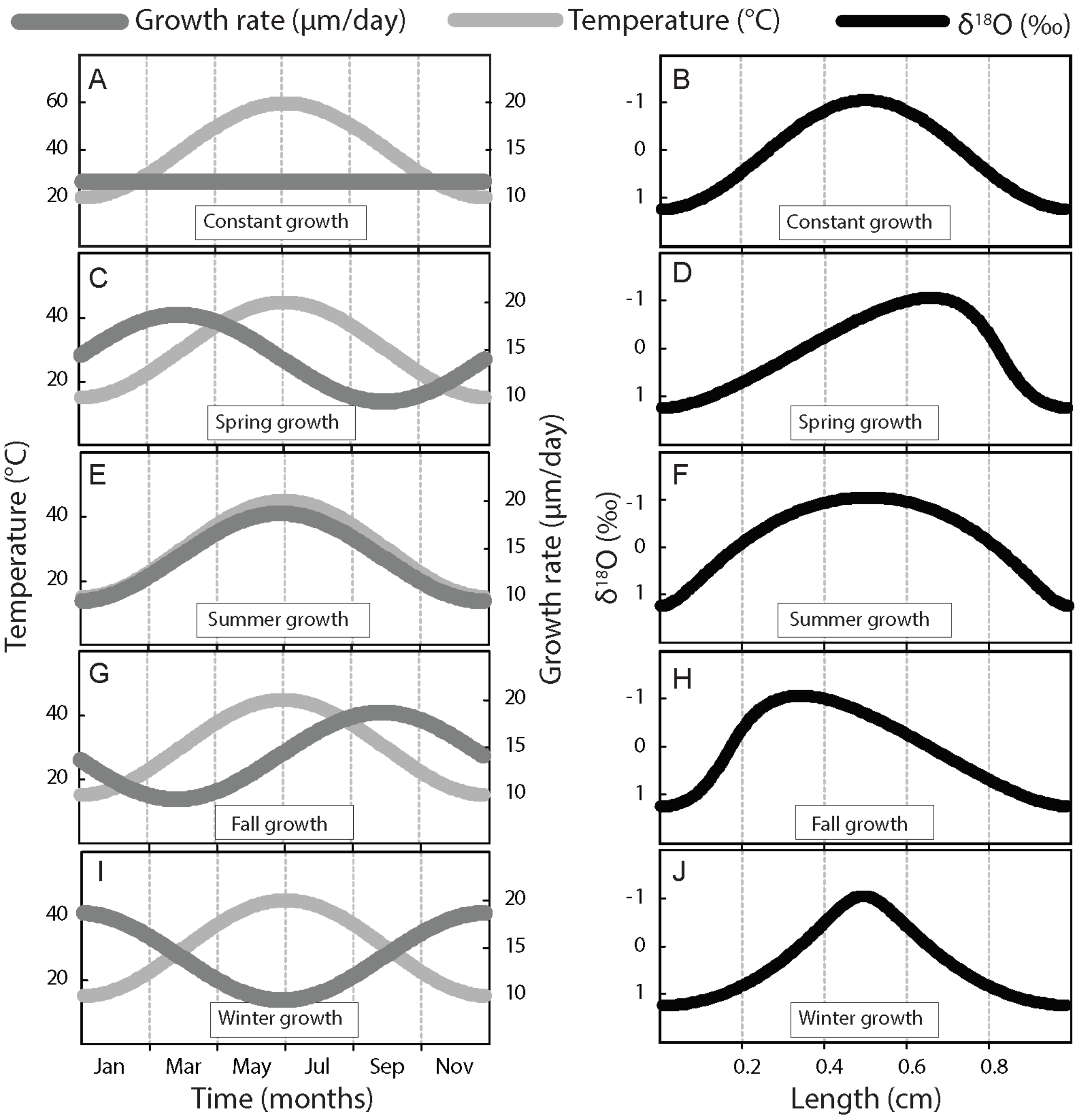

Figure 3.1. Dependence of spatial variation in isotope composition (right column, black lines) on secular variation (left column) in temperature (light gray lines) and growth rate (dark gray lines). All examples assume a sinusoidal temperature variation of 15 ± 5 °C with maximum temperature on July 1, and represent one year and one cm of accretion. Annual changes in growth rates range from invariant (A) to sinusoidal variation, with phase shifts ranging from maxima in the spring

(C), summer (E), fall (G), and winter (I). Spatial distribution of δ18Ocarb resulting from these differences in growth rate result in sinusoidal (B), left-skewed (D), platykurtic (F), right-skewed (H), and leptokurtic (J) profile shapes.

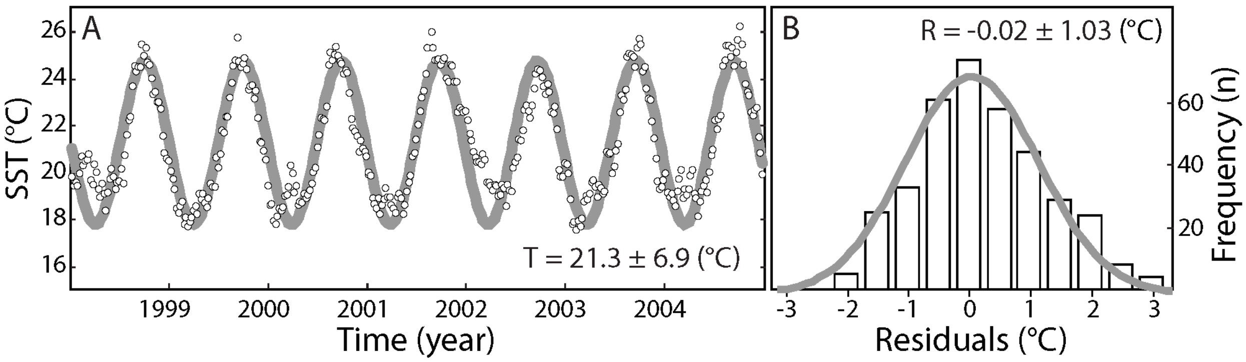

Figure 3.2. Example of sinusoidal temperature variation in nature. A) Secular variation in seven years of weekly resolved sea surface temperature (SST) data (open circles) from coastal Mauritania, NW Africa (Müller et al., 2015; Reynolds et al., 2002), fit with a sinusoid (thick gray line). B) Histogram of residuals from sine fit. Deviations from sinusoidal variation comprise Gaussian noise, centered at ~0oC, with a standard deviation of ~1°C.

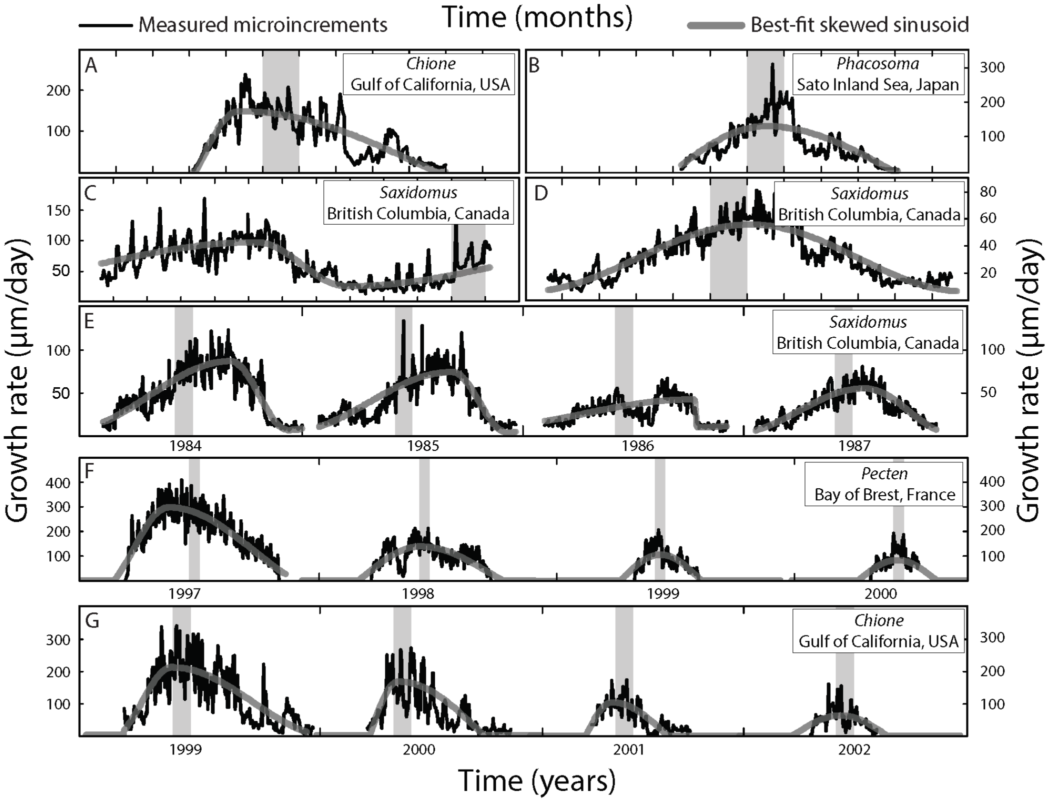

Figure 3.3. Examples of intra-annual variation in growth rate from widths of daily growth bands (thin black lines, published data), with best fit skewed sinusoid functions (thick dark gray lines). Light gray bands span the month of June in each year, for comparison. **A**. *Chione cortezi* from the Gulf of California, USA (Goodwin et al., 2001; specimen IM11-A2L). **B.** *Phacosoma japonicum* from Sato Inland Sea, Japan (Schöne et al., 2003b; specimen SI7-A2). **C**. *Saxidomus gigantea* from British Columbia, Canada (Hallmann et al., 2009; specimen DeRt-1-0787-A3L). **D**. *Saxidomus gigantea* from British Columbia, Canada (Hallmann et al., 2009; specimen DeRt-1-0188-A15L). **E**. Four years of growth of *Saxidomus gigantea* from British Columbia, Canada (Hallmann et al., 2009; specimen DeRt-1-0188-A15L). **F**. Four years of growth of *Pecten maximus* from the Bay of Brest, France (Lorrain et al., 2004; specimen N). **G**. Four years of growth of *Chione cortezi* from the Gulf of California, USA (Goodwin et al., 2003; specimen IP1-A1R).

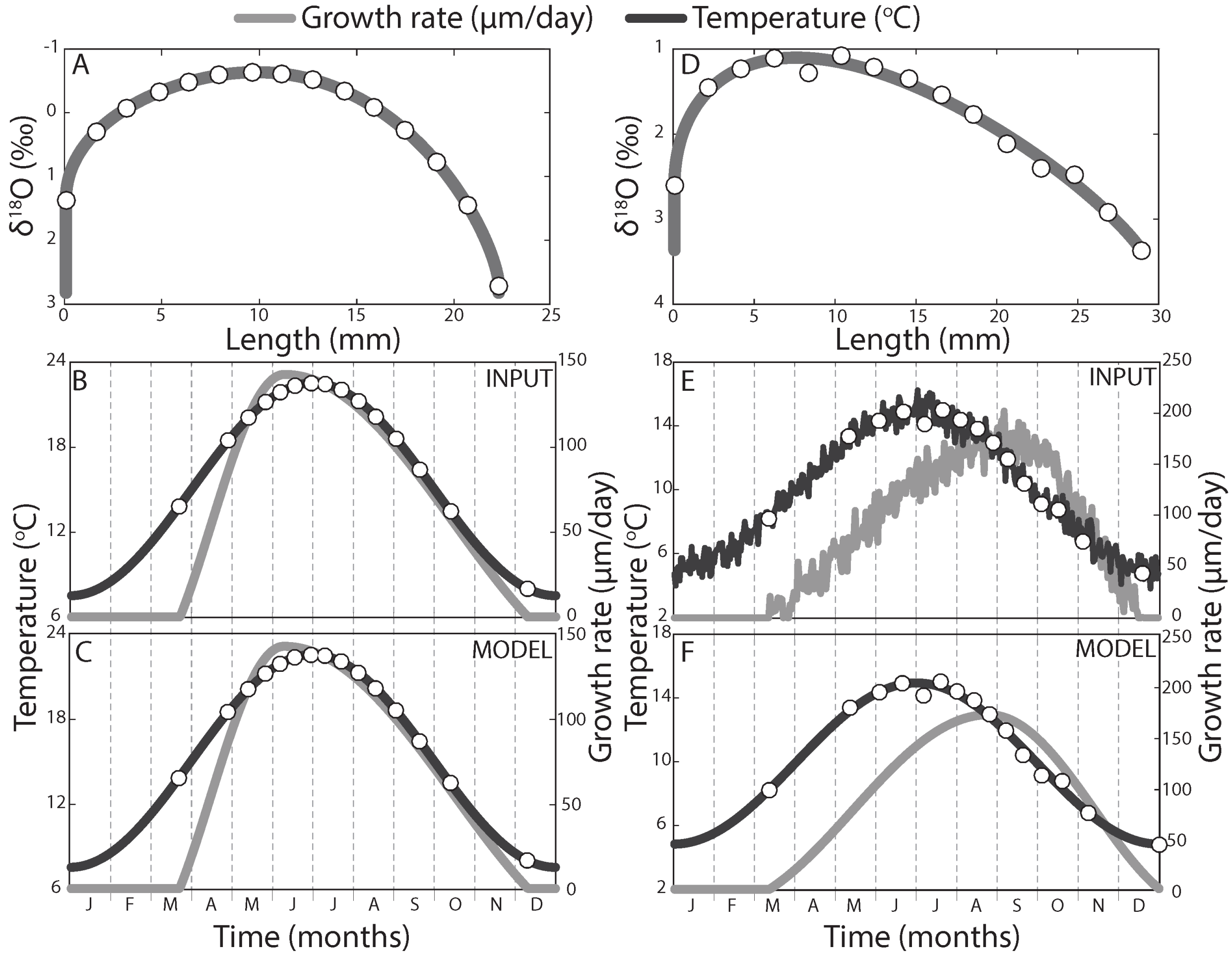

Figure 3.4. Two synthetic examples of the recovery of input temperature and growth curves from evenly spaced geochemical data sampled in distance space over one year of accretion. The synthetic isotope datasets (A and D) are derived from prescribed sinusoidal variation in temperature (B and E; dark gray lines) and skewed sinusoidal variation in growth rate (B and E; light gray line). Black points on temperature curve in panels C and F indicate the temporal placement of samples. In the second example (D-F), the input growth function is superimposed with a fortnightly tidal cycle, and Gaussian Noise is added to both input functions. Modeled solutions (C and F), determined only from the isotope datasets in A and D, are in excellent agreement with the input functions originally used to generate those isotope data.

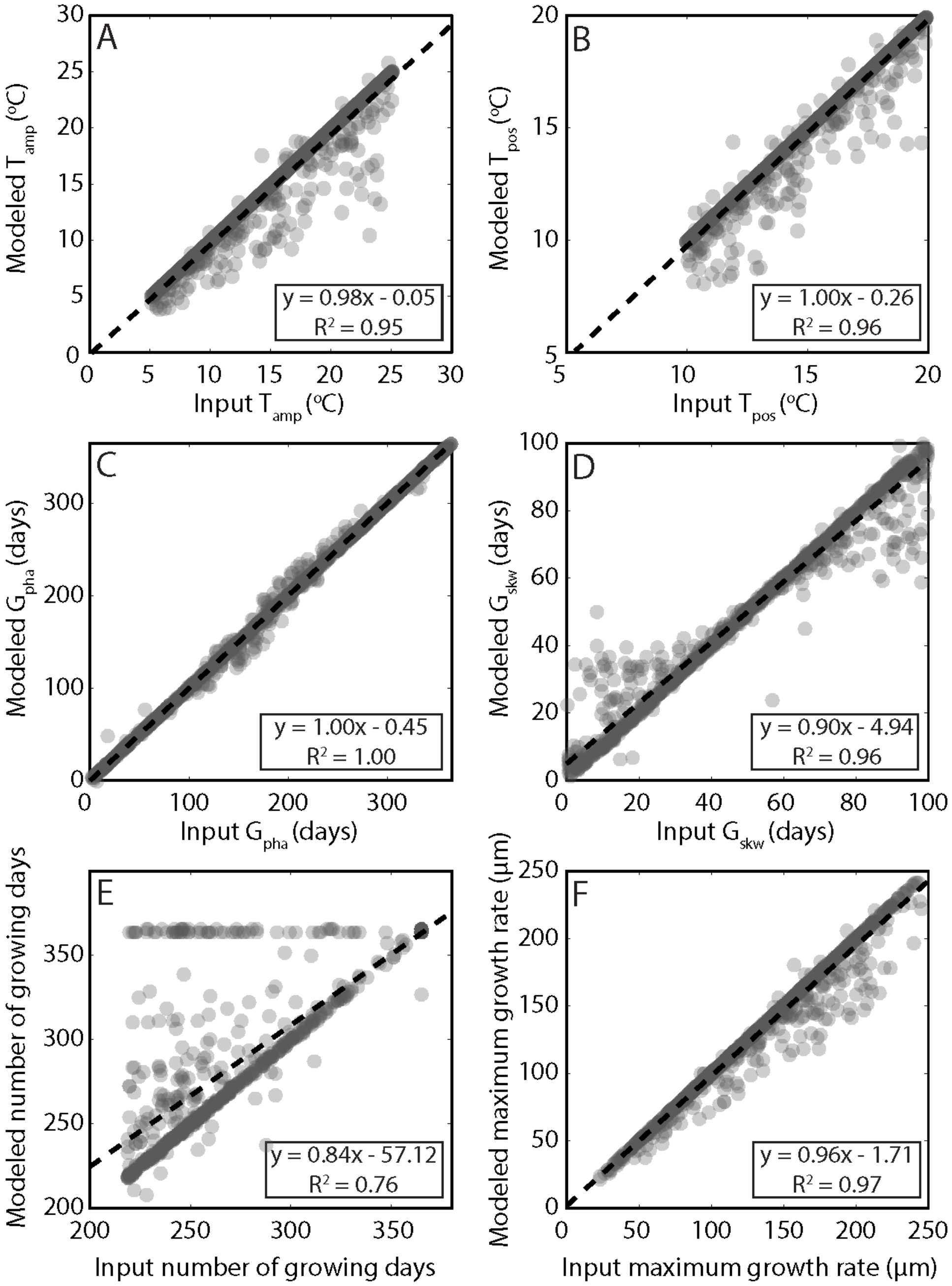

Figure 3.5. Comparison of model results to input variables from 1,000 randomly generated synthetic datasets as a means of testing model fidelity under idealized conditions. Cross plots of input and modeled values of Tamp (A), T_{pos} (B), G_{pha} (C), G_{skw} (D), number of growing days (E), and maximum growth rate (F). Degree of shading reflects density of overlapping points. Inset equations describe the dashed regression lines. Abbreviations as in Table 1.

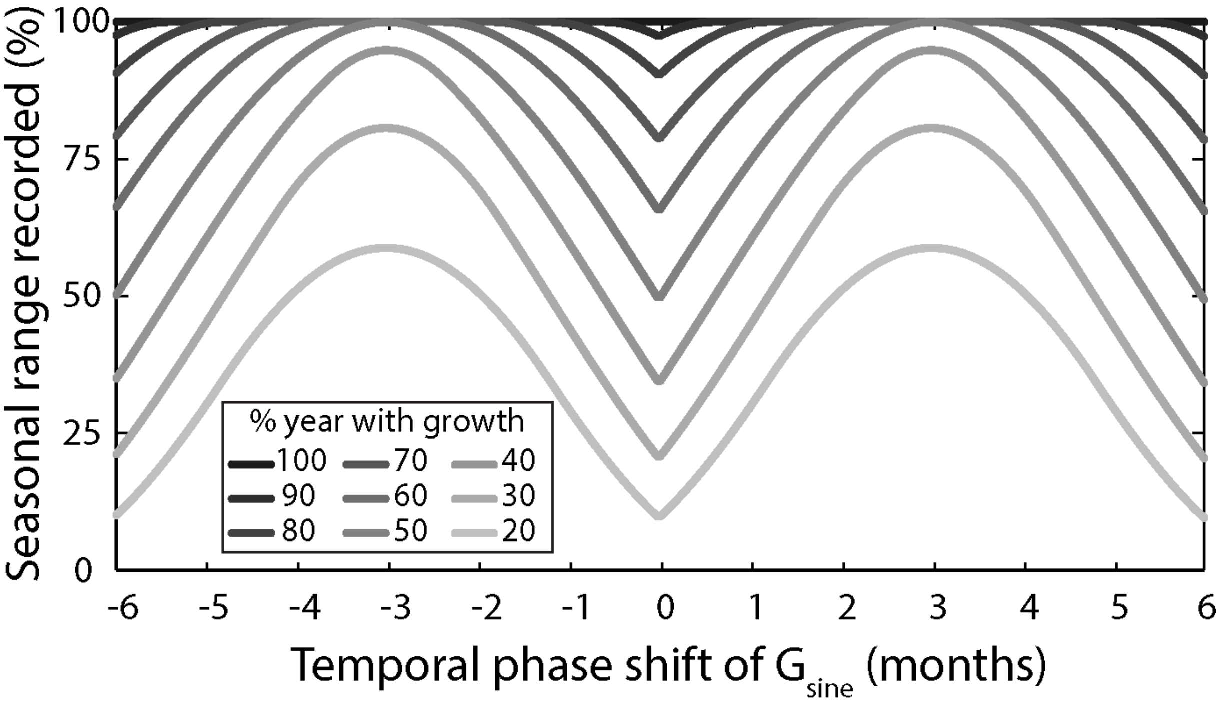

Figure 3.6. Graphical representation of the percent of seasonal range available to be recorded in bivalve shells given varying temporal phase shifts between temperature and growth and duration of growing seasons. There is a higher probability of recovering the full amplitude of seasonality if minimum growth occurs in the fall or spring (i.e., temporal phase shift of -3 or 3 months, respectively). Bivalves that experience growth cessations during peak winter or summer temperatures (i.e., temporal phase shift of 0 or |6| months, respectively) are constrained to record a lower seasonal range. Note that these curves reflect the seasonal range that would be recorded under idealized conditions; an actual sampled transect through carbonate recording these conditions is subject to time averaging, as well as a host of other sampling biases, which could further attenuate the predicted signal.

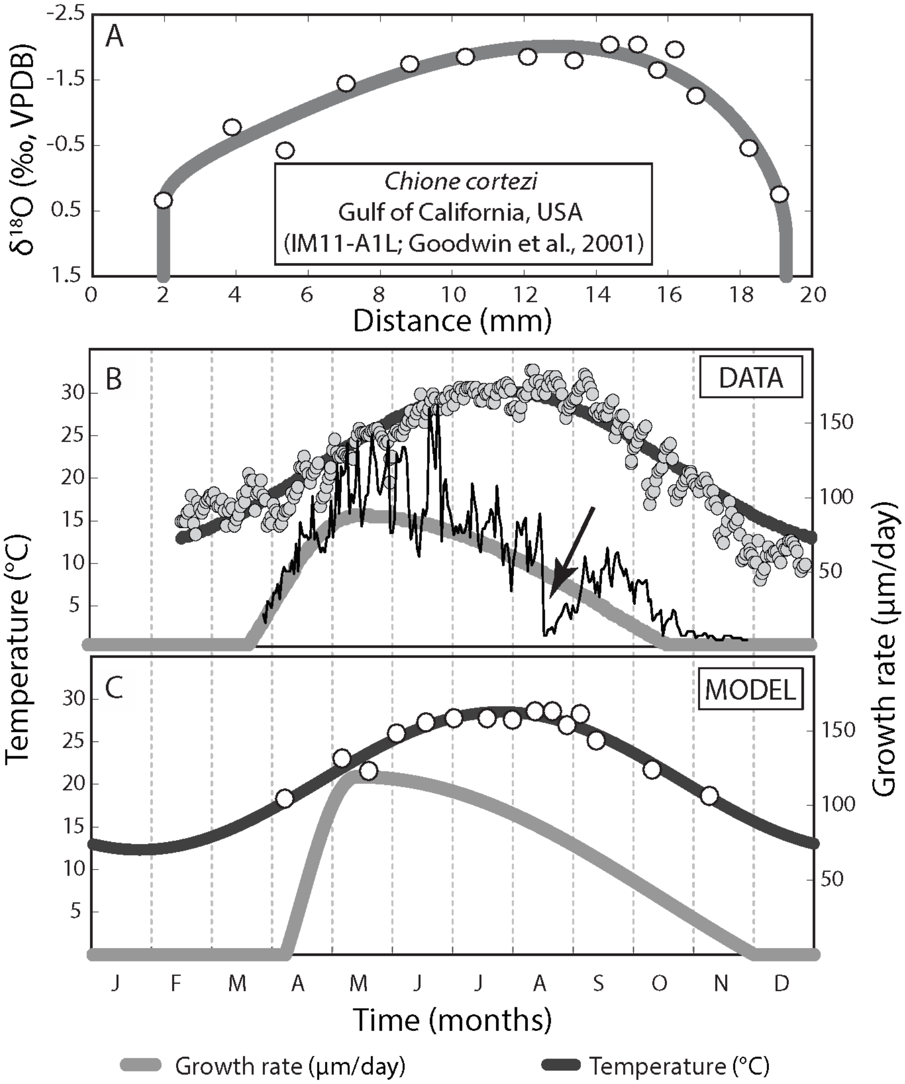

Figure 3.7. *Chione cortezi* from the northern Gulf of California, USA (Goodwin et al., 2001; specimen IM11-A1L). **A**. Stable isotope compositions (open points) and best-fit isotope profile calculated from model temperature and growth functions. **B**. Average daily measured temperature (gray points) fit with a temperature sinusoid (dark gray curve) and measured circalunidian increment widths (black lines) fit with a growth sinusoid (light gray curve). Arrow marks a summer growth cessation. **C**. Modeled temperature (dark gray curve) and growth rate (light gray curve) functions, derived only from the data in panel A. Note the agreement between observed increment width profile and the modeled growth curve.

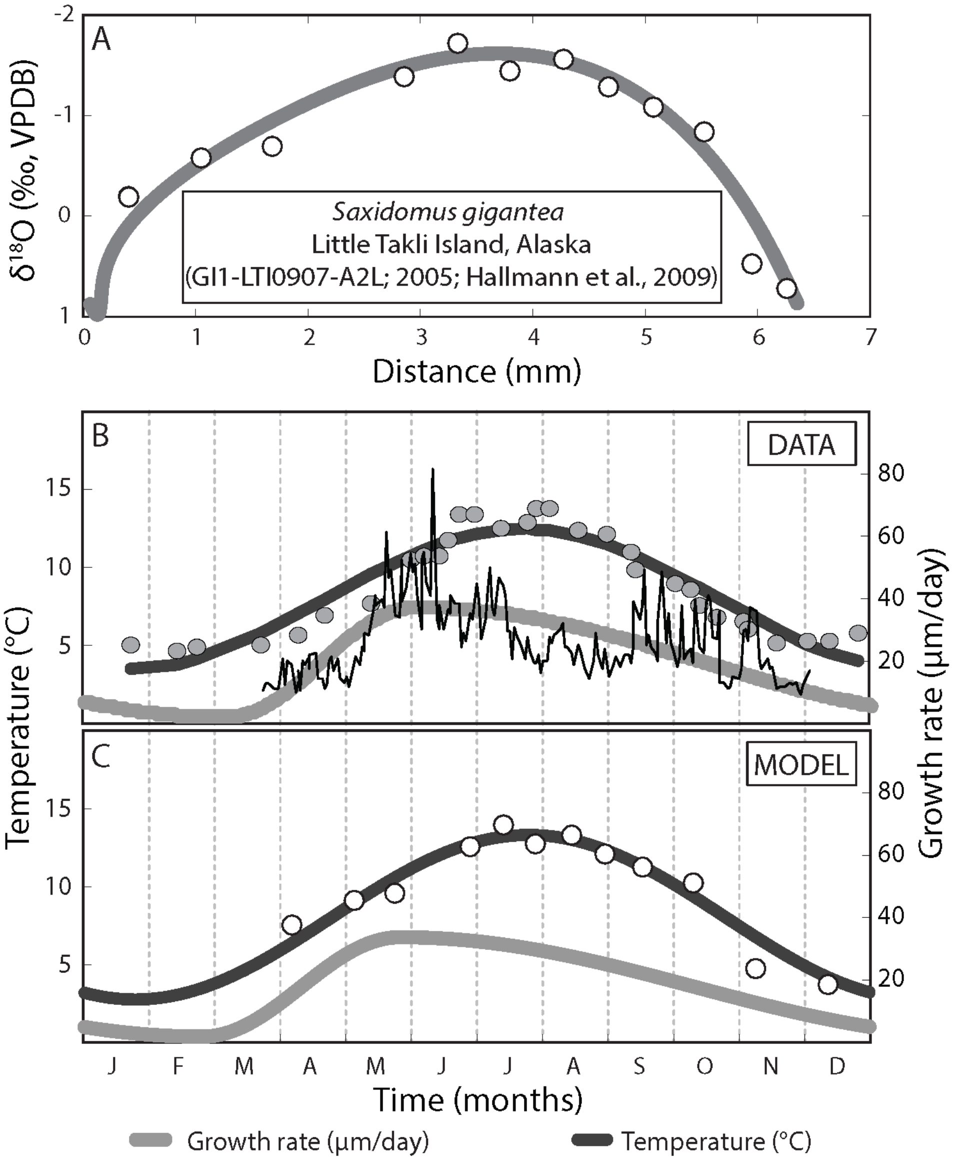

Figure 3.8. *Saxidomus gigantea* from Little Takli Island, Alaska (Hallmann et al., 2009; specimen GI1-LTI0907-A2L). **A**. Stable isotope compositions (open points) and best-fit isotope profile calculated from model temperature and growth functions for growth in 2005. **B**. NOAA sea surface temperatures (gray points) fit with a temperature sinusoid (dark gray curve) and measured lunar daily increment widths (black lines) fit with a growth sinusoid (light gray curve). **C**. Modeled temperature (dark gray curve) and growth rate (light gray curve) functions derived from the isotope data in panel A.

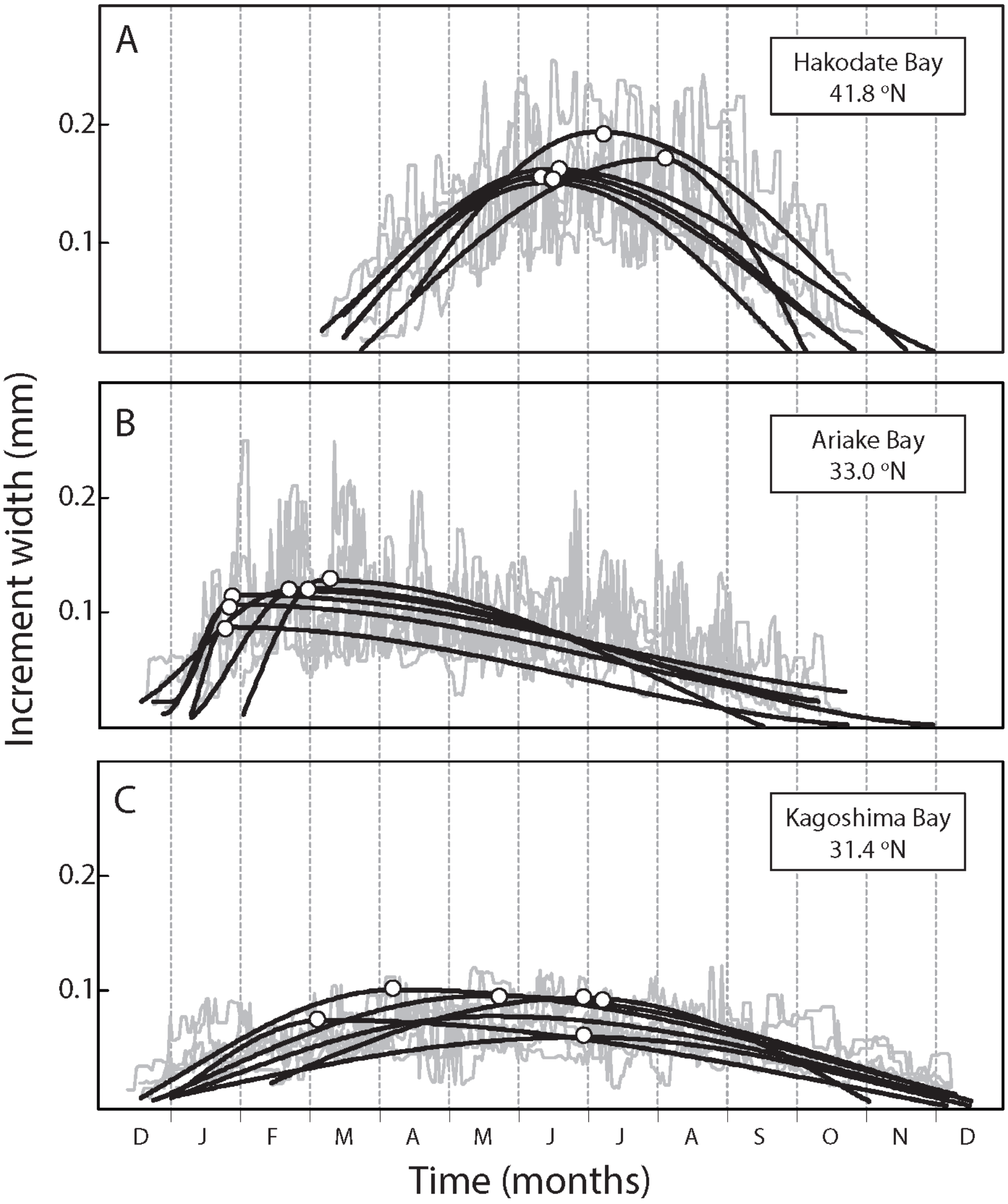

Figure 3.9. Measured (light gray lines) and modeled (dark gray lines) microincrement widths from the third ontogenetic year of 18 specimens of *Phacosoma japonicum* collected Hakodate Bay, Japan (**A**), Ariake, Japan (**B**), and Kagoshima Bay, Japan (**C**) (data from Sato, 1997). Open points locate position of maximum model growth for each specimen. Note that moving from north (Hakodate Bay) to south (Kagoshima Bay), mean growth rates decrease, while the number of growing days increases and growth profiles become more strongly right skewed.

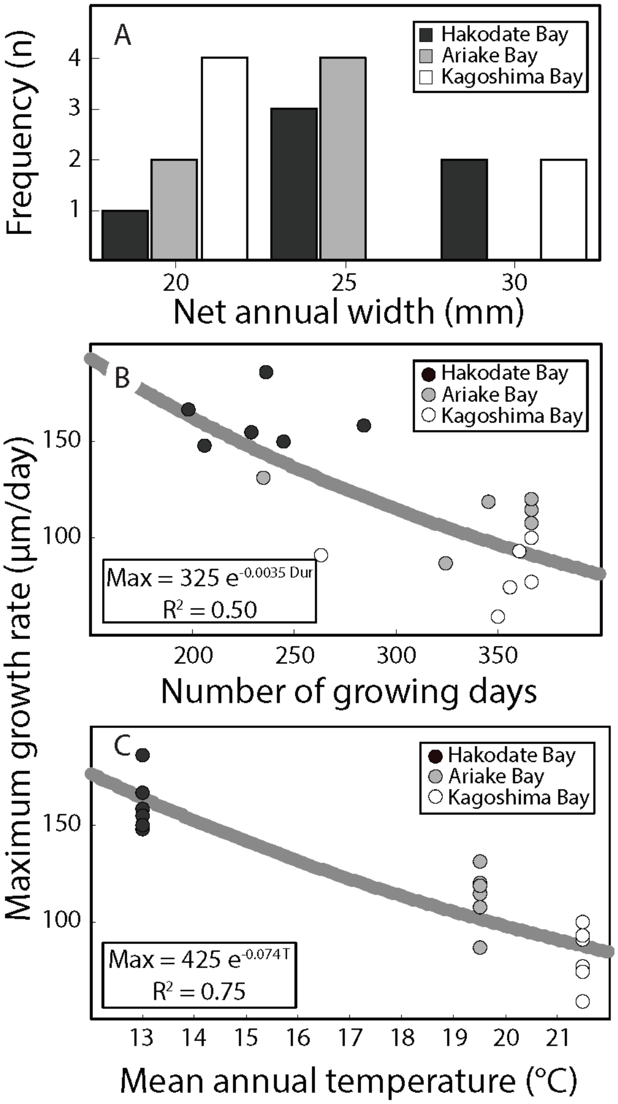

Figure 3.10. Quantifiable relationships afforded by determination of best-fit sinusoids to microincrement widths in Figure 9. The net width of the third year growth band is similar at all three sites (**A**) because durations of shell accretion exhibit a reciprocal relation to maximum modeled band widths (**B**), which decreases with latitude and mean annual temperature (**C**).

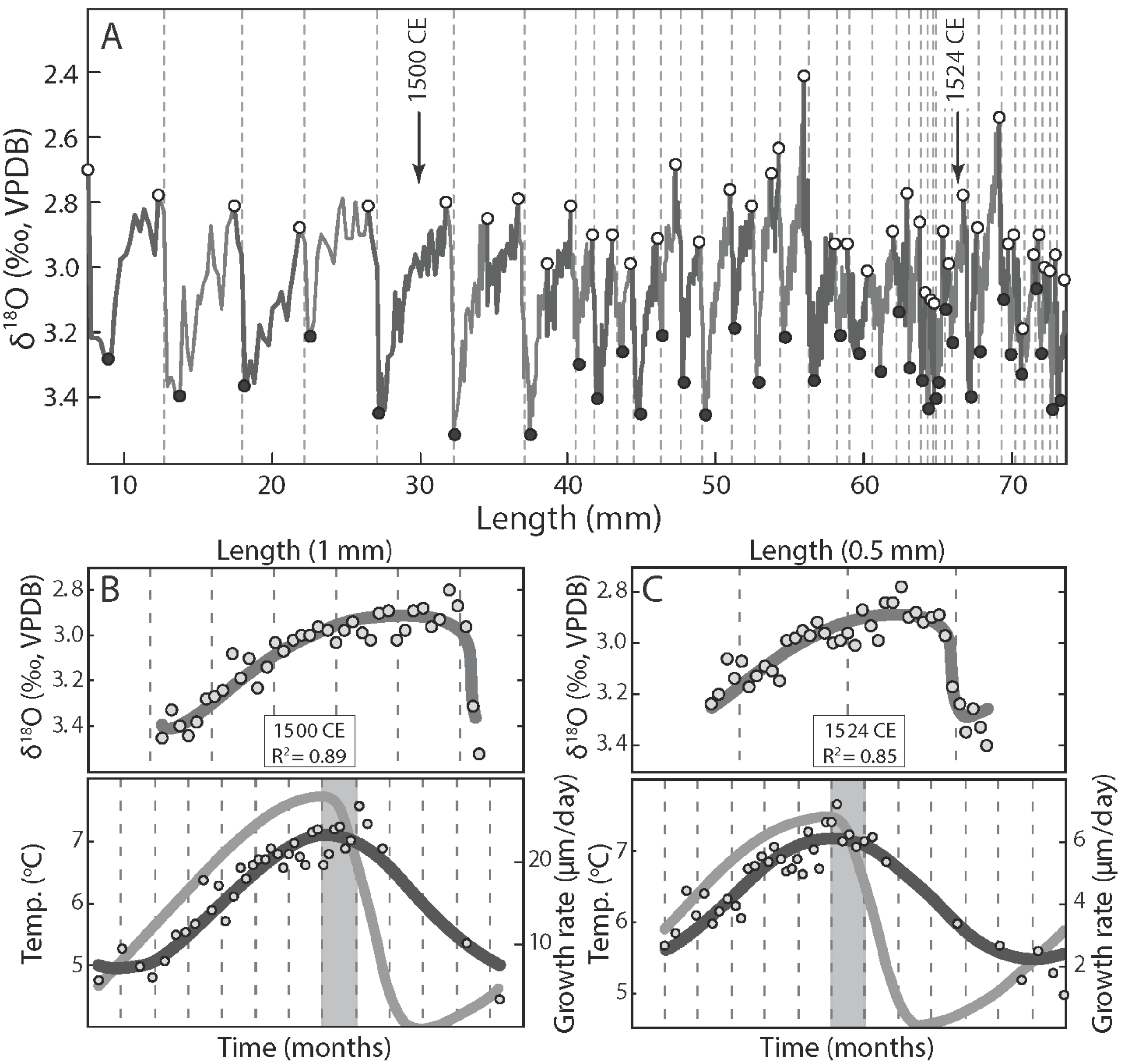

Figure 3.11. 374-year-old *Arctica islandica* from the coast of Iceland (Schöne et al., 2005a). **A**. Intra-annual isotope compositions (alternating years as light and dark gray lines) for the 38 complete years of oxygen isotope data; annual increments for the model runs are delimited by the most enriched values (peak winter; open points); dashed line indicates the placement of annual (fall) growth lines. **B** and **C**. Modeled temperature and growth functions based on annual oxygen isotope profiles from 1500 and 1524 CE, respectively. Gray bands demarcate September.

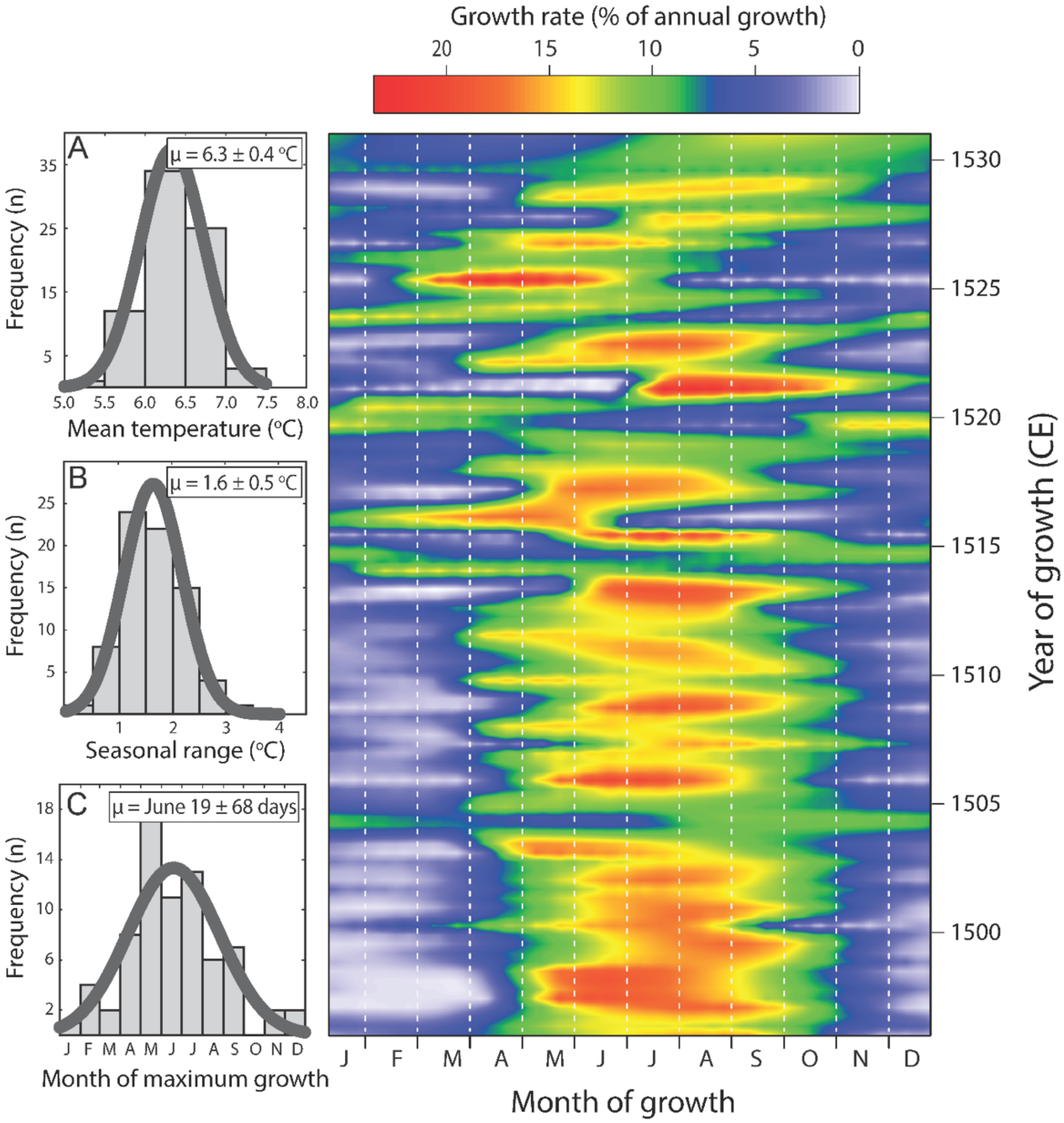

Figure 3.12. Summary statistics for the 38 years of modeled growth of the Methuselah clam. A. Frequency distributions of the modeled values of mean temperature (**A**), and seasonal range of temperatures (**B**), and the date of maximum growth (**C**). **D**. Color map illustrating the percent of annual growth for each day of the year over the 38-year-long time series. Modeled growth profiles are similar for most years, with maximum growth occurring between June and July, and growth cessations from December through March.

Tables

Table 3.1 Input parameters for both the temperature (T_{sine}) and growth (G_{sine}) functions. See Supplemental Materials for equations.

	Parameter	Explanation
Temp. Sinusoid	T_{amp}	amplitude; annual range of temperatures
	T_{per}	period; duration of temperatures under consideration (generally fixed at 365 days)
	T_{pha}	phase; day of the year with the warmest temperature
	T_{pos}	position; mean annual temperature
Growth Sinusoid	G_{amp}	amplitude; annual range of growth rate
	G_{per}	period; duration of growth under consideration (generally fixed at 365 days)
	G_{pha}	phase; day of the year with maximum growth
	G_{pos}	position; mean annual growth rate (not accounting for growth cessations)
	G_{skw}	skewness; measure of asymmetry of growth throughout the year

Table 3.2. Comparison of input and modeled growth parameters for two synthetic datasets (Fig. 4).

	Example 1 (Fig. 4A – 4C)		**Example 2 (Fig. 4D – 4F)**	
	Input	**Modeled**	**Input**	**Modeled**
First day of growth	24 Mar	24 Mar	14 Mar	14 Mar
Last day of growth	10 Dec	10 Dec	19 Dec	31 Dec
Date of maximum growth	10 Jun	10 Jun	06 Sep	25 Aug
Duration of growth (days)	262	262	275	293
Mean non-zero growth rate (µm/day)	85	85	105	98
Maximum daily growth rate (µm/day)	143	142	202	171
Temp. on max day of growth (°C)	22.0	22.0	12.5	12.9
Temp. at onset of growth (°C)	13.9	13.9	8.2	8.3
Temp. at offset of growth (°C)	8.0	8.0	4.8	4.8

Table 3.3. Comparison of observed and modeled growth parameters for two natural system clams (Fig. 7, 8).

	C. cortezi Gulf of California, USA IM11-A1L (Goodwin et al., 2001)			*S. gigantea* Little Takli Island, Alaska, USA GI1-LTI0907-A2L (Hallmann et al., 2009)	
	Observed[1]	Sine fit[2]	Modeled	Sine fit[2]	Modeled
First day of growth	01 Apr	24 Mar	09 Apr	08 Apr[4]	30 Mar[4]
Last day of growth	26 Nov	20 Nov	30 Nov	23 Nov[4]	19 Nov[4]
Date of maximum growth	25 Jun	17 May	13 May	04 Jun	28 May
Duration of growth (days)	240	210	236	226[4]	235[4]
Maximum daily growth (μm)	201	110	120	36	34
Temp. on day of max. growth (^{o}C)	21 – 26[3]	25	22.9	11	11
Growth rate asymmetry (G_{skw})	-	26	15	25	25
Ave. non-zero daily growth (μm)	-	39	73	18[4]	25[4]
Lower temp. threshold (^{o}C)	16.7 – 17[3]	16 – 22	16 – 18	5 – 7[4]	6[4]

[1] Values from Goodwin et al. (2009).

[2] Based on best-fit sinusoid to measured increment width profile (light gray curves in Fig. 7B, 8B).

[3] Combined range from Goodwin et al. (2001) and Schöne et al. (2002a).

[4] Values indicate where daily growth fell below 10 μm (lowest reported increment width from Hallmann et al., 2009).

Table 4. Asymmetric sinusoidal growth (G_{sine}) functions describing intra-annual growth rates for each year in the three ontogenetic sequences depicted in Figure 3.

	Saxidomus gigantea Mink Island, Alaska, USA Specimen DeRt-1-0188-A15L (Hallmann et al., 2009)				*Pecten maximus* Bay of Brest, France Specimen "N" (Lorrain et al., 2004)				*Chione cortezi*, Gulf of California, USA Specimen IP1-A1R (Goodwin et al., 2003)			
Year	1984	1985	1986	1987	1997	1998	1999	2000	1999	2000	2001	2002
Duration of growth (days)	365	365	365	365	336	225	144	151	365	203	142	134
Date of maximum growth	29 Aug	16 Jun	12 Aug	16 Jul	07 Jul	07 Jul	07 Jul	07 Jul	21 Apr	05 Jun	11 Jun	27 May
Average non-zero growth rate (μm/day)	54	46	29	38	195	100	79	74	121	79	51	57
Maximum daily growth	89	77	43	58	294	138	110	90	217	148	100	78
Growth rate asymmetry (Gskw)	72	71	80	58	30	39	46	57	28	22	36	48
Date end winter growth check	01 Jan	01 Jan	01 Jan	01 Jan	11 Mar	30 Mar	09 May	05 May	01 Jan	25 Mar	05 Apr	13 Apr
Date begin winter growth check	31 Dec	01 Jan	01 Jan	01 Jan	01 Jan	09 Nov	31 Aug	21 Aug	01 Jan	13 Oct	16 Aug	23 Aug
R^2 [1]	0.83	0.81	0.55	0.76	0.74	0.79	0.81	0.75	0.74	0.74	0.80	0.80

[1] Fit between observed increment width profiles and best-fit sinusoidal growth functions.

References

Alvarez, M.J., Pérez, D.E., 2016. Gerontic intraspecific variation in the Antarctic bivalve *Retrotapes antarcticus*. Ameghiniana 53, 485–494. doi:10.5710/amgh.05.12.2015.2947

Ballesta, I., Rob, A., Michael, W., Jaap, L.C., 2017. Environmental factors regulating gaping activity of the bivalve *Arctica islandica* in Northern Norway. Mar. Biol. 164, 1–15. doi:10.1007/s00227-017-3144-7

Barker, R.M., 1964. Microtextural variation in pelecypod shells. Malacologia 2, 69–86.

Black, B.A., Griffin, D., van der Sleen, P., Wanamaker, A.D., Speer, J.H., Frank, D.C., Stahle, D.W., Pederson, N., Copenheaver, C.A., Trouet, V., Griffin, S., Gillanders, B.M., 2016. The value of crossdating to retain high-frequency variability, climate signals, and extreme events in environmental proxies. Glob. Chang. Biol. 22, 2582–2595. doi:10.1111/gcb.13256

Boyer, T.P., Antonov, J.I., Baranova, O.K., Coleman, C., Garcia, H.E., Grodsky, A., Johnson, D.R., Locarnini, R.A., Mishonov, A. V, O'Brien, T.D., Paver, C.R., Reagan, J.R., Seidov, D., Smolyar, I. V, Zweng, M.M., 2013. World Ocean Database 2013, NOAA Atlas NESDIS 72. Sydney Levitus, Ed.; Alexey Mishonoc, Tech. Ed. NOAA Atlas, 209. doi:10.7289/V5NZ85MT

Breaker, L.C., 2005. What's happening in Monterey Bay on seasonal to interdecadal time scales. Cont. Shelf Res. 25, 1159–1193. doi:10.1016/j.csr.2005.01.003

Cardoso, J.F.M.F., Nieuwland, G., Witbaard, R., Van Der Veer, H.W., Machado, J.P., 2013. Growth increment periodicity in the shell of the razor clam *Ensis directus* using stable isotopes as a method to validate age. Biogeosciences 10, 4741–4750. doi:10.5194/bg-10-4741-2013

Chauvaud, L., Thouzeau, G., Paulet, Y.M., 1998. Effects of environmental factors on the daily growth rate of *Pecten maximus* juveniles in the Bay of Brest (France). J. Exp. Mar. Bio. Ecol. 227, 83–111. doi:10.1016/S0022-0981(97)00263-3

Davenport, C.B., 1938. Growth lines in fossil pectens as indicators of past climates. J. Paleontol. 12, 514–515.

De Ridder, F., de Brauwere, A., Pintelon, R., Schoukens, J., Dehairs, F., Baeyens, W., Wilkinson, B.H., 2007. Comment on: Paleoclimatic inference from stable isotope profiles of accretionary biogenic hardparts-a quantitative approach to the evaluation of incomplete data, by Wilkinson, B.H., Ivany, L.C., 2002. Palaeogeogr. Palaeocl. Palaeoecol. 185, 95-114. Palaeogeogr. Palaeoclimatol. Palaeoecol. 248, 473–476. doi:10.1016/j.palaeo.2006.08.004

Dettman, D., Reische, A.K., Lohmann, K.C., 1999. Controls on the stable isotope composition of seasonal growth bands in aragonitic fresh-water bivalves (Unionidae). Geochim. Cosmochim. Acta 63, 1049–1057.

Dietl, G.P., Kidwell, S.M., Brenner, M., Burney, D.A., Flessa, K.W., Jackson, S.T., Koch, P.L., 2015. Conservation Paleobiology: Leveraging knowledge of the past to inform conservation and restoration. Annu. Rev. Earth Planet. Sci. 43, 79–103. doi:10.1146/annurev-earth-040610-133349

Duan, Q., Sorooshian, S., Gupta, V., 1992. Effective and efficient global optimization for conceptual rainfall-runoff models. Water Resour. Res. 28, 1015–1031. doi:10.1029/91WR02985

Goodwin, D.H., Flessa, K.W., Schöne, B.R., Dettman, D.L., 2001. Cross-calibration of daily growth increments, stable isotope variation, and temperature in the Gulf of California bivalve mollusk *Chione cortezi*: Implications for paleoenvironmental analysis. Palaios 16, 387–398. doi:10.1669/0883-1351(2001)016

Goodwin, D.H., Paul, P., Wissink, C.L., 2009. MoGroFunGen: A numerical model for reconstructing intra-annual growth rates of bivalve molluscs. Palaeogeogr. Palaeoclimatol. Palaeoecol. 276, 47–55. doi:10.1016/j.palaeo.2009.02.026

Goodwin, D.H., Schöne, B.R., Dettman, D.L., 2003. Resolution and fidelity of oxygen isotopes as paleotemperature proxies in bivalve mollusk shells : Models and Observations. Palaios 18, 110–125. doi:10.1669/0883-1351(2003)182.0.CO;2

Grossman, E.L., Ku, T.L., 1986. Oxygen and carbon isotope fractionation in biogenic aragonite: temperature effects. Chem. Geol. 59, 59–74.

Hall, C.A., Dollase, W.A., Corbató, C.E., 1974. Shell growth in *Tivela stultorum* (Mawe, 1823) and *Callista chione* (Linnaeus, 1758) (Bivalvia): annual periodicity, latitudinal differences, and diminution with age. Palaeogeogr. Palaeoclimatol. Palaeoecol. 15, 33–61. doi:10.1016/0031-0182(74)90036-4

Hallmann, N., Burchell, M., Schöne, B.R., Irvine, G. V., Maxwell, D., 2009. High-resolution sclerochronological analysis of the bivalve mollusk *Saxidomus gigantea* from Alaska and British Columbia: techniques for revealing environmental archives and archaeological seasonality. J. Archaeol. Sci. 36, 2353–2364. doi:10.1016/j.jas.2009.06.018

Haney, R.L., Davies, R.W., 1976. The role of surface mixing in the seasonal variation of the ocean thermal structure. J. Phys. Oceanogr. 6, 504–510. doi:10.1175/1520-0485(1976)006<0504:TROSMI>2.0.CO;2

Ivany, L.C., Brey, T., Huber, M., Buick, D.P., Schöne, B.R., 2011. El Niño in the Eocene greenhouse recorded by fossil bivalves and wood from Antarctica. Geophys. Res. Lett. 38, 2–7. doi:10.1029/2011GL048635

Jones, D.S., Quitmyer, I.R., 1996. Marking time with bivalve shells: Oxygen isotopes and season of annual increment formation. Palaios 11, 340-346. doi:10.2307/3515244

Karney, G.B., Butler, P.G., Scourse, J.D., Richardson, C.A., Lau, K.H., Czernuszka, J.T., Grovenor, C.R.M., 2010. Identification of growth increments in the shell of the bivalve mollusc *Arctica islandica* using backscattered electron imaging. J. Microsc. 241, 29–36. doi:10.1111/j.1365-2818.2010.03403.x

Koike, H., 1980. Seasonal dating by growth-line counting of the clam, *Meretrix lusoria*. Toward a reconstruction of prehistoric shell-collecting activities in Japan. Univ. Museum, Univ. Tokyo, Bull. 18, 104 p.

Kubota, K., Shirai, K., Murakami-sugihara, N., Seike, K., Hori, M., Tanabe, K., 2017. Annual shell growth pattern of the Stimpson's hard clam *Mercenaria stimpsoni* as revealed by sclerochronological and oxygen stable isotope measurements. Palaeogeogr. Palaeoclimatol. Palaeoecol. 465, 307–315. doi:10.1016/j.palaeo.2016.05.016

Lando, B.M., Lando, C.A., 1977. Is the graph of temperature variation a sine curve? An application for trigonometry classes. Math. Teach. 70, 534–537.

Lazareth, C.E., Lasne, G., Ortlieb, L., 2006. Growth anomalies in *Protothaca thaca* (Mollusca, Veneridae) shells as markers of ENSO conditions. Clim. Res. 30, 263–269. doi:10.3354/cr030263

Lorrain, A., Paulet, Y.-M., Chauvaud, L., Dunbar, R., Mucciarone, D., Fontugne, M., 2004. $\delta^{13}C$ variation in scallop shells: Increasing metabolic carbon contribution with body size? Geochim. Cosmochim. Acta 68, 3509–3519. doi:10.1016/j.gca.2004.01.025

Miyaji, T., Tanabe, K., Matsushima, Y., Sato, S., Yokoyama, Y., Matsuzaki, H., 2010. Response of daily and annual shell growth patterns of the intertidal bivalve *Phacosoma japonicum* to

Holocene coastal climate change in Japan. Palaeogeogr. Palaeoclimatol. Palaeoecol. 286, 107–120. doi:10.1016/j.palaeo.2009.11.032

Müller, P., Taylor, M.H., Klicpera, A., Wu, H.C., Michel, J., Westphal, H., 2015. Food for thought: Mathematical approaches for the conversion of high-resolution sclerochronological oxygen isotope records into sub-annually resolved time series. Palaeogeogr. Palaeoclimatol. Palaeoecol. 440, 763–776. doi:10.1016/j.palaeo.2015.09.032

Ohno, T., 1989. Paleotidal characteristics determined by micro-growth patterns in bivalves. Paleontology 32, 237–263.

Reynolds, R.W., Rayner, N.A., Smith, T.M., Stokes, D.C., Wang, W., 2002. An improved in situ and satellite SST analysis for climate. J. Clim. 15, 1609–1625. doi:10.1175/1520-0442(2002)015<1609:AIISAS>2.0.CO;2

Rhoads, D.., Lutz, R.A., 1980. Skeletal Growth of Aquatic Organisms. Plenum Press, New York.

Richaud, B., Kwon, Y., Joyce, T.M., Fratantoni, P.S., Lentz, S.J., 2016. Surface and bottom temperature and salinity climatology along the continental shelf off the Canadian and U . S . East Coasts. Cont. Shelf Res. 124, 165–181. doi:10.1016/j.csr.2016.06.005

Sato, S., 1995. Spawning periodicity and shell microgrowth patterns of the Venerid bivalve *Phacosoma japonicum* (Reeve, 1850). Veliger 38, 61–72.

Sato, S., 1997. Shell microgrowth patterns of bivalves reflecting seasonal change of phytoplankton abundance. Paleontol. Res. 1, 260–266. doi:10.1248/cpb.37.3229

Schneider, C.A., Rasband, W.S., Eliceiri, K.W., 2012. NIH Image to ImageJ: 25 years of image analysis. Nat. Methods 9, 671–675. doi:10.1038/nmeth.2089

Schöne, B.R., 2013. *Arctica islandica* (Bivalvia): A unique paleoenvironmental archive of the northern North Atlantic Ocean. Glob. Planet. Change 111, 199–225.

doi:10.1016/j.gloplacha.2013.09.013

Schöne, B.R., Fiebig, J., Pfeiffer, M., Gleβ, R., Hickson, J., Johnson, A.L.A., Dreyer, W., Oschmann, W., 2005a. Climate records from a bivalved Methuselah (*Arctica islandica*, Mollusca; Iceland). Palaeogeogr. Palaeoclimatol. Palaeoecol. 228, 130–148. doi:10.1016/j.palaeo.2005.03.049

Schöne, B.R., Flessa, K.W., Dettman, D.L., Goodwin, D.H., 2003a. Upstream dams and downstream clams: growth rates of bivalve mollusks unveil impact of river management on estuarine ecosystems (Colorado River Delta, Mexico). Estuar. Coast. Shelf Sci. 58, 715–726. doi:10.1016/S0272-7714(03)00175-6

Schöne, B.R., Goodwin, D.H., Flessa, K.W., Dettman, D.L., Roopnarine, P.D., 2002a. Sclerochronology and Growth of the Bivalve Mollusks *Chione* (*Chionista*) *fluctifraga* and *C.* (*Chionista*) *cortezii* in the Northern Gulf of California, Mexico. The Veliger 45, 45–54.

Schöne, B.R., Lega, J., Flessa, K.W., Goodwin, D.H., Dettman, D.L., 2002b. Reconstructing daily temperatures from growth rates of the intertidal bivalve mollusk *Chione cortezi* (northern Gulf of California, Mexico). Palaeogeogr. Palaeoclimatol. Palaeoecol. 184, 131–146. doi:10.1016/S0031-0182(02)00252-3

Schöne, B.R., Pfeiffer, M., Pohlmann, T., Siegismund, F., 2005b. A seasonally resolved bottom-water temperature record for the period AD 1866-2002 based on shells of *Arctica islandica* (Mollusca, North Sea). Int. J. Climatol. 25, 947–962. doi:10.1002/joc.1174

Schöne, B.R., Tanabe, K., Dettman, D.L., Sato, S., 2003b. Environmental controls on shell growth rates and δ^{18}O of the shallow-marine bivalve mollusk *Phacosoma japonicum* in Japan. Mar. Biol. 142, 473–485. doi:10.1007/s00227-002-0970-y

Smith, T.M., Reynolds, R.W., 2003. Extended reconstruction of global sea surface temperatures based on COADS data (1854-1997). J. Clim. 16, 1495–1510. doi:10.1175/1520-0442-16.10.1495

Steinhardt, J., Butler, P.G., Carroll, M.L., Hartley, J., 2016. The application of long-lived bivalve sclerochronology in environmental baseline monitoring. Front. Mar. Sci. 3, 1–26. doi:10.3389/fmars.2016.00176

Stine, A.R., Huybers, P., Fung, I.Y., 2009. Changes in the phase of the annual cycle of surface temperature. Nature 457, 435–440. doi:10.1038/nature07675

Tanabe, K., 1988. Age and growth rate determinations of an intertidal bivalve, *Phacosoma japonicum*, using internal shell increments. Lethaia 21, 231–241.

Tanabe K., Oba, T., 1988. Latitudinal variation in shell growth patterns of *Phacosoma japonicum* (Bivalvia: Veneridae) from the Japanese coast. Mar. Ecol. Prog. Ser. 47, 75–82. doi:0171-8630/88/0047/0075

Urey, H.C., 1948. Oxygen isotopes in nature and in the laboratory. Science 53, 489-496.

Wanamaker, A.D., Baker, A., Butler, P.G., Richardson, C.A., Scourse, J.D., Ridgway, I., Reynolds, D.J., Wanamaker, A.D., Baker, A., Butler, P.G., Richardson, C.A., Scourse, J.D., Ridgway, I., Reynolds, D.J., 2009. A novel method for imaging internal growth patterns in marine mollusks: A fluorescence case study on the aragonitic shell of the marine bivalve *Arctica islandica* (Linnaeus). Limnol. Oceanogr. Methods 7, 673–681. doi:10.4319/lom.2009.7.673

Wanamaker, A.D., Kreutz, K.J., Schöne, B.R., Introne, D.S., 2011. Gulf of Maine shells reveal changes in seawater temperature seasonality during the Medieval Climate Anomaly and the Little Ice Age. Palaeogeogr. Palaeoclimatol. Palaeoecol. 302, 43–51. doi:10.1016/j.palaeo.2010.06.005

Wanamaker, A.D., Kreutz, K.J., Schöne, B.R., Maasch, K.A., Pershing, A.J., Borns, H.W., Introne, D.S., Feindel, S., 2008. A late Holocene paleo-productivity record in the western Gulf of Maine, USA, inferred from growth histories of the long-lived ocean quahog (*Arctica islandica*). Int. J. Earth Sci. 98, 19–29. doi:10.1007/s00531-008-0318-z

Weidman, C.R., Jones, G.A., Lohmann, K.C., 1994. The long-lived mollusc *Arctica islandica:* A new paleoceanographic tool for the reconstruction of bottom temperatures for the continental shelves of the northern North Atlantic Ocean. J. Geophys. Res. 99, 18305. doi:10.1029/94JC01882

Wilkinson, B.H., Ivany, L.C., 2002. Paleoclimatic inference from stable isotope profiles of accretionary biogenic hardparts - A quantitative approach to the evaluation of incomplete data. Palaeogeogr. Palaeoclimatol. Palaeoecol. 185, 95–114. doi:10.1016/S0031-0182(02)00279-1

Witbaard, R., Duineveld, G.C.A., Bergman, M., 2001. The effect of tidal resuspension on benthic food quality in the southern North Sea. Senckenbergiana maritima 31, 225–234. doi:10.1007/BF03043031

Yan, L., Schöne, B.R., Arkhipkin, A., 2012. *Eurhomalea exalbida* (Bivalvia): A reliable recorder of climate in southern South America? Palaeogeogr. Palaeoclimatol. Palaeoecol. 350–352, 91–100. doi:10.1016/j.palaeo.2012.06.018

Yan, L., Schöne, B.R., Li, S., Yan, Y., 2014. Shells of *Paphia undulata* (Bivalvia) from the South China Sea as potential proxy archives of the East Asian summer monsoon: a sclerochronological calibration study. J. Oceanogr. 70, 35–44. doi:10.1007/s10872-013-0210-8

Chapter 4:

Seasonally resolved proxy data from the Antarctic Peninsula support a heterogeneous middle Eocene Southern Ocean

Chapter 4 is published as:

Judd, E. J., Ivany, L. C., DeConto, R. M., Halberstadt, A. R. W., Miklus, N. M., Junium, C. K., & Uveges, B. T. (2019). Seasonally resolved proxy data from the Antarctic Peninsula support a heterogeneous middle Eocene Southern Ocean. Paleoceanography and Paleoclimatology, 2019PA003581. https://doi.org/10.1029/2019PA003581

4.1 Abstract

Understanding conditions at both global and local scales during the greenhouse climate of the Eocene Epoch is critical for making accurate predictions in our rapidly warming world. Despite the wealth of proxy data and modeling studies, fundamental aspects of the climate system still remain uncertain. For example, accurate austral high-latitude temperatures are necessary to understand the evolution of temperatures during the lead-up to Antarctic glaciation and determine the meridional temperature gradient during greenhouse warmth, yet records are few and disparate. Here we present seasonally resolved temperature and precipitation data from the latest Lutetian (~42 Ma) from the eastern Antarctic Peninsula. Oxygen isotopes from bivalves indicate a mean temperature of 13.1°C and a seasonal range of 8.0°C, slightly (<1°C) more seasonal than modelled temperatures from high-obliquity simulations. Carbon isotopes from driftwood suggest that summer accounts for just over half of annual precipitation. When compared with other austral high-latitude records, the data are consistent with a zonally heterogeneous middle Eocene Southern Ocean. Similar longitudinal variability is observed in the modern boreal high-latitudes, where landmasses subdivide the ocean, subjecting basins to their own distinct circulation patterns and coastal processes. With closed Drake and Tasman passages, the middle Eocene Southern Ocean would also have been noncontiguous, resulting in larger variability of sea surface temperatures along individual zonal bands than today. This interpretation resolves inconsistencies among existing high-austral proxy records, and suggests that the large seasonal range of temperatures may be indicative of regional-scale circulation patterns along the peninsula not captured by low resolution climate simulations.

4.2 Introduction

As climate continues to warm, it becomes increasingly important to make accurate predictions about the climatic conditions we can expect in the future. One of the most productive reservoirs of information in this regard is the rich paleoclimate archive from Earth’s deep past. Recent modelling studies predict that by 2150 CE, little more than 100 years from now, the greenhouse climate of the Eocene Epoch (~56–34 Ma) will offer one of the best analogs for the conditions anticipated over much of Earth’s surface (Burke et al., 2018). For this reason, the Eocene, which records the transition from the warmest temperatures of the Cenozoic to the onset of Southern Hemisphere glaciation (Zachos et al., 2008), has received considerable attention. The majority of studies have focused on climate extremes recorded early in the epoch (i.e., the early Eocene hyperthermals) and at its close (i.e., the Eocene-Oligocene transition), but here we focus in on the middle Eocene to better understand climate conditions and the mechanisms maintaining them during this comparatively stable, intermediate time, particularly in the climatically sensitive austral high latitudes.

Mean annual temperature (MAT) data are the conventional currency for comparing climates in Earth’s past. These data are widely available, often globally synchronized, and provide invaluable information related to large-scale temporal and spatial patterns. Seasonally resolved records, however, are ultimately required to fully understand the climatic conditions of a given location in deep time. While these records are uncommon, even rare snapshots can contextualize existing estimates of MAT, as two regions with the same mean temperature can experience dramatically different seasonal ranges (e.g., Hirahara et al., 2014). The additional perspective of mean annual range of temperature (MART) and seasonal variation in precipitation regime can identify important differences between regions and illuminate the local and regional processes driving those differences (Hansen et al., 2012, 1988; Marshall et al., 2006). In these contexts, seasonally resolved data overall can provide significant insights into the hydrologic cycle (Portmann et al., 2009; Trenberth and Shea, 2005), the biogeographic distributions of organisms (Pörtner, 2001; Portner et al., 2007), the reliability of climate models (Gasson et al., 2014), and even climate sensitivity (Knutti et al., 2006), and are therefore extremely valuable in the reconstructions of ancient climate.

Seasonally resolved proxy data from Antarctica during the Eocene can bring much greater clarity to the climate conditions that prevailed in the warm and largely ice-free polar world and the means by which the climate system evolved during the lead-up to ice sheet growth. Recent studies have suggested the presence of marine-terminating ice in parts of Antarctica as early as the middle-late Eocene (Carter et al., 2016; Gulick et al., 2017). Summer temperatures are the primary control on the inception and expansion of glacial ice; thus, seasonally resolved temperature data from the austral high-latitudes are critical for evaluating this hypothesis. Equally obscure is the high-austral paleoprecipitation regime. Both proxy and model-based studies indicate intensification of the hydrologic cycle during greenhouse conditions (Carmichael et al., 2016; Feakins et al., 2012; Huber and Goldner, 2012), however the seasonal phasing of precipitation patterns in the high-latitudes remains enigmatic. Recent evidence suggests a highly seasonal, summertime-dominated precipitation regime in both the Antarctic (Jacques et al., 2014) and Arctic (Schubert et al., 2012), akin to monsoons. Modern monsoons are restricted to low latitudes, so the potential for their presence in polar regions during greenhouse climates requires a significant departure from the present-day climate system and warrants further investigation.

Here, we present a robust assessment of seasonal climate conditions on the Antarctic Peninsula during the latest Lutetian (~42 Ma) using subannually resolved accretionary archives from the La

Meseta Formation, Seymour Island, Antarctica. Oxygen isotope analyses of serially sampled fossil bivalves reveal the annual temperature cycle in nearshore Antarctic waters and carbon isotope analyses of serially sampled organic carbon from fossil driftwood provide insights into the seasonal precipitation regime, both of which are evaluated using a suite of global climate model (GCM) simulations. We explore our results in the context of existing proxy data from other middle Eocene austral high-latitude sites, modern sea-surface temperature (SST) data, and dynamic coastal processes that can serve to inflate or deflate the seasonal temperature range above the zonal mean value. This broad integrative approach enables a better understanding of the climatic factors at play across the continent during this interval of transition between early Eocene global warmth and Eocene-Oligocene growth of significant ice sheets.

4.3 Materials and methods

4.3.1 Geologic Setting

Seymour Island, Antarctica (~64°S, 54°W), is located approximately 100 km east of the Antarctic Peninsula (Fig. 1). Outcropping on the northeastern third of the island, Eocene marine sediments comprising the La Meseta Formation (Elliot and Trautman, 1982) accumulated on the shelf at a paleolatitude of ~70°S (van Hinsbergen et al., 2015). The formation consists of poorly consolidated sandstones, mudstones, and shell beds interpreted to represent deposition in an incised valley estuary (Porebski, 1995). Specimens analyzed in the current study were collected from shell beds in the stratigraphic subdivision known as Telm 5 (Sadler, 1988). This unit is highly fossiliferous, with exceptional preservation of diverse marine fauna (Stilwell and Zinsmeister, 1992) including articulated bivalves and mummified driftwood, presumably originating from the nearby peninsular coast. Dinoflagellate biostratigraphy of the unit is consistent with a latest Lutetian age (~42.0 – 41.5 Ma; Douglas et al., 2014), just preceding the opening of the Drake Passage (Scher and Martin, 2006) and the short-lived warming of the middle Eocene climatic optimum (Bohaty et al., 2009; Bohaty and Zachos, 2003).

4.3.2 Sea surface temperature estimates from fossil bivalves

Eight specimens of fossil bivalves belonging to the genera *Cucullaea* and *Retrotapes* (formerly *Eurhomalea*, Alvarez and Pérez, 2016) were serially (i.e., sequentially) sampled at high spatial/temporal resolution across growth increments to constrain intra-annual temperature variation during the middle Eocene. Specimens come from four horizons spanning the stratigraphic extent of Telm 5 (Fig. 1). X-Ray diffraction (XRD) and trace element analyses were performed on samples of each shell to evaluate preservation of the original aragonite mineralogy. Pristine specimens were incrementally sampled for stable isotopes on either the cleaned exterior surface or a polished section through the axis of maximum growth (Supplemental Tables S1 and S2) using an ESI/New Wave/Merchantek MicroMill. A total of 49 years of growth were sampled at an average resolution of 8.5 samples per year. Years were initially recognized by sculptured growth lines on the exterior or dark growth bands on the interior of the shells (Jones, 1980), and subsequently confirmed to be annual with cyclic variation in isotope values. Samples were analyzed for their stable oxygen ($\delta^{18}O_{carb}$) and carbon ($\delta^{13}C_{carb}$) isotopic compositions using a Finnegan MAT 251 or 253 mass spectrometer coupled to a Kiel automated carbonate preparation device. Data are reported relative the Vienna PeeDee Belemnite (VPDB) standard and were corrected using international reference materials NBS-18 and NBS-19. Average precision is better than 0.04‰.

To account for biases related to variable intra-annual growth rates, oxygen isotope profiles from discrete years of data were transformed from the distance into the time domain using the bivalve growth model of Judd et al. (2017). This procedure facilitates climatological analysis by permitting all samples from a given horizon to be pooled into a single, densely sampled, average annual cycle that can be fit with a sinusoid and associated error envelope (Supplemental Table S3). Temperatures were calculated using the empirically derived biogenic aragonite paleotemperature equation of Grossman and Ku (1986) modified for SMOW (Dettman et al., 1999), using clumped isotope-derived estimates of the oxygen isotopic composition of seawater ($\delta^{18}O_{seawater}$) from shells of the same taxa collected within Telm 5 (Douglas et al., 2014).

4.3.3 Precipitation of seasonality from fossil driftwood

Fossil driftwood specimens come from a single horizon approximately midway through Telm 5 (Fig. 1), and stratigraphically between Horizons 2 and 3. Two thick sections of mummified wood, cut perpendicular to the growth axis, were sampled by hand using a razor blade across 8 years of growth, with an average resolution of 17 samples per annual growth ring. Samples were acidified with 3M HCl to remove secondary carbonate, then rinsed, dried, and weighed into pure tin capsules. Samples were analyzed for $\delta^{13}C$ of organic matter ($\delta^{13}C_{org}$) using an IsoPrime Elementar Cube combustion autosampler coupled to an IsoPrime 100 Stable Isotope Ratio Mass Spectrometer. Data are normalized to the VPDB scale (Coplen et al., 2006) using international reference materials NIST 1547 and NIST 8542.

We calculate the ratio of summertime to wintertime precipitation from the seasonal variability in $\delta^{13}C_{org}$ using the equation of Schubert and Jahren (2011):

$$Ln\left({}^{P_1}/_{P_2}\right) = \frac{\Delta\delta^{13}C_{meas} - \Delta\delta^{13}C_{CO_2} - 0.73}{-0.82} \qquad \text{(eq. 4.1)}$$

where P_1/P_2 is the ratio of summertime to wintertime precipitation, $\Delta\delta^{13}C_{meas}$ is the average difference between the maximum isotope value of a given year and the minimum value from the preceding year, and $\Delta\delta^{13}C_{CO2}$ is the inferred intra-annual variation in the carbon isotopic composition of atmospheric carbon dioxide. This equation was empirically derived using globally distributed modern isotope and environmental data (Schubert and Jahren, 2011), and has been previously applied to high-latitude Eocene specimens (Schubert et al., 2012). As there is thus far no reliable method through which to estimate the $\Delta\delta^{13}C_{CO2}$ value in the geologic past, we have opted to use the modern value of 0.05‰, which provides a minimum estimate of the seasonal precipitation ratio (see results below). Here, summer and winter are defined as six-month blocks spanning November through April and May through October, respectively, in the southern hemisphere.

4.3.4 GENESIS climate model simulations

In order to constrain the conditions required to produce the seasonal patterns observed in our proxy data and to better understand the seasonal response to changing baseline conditions in this region, we ran multiple climate simulations using the Genesis 3.0 GCM (Alder et al., 2011) with a computationally efficient slab-ocean/sea ice component rather than an optional full depth ocean model, coupled to the BIOME4 equilibrium vegetation model (Kaplan, 2003). Each simulation was run for 50 years with a middle-late Eocene paleogeography (Feakins et al., 2014) and a range of pCO_2, ice volume, and orbital parameters; results reflect an average of the last ten years of each simulation, with errors based on the one sigma standard deviation of the last decade. A summary of model configurations can be found in Supplemental Table S4. The surface model has a spatial resolution of 2° x 2°; mean monthly SSTs were extracted at the paleolocation of Seymour Island at ~70.8°S, 69.4°W (Supplemental Fig. S1). Once the parameters that best approximate proxy-based seasonal temperatures are identified, we assess the compatibility of the fossil wood analyses with the modelled mean monthly precipitation rate. The 18-layer atmosphere has a spatial resolution of ~3.75 ° x 3.75°; onshore precipitation values were extracted from the land just west of the Seymour Island site (~70.9°S, 73.9°W; Supplemental Fig. S1).

4.4 Results

4.4.1 Seasonal temperature analysis

All shells retain their original aragonitic mineralogy, and trace element concentrations are consistent with values from modern aragonitic bivalves (Supplemental Fig. S2; Morrison and Brand, 1986), indicating that shells have not undergone diagenetic alteration and that stable isotope values therefore reflect original depositional conditions. Individual isotope profiles exhibit consistent high amplitude cyclicity, coincident with external sculpturing and internal growth bands, and thus are confirmed to be annual (Fig. 2a). When taken as a whole, oxygen isotope data show a gradual depletion through time over the four horizons sampled (Fig. 2b), which, if reflective solely of changes in temperature, suggests a warming trend of about 2°C. However, clumped isotope-derived estimates of $\delta^{18}O_{seawater}$ from shells in the stratigraphically lowest and highest horizons (Douglas et al., 2014) indicate that the local seawater value was also decreasing through this interval, from -1.22 to -1.71‰. Assuming a constant linear depletion of $\delta^{18}O_{seawater}$ across all four horizons, mean paleotemperatures from best-fit sinusoids through the isotope data overlap, with MAT for each of the 4 horizons ranging between 12.5 and 13.7°C. MART inferred from the sinusoidal fits ranges between 7.6 and 8.3°C, with the exception of the lowermost horizon (amplitude of 4.9°C). These latter data come from a single *Cucullaea* specimen sampled in cross section later in ontogeny (Buick and Ivany, 2004) and are likely time averaged due to the comparatively compressed growth increments. Thus, while the attenuated seasonal range could represent a true climate signal, it is more likely a sampling bias.

Similarity in MAT across the four horizons suggests that all sampled shells record similar climatic conditions. This consistency permits us to pool all temporally aligned isotope data and overlay them on the same one-year cycle to constrain the seasonal temperature regime of the latest Lutetian. A best-fit sinusoid through Horizons 2 – 4 yields a MAT of 13.1°C with a MART of 8.0°C (Fig. 3, solid black line; $R^2 = 0.69$, $p \ll 0.001$). Including Horizon 1 in the composite dataset has little impact on MAT (13.2°C), however the inferred MART is reduced to 7.2°C (Fig. 3, solid gray line; $R^2 = 0.65$, $p \ll 0.001$).

The climate model simulation that best approximates the middle Eocene proxy data is forced with 2,000 ppm pCO_2, no Antarctic ice sheet, and high obliquity (24.5°). The resulting annual SST cycle in the vicinity of Seymour Island has a MAT of 12.6 ± 0.2 °C and a MART of 7.3 ± 0.6 °C, falling entirely within the 95% confidence interval of the proxy-derived seasonal curve (Fig. 3, dashed gray line). Linear regression between the sine-fit, proxy-derived, mean monthly temperatures and modelled mean monthly temperatures defines a significant relationship ($R^2 = 0.95$, $p \ll 0.001$) with a slope of 0.90. Of note, proxy-based estimated of middle Eocene pCO_2 indicate substantially lower concentrations than those employed here (e.g., Maxbauer et al., 2014). GCM simulations routinely require unrealistically high pCO_2 in order to match proxy data (e.g., Huber and Caballero, 2011; Lunt et al., 2012), particularly those with relatively low climate sensitivity, such as GENESIS (Gasson et al., 2014), and are not necessarily geologically significant.

4.4.2 Seasonal precipitation analysis

Thin sections indicate that the fossil driftwood most likely belongs to the genus *Eucryphiaceoxylon* (Fig. 4a,b; Poole et al., 2003), and the sinusoidal pattern of the organic carbon isotope profiles are consistent with an evergreen species (Fig. 4c; Schubert and Jahren, 2011). Isotope values exhibit low amplitude annual cyclicity with an average $\Delta\delta^{13}C_{meas}$ of 0.57 ± 0.14‰ (1σ; Supplemental Table S5). Using eq. 4.1, with a $\Delta\delta^{13}C_{CO2}$ value of 0.05‰ results in a P_1/P_2 value of 1.31, indicating that the six-month summer was 1.31 times rainier than the six-month winter, accounting for approximately 57 ± 4% of all annual precipitation. These results suggest a slightly more seasonal precipitation regime than that reconstructed by the climate model simulation most consistent with proxy temperature data, which predicts that the six-month summer accounts for approximately 49 ± 6% of all annual precipitation, with a mean annual precipitation (MAP) of 885 ± 73 mm and an average summer daily precipitation rate of 2.4 ± 0.4 mm/day. Combining modelled MAP with the proxy-derived P_1/P_2 values, results in ~505 mm of summer precipitation, and ~380 mm of winter precipitation, in good agreement with the modelled values of ~435 mm and 450 mm, respectively.

The largest source of uncertainty in the proxy-based precipitation estimate comes from the assumption of a similar-to-modern $\Delta\delta^{13}C_{CO2}$. Today, this value is low (0.05‰) and invariant over most of the Southern Hemisphere due largely to the lower and less vegetated land area, limiting the potential range of variation imparted by seasonal fluctuations in photosynthesis and respiration. The Southern Hemisphere $\Delta\delta^{13}C_{CO2}$ could have been higher during the warmer and presumably greener Eocene, which would increase the estimated summertime to wintertime precipitation ratio. However, overlap in the one sigma error between the proxy-derived and modelled ratio of summer-to-winter precipitation suggests that we have not underestimated this value. Previous estimates of MAP from Seymour Island using coexistence analysis and (733 mm; Poole et al., 2005) and CLAMP (Climate Leaf Analysis Multivariate Program; Wolfe, 1993) analysis (1534 mm; Francis et al., 2008) bracket our results, lending further confidence to the fidelity of the model prediction.

4.5 Discussion

Austral high-latitude paleoclimate data play a critical role in helping to understand both climatic conditions during greenhouse intervals and the evolution of Earth's climate into an icehouse. Reconstructions of high-latitude conditions are requisite to defining latitudinal temperature gradients and the impact of polar amplification under varying climate regimes, yet they remain frustratingly difficult to reproduce with climate models. For these reasons, a number of Eocene proxy studies have focused on the polar regions, constraining temperature (e.g., Burgess et al., 2008; Douglas et al., 2014; Hollis et al., 2012), precipitation (e.g., Feakins et al., 2014; Jacques et al., 2014; Poole et al., 2005), ice sheet history (e.g., Carter et al., 2017; Galeotti et al., 2016; Gulick et al., 2017), and the tectonic opening of ocean gateways and Southern Ocean circulation (e.g., Livermore et al., 2007; Scher and Martin, 2006; Stickley et al., 2004). Despite the wealth of existing data, a variety of factors including fidelity of proxy calibration, inconsistency among proxies, data-model mismatches, and age uncertainties, have hindered a straightforward interpretation of Eocene Antarctic climates.

The proxy data presented here indicate that latest Lutetian nearshore Antarctic Peninsula water temperatures were warm and seasonal and that the onshore paleoprecipitation regime was fairly equable, with just over half the annual rainfall occurring in the (six-month) summer. While internally consistent, these data do not always agree with those derived from other proxies and regions on the continent. In the following discussion, we attempt to resolve these differences within a single framework. We address the fidelity of, and possible sources of uncertainty in both our proxy data and model results, and compare our findings with other coeval austral high-latitude proxy data to produce a coherent picture of middle Eocene Antarctic climatic conditions.

4.5.1 Assessing the fidelity of the proxy data and climate model

Temperature. Sine-fit, isotope-derived MAT (~13ºC) is in good agreement with estimates of MAT from clumped isotopes (12.6ºC; Douglas et al., 2014), TEX_{86}^{L} (15.4ºC; Douglas et al., 2014), and bulk oxygen isotope analyses of Telm 5 carbonates (~10–14.5ºC; Dutton et al., 2002; Ivany et al., 2008 and references therein). The seasonal SST data are more difficult to contextualize, as there are few data with which to compare our findings. Despite the highly seasonal air temperatures observed on the Antarctic continent in the modern world, the austral high-latitudes exhibit exceedingly low-amplitude variability in SSTs (see Fig. 5; Hirahara et al., 2014). Winter temperatures are constrained by the freezing point of seawater, and summer temperatures rarely warm much above freezing, as the Antarctic Circumpolar Current limits the transport of equatorial-derived water south of the Polar Front, and waters are further kept cool in the summer due to latent heat loss from melting sea ice. Therefore, under greenhouse conditions where thermal thresholds no longer restrict temperature variability and there is little or no seasonal sea ice, the amplitude of seasonal SST variability should increase, as is observed in our proxy data. The climate model is, however, only able to approximate the proxy-derived MART (~8 ºC) when forced with a high obliquity orbital configuration, which maximizes the difference between winter and summer insolation.

Is the seasonal range overestimated by the proxy data, or underestimated by the climate model? The sampled horizons from the La Meseta Formation span several hundred thousand years (Douglas et al., 2014), so unless deposition of the shell beds themselves is governed by Milankovitch-controlled processes, it is unlikely that shells from each horizon coincidentally come from an interval of high obliquity. Nor is it likely that the composite proxy dataset overestimates the intra-annual variability of $\delta^{18}O_{carb}$, for several reasons. First, data are averaged over more than 30 discrete sampled years, providing a true climatological mean but potentially underestimating shorter-term temporal variability. Second, although care was taken to maximize the spatial/temporal resolution while sampling, time-averaging is inevitable given the slow growth of the sampled taxa (Moss et al., 2017), particularly during summers when the rate of shell accretion decreases (Buick and Ivany, 2004). Third, bivalves are benthic organisms and the seasonal range of water temperature attenuates with depth (Prandle and Lane, 1995). Proxy data are therefore more likely to underestimate the seasonal range of surface water temperatures.

While the observed intra-annual $\delta^{18}O_{carb}$ variation is conservative, several other factors, independent of true temperature seasonality, could serve to increase this value on the Antarctic Peninsula locally or regionally. High volumes of isotopically depleted seasonal (summertime) runoff could artificially inflate the range of nearshore $\delta^{18}O_{seawater}$ values and hence skew the perceived MART (e.g., Keating-Bitonti et al., 2011). This is unlikely, however, given that driftwood analyses and modelled precipitation results both suggest a fairly equable intra-annual precipitation pattern. Seasonal runoff of meltwater from alpine glaciers would similarly serve to increase the inferred MART. Tillites on King George Island dated to the middle Eocene provide evidence for alpine glaciers (Birkenmajer et al., 2005), however age control is poor and the potential extent of glaciers and their drainage pattern on the eastern side of the peninsula is unconstrained.

If the $\delta^{18}O_{carb}$ range truly reflects temperature seasonality, it is nevertheless possible that this range does not reflect typical open shelf conditions. Shallow protected water in a semi-confined inner estuary channel, as suggested for the La Meseta Formation (Marenssi et al., 2002), could experience a larger range of temperatures than the adjacent open shoreface due to the combination of summer warming and restricted circulation. However, sedimentological studies suggesting deposition in a marine-flushed, tide-dominated estuary mouth (Porebski, 1995), and the high molluscan biodiversity (Stilwell and Zinsmeister, 1992) and persistent occurrence of stenohaline organisms such as brachiopods (Ager, 1967; Aronson et al., 2009) imply normal marine salinity and hence a well-mixed environment during the times of shell precipitation. Our data therefore likely capture at least a minimum estimate of the real seasonal temperature range on the middle Eocene Antarctic shelf.

Errors associated with highly parameterized model physics could partially resolve the discrepancy between proxy-derived and modelled seasonal SST ranges. As a first-order approximation, seasonality is controlled by intra-annual variations in solar insolation and should therefore correlate with latitude. However, atmospheric and oceanic circulation patterns also play a role, modifying the otherwise-anticipated zonal patterns (e.g., Gill and Niller, 1973; Glorioso, 1987; Marshall et al., 2006), particularly in nearshore environments (e.g., Hirahara et al., 2014). The GCM uses a slab ocean, which captures fundamental zonal SST trends, but doesn’t resolve vertical water column structure or ocean dynamics, such as coastal currents, regions of ocean downwelling and upwelling, and localized eddies that could be influential at our nearshore location. Thus, the higher seasonal range reconstructed from the proxy data could be related to a regional oceanographic effect not captured by the model. This is discussed further in Section 4.2.3, below in the context of potential modern analogs.

Precipitation. Using a six-month seasonal delineation (Schubert and Jahren, 2011), the climate model predicts essentially equal ‘summer’ and ‘winter’ precipitation, in good agreement with the proxy data from fossil wood. However, when model output is viewed as a time series, annual cyclicity is apparent (Fig. 4d), with maximum rainfall rates occurring in the late summer and autumn, suggesting that partitioning into the pre-defined six-month ‘summer’ and ‘winter’ blocks gives the illusion of more equable seasonal precipitation.

The seasonality of rainfall near the poles in greenhouse climates is still an open question, with some studies suggesting ever-wet conditions (Poole et al., 2005; West et al., 2015) and others finding highly seasonal summer precipitation patterns (Jacques et al., 2014; Schubert et al., 2012). These latter studies meet the definition of monsoon proposed by Zhang and Wang, (2008), with summer rainfall rates ≥ 3 mm/day and more than 55% of precipitation occurring in the five-month summer (NDJFM in the Southern Hemisphere). Results from Seymour Island are somewhat ambiguous in this context. Model output suggests the five-month summer as defined above accounts for only 38 ± 5% of annual precipitation, much lower than the 60% inferred from CLAMP analysis of early-middle Eocene floras on King George Island to the west of the Antarctic Peninsula (Jacques et al., 2014), and certainly well below the threshold for a monsoonal regime. Further, modelled rainfall rates in the three rainiest months (MAM; 3.1 ± 0.8 mm/day) rise just to the threshold characteristic of ‘monsoons’, but are significantly less than the >6 mm/day inferred for the five-month summer on King George Island (Jacques et al., 2014). While models frequently underestimate high-latitude precipitation during warm climates (Carmichael et al., 2016), and it is plausible that Southern Hemisphere seasonal $\Delta\delta^{13}C_{CO2}$ was higher during the Eocene (thereby increasing the P_1/P_2 ratio), neither the proxy nor the model results provide compelling evidence in favor of a monsoonal precipitation regime.

The slightly older and hence warmer King George Island data could reflect wetter and more seasonal conditions that had moderated by the time of deposition of Telm 5. This interpretation is consistent with clay mineral assemblage data from the La Meseta Formation suggesting a transition within the underlying Telm 3 (mid Lutetian; Douglas et al., 2014) from wet, strongly seasonal conditions to wet, non-seasonal conditions (Dingle et al., 1998). Alternatively, the discrepancy between seasonal precipitation regimes on either side of the peninsula could be explained by an orographic effect from westerly subtropical-derived air masses moving across the peninsular mountains.

4.5.2 Seymour Island in the context of existing paleoclimate data

Ice sheet evolution. An extensive West Antarctic Ice Sheet was not established until the Eocene-Oligocene Transition (~34 Ma; Sorlien et al., 2007; Wilson et al., 2013), with the first evidence for a marine terminating ice sheet dated at ~32.8 Ma (Galeotti et al., 2016). However, recent studies indicate marine terminating ice along the Sabrina Coast by the middle Eocene (Gulick et al., 2017), and along the southern Weddell Sea embayment by the late Eocene (Carter et al., 2016). Seasonally-resolved proxy data from this study estimate winter SSTs near 9ºC and summer SSTs around 17ºC, indicating that the eastern peninsula was far too warm to support significant ice accumulation at low elevation during the latest Lutetian. Given that water on the east side of the peninsula likely originated farther south in the Weddell Sea, it is unlikely that land-based ice could survive in proximity to the coast there at this time. The presence of marine-terminating glaciers along the Sabrina coast (Gulick et al., 2017), at a slightly lower latitude and on the opposite side of the Antarctic continent, is difficult to reconcile with the proxy data presented here. Modelled temperatures in this region are also too warm and seasonal to allow for substantial ice growth or even sustain seasonal sea ice, and thus would have required rapid delivery of ice from significantly higher and colder elevations, or large zonal temperature variability not captured by the climate model.

Zonal heterogeneity in temperature and precipitation. Although there are a wealth of paleotemperature data from the austral high-latitudes (e.g., Bijl et al., 2009; Burgess et al., 2008; Douglas et al., 2014; Hollis et al., 2012), estimates from different sectors of the Southern Ocean are not always in agreement with each other. Past studies have attempted to resolve the apparent discrepancy by applying a multiproxy approach to identify systematic offsets between proxies at single localities (e.g., Hollis et al., 2012), and the same proxy to multiple sites to minimize differences due to proxy biases or uncertainties (e.g., Douglas et al., 2014). Despite this, proxy data still indicate substantially warmer conditions during the middle Eocene in the southwestern Pacific (i.e., the Ross Sea) than the southeastern Atlantic (i.e., the Weddell Sea). Douglas et al. (2014) propose that such zonal variability is a real feature of the climate system, arguing that the differences in MAT are best explained by an ocean circulation pattern with higher ocean heat transport in the Pacific Ocean and deep-water formation in the Ross Sea. However, in a paper introducing a new paleolatitude calculator based on detailed plate reconstructions and updated paleomagnetic reference frames, Van Hinsbergen et al. (2015) dispute this hypothesis, suggesting instead that by using corrected paleolatitudes, the high-austral data are latitudinally disparate enough to negate the need for such an explanation.

Despite using the adjusted paleolatitudes (Van Hinsbergen et al., 2015), SST estimates from the Ross Sea region remain warmer than values predicted by the climate model simulation that best captures our proxy data (Supplemental Fig. S3). Conversely, though no SST estimates exist for the southern Indian Ocean, the presence of a marine terminating ice along the Sabrina Coast seems to necessitate cold temperatures. Therefore, the existing proxy data best support the previously proposed hypothesis for a heterogenous Southern Ocean with respect to SST. While the presence of a fully-developed Antarctic Circumpolar Current (ACC) precludes large-scale heterogeneity in the modern Southern Ocean, such zonal variability is observed in the modern northern hemisphere high-latitudes, where water masses are not fully contiguous (Fig. 5). Here, MAT and MART values exhibit little dependence on latitude, but rather vary regionally in response to basin dynamics and local coastal properties. Thus, regardless of the climate state, in a world with subdivided Southern Ocean basins, increased zonal heterogeneity is expected. In the absence of open Drake and Tasman passages, such a continental configuration would have characterized the middle Eocene Southern Ocean, allowing for regional differentiation of temperature and precipitation patterns in different sub-basins, around the zonal mean.

Under this interpretation, the existing proxy data begin to form a more cohesive story. The Ross Sea would have been kept warm by enhanced Pacific Ocean heat transport, rapid circulation in a small basin, and mixing with subtropical currents (Bijl et al., 2009; Douglas et al., 2014). The warmer climate in this basin would also promote higher precipitation rates, consistent with the proposed monsoonal precipitation regime on the western side of the Antarctic Peninsula (Jacques et al., 2014). The Weddell Sea would be cooler than the Ross Sea due to its more polar extent and longer residence time of water along the Antarctic coastline, however peninsular temperatures could be kept warmer and more seasonal than the rest of the basin due to the southern extension of South Atlantic branch currents or geostrophic frictional flow of warm Ross Sea water across a shallow Drake Passage (see discussion below). The peninsular mountains would create an orographic effect, with lower overall MAP on the east coast and different seasonal phasing of precipitation, again consistent with proxy data.

It should be noted that we are explicitly not invoking changes in ocean surface circulation as a driver for Antarctic cooling during the Eocene. Climate model simulations have already highlighted the importance of pCO_2 in Eocene cooling and the inception of the Antarctic Ice Sheet (e.g., DeConto and Pollard, 2003; Huber and Nof, 2006). However, regardless of the controls on the zonal mean itself, the configuration of land masses and surface currents surrounding Antarctica must play a dominant role in governing the magnitude of variance around the zonal mean, particularly in coastal settings.

4.5.3 Modern analog for the eastern Antarctic Peninsula

If the proposed hypothesis for zonal temperature heterogeneity is correct, then the higher amplitude of seasonal variability recorded by proxy data when compared with modelled SSTs is most likely a function of circulation patterns and coastal dynamics. In the modern ocean, only one Southern Hemisphere location exhibits an annual temperature cycle comparable to that inferred for the Eocene eastern Antarctic Peninsula: nearshore waters off the coast of Argentina (~39–42°S). Here, MAT and MART are within 1°C of the proxy data, and onshore precipitation patterns, both in terms of MAP and seasonal phasing, are similar to those inferred from the combined proxy and model results (Fig. 6; Hirahara et al., 2014; Schneider et al., 2015), making this site a good analog for the climate of Seymour Island during the latest Lutetian. This region lies within the confluence system of the subtropical Brazil Current and the subpolar Malvinas (Falkland) Current (Severov et al., 2012). Interestingly, the position of this confluence oscillates seasonally such that warm equatorial water is delivered during the summer and cold polar water dominates during the winter (Wainer et al., 2000), increasing the seasonal range of temperatures well above the anticipated zonal MART (Hirahara et al., 2014). A similar phenomenon could have characterized the east coast of the middle Eocene peninsular region. Tremblin et al. (2016) hypothesize that during the middle Eocene, in the absence of the Antarctic Circumpolar Current and with a closed Drake Passage, the South Atlantic Gyre extended farther south. This interpretation hints at the possibility that an associated branch current or, alternatively, frictional flow of equatorial-derived water across a shallow Drake Passage, could have extended down the northeastern margin of the Antarctic Peninsula where it met cooler, north-flowing waters from the proto-Weddell Gyre. Thus, a current configuration similar to the Brazil-Malvinas Confluence may have existed this region during the Eocene, seasonally oscillating and inflating seasonal range beyond that expected for that latitude, however high-resolution, eddy-resolved modelling studies are required to test this hypothesis.

Implications for determining meridional temperature gradients. Our data, evaluated in the context of existing austral high latitude proxy records, are consistent with the hypothesis of middle Eocene zonal heterogeneity in SSTs (Douglas et al., 2014). This interpretation has broad implications for determining the pole-to-equator temperature gradient, one of the most enigmatic yet critically important variables needed to constrain and understand greenhouse climate conditions. The majority of middle Eocene SST proxy records come from nearshore environments (e.g., Bijl et al., 2009; Burgess et al., 2008; Douglas et al., 2014; Hollis et al., 2012). Observation of modern SST variability (Fig. 5) indicates that proximity to a coastline, particularly in separated basins (i.e., the modern northern hemisphere), correlates with significant deviations from the zonal mean. In isolation, most proxy-based estimates of MAT and MART are therefore unlikely to be representative of the true zonal average. This implies that paleolongitude, paleogeography, oceanic circulation, bathymetry, and distance from a coastline must be considered when estimating the fit of proxy data to modelled meridional temperature gradients.

4.6 Conclusions

Seasonally resolved temperature and precipitation data from the northeastern coast of the Antarctic Peninsula offer a detailed picture of climate conditions during the late-middle Eocene. The amplitude of the reconstructed annual SST cycle exceeds predictions from a model, even when forced with high obliquity, and paleoprecipitation data indicate equable annual phasing despite evidence for monsoonal precipitation on the western side of the peninsula. These discrepancies imply that some aspect of the climate system is not captured by the GCM. We argue that our proxy records are best explained by zonally variable MAT and MART values in the middle Eocene Southern Ocean, a phenomenon observed in the modern boreal high latitudes where continents subdivide the ocean basins. With closed or shallow Drake and Tasman passages, the middle Eocene austral high-latitude oceans would also have been noncontiguous, and thus should likewise have exhibited a broader distribution of MAT and MART values along individual zonal bands than today. With the additional insight from MART reconstructions, Eocene coastal dynamics in the context of modern analogs suggests that the eastern margin of the middle Eocene Antarctic Peninsula may have been kept warmer than the rest of the Weddell basin by a subtropical derived branch current, from either the South Atlantic gyre or frictional flow across a shallow Drake Passage. This interpretation reconciles inconsistencies among existing proxy records of both temperature and precipitation, and allows for a more holistic evaluation of the conditions prevailing around Antarctica at the time. It also cautions against fitting meridional temperature gradients to single estimates of SST from nearshore environments, as they likely deviate from the true zonal mean.

Figures

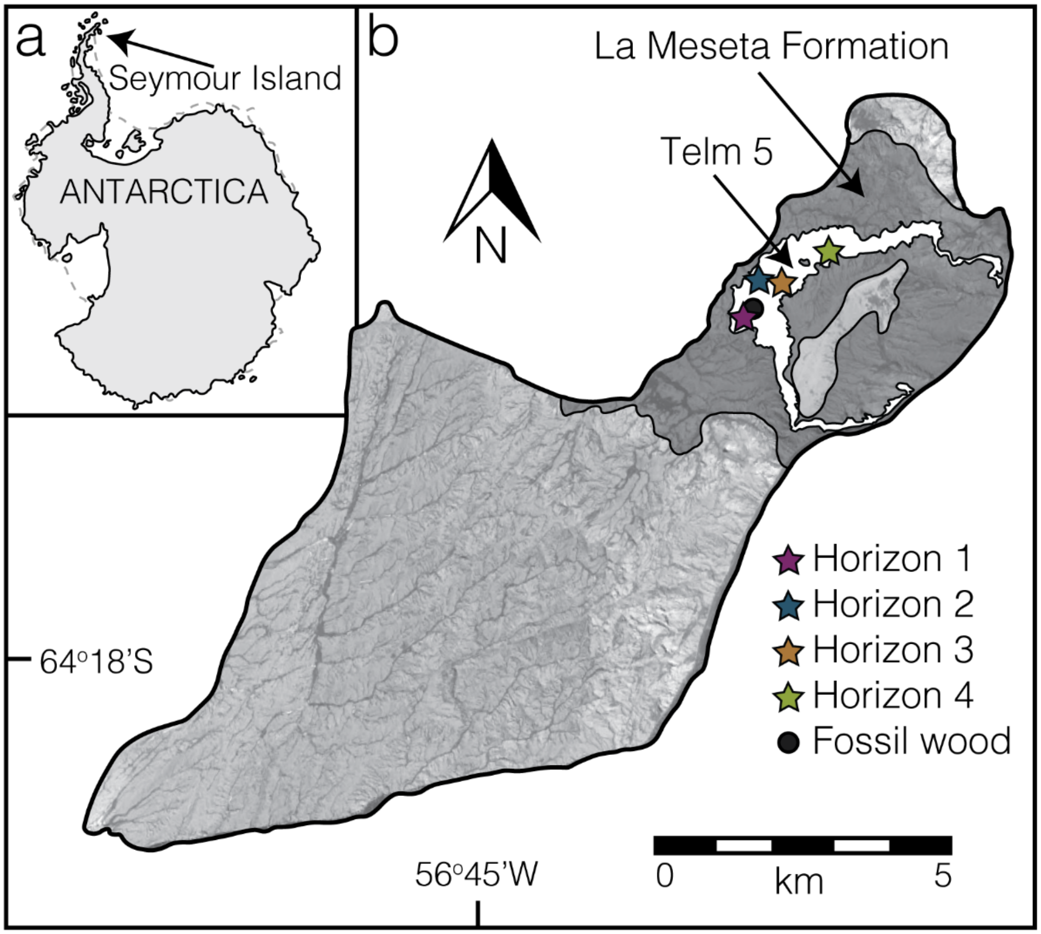

Figure 4.1. Site map. **A**. Location of Seymour Island in the context of the Antarctic continent. **B**. Enlarged view of Seymour Island. Dark gray denotes the surface extent of the Eocene La Meseta Formation, while the white band highlights the aerial extent of the latest Lutetian Telm 5 sediments. Fossil bivalve collection locations are marked with stars and the fossil driftwood site is marked with a circle.

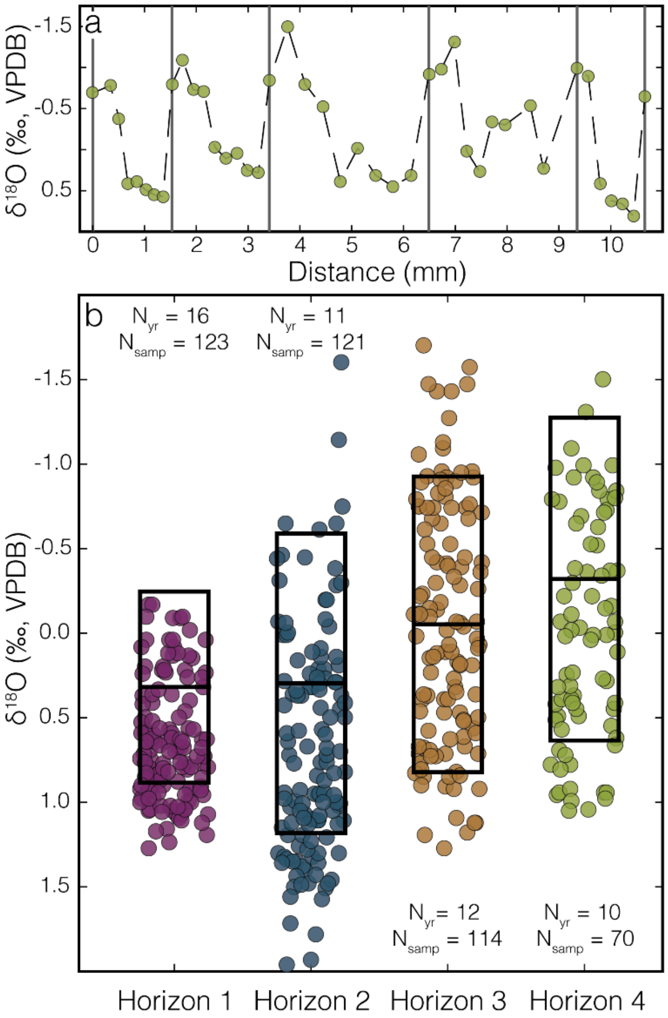

Figure 4.2. Summary of high-resolution oxygen isotope data from fossil bivalves. A. Example isotope profile from a Horizon 4 Cucullaea specimen (ID: 03-600-C2), plotted versus sampling distance. Points indicate discrete samples and the gray lines denote the placement of growth bands. Note that growth bands generally correspond with enriched values, indicating that growth slowed during the late fall to winter season. B. Summary of all isotope values from sequentially sampled shells plotted as a function of horizon, where Horizon 1 is stratigraphically lowest. Points depict discrete isotope measurements. Outlined boxes and horizontal lines depict the amplitude (range) and position (mean), respectively, of the sinusoidal fit to the stack of temporally aligned data from each horizon.

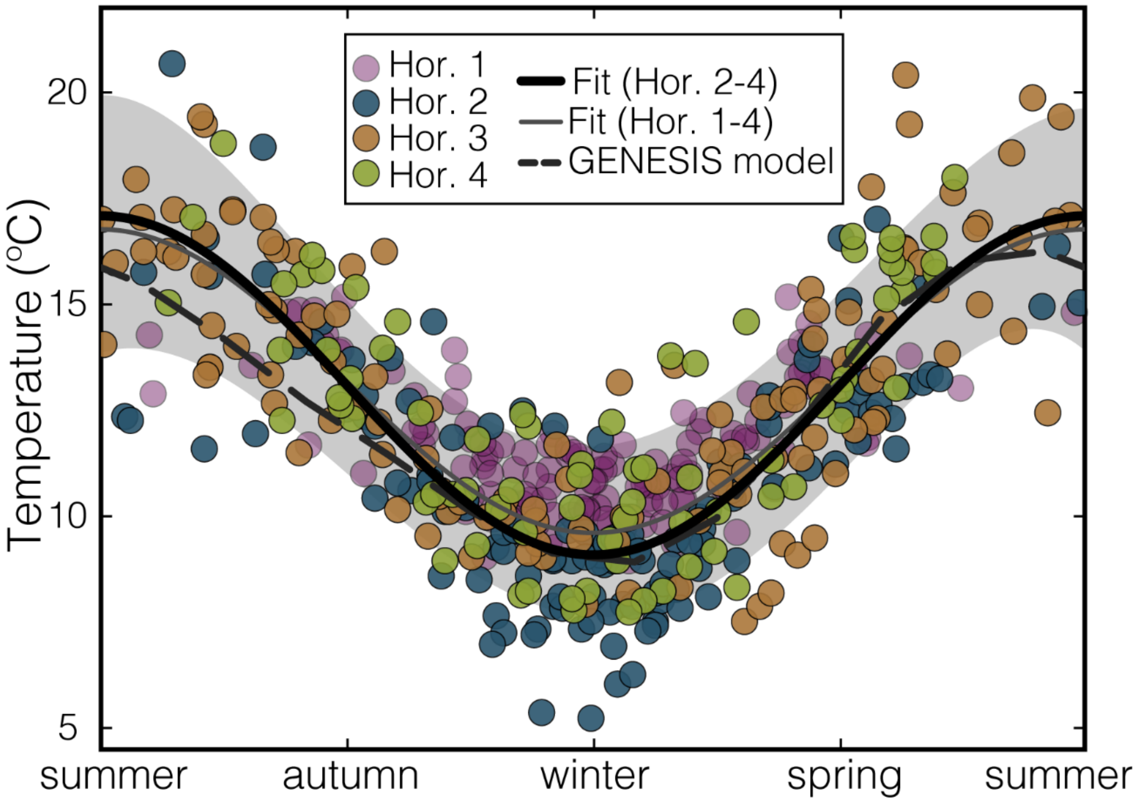

Figure 4.3. Summary of proxy- and model-derived seasonal temperature data. Isotope-derived temperature estimates (colored points) positioned on the annual cycle (Judd et al., 2017) were calculated using $\delta^{18}O_{seawater}$ from Douglas et al. (2014) and fit with a sinusoid to characterize the seasonal climate regime. The best-fit sinusoid through Horizons 2 – 4 (thick black line) suggests a MAT of 13.1°C and a MART of 8.0°C. The modelled seasonal regime (dashed gray line) falls entirely within the 95% confidence interval (gray band) of proxy-derived temperatures.

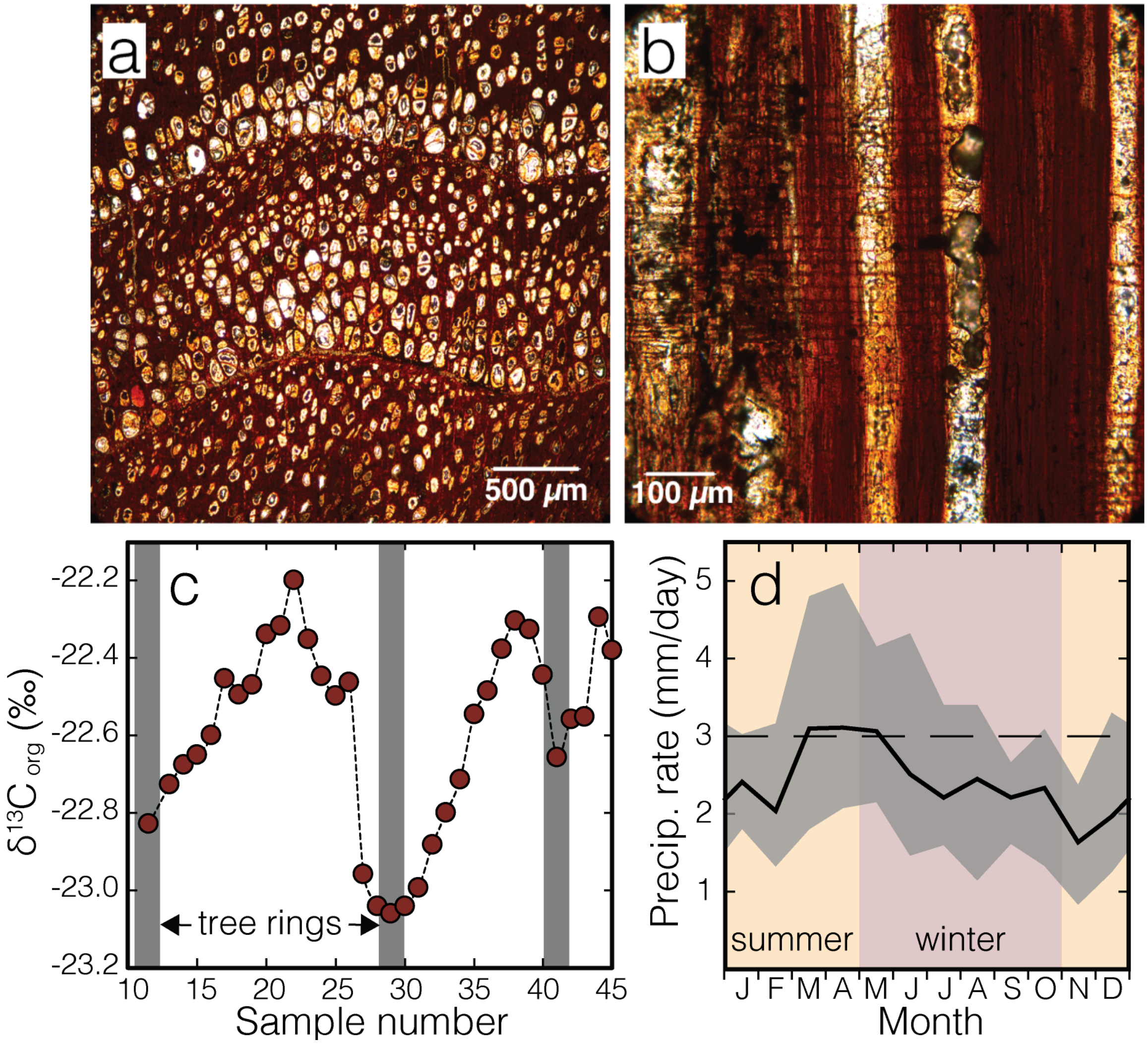

Figure 4.4. Summary of proxy and model-based precipitation data. A. Transverse thin section of sampled wood, showing annual tree rings. B. Longitudinal thin section of sampled wood. C. Two-year-long example record of organic carbon isotope measurements from fossil wood, used to calculate seasonality of paleoprecipitation. D. Modelled mean monthly precipitation rates (black line), with a 95% confidence interval. The dashed horizontal line denotes the five-month (NDJFM) cutoff threshold for a monsoonal precipitation regime, as defined by Zhang and Wang (2008). The orange and red bands indicate the six-month summer and winter periods, respectively, as defined Schubert and Jahren (2011).

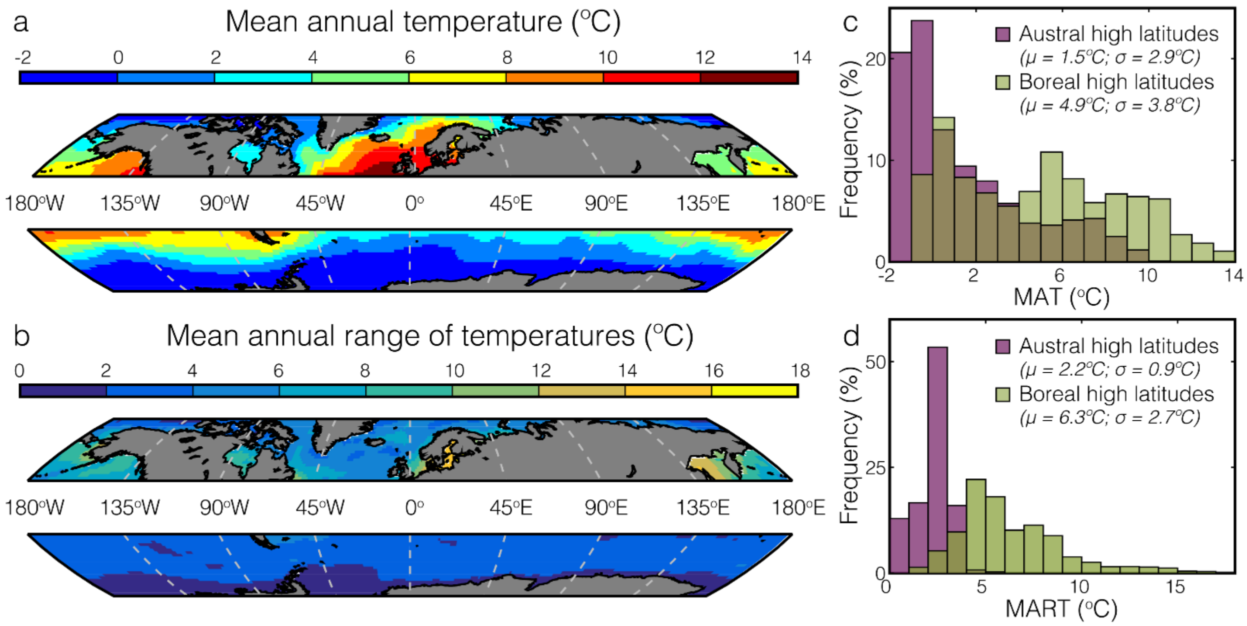

Figure 4.5. Comparison of modern boreal (50 – 75°N) and austral (50 – 75°S) high latitude MAT (A) and MART (B), and their respective frequency distributions (C, D). Data come from Hirahara et al. (2014).

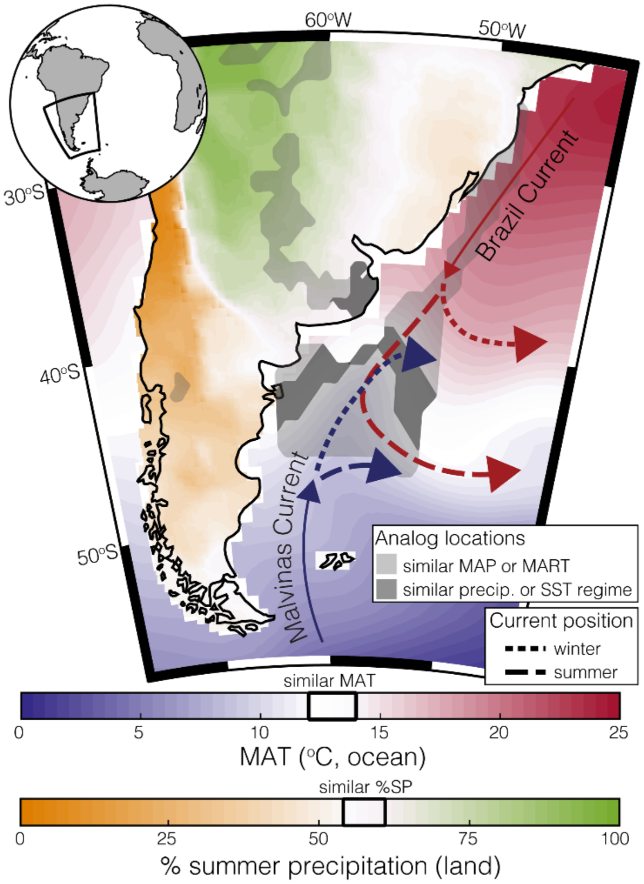

Figure 4.6. Comparison of proxy- and model-derived estimates of Eocene Antarctic climate with modern values (data come from Hirahara et al., 2014; Schneider et al., 2015). Terrestrial environments are colored based on the modern percent of annual precipitation that occurs during the six-month summer period, where white regions (black box on color-scale) indicate locations within ±1σ of the Eocene proxy value. Marine environments are colored based the modern MAT, where white regions indicate locations within ±1°C of the Eocene proxy value. Light gray regions are where MAP falls within ±1σ of the model value in the terrestrial environment or MART falls within ±1°C of the proxy value in the marine environments. Modern analog locations are in dark gray, where modern precipitation values, both in terms of percent summer precipitation and MAP, fall within ±1σ of the Eocene estimates or where modern SST values, both in terms of MAT and MART, fall within ±1°C of Eocene estimates.

Supporting information

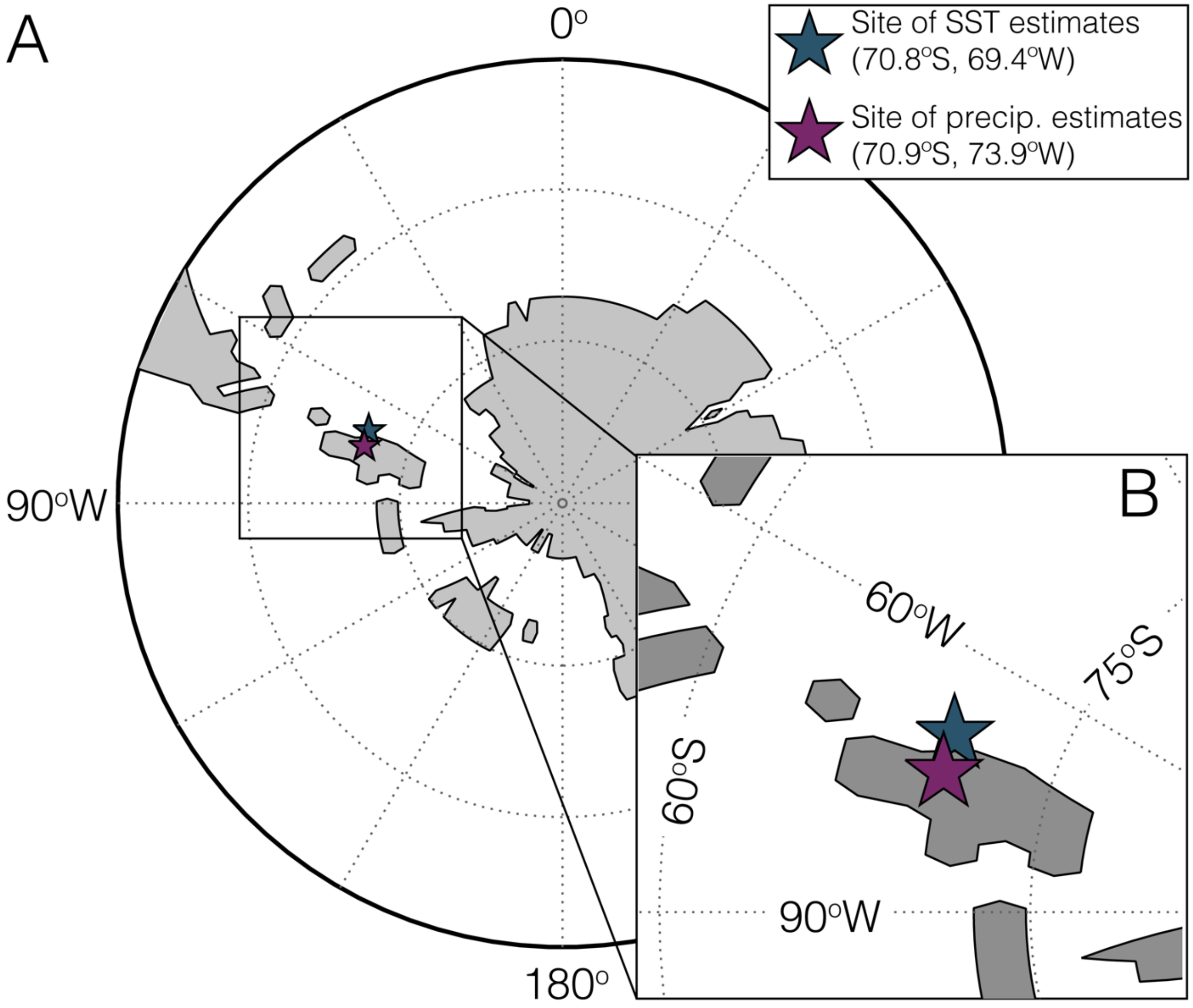

Figure S1. Paleogeography used in the GCM simulations. **A**. Southern hemisphere projection. **B**. Enlarged view of the locations from which SST and precipitation were estimated.

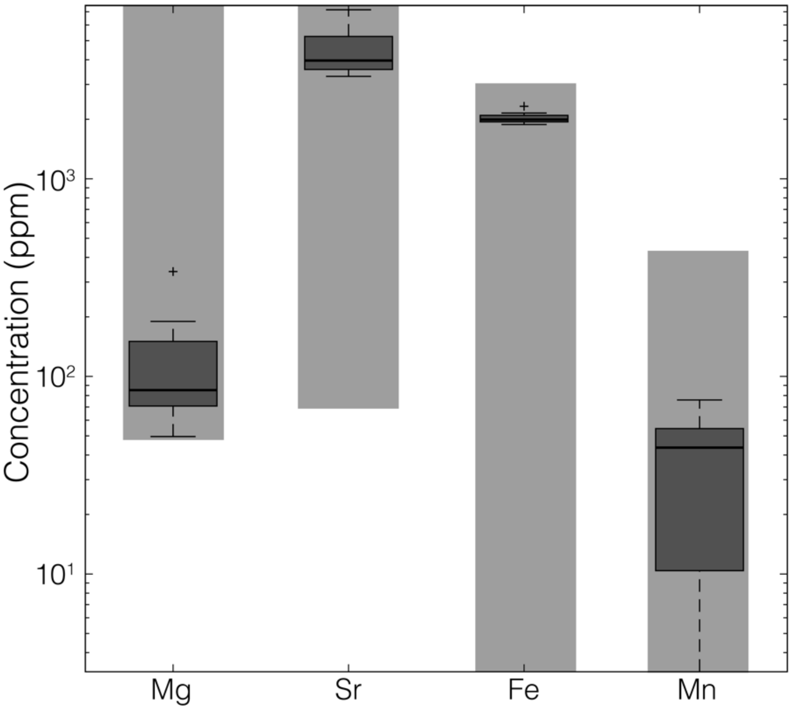

Figure S2: Box plots of trace element data used to assess potential diagenetic alteration. Light gray bands indicate the range of modern aragonitic bivalves for each element, as reported by Morrison and Brand (1986). Trace element analyses were performed on all eight shells from which isotope transects were generated, and in all cases fall within the range of unaltered aragonitic values.

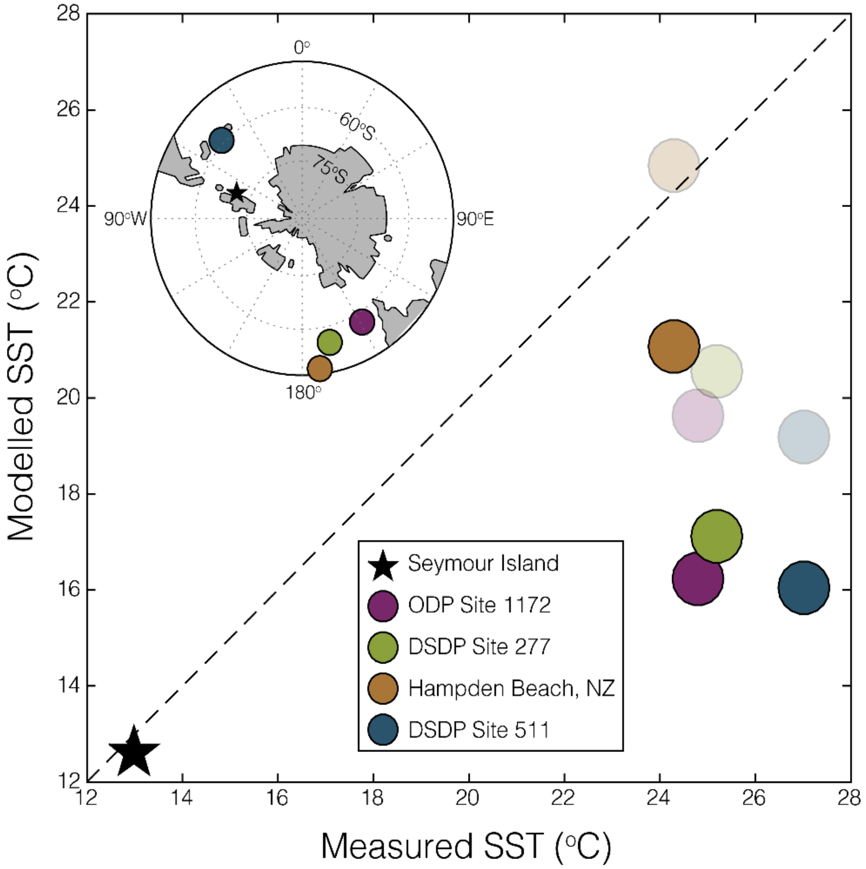

Figure S3. Comparison between proxy-derived and modelled sea surface temperature estimates for austral high-latitude Eocene sites, with inset map showing the paleogeographic location of each site. Data come from Bijl et al. (2009), Burgess et al. (2008), Hollis et al. (2009), and Houben (2012), using updated paleolatitudes from Van Hinsbergen et al. (2015). With the exception of the Seymour Island data, presented here, all data reflect TEX_{86}-derived SST values, calibrated to TEX_{86}^{H}. Comparison between measured SST and modelled MAT are shown by the full opacity points. To address the potential summertime bias of TEX_{86}-derived SSTs (e.g., Bijl et al., 2009), the transparent points reflect comparison between measured SST and an average of the three warmest modelled months. Measured SST is routinely warmer than modelled values, even when compared with summer temperatures, indicating true heterogeneity not captured by the model.

Table S1: Summary of all sampled bivalves. All values reflect $\delta^{18}O_{carb}$ (‰, VPDB). MSE refers to the average mean square error of the bivalve growth rate model results.

Horizon	Shell ID	Latitude	Longitude	Genus	Surface sampled	No. yrs sampled	No. of samples	SHELL AVERAGES[1]				YEARLY AVERAGE[2]				MODELED YEARLY AVERAGE[3]				
								Min	Max	Range	Mean	Min	Max	Range	Mean	Min	Max	Range	Mean	MSE
1	01-43-C3*	64°14.67S	56°40.59W	*Cucullaea*	Interior	16	123	-0.17	1.27	1.45	0.71	0.04	1.05	1.01	0.64	-0.85	0.98	1.83	0.06	0.11
2	01-77-E1	64° 14.36S	56° 39.75W	*Retrotapes*	Exterior	4	57	-1.14	1.96	3.10	0.73	-0.59	1.28	1.87	0.66	-1.18	1.22	2.40	0.02	0.75
	01-77-E2	64° 14.36S	56° 39.75W	*Retrotapes*	Exterior	5	36	0.21	1.48	1.27	1.06	0.38	1.27	0.89	0.97	-0.76	1.24	2.00	0.24	0.11
	01-77-E4	64° 14.36S	56° 39.75W	*Retrotapes*	Exterior	2	28	-1.60	1.57	3.17	0.18	-1.11	1.12	2.22	0.19	-1.22	0.99	2.21	-0.11	0.30
3	01-29-C1	64° 14.36S	56° 40.28W	*Cucullaea*	Exterior	7	60	-1.70	1.27	2.96	0.29	-0.65	0.89	1.53	0.31	-0.86	1.02	1.87	0.08	0.27
	01-106-E1	64° 14.36S	56° 40.28W	*Retrotapes*	Exterior	5	54	-1.57	0.73	2.30	-0.39	-1.26	0.51	1.78	-0.38	-1.37	0.69	2.05	-0.34	0.55
4	03-505-C1	64° 14.19S	56° 39.12W	*Cucullaea*	Interior	5	28	-0.63	1.05	1.68	0.43	-0.35	0.99	1.34	0.33	-1.22	1.11	2.34	-0.05	0.07
	03-600-C2	64° 14.05S	56° 38.60W	*Cucullaea*	Interior	5	42	-1.50	0.81	2.31	-0.20	-1.14	0.48	1.61	-0.24	-1.52	0.43	1.94	-0.54	0.26

[*] Data from Buick and Ivany (2004)

[1] Shell averages reflect the absolute minimum, maximum, range, and mean oxygen isotope values from the raw profile

[2] Yearly averages reflect the average of the minimum, maximum, range, and mean oxygen isotope values from each sampled year within a profile

[3] Modeled yearly averages reflect the average of the minimum, maximum, range, and mean oxygen isotope value from the output of the bivalve growth rate model

Table S2. Raw oxygen isotope data from serially sampled bivalves, by horizon and shell ID.

Horizon	Shell ID	Sample No.	Distance (mm)	δ^{18}O (VPDB)
1	01-43-C3*	1	0.611	-0.02
		2	0.709	0.75
		3	0.805	0.95
		4	0.899	0.93
		5	0.997	0.77
		6	1.092	0.69
		7	1.190	0.87
		8	1.285	0.92
		9	1.381	1.27
		10	1.478	0.92
		11	1.574	0.81
		12	1.671	0.56
		13	1.767	0.88
		14	1.886	0.22
		15	2.002	0.64
		16	2.122	0.97
		17	2.240	0.71
		18	2.356	0.77
		19	2.473	0.93
		20	2.591	1.05
		21	2.709	1.07
		22	2.826	1.07
		23	2.945	0.93
		24	3.060	0.63
		25	3.192	0.20
		26	3.323	0.57
		27	3.454	0.90
		28	3.610	1.16
		29	3.761	0.98
		30	3.915	0.80
		31	4.071	0.79
		32	4.223	0.83
		33	4.375	0.67
		34	4.529	0.41
		35	4.665	0.15
		36	4.787	-0.09
		37	4.905	0.37
		38	5.025	0.91
		39	5.145	1.05
		40	5.267	0.57
		41	5.384	0.99
		42	5.506	1.09
		43	5.627	0.86
		44	5.746	0.83
		45	5.866	0.57
		46	5.987	0.23
		47	6.106	0.40
		48	6.250	0.68
		49	6.397	0.96
		50	6.543	0.64
		51	6.686	0.70
		52	6.830	0.74

Horizon	Shell ID	Sample No.	Distance (mm)	$\delta^{18}O$ (VPDB)
		53	6.976	0.85
		54	7.119	0.63
		55	7.265	0.13
		56	7.410	1.04
		57	7.544	1.02
		58	7.680	0.77
		59	7.812	0.84
		60	7.948	0.93
		61	8.083	0.85
		62	8.217	0.59
		63	8.318	0.42
		64	8.423	0.32
		65	8.526	0.04
		66	8.629	0.60
		67	8.744	0.86
		68	8.850	0.77
		69	8.959	0.73
		70	9.066	0.50
		71	9.171	0.62
		72	9.280	0.24
		73	9.386	0.08
		74	9.491	0.79
		75	9.656	1.00
		76	9.816	0.76
		77	9.977	0.26
		78	10.137	0.68
		79	10.300	0.83
		80	10.458	0.46
		81	10.580	0.12
		82	10.695	0.53
		83	10.826	1.00
		84	10.974	0.64
		85	11.114	1.07
		86	11.263	1.02
		87	11.410	1.04
		88	11.552	0.96
		89	11.700	0.59
		90	11.845	0.79
		91	11.989	1.19
		92	12.133	1.17
		93	12.279	0.87
		94	12.425	0.63
		95	12.570	0.80
		96	12.693	0.66
		97	12.811	0.70
		98	12.928	0.86
		99	13.050	0.73
		100	13.172	-0.17
		101	13.290	0.52
		102	13.412	1.12
		103	13.532	0.68
		104	13.666	0.64
		105	13.798	0.94
		106	13.932	0.36
		107	14.066	0.64

Horizon	Shell ID	Sample No.	Distance (mm)	$\delta^{18}O$ (VPDB)
		108	14.201	1.24
		109	14.333	1.11
		110	14.468	0.33
		111	14.601	0.04
		112	14.734	0.56
		113	14.869	1.04
		114	15.004	0.83
		115	15.119	1.06
		116	15.235	0.22
		117	15.351	-0.10
		118	15.467	0.76
		119	15.581	0.90
		120	15.698	0.98
		121	15.816	1.03
		122	15.930	0.82
		123	16.035	0.50
2	01-77-E1	1	0.000	-1.14
		2	0.331	0.37
		3	0.573	0.24
		4	0.809	1.19
		5	1.041	0.82
		6	1.267	1.56
		7	1.493	0.94
		8	1.730	1.93
		9	1.956	1.36
		10	2.181	1.96
		11	2.400	1.78
		12	2.503	1.72
		13	2.616	1.46
		14	2.754	1.30
		15	2.888	1.48
		16	3.014	1.43
		17	3.136	1.12
		18	3.257	1.01
		19	3.375	0.98
		20	3.499	1.00
		21	3.625	0.96
		22	3.756	1.05
		23	3.876	1.49
		24	3.994	1.28
		25	4.114	1.23
		26	4.232	1.13
		27	4.351	1.36
		28	4.470	1.00
		29	4.593	0.87
		30	4.712	0.83
		31	4.843	0.57
		32	5.083	0.59
		33	5.312	0.27
		34	5.598	-0.65
		35	5.909	0.41
		36	6.172	-0.06
		37	6.461	0.28
		38	6.721	0.68

Horizon	Shell ID	Sample No.	Distance (mm)	$\delta^{18}O$ (VPDB)
		39	7.014	0.77
		40	7.284	1.09
		41	7.544	0.70
		42	7.816	-0.28
		43	8.070	-0.30
		44	8.335	0.34
		45	8.846	0.50
		46	9.135	0.16
		47	9.549	0.14
		48	9.712	0.09
		49	9.874	0.11
		50	10.063	0.60
		51	10.248	0.58
		52	10.414	0.29
		53	10.577	0.19
		54	10.739	0.14
		55	10.898	0.30
		56	11.058	0.26
		57	11.387	0.33
	01-77-E2	1	0.000	1.03
		2	0.284	0.96
		3	0.754	1.11
		4	1.029	0.94
		5	1.298	0.95
		6	1.575	1.13
		7	1.862	1.02
		8	2.153	1.11
		9	2.573	0.99
		10	2.822	0.93
		11	3.075	0.21
		12	3.332	0.84
		13	3.582	1.21
		14	3.833	1.05
		15	4.086	1.19
		16	4.346	1.35
		17	4.609	1.10
		18	4.872	1.30
		19	5.145	1.10
		20	5.481	1.32
		21	5.919	1.26
		22	6.204	0.76
		23	6.482	1.34
		24	6.770	1.11
		25	7.084	0.45
		26	7.382	0.32
		27	7.660	0.95
		28	8.072	1.07
		29	8.472	0.72
		30	8.756	1.40
		31	9.094	1.48
		32	9.568	1.08
		33	9.842	1.38
		34	10.116	1.35
		35	10.399	1.44

Horizon	Shell ID	Sample No.	Distance (mm)	$\delta^{18}O$ (VPDB)
		36	10.690	1.15
	01-77-E4	1	0.000	-0.04
		2	0.281	0.64
		3	0.564	1.50
		4	0.708	1.51
		5	1.128	1.57
		6	1.410	1.32
		7	1.693	1.01
		8	2.119	0.36
		9	2.380	0.01
		10	2.693	-0.31
		11	2.852	-0.75
		12	2.994	-1.60
		13	3.127	-0.20
		14	3.255	0.43
		15	3.507	0.37
		16	3.734	0.29
		17	3.962	0.37
		18	4.189	0.44
		19	4.418	-0.07
		20	4.646	-0.38
		21	5.046	-0.61
		22	5.343	-0.46
		23	5.651	-0.44
		24	5.951	-0.45
		25	6.207	-0.08
		26	6.454	0.01
		27	6.701	0.00
		28	6.957	0.67
3	01-29-C1	1	0.000	0.17
		2	0.477	1.27
		3	0.835	1.19
		4	1.048	1.12
		5	1.262	0.85
		6	1.575	0.91
		7	1.863	0.82
		8	2.174	0.47
		9	2.502	0.19
		10	2.812	0.71
		11	3.109	0.92
		12	3.303	0.77
		13	3.978	0.47
		14	4.263	0.03
		15	4.614	-1.70
		16	4.941	-1.47
		17	5.773	-0.40
		18	6.074	0.37
		19	6.606	0.68
		20	7.109	0.69
		21	7.442	0.85
		22	7.824	0.83
		23	8.223	0.84
		24	8.615	0.51
		25	8.978	0.36

Horizon	Shell ID	Sample No.	Distance (mm)	δ^{18}O (VPDB)
		26	9.247	0.81
		27	9.429	0.92
		28	9.667	0.90
		29	9.893	1.18
		30	10.059	1.12
		31	10.249	1.09
		32	10.615	0.39
		33	11.034	-0.11
		34	11.244	0.63
		35	11.406	0.73
		36	11.577	0.71
		37	11.755	0.52
		38	12.127	-0.07
		39	12.318	0.11
		40	12.523	0.39
		41	12.895	0.67
		42	13.634	0.35
		43	14.012	0.07
		44	14.309	-0.36
		45	14.750	-0.45
		46	14.980	-0.30
		47	15.211	0.14
		48	15.490	-0.23
		49	15.776	-0.74
		50	15.978	-0.71
		51	16.175	-0.33
		52	16.304	-0.22
		53	16.484	0.09
		54	16.691	0.18
		55	16.914	0.59
		56	17.137	0.46
		57	17.360	0.02
		58	17.514	0.23
		59	17.835	-0.68
		60	18.189	-0.86
	01-106-E1	1	0.000	-0.28
		2	0.134	-0.39
		3	0.271	-0.14
		4	0.409	-0.65
		5	0.546	-0.06
		6	0.679	0.67
		7	0.886	0.56
		8	1.159	-0.18
		9	1.432	-1.57
		10	1.708	-0.93
		11	1.973	-0.68
		12	2.246	-0.92
		13	2.554	-0.96
		14	2.825	-0.61
		15	3.105	-0.96
		16	3.372	-0.92
		17	3.640	-0.74
		18	3.909	0.32
		19	4.176	-0.02

Horizon	Shell ID	Sample No.	Distance (mm)	$\delta^{18}O$ (VPDB)
		20	6.110	-0.07
		21	6.590	0.69
		22	6.950	0.94
		23	7.310	0.98
		24	7.670	0.78
		25	8.390	0.72
		26	8.750	0.42
		27	9.110	-0.15
		28	9.650	-0.11
	03-600-C2	1	0.000	-0.69
		2	0.340	-0.78
		3	0.510	-0.38
		4	0.680	0.41
		5	0.850	0.39
		6	1.020	0.49
		7	1.190	0.55
		8	1.360	0.57
		9	1.530	-0.79
		10	1.740	-1.09
		11	1.940	-0.73
		12	2.150	-0.71
		13	2.360	-0.03
		14	2.570	0.11
		15	2.780	0.04
		16	2.990	0.25
		17	3.200	0.28
		18	3.410	-0.84
		19	3.760	-1.50
		20	4.100	-0.80
		21	4.440	-0.52
		22	4.780	0.39
		23	5.120	-0.02
		24	5.460	0.31
		25	5.800	0.45
		26	6.140	0.32
		27	6.490	-0.92
		28	6.730	-0.98
		29	6.980	-1.31
		30	7.220	0.02
		31	7.470	0.27
		32	7.710	-0.34
		33	7.960	-0.30
		34	8.450	-0.53
		35	8.700	0.23
		36	9.350	-0.99
		37	9.570	-0.89
		38	9.790	0.41
		39	10.010	0.62
		40	10.220	0.66
		41	10.440	0.81
		42	10.660	-0.65

[*] Data from Buick and Ivany (2004)

Table S3. Summary of best fit sines through temporally aligned proxy data by horizon.

Horizon	**N_{shell} ($N_{samples}$)**	**MAT (T_{pos})**	**MART (T_{amp})**	**R^2**
1	1 (123)	4.9	13.1	0.59
2	3 (121)	7.7	12.5	0.67
3	2 (104)	7.6	13.3	0.65
4	2 (70)	8.4	13.7	0.70
All	9 (418)	7.2	13.3	0.65
2 – 4	8 (295)	8.0	13.1	0.69

Table S4. Summary of all GCM simulation parameters.

	SIMULATION CONFIGURATION				
MODEL ID	**ice sheet**	**pCO2 (ppm)**	**obliquity (degrees)**	**eccentricity**	**precession (degrees)**
LENO2000H	none	2000	24.5	0	0
LENO1500H	none	1500	24.5	0	0
LEMED750L	medium	750	22	0	0
LEMED1500L	medium	1500	22	0	0
LEMED1500M	medium	1500	22	0.06	270

Table S5. Summary of fossil driftwood analyses

Specimen	Year	No. of Samples	Ave. % C_{org}	$\Delta\delta C_{org}$	P1/P2	% summer precipitation
01-48-W2	1	17	52.9	0.63	1.20	55
	2	12	50.2	0.76	1.03	51
	3	18	49.4	0.49	1.43	59
01-48-W6	1	16	53.0	0.72	1.08	52
	2	29	49.9	0.54	1.34	57
	3	12	51.1	0.43	1.54	61
	4	16	47.0	0.34	1.70	63
	5	19	53.0	0.59	1.26	56
Average:		17.4	50.8	0.56	1.31	57

References

Ager, D.V., 1967. Brachiopod palaeoecology. Earth-Science Rev. 3, 157–179. doi:10.1016/0012-8252(67)90375-3

Alder, J.R., Hostetler, S.W., Pollard, D., Schmittner, A., 2011. Evaluation of a present-day climate simulation with a new coupled atmosphere-ocean model GENMOM. Geosci. Model Dev. 4, 69–83. doi:10.5194/gmd-4-69-2011

Alvarez, M.J., Pérez, D.E., 2016. Gerontic intraspecific variation in the Antarctic bivalve *Retrotapes antarcticus*. Ameghiniana 53, 485–494. doi:10.5710/amgh.05.12.2015.2947

Aronson, R.B., Moody, R.M., Ivany, L.C., Blake, D.B., Werner, J.E., Glass, A., 2009. Climate change and trophic response of the Antarctic bottom fauna. PLoS One 4. doi:10.1371/journal.pone.0004385

Bijl, P.K., Schouten, S., Sluijs, A., Reichart, G.-J., Zachos, J.C., Brinkhuis, H., 2009. Early Palaeogene temperature evolution of the southwest Pacific Ocean. Nature 461, 776–779. doi:10.1038/nature08399

Birkenmajer, K., Gaździcki, A., Krajewski, K.P., Przybycin, A., Solecki, A., Tatur, A., Yoon, H. Il, 2005. First Cenozoic glaciers in West Antarctica. Antarct. Sci. 26, 3–12.

Bohaty, S.M., Zachos, J.C., 2003. Significant Southern Ocean warming event in the late middle Eocene. Geology 31, 1017–1020. doi:10.1130/G19800.1

Bohaty, S.M., Zachos, J.C., Florindo, F., Delaney, M.L., 2009. Coupled greenhouse warming and deep-sea acidification in the middle Eocene. Paleoceanography 24, 1–16. doi:10.1029/2008PA001676

Buick, D.P., Ivany, L.C., 2004. 100 years in the dark: Extreme longevity of Eocene bivalves from Antarctica. Geology 32, 921–924. doi:10.1130/G20796.1

Burgess, C.E., Pearson, P.N., Lear, C.H., Morgans, H.E.G., Handley, L., Pancost, R.D., Schouten, S., 2008. Middle Eocene climate cyclicity in the southern Pacific: Implications for global ice volume. Geology 36, 651. doi:10.1130/G24762A.1

Burke, K.D., Williams, J.W., Chandler, M.A., Haywood, A.M., Lunt, D.J., Otto-Bliesner, B.L., 2018. Pliocene and Eocene provide best analogs for near-future climates. Proc. Natl. Acad. Sci. 115, 201809600. doi:10.1073/pnas.1809600115

Carmichael, M.J., Lunt, D.J., Huber, M., Heinemann, M., Kiehl, J., LeGrande, A., Loptson, C.A., Roberts, C.D., Sagoo, N., Shields, C., Valdes, P.J., Winguth, A., Winguth, C., Pancost, R.D., 2016. A model-model and data-model comparison for the early Eocene hydrological cycle. Clim. Past 12, 455–481. doi:10.5194/cp-12-455-2016

Carter, A., Riley, T.R., Hillenbrand, C.D., Rittner, M., 2017. Widespread Antarctic glaciation during the Late Eocene. Earth Planet. Sci. Lett. 458, 49–57. doi:10.1016/j.epsl.2016.10.045

Carter, A., Riley, T.R., Hillenbrandt, C.-D., Rittner, M., 2016. Widespread Antarctic glaciation during the Late Eocene. Earth Planet. Sci. Lett. 458, 49–57. doi:10.1016/j.epsl.2016.10.045

Coplen, T.B., Brand, W.A., Gehre, M., Gröning, M., Meijer, H.A.J., Toman, B., Verkouteren, R.M., 2006. New Guidelines for δ13 C Measurements. Anal. Chem. 78, 2439–2441. doi:10.1021/ac052027c

DeConto, R.M., Pollard, D., 2003. Rapid Cenozoic glaciation of Antarctica induced by declining atmospheric CO2. Nature 421, 245–249. doi:10.1038/nature01290

Dettman, D., Reische, A.K., Lohmann, K.C., 1999. Controls on the stable isotope composition of seasonal growth bands in aragonitic fresh-water bivalves (unionidae). Geochim. Cosmochim. Acta 63, 1049–1057.

Dingle, R. V., Marenssi, S.A., Lavelle, M., 1998. High latitude Eocene climate deterioration:

Evidence from the northern Antarctic Peninsula. J. South Am. Earth Sci. 11, 571–579. doi:10.1016/S0895-9811(98)00035-2

Douglas, P.M.J., Affek, H.P., Ivany, L.C., Houben, A.J.P., Sijp, W.P., Sluijs, A., Schouten, S., Pagani, M., 2014. Pronounced zonal heterogeneity in Eocene southern high-latitude sea surface temperatures. Proc. Natl. Acad. Sci. U. S. A. 111, 1–6. doi:10.1073/pnas.1321441111

Dutton, A.L., Lohmann, K.C., Zinsmeister, W.J., 2002. Stable isotope and minor element proxies for Eocene climate of Seymour Island, Antarctica. Paleoceanography 17, 6-1-6–13. doi:10.1029/2000PA000593

Elliot, D.H., Trautman, T.A., 1982. Lower Tertiary strata on Seymour Island, Antarctic Peninsula, in: Craddock, C. (Ed.), Antarctic Geosciences. University of Wisconsin Press, pp. 287–297.

Feakins, S.J., Warny, S., Deconto, R.M., 2014. Snapshot of cooling and drying before onset of Antarctic Glaciation. Earth Planet. Sci. Lett. 404, 154–166. doi:10.1016/j.epsl.2014.07.032

Feakins, S.J., Warny, S., Lee, J., 2012. Hydrologic cycling over Antarctica during the middle Miocene warming. Nat. Geosci. 5, 557–560. doi:10.1038/ngeo1498

Francis, J.E., Ashworth, A., Cantrill, D.J., Crame, J.A., Stephens, R., Tosolini, A.-M., Thorn, V., 2008. 100 millions years of Antarctic climate evolution, in: Cooper, A.K., Barrett, P., Storey, B., Stump, E., Wise, W. (Eds.), Antarctica: A Keystone in a Changing World. National Academies Press, Washington, D.C., pp. 19–28. doi:10.17226/12168

Galeotti, S., DeConto, R., Naish, T., Stocchi, P., Florindo, F., Pagani, M., Barrett, P., Bohaty, S.M., Lanci, L., Pollard, D., Sandroni, S., Talarico, F.M., Zachos, J.C., 2016. Antarctic Ice Sheet variability across the Eocene-Oligocene boundary climate transition. Science (80-.).

352, 76–80. doi:10.1126/science.aab0669

Gasson, E., Lunt, D.J., Deconto, R., Goldner, A., Heinemann, M., Huber, M., Legrande, A.N., Pollard, D., Sagoo, N., Siddall, M., Winguth, A., Valdes, P.J., 2014. Uncertainties in the modelled CO2 threshold for Antarctic glaciation. Clim. Past 10, 451–466. doi:10.5194/cp-10-451-2014

Gill, A.E., Niller, P.P., 1973. The theory of the seasonal variability in the ocean. Deep. Res. Oceanogr. Abstr. 20, 141–177. doi:10.1016/0011-7471(73)90049-1

Glorioso, P.D., 1987. Temperature distribution related to shelf-sea fronts on the Patagonian Shelf. Cont. Shelf Res. 7, 27–34. doi:10.1016/0278-4343(87)90061-6

Grossman, E.L., Ku, T.L., 1986. Oxygen and carbon isotope fractionation in biogenic aragonite: temperature effects. Chem. Geol. 59, 59–74.

Gulick, S.P.S., Shevenell, A.E., Montelli, A., Fernandez, R., Smith, C., Warny, S., Bohaty, S.M., Sjunneskog, C., Leventer, A., Frederick, B., Blankenship, D.D., 2017. Initiation and long-term instability of the East Antarctic Ice Sheet. Nature 552, 225–229. doi:10.1038/nature25026

Hansen, J., Fung, I., Lacis, A., Rind, D., Lebedeff, S., Ruedy, R., Russell, G., Stone, P., 1988. Global climate changes as forecast by Goddard Institute for Space Studies three-dimensional model. J. Geophys. Res. 93, 9341. doi:10.1029/JD093iD08p09341

Hansen, J., Sato, M., Ruedy, R., 2012. Perception of climate change. Proc. Natl. Acad. Sci. 109, E2415–E2423. doi:10.1073/pnas.1205276109

Hirahara, S., Ishii, M., Fukuda, Y., 2014. Centennial-scale sea surface temperature analysis and its uncertainty. J. Clim. 27, 57–75. doi:10.1175/JCLI-D-12-00837.1

Hollis, C.J., Taylor, K.W.R., Handley, L., Pancost, R.D., Huber, M., Creech, J.B., Hines, B.R., Crouch, E.M., Morgans, H.E.G., Crampton, J.S., Gibbs, S., Pearson, P.N., Zachos, J.C., 2012. Early Paleogene temperature history of the Southwest Pacific Ocean: Reconciling proxies and models. Earth Planet. Sci. Lett. 349–350, 53–66. doi:10.1016/j.epsl.2012.06.024

Houben, A., 2012. *Triggers and consequences of glacial expansion across the Eocene-Oligocene Transition*. Utrecht.

Huber, M., Caballero, R., 2011. The early Eocene equable climate problem revisited. Clim. Past 7, 603–633. doi:10.5194/cp-7-603-2011

Huber, M., Goldner, A., 2012. Eocene monsoons. J. Asian Earth Sci. 44, 3–23. doi:10.1016/j.jseaes.2011.09.014

Huber, M., Nof, D., 2006. The ocean circulation in the southern hemisphere and its climatic impacts in the Eocene. Palaeogeogr. Palaeoclimatol. Palaeoecol. 231, 9–28. doi:10.1016/j.palaeo.2005.07.037

Ivany, L.C., Lohmann, K.C., Hasiuk, F., Blake, D.B., Glass, A., Aronson, R.B., Moody, R.M., 2008. Eocene climate record of a high southern latitude continental shelf: Seymour Island, Antarctica. Geol. Soc. Am. Bull. 120, 659–678. doi:10.1130/B26269.1

Jacques, F.M.B., Shi, G., Li, H., Wang, W., 2014. An early-middle Eocene Antarctic summer monsoon: Evidence of “fossil climates.” Gondwana Res. 25, 1422–1428. doi:10.1016/j.gr.2012.08.007

Jones, D., 1980. Annual Cycle of Shell Growth Increment Formation in Two Continental Shelf Bivalves and its Paleoecologic Significance. Paleobiology 6, 331–340.

Judd, E.J., Wilkinson, B.H., Ivany, L.C., 2017. The life and time of clams: Derivation of intra-annual growth rates from high-resolution oxygen isotope profiles. Palaeogeogr.

Palaeoclimatol. Palaeoecol. 490, 70–83. doi:10.1016/j.palaeo.2017.09.034

Kaplan, J.O., 2003. Climate change and Arctic ecosystems: 2. Modeling, paleodata-model comparisons, and future projections. J. Geophys. Res. 108, 8171. doi:10.1029/2002JD002559

Keating-Bitonti, C.R., Ivany, L.C., Affek, H.P., Douglas, P., Samson, S.D., 2011. Warm, not super-hot, temperatures in the early Eocene subtropics. Geology 39, 771–774. doi:10.1130/G32054.1

Knutti, R., Meehl, G.A., Allen, M.R., Stainforth, D.A., 2006. Constraining climate sensitivity from the seasonal cycle in surface temperature. J. Clim. 19, 4224–4233. doi:10.1175/JCLI3865.1

Livermore, R., Hillenbrand, C.D., Meredith, M., Eagles, G., 2007. Drake Passage and Cenozoic climate: An open and shut case? Geochemistry, Geophys. Geosystems 8. doi:10.1029/2005GC001224

Lunt, D.J., Jones, T.D., Heinemann, M., Huber, M., LeGrande, A., Winguth, A., Loptson, C., Marotzke, J., Roberts, C.D., Tindall, J., Valdes, P., Winguth, C., 2012. A model-data comparison for a multi-model ensemble of early Eocene atmosphere-ocean simulations: EoMIP. Clim. Past 8, 1717–1736. doi:10.5194/cp-8-1717-2012

Marenssi, S.A., Net, L.I., Santillana, S.N., 2002. Provenance, environmental and paleogeographic controls on sandstone composition in an incised-valley system: The Eocene La Meseta Formation, Seymour Island, Antarctica. Sediment. Geol. 150, 301–321. doi:10.1016/S0037-0738(01)00201-9

Marshall, G.J., Orr, A., van Lipzig, N.P.M., King, J.C., 2006. The impact of a changing Southern Hemisphere Annular Mode on Antarctic Peninsula summer temperatures. J. Clim. 19, 5388–5404. doi:10.1175/JCLI3844.1

Maxbauer, D.P., Royer, D.L., LePage, B.A., 2014. High Arctic forests during the middle Eocene supported by moderate levels of atmospheric CO2. Geology 42, 1027–1030. doi:10.1130/G36014.1

Morrison, J.O., Brand, U., 1986. Paleoscene# 5. Geochemistry of recent marine invertebrates. Geosci. Canada 13.

Moss, D.K., Ivany, L.C., Silver, R.B., Schue, J., Artruc, E.G., 2017. High latitude settings promote extreme longevity in fossil marine bivalves. Paleobiology 43, 365–382.

Poole, I., Cantrill, D., Utescher, T., 2005. A multi-proxy approach to determine Antarctic terrestrial palaeoclimate during the Late Cretaceous and Early Tertiary. Palaeogeogr. Palaeoclimatol. Palaeoecol. 222, 95–121. doi:10.1016/j.palaeo.2005.03.011

Poole, I., Mennega, A.M.W., Cantrill, D.J., 2003. Valdivian ecosystems in the Late Cretaceous and Early Tertiary of Antarctica: Further evidence from myrtaceous and eucryphiaceous fossil wood. Rev. Palaeobot. Palynol. 124, 9–27. doi:10.1016/S0034-6667(02)00244-0

Porebski, S.J., 1995. Facies architecture in a tectonically-controlled incised-valley estuary: La Meseta Formation (Eocene) of Seymour Island, Antarctic Peninsula. Stud. Geol. Pol.

Portmann, R.W., Solomon, S., Hegerl, G.C., 2009. Spatial and seasonal patterns in climate change, temperatures, and precipitation across the United States. Proc. Natl. Acad. Sci. 106, 7324–7329. doi:10.1073/pnas.0808533106

Pörtner, H., 2001. Climate change and temperature-dependent biogeography: Oxygen limitation of thermal tolerance in animals. Naturwissenschaften 88, 137–146. doi:10.1007/s001140100216

Portner, H.O., Peck, L., Somero, G., 2007. Thermal limits and adaptation in marine Antarctic ectotherms: an integrative view. Philos. Trans. R. Soc. B Biol. Sci. 362, 2233–2258. doi:10.1098/rstb.2006.1947

Prandle, D., Lane, A., 1995. The annual temperature cycle in shelf seas. Cont. Shelf Res. 15, 681–704. doi:10.1016/0278-4343(94)E0029-L

Sadler, P.M., 1988. Geometry and stratification of uppermost Cretaceous and Paleogene units on Seymour Island, northern Antarctic Peninsula, in: Feldmann, R.M., Woodburne, M.O. (Eds.), Geology and Paleontology of Seymour Island, Antarctic Peninsula. Geological Society of America Memoir 169, pp. 303–320.

Scher, H.D., Martin, E.E., 2006. Timing and climatic consequences of the opening of Drake Passage. Science (80-.). 312, 428–430. doi:10.1126/science.1120044

Schneider, U., Becker, A., Finger, P., Meyer-Christoffer, A., Rudolf, B., Ziese, M., 2015. GPCC Full Data Monthly Product Version 7.0 at 0.5°: Monthly Land-Surface Precipitation from Rain-Gauges built on GTS-based and Historic Data. doi:10.5676/DWD_GPCC/FD_M_V7_050

Schubert, B.A., Jahren, A.H., 2011. Quantifying seasonal precipitation using high-resolution carbon isotope analyses in evergreen wood. Geochim. Cosmochim. Acta 75, 7291–7303. doi:10.1016/j.gca.2011.08.002

Schubert, B.A., Jahren, A.H., Eberle, J.J., Sternberg, L.S.L., Eberth, D.A., 2012. A summertime rainy season in the Arctic forests of the Eocene. Geology 40, 523–526. doi:10.1130/G32856.1

Severov, D.N., Pshennikov, V., Remeslo, A.V., 2012. Fronts and thermohaline structure of the Brazil – Malvinas Confluence System. Adv. Sp. Res. 49, 1373–1387. doi:10.1016/j.asr.2012.01.024

Sorlien, C.C., Luyendyk, B.P., Wilson, D.S., Decesari, R.C., Bartek, L.R., Diebold, J.B., 2007. Oligocene development of the West Antarctic Ice Sheet recorded in eastern Ross Sea strata. Geology 35, 467. doi:10.1130/G23387A.1

Stickley, C.E., Brinkhuis, H., Schellenberg, S.A., Sluijs, A., Röhl, U., Fuller, M., Grauert, M., Huber, M., Warnaar, J., Williams, G.L., 2004. Timing and nature of the deepening of the Tasmanian Gateway. Paleoceanography 19, 1–18. doi:10.1029/2004PA001022

Stilwell, J.D., Zinsmeister, W.J., 1992. Molluscan Systematics and Biostratigraphy: Lower Tertiary La Meseta Formation, Seymour Island, Antartic Peninsula, Antarctic Research Series. American Geophysical Union, Washington, D. C. doi:10.1029/AR055

Tremblin, M., Hermoso, M., Minoletti, F., 2016. Equatorial heat accumulation as a long-term trigger of permanent Antarctic ice sheets during the Cenozoic. Proc. Natl. Acad. Sci. 113, 11782–11787. doi:10.1073/pnas.1608100113

Trenberth, K.E., Shea, D.J., 2005. Relationships between precipitation and surface temperature. Geophys. Res. Lett. 32, 1–4. doi:10.1029/2005GL022760

van Hinsbergen, D.J.J., de Groot, L. V., van Schaik, S.J., Spakman, W., Bijl, P.K., Sluijs, A., Langereis, C.G., Brinkhuis, H., 2015. A Paleolatitude Calculator for Paleoclimate Studies. PLoS One 10, e0126946. doi:10.1371/journal.pone.0126946

Wainer, I., Gent, P., Goni, G., 2000. Annual cycle of the Brazil-Malvinas confluence region in the National Center for Atmospheric Research Climate System Model. J. Geophys. Res. Ocean. 105, 26167–26177. doi:10.1029/1999JC000134

West, C.K., Greenwood, D.R., Basinger, J.F., 2015. Was the Arctic Eocene “rainforest” monsoonal? Estimates of seasonal precipitation from early Eocene megafloras from Ellesmere Island, Nunavut. Earth Planet. Sci. Lett. 427, 18–30.

doi:10.1016/j.epsl.2015.06.036

Wilson, D.S., Pollard, D., Deconto, R.M., Jamieson, S.S.R., Luyendyk, B.P., 2013. Initiation of the West Antarctic Ice Sheet and estimates of total Antarctic ice volume in the earliest Oligocene. Geophys. Res. Lett. 40, 4305–4309. doi:10.1002/grl.50797

Wolfe, J.A., 1993. A method of obtaining climatic parameters from leaf assemblages. US Geol. Surv. Bull. 2040, 1–71.

Zachos, J.C., Dickens, G.R., Zeebe, R.E., 2008. An early Cenozoic perspective on greenhouse warming and carbon-cycle dynamics. Nature 451, 279–283. doi:10.1038/nature06588

Zhang, S., Wang, B., 2008. Global summer monsoon rainy seasons. Int. J. Climatol. 28, 1563–1578. doi:10.1002/joc.1659

Chapter 5:

Late Eocene reduction in summer ocean temperatures drives cooling on the Antarctic Peninsula

5.1 Abstract

Austral high-latitude paleoclimate data from the Eocene are integral to understanding conditions during the evolution of Earth's climate into an icehouse. However, records of mean annual temperature from the Eocene Southern Ocean are highly variable and often difficult to reproduce with models, making it challenging to determine the mechanism(s) responsible for late Eocene cooling. Novel approaches, such as high-resolution seasonal data, can contextualize existing Eocene proxy records and provide unique insights into prevailing conditions not afforded by lower-resolution temperature proxies. Here, we assess seasonal temperature variations in shallow nearshore waters along the eastern margin of the Antarctic Peninsula during the late Eocene (~37.4 Ma) inferred from serially-sampled oxygen isotope profiles from accretionary bivalve shells. Results suggest a mean annual temperature of 10.8 ^{o}C with a seasonal amplitude of 2.0 ^{o}C. Comparison with data from the middle Eocene of the same formation, indicates a significant attenuation in late Eocene seasonality primarily brought about by a reduction in summertime temperatures. We propose that the observed reduction in seasonality between the middle and late Eocene is best explained by changes in surface ocean circulation as a result of the opening of the Drake Passage and initiation of a weak proto-Antarctic Circumpolar Current. This interpretation lends support to the hypothesis that initial late Eocene cooling was driven by tectonically-induced changes in circulation, rather than a decrease in pCO_2, preconditioning the continent for large-scale glaciation at the close of the epoch.

5.2 Introduction

The Eocene Epoch (~ 56-34 Ma) represents a time of large-scale global climate change. The early Eocene was marked by several hyperthermal events, including the Paleocene-Eocene Thermal Maximum and the Early Eocene Climatic Optimum, two of the warmest intervals of the

Cenozoic Era (Zachos et al., 2008). The ca. 17 million years following the climatic optimum exhibit relatively consistent cooling, eventually culminating in the onset of sustained Southern Hemisphere continental glaciation around the time of the Eocene–Oligocene transition (Coxall et al., 2005; Galeotti et al., 2016). This boundary represents the most recent large-scale transition from a greenhouse climate regime, with ice-free poles and a low latitudinal temperature gradient, to an icehouse climate regime, with polar ice and a steeper latitudinal temperature gradient (Bijl et al., 2009; Evans et al., 2018; Hines et al., 2017).

Two primary mechanisms have been proposed to explain the climatic changes associated with the inception of a Southern Hemisphere ice sheet: 1) the thermal isolation of Antarctica driven by the opening of the Drake and Tasman Gateways and the initiation of the Antarctic Circumpolar Current (ACC; Kennett, 1977), or 2) a decrease in atmospheric CO_2 levels (Anagnostou et al., 2016; Deconto and Pollard, 2003; Raymo and Ruddiman, 1992). The former hypothesis largely fell out of favor after modeling studies highlighted the importance of pCO_2 in providing a threshold for glaciation (Deconto and Pollard, 2003) and implied that ocean circulation played only a small role in controlling latitudinal heat transport (Huber et al., 2004). However, recent evidence of ephemeral glacial ice prior to the Eocene-Oligocene transition (e.g., Carter et al., 2017; Gulick et al., 2017; Scher et al., 2014), discrepancies in model-specific pCO_2 glaciation thresholds (e.g., Gasson et al., 2014), and late Eocene cooling trends independent of consistent changes in pCO_2 (e.g., Zhang et al., 2013) have reinvigorated discussions on the cause(s) of late Eocene cooling.

While the temporal record of mean global temperatures is reasonably well constrained throughout this transition (e.g. Zachos et al., 2008), relatively little is known about the accompanying changes in seasonality, and most of these studies have been at lower latitudes

(Ivany et al., 2000; Keating-Bitonti et al., 2011; Kobashi et al., 2001). As summer temperatures are the primary control on inception and expansion of ice sheets, seasonally resolved data from nearshore Antarctic waters are critical for evaluating the mechanisms responsible for global cooling over this time interval. Further, the existing records of mean annual temperature (MAT) from the Eocene Southern Ocean are highly variable (e.g., Bijl et al., 2009; Burgess et al., 2008; Creech et al., 2010; Douglas et al., 2014; Hines et al., 2017; Hollis et al., 2009; Inglis et al., 2015; Ivany et al., 2008; Liu et al., 2009), obfuscating direct interpretation of high-austral conditions during this important climate transition. The added insight from seasonally-resolved data may be able to help contextual conflicting MAT records, by identifying seasonal biases within proxy methods.

Seasonal temperature data can also provide information not readily available from MAT data alone, particularly with respect to the means by which climate changes. For example, a decrease in mean annual temperature can be achieved by vertically phase shifting the existing seasonal amplitude, by preferential summertime cooling such that the seasonal amplitude is dampened, or by preferential wintertime cooling, which increases the seasonal amplitude. While all three scenarios result in the same overall change in mean annual temperature, each has unique consequences for the biotic and hydrologic responses to climate change, as well as different implications for the mechanisms responsible for the observed climate change. This latter point is particularly pertinent during the transition from the middle to late Eocene, as the mechanism(s) driving global cooling and ice sheet inception remain unclear. Conceptually, the annual temperature cycle would likely respond differently to cooling driven by changes in ocean circulation than that driven by decreasing pCO_2, making seasonally-resolved Antarctic SSTs unique in their ability to distinguish between the two proposed mechanism.

5.3 Materials and Methods

5.3.1 High-resolution stable isotope analyses from fossil bivalves

Fossil bivalve specimens come from the La Meseta Formation (Elliot and Trautman, 1982), Seymour Island, Antarctica (~64ºS, 54ºW), situated ~100 km east of the Antarctic Peninsula. The La Meseta Formation, which preserves the only known *in situ* Eocene marine outcrop in all of Antarctica, is a highly fossiliferous marine succession consiting of poorly consolidated sandstones, mudstones, and shell beds. The specimens for this study were collected from two shell beds, located approximately halfway up the stratigraphic subdivision known as Telm 7 (Sadler, 1988). Telm 7 consists of flat-lying heterolithic sandstone, interpreted to have been deposited along a shallow marine shoreface (Marenssi et al., 2002; Porebski, 1995). Dinoflagellate biostratigraphy of the sampled horizons is consistent with an early Priabonian age (~37.4 Ma; Douglas et al., 2014).

Six specimens of fossil bivalves belonging to the genera *Cucullaea* and *Retrotapes* (formerly *Eurhomalea*, Alvarez and Pérez, 2016) were serially (i.e., sequentially) sampled at high spatial/temporal resolution across growth increments to constrain intra-annual temperature variation during the late Eocene. X-Ray diffraction (XRD) and trace element analyses were performed on samples of shell material from each horizon to evaluate preservation of the original aragonite mineralogy. Pristine specimens were incrementally sampled for stable isotopes on either the cleaned shell exterior or a polished section through the axis of maximum growth (Tables S1-3) using an ESI/New Wave/Merchantek MicroMill. A total of 31 years of growth were sampled at an average resolution of 9.5 samples per year. Samples were analyzed for their stable oxygen ($\delta^{18}O_{carb}$) and carbon ($\delta^{13}C_{carb}$) isotopic compositions using a Finnegan MAT 251 or 253 mass spectrometer coupled to a Kiel automated carbonate preparation device. Data are reported relative the Vienna PeeDee Belemnite (VPDB) standard and were corrected using international reference materials NBS-18 and NBS-19. Average precision is better than 0.04‰.

5.3.2 Seasonally-resolved sea surface temperature estimates

In order to reconstruct the annual temperature cycle, isotope profiles are transformed from the distance domain into a temporal framework, and SSTs are estimated from the $\delta^{18}O_{carb}$ values. To account for variable intra-annual growth rates of bivalves, we apply the bivalve growth model of Judd et al. (2017), which derives seasonal growth rate and temperature functions using only serially sampled $\delta^{18}O_{carb}$ data and associated distance values. All 31 years of temporally-aligned data can then be converted to temperature estimates, combined into a single densely sampled annual cycle, and fit with a sinusoid, enabling a true climatological analysis.

Temperatures are calculated using the empirically derived biogenic aragonite paleotemperature equation of Grossman and Ku (1986) modified for SMOW (Dettman et al., 1999). This equation, however, requires knowledge of or an assumption about the oxygen isotopic composition of seawater ($\delta^{18}O_{seawater}$) at the time of shell precipitation, which fluctuates temporally as a function of ice volume and spatially as a function of the ratio of precipitation (and runoff) to evaporation. In the Eocene, uncertainties regarding the precise timing, extent, and possible ephemeral nature of glacial ice during the late Eocene (Carter et al., 2017; Gulick et al., 2017; Scher et al., 2014) make this value exceedingly difficult to estimate. One method for determining local seawater composition is to calculate SST using an independent proxy and use that temperature estimate to solve for the $\delta^{18}O_{seawater}$ (e.g., Keating-Bitonti et al., 2011; Lear et al., 2000). However, clumped isotope-derived SST estimates from bivalves within Telm 7 span a broad range of temperatures

(9.2 – 16.9 °C), each associated with a sizeable standard error (Douglas et al., 2014), giving rise to a large range of possible $\delta^{18}O_{seawater}$ values.

To estimate the annual temperature cycle, we must therefore account for this uncertainty, as well as the potential for variable inter-shell $\delta^{18}O_{seawater}$ values, driven by local variability during a time of dynamic climate and environmental change. To do this, we estimate SSTs of the temporally-aligned isotope profiles of each individual shell using a suite of seawater values ranging between -1.0 and -0.4‰ (0.1‰ step; n = 7). We then systematically cycle through every possible permutation of these temperature estimates, allowing for unique seawater compositions of each shell. With each permutation, we stack all temperature values on the same annual cycle, fit them with a sinusoid, and record the R^2 and p-value of the fit (n = 117,649). We ultimately assign a $\delta^{18}O_{seawater}$ value to each shell by selecting the combination that yields the highest, statistically significant R^2value of the sinusoidal fit. This procedure assumes that all specimens are recording the same temperatures and that inter-shell offsets in $\delta^{18}O_{carb}$ thus reflect short-term changes in local $\delta^{18}O_{seawater}$.

5.3.3 GENESIS climate model simulations

To constrain the conditions required to produce the seasonal patterns observed in our proxy data and to better understand the seasonal response to changing baseline conditions in this region, we run multiple climate simulations using the Genesis 3.0 Global Circulation Model (Alder et al., 2011), coupled to the BIOME4 equilibrium vegetation model (Kaplan, 2003). By using a computationally efficient slab-ocean/sea ice component rather than a full depth ocean model, we can assess the role of pCO_2 in driving seasonal variations independent from any change in ocean circulation. Each simulation was run for 50 years with a middle-late Eocene paleogeography

(Feakins et al., 2014) and a range of pCO_2, ice volume, and orbital parameters (Table S4); results reflect an average of the last ten years of each simulation. The surface model has a spatial resolution of 2° x 2°; mean monthly SSTs were extracted at the paleolocation of Seymour Island at ~68.8°S, 69.4°W.

5.4 Results

5.4.1 High-resolution stable isotope analyses from fossil bivalves

All analyzed shells retain their original aragonitic mineralogy, and trace element concentrations are consistent with values from modern aragonitic bivalves (Fig. S1; Morrison and Brand, 1986), indicating that they have not undergone diagenetic alteration and that isotope values reflect original depositional conditions. Individual isotope profiles consistently exhibit low amplitude variability, which can make it difficult to discern discrete years. However, a number of factors lend confidence to the assertion that growth bands are formed on an annual basis. These factors include (1) small annual cycles in $\delta^{18}O_{carb}$ in association with growth bands (Fig. 1A), 2), (2) strong cyclicity in $\delta^{13}C_{carb}$ profiles coincident with growth banding (Fig. S2), and (3) previous studies of these taxa from the middle Eocene, which have confirmed the annual nature of internal growth bands and external sculpturing (Buick and Ivany, 2004; Dutton et al., 2002; Ivany et al., 2008; Judd et al., 2019).

Across the whole population, discrete profiles exhibit comparatively similar means and ranges of oxygen isotope values (Fig. 1B), spanning between ~0.5 and 2‰. Specimens C20154 and C40154 have smaller ranges than the other shells. However, these shells were sampled at a lower resolution in cross section later in ontogeny (Miklus, 2008) and thus are likely time averaged. Specimens E1006 and C10181 both exhibit a similar range in isotope values as other sampled shells, however the overall values from E1006 are generally more depleted while values from C10181 are generally more enriched. As the specimens come from shell beds that temporally average material, these differences likely indicating local seawater $\delta^{18}O_{seawater}$ variability.

5.4.2 Seasonal temperature analysis

The combination of seawater values that yields the highest R^2 value of the sine-fit temporally-aligned temperature data support a late Eocene MAT of 10.8 ^{o}C and a mean annual range of temperatures (MART) of 2.0 ^{o}C (Fig. 1C; Table S1; $R^2 = 0.53$; $p\text{-value} \ll 0.001$). The iterative fitting procedure, which allowed for variable inter-shell $\delta^{18}O_{seawater}$ values and maximized the overall fit of the total dataset, suggests that seawater values were tightly clustered ($\delta^{18}O_{seawater} = -0.86 \pm 0.11$‰;1σ), with the exception of C18101 ($\delta^{18}O_{seawater} = -0.4$‰). Of note, removing the two lower amplitude specimens (C20154 and C20154) has no impact on the best-fit shell $\delta^{18}O_{seawater}$ values nor MAT, and minimal impact on MART (2.2 ^{o}C) and the R^2 value of the fit (0.54). Similarly, while removing the most enriched specimen (C10181) does increase the overall MAT (11.3 ^{o}C) by consistently shifting all shell $\delta^{18}O_{seawater}$ values toward more enriched values, ultimately it has little impact on either MART (2.1 ^{o}C) or the R^2 value of the fit (0.54). As such, we include all sampled specimens in the final temperature solution.

5.4.3 GENESIS climate model simulations

To better understand how changing pCO_2, ice volume, and orbital parameters effect the seasonal range of nearshore peninsular waters, we ran a suite of five simulations, systematically varying each forcing. Changing pCO_2 alone had no effect on MART; a finding that held true regardless of whether there was an Antarctic ice sheet or not (Table S4). Conversely, holding pCO_2 constant but adding a medium-size ice sheet and decreasing obliquity (from 24.5 to 22^{o}) lowered

MART by 1.2 ºC, and, interestingly, MAT by 2.6 ºC. Even under the lowest seasonality configuration (i.e., low obliquity, high eccentricity, July perihelion, and a medium sized ice sheet) the seasonal range at the paleolocation of Seymour Island only decreased to 5.1 ºC, and, ultimately, we were unable to approximate the small seasonal range observed in the proxy data. Given that these simulations utilize a slab ocean, these findings suggest that changes in surface ocean circulation likely played a large role in controlling the seasonal variability of nearshore peninsular waters.

5.5 Discussion

The proxy data presented here suggest an early Priabonian MAT of 10.8 ºC with a small seasonal range of ~2.0 ºC. In the following sections, we compare these data with seasonally-resolved values from the late Lutetian (Judd et al., 2019) and propose a model for the reconfiguration of surface ocean currents between the middle and late Eocene that accounts for observed changes in seasonality. Additionally, we demonstrate that seasonally-resolved data can help identify seasonal biases in other temperature proxies, and explore cooling trends from existing proxy data across the Eocene Southern Ocean and their consistency with our proposed model. To facilitate a direct comparison between time intervals, all proxy records discussed in the following sections have been averaged across the Priabonian (37.8 – 33.9 Ma) and the late Lutetian (45.1 – 41.2 Ma), with each time bin representing ~3.9 Ma.

5.5.1 Middle to late Eocene reduction in seasonality

Seasonally-resolved oxygen isotope-derived SST data from the stratigraphically lower and older unit, Telm 5, of the La Meseta Formation indicate a late Lutetian (~42-41.5 Ma) MAT of 13.1 ºC and MART of 8.0 ºC (Judd et al., 2019). This indicates a cooling between the late Lutetian and early Priabonian of ~2.3 ^{o}C, accompanied by an attenuation of seasonality by ~6 ^{o}C (Fig. 2). Remarkably, winter temperatures are statistically indistinguishable, implying that late Eocene cooling along the eastern Antarctic Peninsula was driven entirely by a reduction in summertime temperatures.

A similar pattern of seasonal attenuation brought about by a reduction of summertime temperatures is also indicative of increasing water depth (Prandle and Lane, 1995; Wilkinson and Ivany, 2002). Thus, given the unique nature of the cooling trend inferred from the seasonal data, establishing whether this pattern represents a true climate signal or simply a change in paleodepth is important. Despite a notable facies change between Telms 5 and 7, interpreted as a transition from tidally-dominated estuary mouth to low-energy shoreface environment with a straightened coastline (Marenssi et al., 2002; Porebski, 1995; Porębski, 2000; Sadler, 1988), several lines of evidence suggest that these data are indeed representative of climatic conditions. First, faunal turnover between Telms 5 and 7 are best explained by a cooling climate rather than a significant change in paleodepth (Jadwiszczak, 2010). Second, sedimentological evidence indicates an increase in the sand-sized grain fraction from Telm 5 to 7, with higher contributions of felspar and lithic fragments, indicative of shallow shelf deposition under temperate conditions favoring physical weathering (Dingle et al., 1998; Marenssi et al., 2002). Similarly, sedimentary structures (e.g., tidal sand-waves) are consistent with shallow coastal deposition (Marenssi et al., 2002). Finally, because winter temperatures remain consistent between the middle and late Eocene, if the decrease in seasonal range did reflect changes in paleodepth rather than overall climate state, our results would indicate stable temperatures between the middle and late Eocene. This becomes difficult to reconcile with TEX_{86} data (Douglas et al., 2014) and the global benthic oxygen isotope stack (Zachos et al., 2008), both of which indicate substantial cooling over this time frame. Thus, since biologic, lithologic, and sedimentologic evidence all support the assumption of shallow coastal deposition, and the observed cooling trend is consistent with existing climatologic data, we feel confident in assessing the trends in seasonality in the context of a true climate signal.

Provided that these data reflect a true collapse in seasonality in nearshore waters along the eastern margin of the Antarctic Peninsula between the middle and late Eocene, what information does can be gleaned regarding seasonal variability during large-scale climate transitions? As a first order approximation, seasonality is controlled by intra-annual variations in solar insolation, and thus should therefore correlate with latitude. However, several other factors, including atmospheric and oceanic circulation patterns, play a large role in controlling MART (e.g., Glorioso, 1987; Marshall et al., 2006; Gill and Niller, 1973). Today, despite highly seasonal Antarctic air temperatures, the seasonal range of temperatures of seawater in the austral high latitudes is low (<1ºC; Hirahara et al., 2014), as it is restricted by the freezing point of salt water and minimized by latent and sensible heat exchange associated with seasonal sea ice. Thus, in a warmer world, one would anticipate a larger seasonal range of SST, manifest as preferential summertime warming, as observed here.

Analysis of modern global trends indicate that the recent anthropogenic increase in near-surface MAT is largely manifest as preferential summertime warming (Hansen et al., 2012, 1988), though regional patterns, particularly in the climatically sensitive high latitudes, are far from straightforward (e.g., Turner et al., 2005; Marshall et al., 2006). In a reversal of the findings presented here, previous studies of temporal changes in seasonality with cooling across the Eocene-Oligocene Transition, in both terrestrial (Eldrett et al., 2009; Zanazzi et al., 2015) and marine (Ivany et al., 2000; Kobashi et al., 2001) environments have all found evidence for increased seasonality, brought about by a preferential decrease in winter temperature. Though convincing in its consistency, this pattern is based on a limited number of studies all of which are concentrated in the low or midlatitudes of North America, with just a single study focused on high-boreal terrestrial change (Eldrett et al., 2009).

5.5.2 Seasonally resolved data as a means of identifying seasonal biases in other proxies

The seasonally resolved proxy data from this study and those of Judd et al. (2019) indicate a late Lutetian to early Priabonian cooling of MAT of ~2.3 ^{o}C. We find that the decrease in MAT was brought about by a reduction in summer temperatures by ~6.4 ^{o}C, with no discernable change in winter temperature. The overall decrease in MAT is in excellent agreement with cooling inferred from clumped isotopes of bivalves from the same section (2.2 ^{o}C; Douglas et al., 2014), although the absolute temperatures of the clumped isotope measurements are systematically warmer (Fig. 3). This offset could be due to uncertainties in the inferred $\delta^{18}O_{seawater}$ value, time averaging across an ~3.9 myr bin (i.e., reflective of true climate variability), or from early-stage solid-state diffusion, driving slightly warmer clumped values (Henkes et al., 2014).

However, the cooling trend inferred from the organic biomarker SST proxy, TEX_{86} is quite different. BAYSPAR-calibrated (Tierney and Tingley, 2015) TEX_{86} SST estimates from the La Meseta Formation yield a mean late Lutetian SST estimate of 20.5 ^{o}C and a Priabonian SST estimate of 13.1 ^{o}C, indicating an overall cooling of 7.4 ^{o}C. While the uncertainties of these estimates are large, it is interesting that in both time intervals, the Tex_{86}-derived SST estimates more closely approximates the estimated summer temperatures from seasonally-resolved oxygen isotope data (Fig. 3). Further, the overall cooling trend in the TEX_{86} data is in good agreement with the inferred diminution of summer temperatures between the middle and late Eocene.

Seemingly regardless of the calibration used, TEX_{86} temperatures are often warmer than SSTs inferred from other proxies. This realization has led several authors to suggest a summertime bias in the proxy, particularly in high latitude environments where the production of the biomarker might be seasonally limited by sunlight or nutrient availability (e.g., Hollis et al., 2012; Sluijs et al., 2011, 2006; but see also Tierney, 2013). Consistent with this hypothesis, our analyses provide evidence in favor of a seasonal bias in TEX_{86}-derived SST values at Seymour Island. Specifically, we observe that both the middle and late Eocene TEX_{86}-derived temperatures are in better agreement with our inferred summer temperatures than the overall MAT, and that the TEX_{86}-inferred cooling between the middle and late Eocene matches our observed reduction in summertime temperatures.

This finding has important implications for inferring climate change using TEX_{86} data. If the proxy is recording changes in summer temperature, rather than overall MAT, at other locations, then it will be difficult to deconvolve the true magnitude of climate change within a record from the changes in seasonality. Further, this highlights the necessity of multi-proxy approaches involving seasonally-resolved data for evaluating this hypothesis in other locations, across a range of latitudes.

4.3 A proposed model of changes in surface ocean circulation to explain reduced seasonality

The proxy-data presented here indicate that late Eocene cooling along the eastern Antarctic Peninsula was driven primarily by a reduction in summertime temperatures. However, in a suite of climate model simulations with systematically varying pCO_2, ice volume, and orbital configuration, we are unable to match the low seasonality of the late Eocene. Similarly, even under a high seasonality orbital configuration, the model underestimates the amplitude of annual variability of the late Lutetian data. This suggests that surface ocean circulation likely exerts a large influence on the amplitude of seasonality observed middle and late Eocene, as it is one of the only variables capable of influencing the seasonal cycle not accounted for in our model (Judd et al., *submitted*).

Using modern analog locations (i.e., locations in today's oceans that have similar MAT and MART values to observed data) as a guide, Judd et al. (2019) postulate that during the middle Eocene, in the absence of the ACC, Seymour Island was situated at the convergence of two currents: the colder western boundary of the proto-Weddell Gyre and a warmer branch current, derived from either the South Atlantic Gyre or the South Pacific Gyre. They hypothesize that the position of these currents oscillated seasonally, similar to the modern Brazil-Malvinas Confluence, such that warm equatorial-derived water was delivered during the summer and cold polar-derived water dominated during the winter (Fig. 4A). The current configuration would therefore increase the range of seasonal temperatures above the anticipated zonal MART value in nearshore Peninsular water. This interpretation is consistent with a comparison of the terrestrial floral and faunal assemblages of the middle Eocene section of the La Meseta Formation with the nearshore SST, which indicate a decoupling of terrestrial and marine climates along the eastern margin of the peninsula, similarly attributed to the influx of a warm surface current (Cione et al., 2007).

The precise timing of the initiation of the ACC remains highly debated (e.g., (Barker et al., 2007; Pfuhl and McCave, 2005; Sarkar et al., 2019; Scher et al., 2015; Scher and Martin, 2006, 2004). However, there is strong evidence that at ~41 Ma, the Drake Passage opened to intermediate water depths (Scher and Martin, 2006, 2004), and that some semblance of a proto-ACC existed by ~36 Ma (Sarkar et al., 2019). Even a weak zonal current could likely contract the subtropical

South Atlantic Gyre equatorward and deflect any potential branch currents from reaching peninsular waters (Fig. 4B). Holding pCO_2 more-or-less constant (Jagniecki et al., 2015; Pagani et al., 2011; Zhang et al., 2013), nearshore Peninsular environments would experience the same wintertime temperatures, but the proto-ACC would prohibit poleward summertime heat transport, preferentially cooling summers and attenuating the overall seasonal amplitude. Cooler summertime temperatures would therefore allow for the growth and expansion of the Antarctic Ice Sheet, predating any decrease in pCO_2. In turn, an increase in ice volume would lower eustatic sea level, exposing shelfal silicates to be weathered, and the cooling of Antarctic waters would increase the effectiveness of the biological pump, repartition atmospheric CO_2 to the oceans, and expediting carbon sequestration, ultimately lowering global pCO_2. Continued lowering of pCO_2, likely below some threshold value, would then allow for a full descent into global icehouse conditions.

5.5.3 Southern Ocean SSTs in the context of the proposed model

The Southern Ocean played a key role in late Eocene cooling. As such, reconstructing high-austral conditions throughout the Eocene is essential to identifying changes in the latitudinal temperature gradients and the magnitude of polar amplification, as well as ultimately identifying the mechanism responsible for the onset of South Hemisphere glaciation. However, despite the wealth of proxy data, SSTs from high-austral settings are highly variable (Fig. 5A,B; Bijl et al., 2009; Burgess et al., 2008; Creech et al., 2010; Douglas et al., 2014; Hines et al., 2017; Hollis et al., 2009; Inglis et al., 2015; Liu et al., 2009; Petersen and Schrag, 2015). Further, diverging trends in late Eocene cooling (Fig. 5C) and difficulty reproducing the observed patterns with climate models, compounded by uncertainties in proxy calibration and age models and inconsistency among proxies, have made it difficult to reconstruct Eocene South Ocean conditions. However, our proposed model for middle to late Eocene changes in surface circulation is generally consistent with the existing proxy data from the Southern Ocean.

Southern Ocean proxy data are consistently warmer in the South Pacific sector than the in the South Atlantic sector, especially those from New Zealand (Fig. 5A, B). Surface circulation patterns near New Zealand are complex today and were likely even more nuanced in the Eocene, when the Tasman Gateway was closed (Bijl et al., 2013, 2009; Houben et al., 2019). These sites were probably kept warm by lower latitude branch currents extending from the South Pacific Gyre. Interestingly, between the middle and late Eocene, TEX_{86} data from the East Tasman Plateau (Bijl et al., 2009) record a similar magnitude of cooling to that inferred from clumped isotope and TEX_{86} data from Seymour Island (Douglas et al., 2014), while Mg/Ca-derived SSTs indicate a warming in nearshore New Zealand (Fig. 5C; Hines et al., 2017). These trends are consistent with the initiation of a circumpolar current, which would cool sites within its reach (i.e., East Tasman Plateau and Seymour Island) while deflection of lower latitude source currents would warm New Zealand.

The hypothesized changes in surface circulation between the middle and late Eocene are also consistent with SST data from the equatorial Atlantic and Indian Oceans which show no evidence of cooling between the middle and late Eocene (Pearson et al., 2007; Tremblin et al., 2016; but see also Cramwinckel et al., 2018) despite Southern Ocean cooling (Inglis et al., 2015) and little evidence for dramatic changes in pCO_2 levels (Jagniecki et al., 2015; McKay et al., 2016; Steinthorsdottir et al., 2019; Zhang et al., 2013). Additionally, a recent study using dinoflagellate cyst assemblages to track surface circulation identified a reorganization of currents at ~36 Ma, although this was interpreted as an intensification of a westward countercurrent (Houben et al., 2019). Regardless of the direction of flow, any circumpolar current should be capable of deflecting warmer, lower-latitude currents away from the Antarctic Peninsula. Further, circulation-driven changes in seasonality, rather than pCO_2, helps reconcile the contrasting (though albeit sparse) records of seasonal variability with cooling between the Northern and Southern Hemisphere (Eldrett et al., 2009; Ivany et al., 2000; Kobashi et al., 2001; Zanazzi et al., 2015).

5.6 Conclusions

Seasonally-resolved proxy data from nearshore eastern Antarctic Peninsula waters indicate an early Priabonian MAT of 10.8 ^{o}C and MART of 2.0 ^{o}C. Comparison with similar proxy data from the same formation during the late Lutetian indicates a middle to late Eocene cooling of 2.3 ^{o}C brought about entirely through a reduction in summertime temperatures of ~6 ^{o}C. Climate model simulations, run with a slab ocean and parameterized with varying pCO_2, ice volume, and orbital parameters, were unable to reproduce the low amplitude seasonality of the late Eocene data, suggesting that changes in wind-driven surface ocean circulation played the dominant role in suppressing the seasonal amplitude. Previously published TEX_{86} data from the same formation and over the same time interval record a similar cooling trend (~7.5 ^{o}C) and are consistently warmer than our reconstructed MAT values and, suggesting that the TEX_{86} proxy is recording summertime temperatures rather than MAT in the high latitude setting of Seymour Island. This finding highlights the utility of subannually-resolved data in identifying seasonal biases in other SST proxies and cautions against inferring absolute cooling or warming trends from TEX_{86} data from environments that may be subject to preferential seasonal formation of the biomarker.

We propose that the decrease in both MAT and MART between the middle and late Eocene was driven by a reconfiguration of Southern Ocean surface currents after the initiation of the proto-

ACC. Deflection of warm south-flowing currents led to preferential summertime cooling, allowing for the inception of late Eocene glaciation. Feedbacks related to increased ice volume and cooler Southern Ocean MAT led to a decrease in global pCO_2. Once pCO_2 declined sufficiently, the global climate cooled allowing for a full descent into icehouse conditions. Thus, similar to the findings of other recent studies, we suggest that despite the inferred pCO_2 threshold for continental ice sheet formation, tectonically-induced reorganization of surface currents initiated Antarctic cooling and preconditioned the continent for large-scale glaciation.

Figures

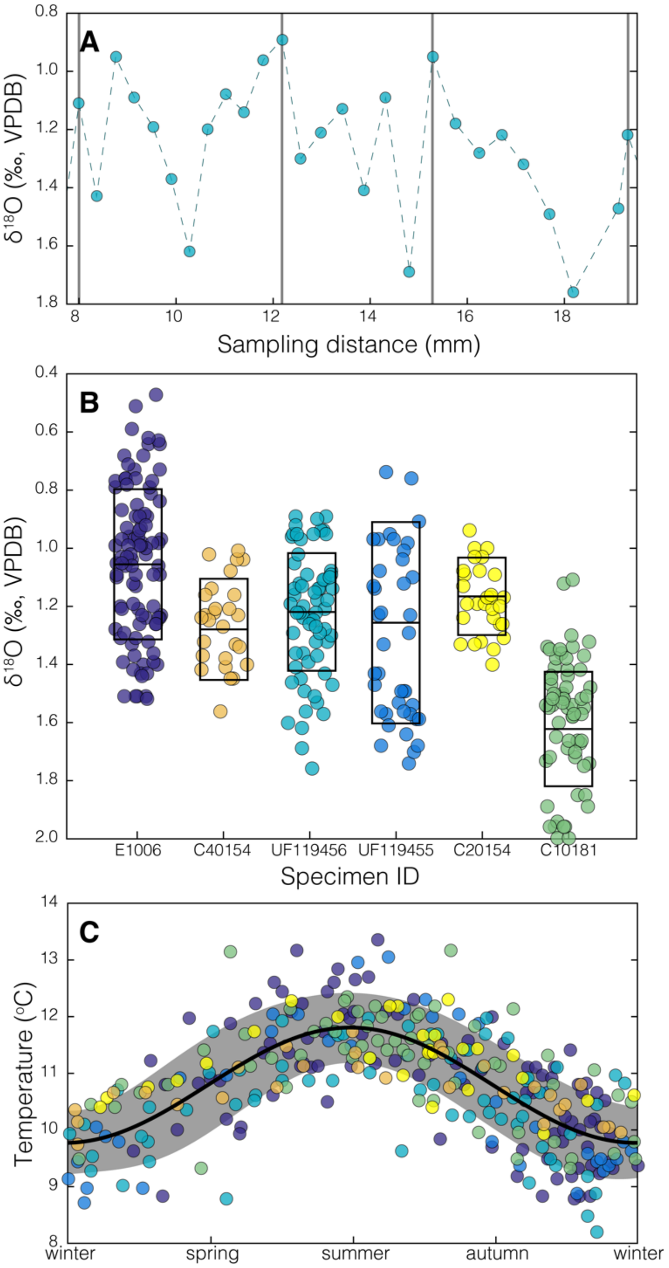

Figure 5.1. Summary of seasonally-resolved oxygen isotope profiles from early Priabonian fossil bivalves of the La Meseta Formation, Seymour Island, Antarctica. **A.** Example of a high-resolution oxygen isotope profile (Specimen ID: UF119456). Gray bands denote the location of annual external sculpturing. **B.** Summary of oxygen isotope values from all six sequentially sampled shells. Points depict discrete isotope measurements. Outlined boxes and horizontal lines depict the amplitude (range) and position (mean), respectively, of the sinusoidal fit to the stack

of temporally aligned data from each horizon. **C.** Summary of proxy-derived seasonal temperature data. Isotope-derived temperature estimates (colored points) positioned on the annual cycle (Judd et al., 2017) were estimated using a range of $\delta^{18}O_{seawater}$ values from Douglas et al. (2014) (see text for details) and fit with a sinusoid to characterize the seasonal climate regime. The best-fit sinusoid through all data (±1σ; gray band) suggests a mean annual temperature of 10.8°C and a mean annual range of temperatures of 2.0 °C.

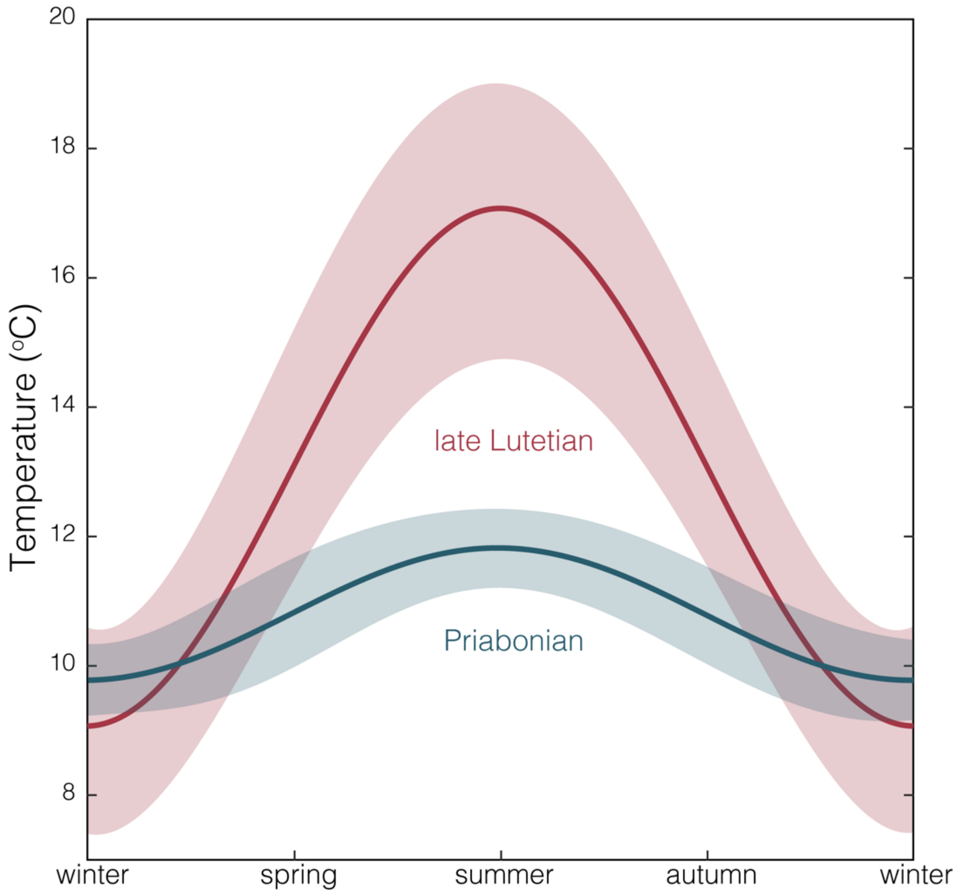

Figure 5.2. Summary of the seasonal ranges (±1σ) during the early Priabonian (blue) and the late Lutetian (red), inferred from high-resolution oxygen isotope profiles from bivalves deposited within the La Meseta Formation, Seymour Island, Antarctica.

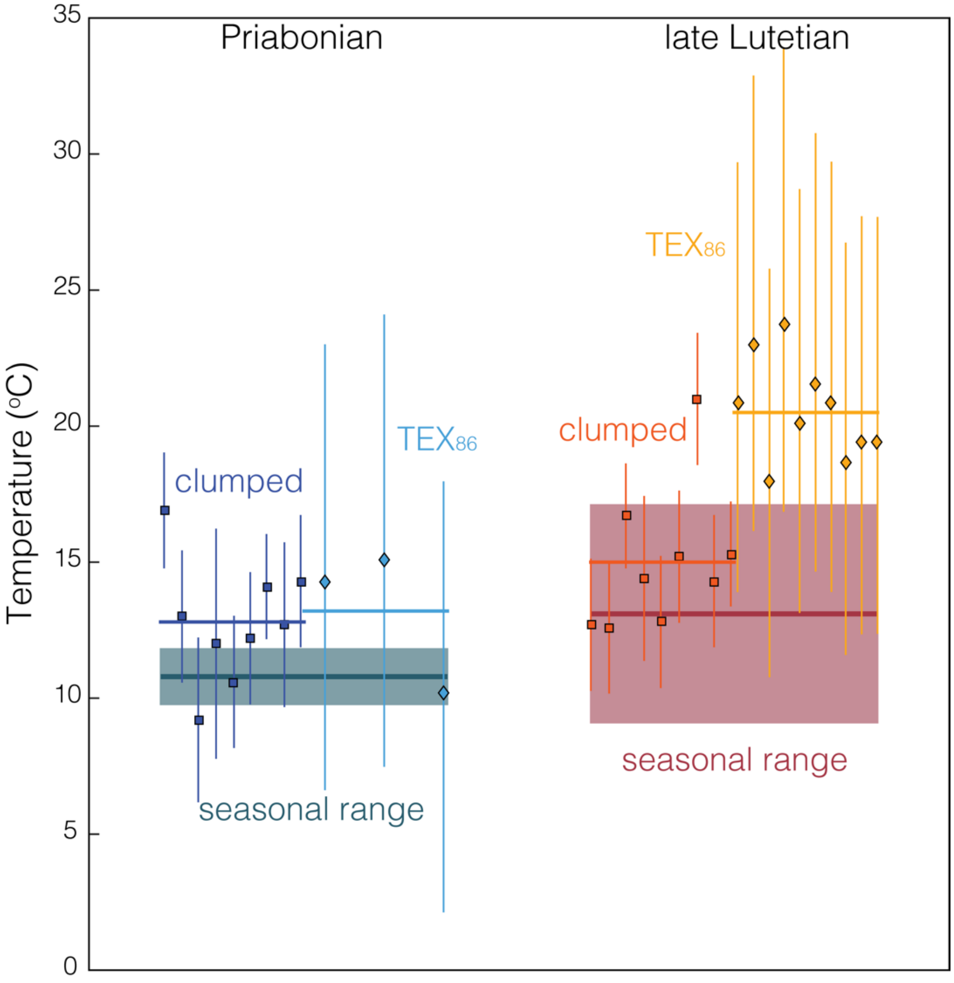

Figure 5.3. Summary of temperature estimates from the Priabonian (37.8-33.9 Ma; cool colors) and the late Lutetian (45.1-41.2 Ma; warm colors) of the La Meseta Formation, Seymour Island, Antarctica. Diamonds denote TEX_{86}-derived SST estimates (Douglas et al., 2014), calibrated to BAYSPAR (Tierney and Tingley, 2015). Squares denote clumped isotope-derived SST estimates (Douglas et al., 2014). Rectangles indicate the seasonal range inferred from high-resolution oxygen isotope profiles, and thick horizontal lines indicate the estimated MAT.

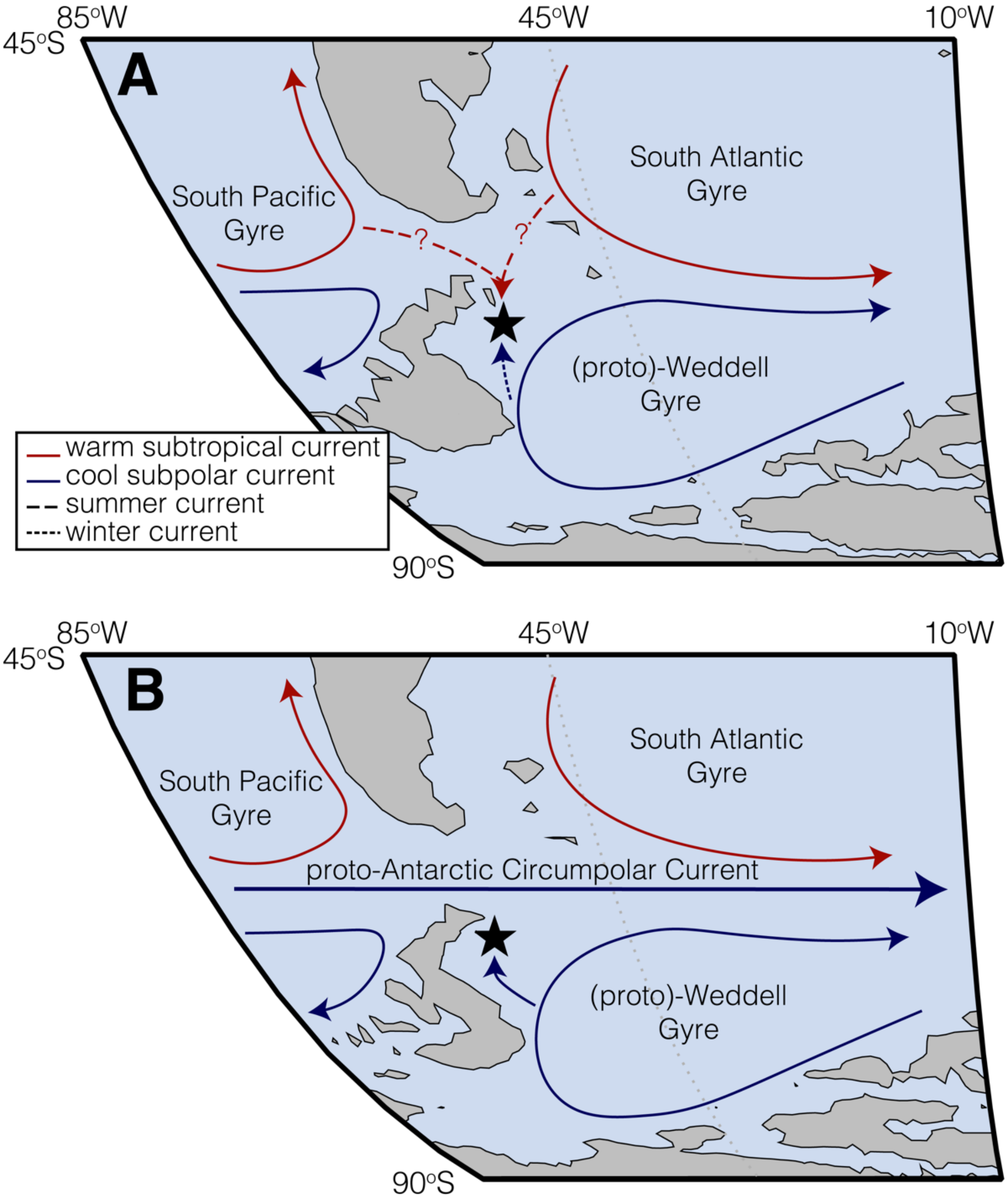

Figure 5.4. Conceptual model for changes in wind-driven surface ocean circulation between the late Lutetian (**A**) and Priabonian (**B**).

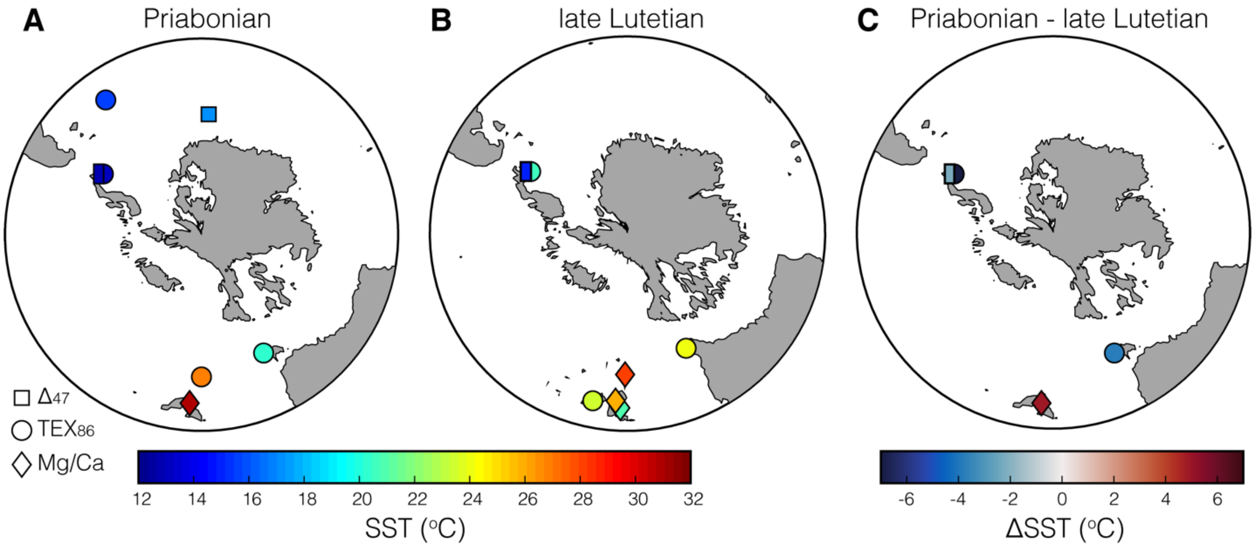

Figure 5.5. Comparison of Southern Ocean SST proxy data from the Priabonian (**A**) and late Lutetian (**B**), and the difference in SST between the two intervals for all sites with data in both time intervals (**C**).

Supporting Information

Figures

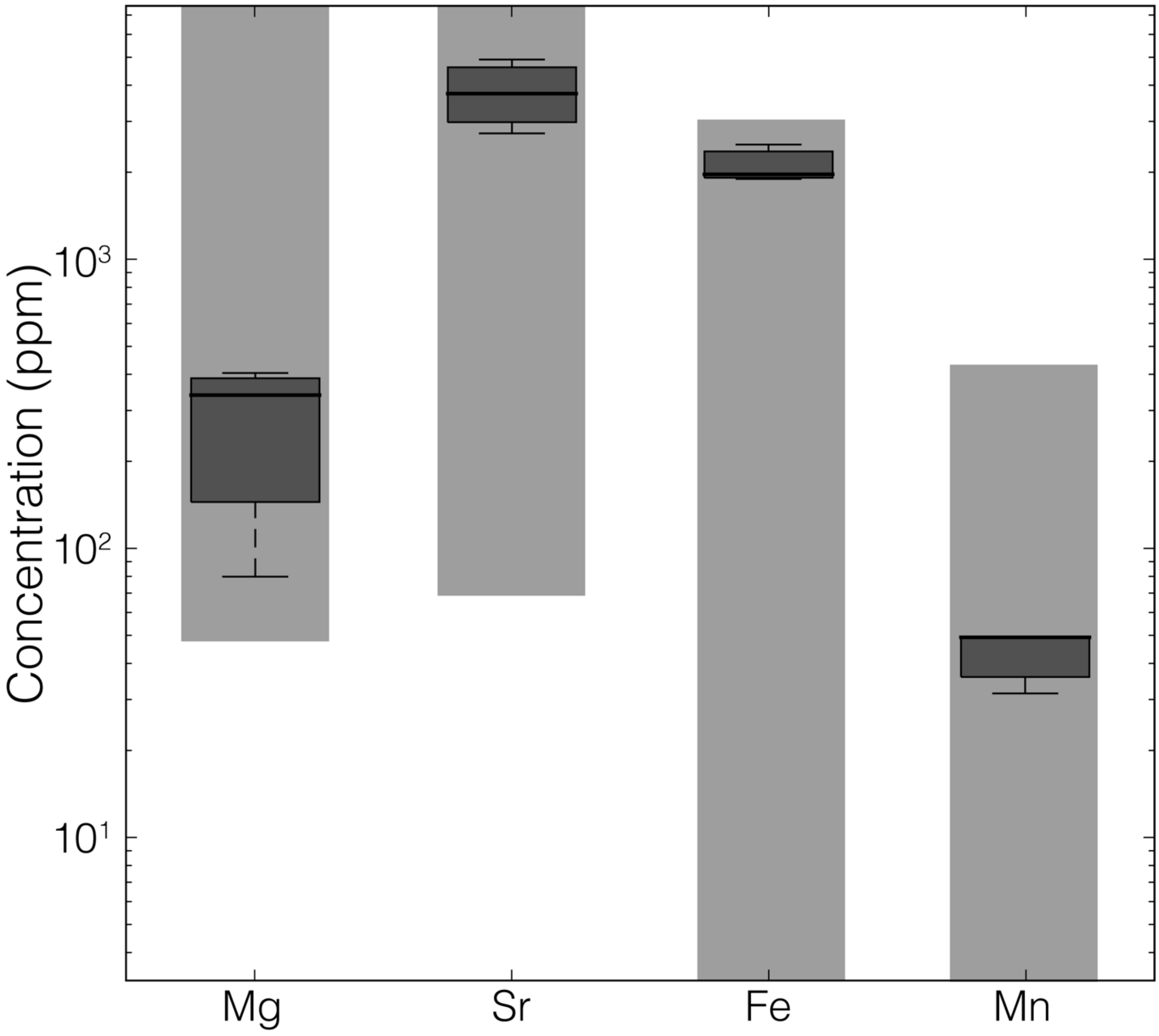

Figure S1. Box plots of trace element data used to assess potential diagenetic alteration. Light gray bands indicate the range of modern aragonitic bivalves for each element, as reported by Morrison and Brand (1986). Trace element analyses were performed on shells from each of the horizons from which isotope transects were generated, and in all cases fall within the range of unaltered aragonitic values.

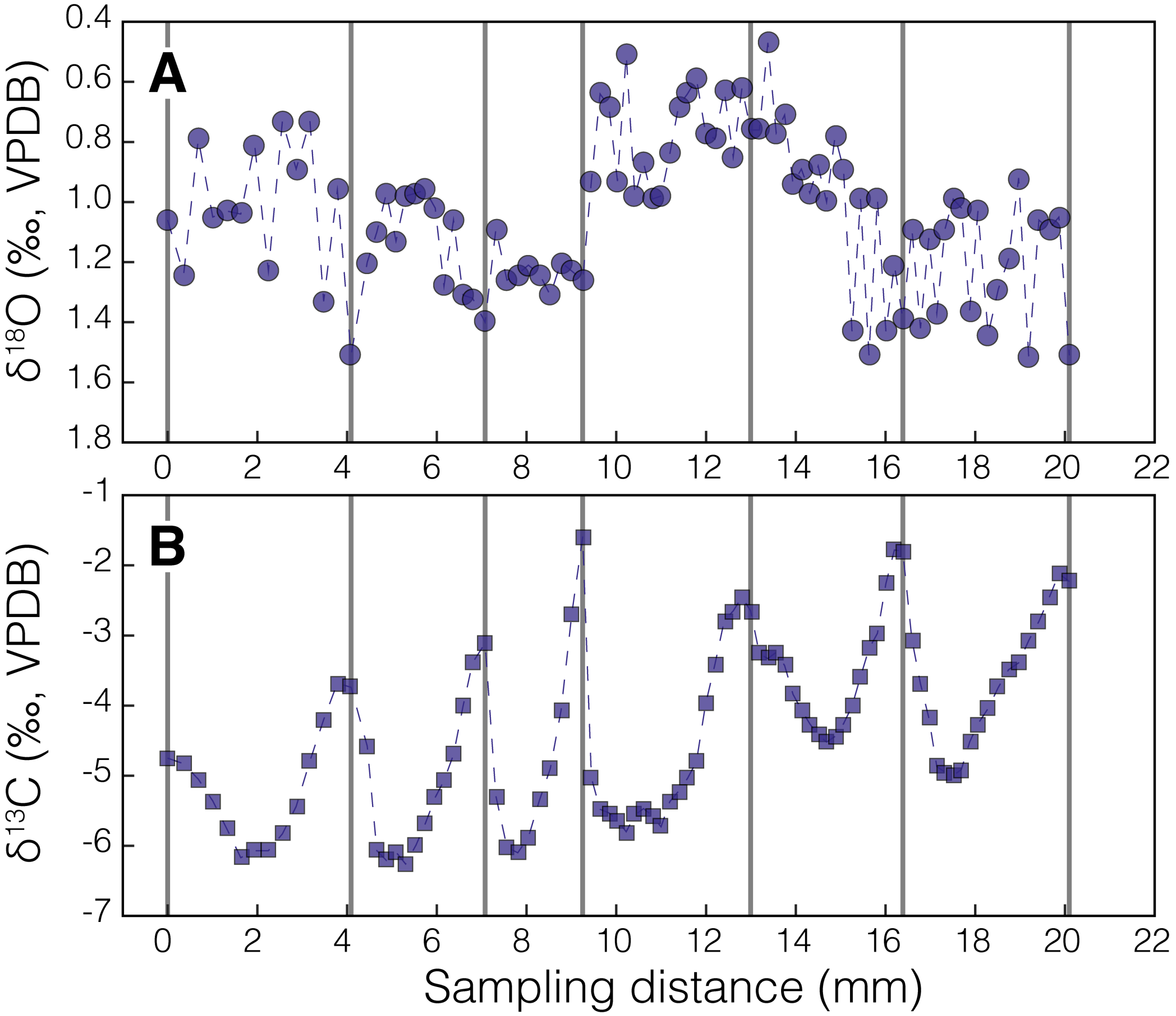

Figure S2. Oxygen (**A**) and carbon (**b**) isotope profile of specimen E1006. Thick gray lines denote the placement of externally sculpture ridges. While it is difficult to discern discrete years in the oxygen isotope profile, the consistent cyclicity within the carbon isotope profile lends confidence to the assertion that external banding is indeed annual.

Tables

Table S1: Summary of all Telm 7 sampled bivalves.

Specimen ID	**Genus**	**Sampled surface**	**No. years sampled**	**No. samples**	**$\delta^{18}O_{seawater}$**
C10181	*Cucullaea*	Exterior	6	58	-0.4
C20154*	*Cucullaea*	Interior	4	24	-0.7
C40154*	*Cucullaea*	Interior	4	26	-0.9
E1006	*Retrotapes*	Exterior	6	91	-1.0
UF119455	*Cucullaea*	Exterior	3	38	-0.8
UF119456	*Cucullaea*	Exterior	8	58	-0.91

[*] Data from Miklus (2008)

Table S2. Summary of sampled bivalves.

			Raw oxygen isotope data				**Growth modelled value[3]**			
Specimen ID	**Year**	**No. samples**	**Min**	**Max**	**Range**	**Mean**	**Min**	**Max**	**Range**	**Mean**
C10181	1	8	1.34	1.96	0.62	1.71	1.21	1.87	0.66	1.54
	2	22	1.41	2.00	0.59	1.56	1.47	2.28	0.81	1.87
	3	10	1.30	1.85	0.55	1.46	1.35	2.21	0.85	1.78
	4	6	1.12	1.96	0.84	1.65	0.74	1.88	1.13	1.31
	5	5	1.11	1.89	0.78	1.47	0.92	1.94	1.02	1.43
	6	7	1.32	1.70	0.38	1.48	1.32	1.70	0.38	1.51
Yearly average[1]:		*10*	*1.27*	*1.89*	*0.63*	*1.56*	*1.17*	*1.98*	*0.81*	*1.57*
Shell average[2]:		*58*	*1.11*	*2.00*	*0.89*	*1.56*	*1.43*	*1.82*	*0.39*	*1.62*
C20154	1	7	1.22	1.42	0.20	1.36	1.19	1.42	0.23	1.30
	2	5	1.23	1.56	0.33	1.35	1.26	1.65	0.38	1.46
	3	5	1.02	1.45	0.43	1.19	1.03	1.47	0.45	1.25
	4	7	1.01	1.24	0.23	1.15	1.06	1.38	0.32	1.22
Yearly average[1]:		*6*	*1.12*	*1.42*	*0.30*	*1.26*	*1.13*	*1.48*	*0.34*	*1.31*
Shell average[2]:		*24*	*1.11*	*2.00*	*0.89*	*1.56*	*1.11*	*1.45*	*0.35*	*1.28*
C40154	1	2	0.94	1.35	0.41	1.15	0.95	1.37	0.42	1.16
	2	7	1.00	1.33	0.33	1.22	0.96	1.30	0.34	1.13
	3	8	1.08	1.40	0.32	1.20	1.08	1.40	0.32	1.24
	4	9	1.03	1.33	0.30	1.18	0.96	1.27	0.31	1.12
Yearly average[1]:		*7*	*1.01*	*1.35*	*0.34*	*1.19*	*0.99*	*1.33*	*0.35*	*1.16*
Shell average[2]:		*26*	*0.94*	*1.40*	*0.46*	*1.19*	*1.03*	*1.30*	*0.27*	*1.17*
E1006	1	13	0.73	1.33	0.60	0.99	0.73	1.32	0.60	1.02
	2	13	0.96	1.51	0.55	1.14	1.00	1.51	0.51	1.25
	3	9	1.09	1.40	0.31	1.24	0.69	1.31	0.62	1.00
	4	19	0.51	1.26	0.75	0.80	0.72	1.76	1.04	1.24
	5	18	0.47	1.51	1.04	0.97	0.68	1.37	0.69	1.02
	6	19	0.92	1.52	0.60	1.21	0.65	1.29	0.64	0.97
Yearly average[1]:		*15*	*0.78*	*1.42*	*0.64*	*1.06*	*0.74*	*1.43*	*0.68*	*1.08*
Shell average[2]:		*91*	*0.47*	*1.52*	*1.05*	*1.04*	*0.80*	*1.31*	*0.52*	*1.06*
UF119455	1	14	1.43	1.74	0.31	1.57	0.84	1.59	0.75	1.21
	2	12	0.95	1.70	0.75	1.31	0.95	1.67	0.72	1.31
	3	12	0.74	1.43	0.69	1.06	0.88	1.48	0.61	1.18
Yearly average[1]:		*13*	*1.04*	*1.62*	*0.58*	*1.31*	*0.89*	*1.58*	*0.69*	*1.23*
Shell average[2]:		*38*	*0.74*	*1.74*	*1.00*	*1.33*	*0.91*	*1.60*	*0.69*	*1.26*
UF119456	1	7	1.12	1.56	0.44	1.37	0.57	1.38	0.80	0.98
	2	5	0.94	1.60	0.66	1.22	1.04	1.63	0.59	1.34
	3	6	1.14	1.57	0.43	1.30	0.65	1.35	0.70	1.00
	4	11	0.95	1.62	0.67	1.19	0.97	1.63	0.66	1.30

			Raw oxygen isotope data				Growth modelled value[3]			
Specimen ID	**Year**	**No. samples**	**Min**	**Max**	**Range**	**Mean**	**Min**	**Max**	**Range**	**Mean**
UF119456	5	7	0.89	1.69	0.80	1.25	0.45	1.56	1.11	1.01
	6	8	0.95	1.76	0.81	1.33	1.02	1.65	0.63	1.33
	7	6	0.90	1.51	0.61	1.21	0.84	1.47	0.63	1.15
	8	8	0.92	1.46	0.54	1.12	0.87	1.50	0.63	1.19
Yearly average[1]:		*7*	*0.98*	*1.60*	*0.62*	*1.25*	*0.80*	*1.52*	*0.72*	*1.16*
Shell average[2]:		*58*	*0.89*	*1.76*	*0.87*	*1.24*	*1.02*	*1.42*	*0.41*	*1.22*

[1] Yearly averages reflect the average of the minimum, maximum, range, and mean oxygen isotope values from each sampled year within a profile

[2] Shell averages reflect the absolute minimum, maximum, range, and mean oxygen isotope values from the raw profile

[3] Modeled yearly averages reflect the average of the minimum, maximum, range, and mean oxygen isotope value from the output of the bivalve growth rate model

Table S3. Raw oxygen isotope data from serially sampled bivalves, by horizon and shell ID.

Specimen ID	Sample No.	Distance (mm)	$\delta^{18}O_{carb}$ (‰; VPDB)
C10181	1	0	1.96
	2	0.34716	1.6
	3	0.66384	1.94
	4	0.9728	1.73
	5	1.2758	1.96
	6	1.6601	1.34
	7	1.9415	1.58
	8	2.4967	1.54
	9	2.7984	2
	10	3.0618	1.58
	11	3.3241	1.55
	12	3.5854	1.67
	13	3.8461	1.54
	14	4.1114	1.44
	15	4.408	1.41
	16	4.6564	1.44
	17	4.8751	1.51
	18	5.1085	1.55
	19	5.347	1.5
	20	5.5726	1.55
	21	5.7888	1.48
	22	6.0991	1.52
	23	6.3291	1.48
	24	6.5567	1.52
	25	6.7827	1.47
	26	7.0153	1.72
	27	7.2531	1.57
	28	7.4914	1.72
	29	7.7423	1.51
	30	8.0164	1.65
	31	8.2394	1.85
	32	8.4981	1.3
	33	8.7462	1.36
	34	9.0019	1.42
	35	9.2637	1.34
	36	9.5142	1.38

Specimen ID	Sample No.	Distance (mm)	$\delta^{18}O_{carb}$ (‰; VPDB)
	37	10.29	1.54
	38	10.544	1.38
	39	10.802	1.5
	40	11.321	1.53
	41	12.146	1.96
	42	12.578	1.74
	43	13.011	1.75
	44	13.443	1.69
	45	13.876	1.66
	46	14.308	1.12
	47	14.741	1.89
	48	15.173	1.11
	49	15.605	1.42
	50	16.049	1.57
	51	16.481	1.35
	52	16.946	1.66
	53	17.368	1.52
	54	17.789	1.45
	55	18.242	1.35
	56	18.756	1.32
	57	19.301	1.37
	58	19.841	1.7
C20154*	1	3	1.22
	2	4	1.33
	3	5.5	1.42
	4	7	1.4
	5	8.5	1.41
	6	10	1.37
	7	11	1.34
	8	12	1.23
	9	13	1.38
	10	14	1.56
	11	15	1.25
	12	16	1.32
	13	17	1.45
	14	18	1.27
	15	19	1.14
	16	20	1.02
	17	21.5	1.08

Specimen ID	Sample No.	Distance (mm)	$\delta^{18}O_{carb}$ (‰; VPDB)
	18	23.5	1.04
	19	25	1.16
	20	26	1.16
	21	27	1.01
	22	28	1.21
	23	29	1.21
	24	30	1.24
C40154*	1	1	0.94
	2	2	1.35
	3	3	1
	4	4	1.26
	5	5	1.33
	6	6	1.31
	7	7	1.19
	8	8	1.19
	9	9	1.24
	10	10	1.09
	11	11	1.13
	12	13	1.17
	13	15	1.32
	14	16	1.4
	15	17	1.21
	16	19	1.17
	17	20	1.08
	18	22	1.03
	19	23	1.08
	20	24	1.19
	21	26	1.17
	22	27	1.2
	23	28	1.24
	24	29	1.16
	25	30	1.33
	26	31	1.26
E1006	1	0	1.06
	2	0.35733	1.24
	3	0.68284	0.79
	4	1.0053	1.05
	5	1.3204	1.03
	6	1.6297	1.04

Specimen ID	Sample No.	Distance (mm)	$\delta^{18}O_{carb}$ (‰; VPDB)
	7	1.9392	0.81
	8	2.2458	1.23
	9	2.5581	0.73
	10	2.864	0.89
	11	3.1713	0.73
	12	3.4775	1.33
	13	3.7829	0.96
	14	4.089	1.51
	15	4.4491	1.2
	16	4.6626	1.1
	17	4.8763	0.97
	18	5.0896	1.13
	19	5.3036	0.98
	20	5.5363	0.97
	21	5.7388	0.96
	22	5.9639	1.02
	23	6.159	1.28
	24	6.3714	1.06
	25	6.5836	1.31
	26	6.7959	1.32
	27	7.0752	1.4
	28	7.316	1.09
	29	7.5626	1.26
	30	7.8033	1.24
	31	8.0398	1.21
	32	8.2873	1.24
	33	8.528	1.31
	34	8.7687	1.2
	35	9.0104	1.23
	36	9.2511	1.26
	37	9.4446	0.93
	38	9.638	0.64
	39	9.8327	0.68
	40	10.026	0.93
	41	10.221	0.51
	42	10.414	0.98
	43	10.608	0.87
	44	10.802	0.99
	45	10.997	0.98

Specimen ID	Sample No.	Distance (mm)	$\delta^{18}O_{carb}$ (‰; VPDB)
	46	11.193	0.84
	47	11.389	0.68
	48	11.586	0.64
	49	11.786	0.59
	50	11.99	0.77
	51	12.199	0.79
	52	12.406	0.63
	53	12.606	0.85
	54	12.801	0.62
	55	12.994	0.76
	56	13.19	0.76
	57	13.378	0.47
	58	13.564	0.77
	59	13.752	0.71
	60	13.939	0.94
	61	14.125	0.89
	62	14.313	0.97
	63	14.499	0.88
	64	14.687	1
	65	14.876	0.78
	66	15.064	0.89
	67	15.253	1.43
	68	15.443	0.99
	69	15.632	1.51
	70	15.82	0.99
	71	16.009	1.43
	72	16.198	1.21
	73	16.386	1.39
	74	16.589	1.09
	75	16.78	1.42
	76	16.964	1.12
	77	17.144	1.37
	78	17.326	1.09
	79	17.509	0.99
	80	17.692	1.02
	81	17.876	1.36
	82	18.061	1.03
	83	18.289	1.44
	84	18.515	1.29

Specimen ID	Sample No.	Distance (mm)	$\delta^{18}O_{carb}$ (‰; VPDB)
	85	18.741	1.19
	86	18.968	0.92
	87	19.194	1.52
	88	19.419	1.06
	89	19.642	1.09
	90	19.865	1.05
	91	20.098	1.51
UF119455	1	0	1.54
	2	0.2498	1.57
	3	0.51607	1.61
	4	0.77756	1.59
	5	1.0578	1.56
	6	1.3281	1.49
	7	1.6086	1.53
	8	1.912	1.64
	9	2.2185	1.57
	10	2.5251	1.74
	11	2.8396	1.43
	12	3.1215	1.47
	13	3.4932	1.49
	14	3.9872	1.68
	15	4.2858	1.23
	16	4.5878	1.49
	17	4.885	1.59
	18	5.192	1.29
	19	5.4999	1.7
	20	5.8	1.56
	21	6.1052	1.68
	22	6.4148	1.22
	23	6.7238	0.97
	24	7.0507	1.1
	25	7.4483	0.95
	26	7.6925	0.98
	27	7.931	0.97
	28	8.1718	1.08
	29	8.4335	0.76
	30	8.8408	0.74
	31	9.1095	1.14
	32	9.4009	0.91

Specimen ID	Sample No.	Distance (mm)	$\delta^{18}O_{carb}$ (‰; VPDB)
	33	9.7069	1.13
	34	10.017	1.12
	35	10.288	1.01
	36	10.539	1.33
	37	11.035	1.43
	38	11.313	1.04
UF119456	1	0	1.56
	2	0.52852	1.53
	3	1.0552	1.12
	4	1.6309	1.36
	5	2.1872	1.45
	6	2.7495	1.18
	7	3.3258	1.39
	8	3.8899	0.94
	9	4.4471	1.16
	10	4.8351	1.6
	11	5.182	1.24
	12	5.5279	1.14
	13	5.8736	1.14
	14	6.2204	1.36
	15	6.5656	1.24
	16	6.9175	1.15
	17	7.2731	1.32
	18	7.6285	1.57
	19	8.0007	1.11
	20	8.364	1.43
	21	8.7566	0.95
	22	9.1431	1.09
	23	9.5224	1.19
	24	9.9035	1.37
	25	10.281	1.62
	26	10.655	1.2
	27	11.03	1.08
	28	11.408	1.14
	29	11.802	0.96
	30	12.183	0.89
	31	12.575	1.3
	32	12.979	1.21
	33	13.434	1.13

Specimen ID	Sample No.	Distance (mm)	$\delta^{18}O_{carb}$ (‰; VPDB)
	34	13.879	1.41
	35	14.318	1.09
	36	14.812	1.69
	37	15.283	0.95
	38	15.76	1.18
	39	16.242	1.28
	40	16.71	1.22
	41	17.166	1.32
	42	17.693	1.49
	43	18.176	1.76
	44	19.111	1.47
	45	19.311	1.22
	46	19.92	1.51
	47	20.514	1.25
	48	20.992	1.26
	49	21.655	1.1
	50	22.095	0.9
	51	22.555	1.29
	52	22.978	1.27
	53	23.391	0.97
	54	23.806	1.46
	55	24.213	0.92
	56	24.616	0.95
	57	25.018	1.05
	58	25.418	1.02

[*] Data from Miklus (2008); distance data are unavailable, but samples were taken at a fixed rate. Distance values therefore reflect the sample number, but are unitless.

Table S4. Summary of GENESIS model simulation configurations.

	Simulation configuration					SST results* (ºC)			
Model ID	**ice sheet**	**pCO2**	**obliquity**	**eccentricity**	**precession**	**min**	**max**	**range**	**mean**
LEMED750L	medium	750	22	0	0	1.0	6.8	5.9	3.9
LEMED1500L	medium	1500	22	0	0	5.5	11.4	5.9	8.5
LEMED1500M	medium	1500	22	0.06	270	6.2	11.2	5.1	8.7
LENO1500H	none	1500	24.5	0	0	7.6	14.7	7.1	11.1
LENO2000H	none	2000	24.5	0	0	9.2	16.4	7.2	12.8

*SST results from the paleolocation of Seymour Island, situated at 68.8ºS, 69.4ºW

References

Alder, J.R., Hostetler, S.W., Pollard, D., Schmittner, A., 2011. Evaluation of a present-day climate simulation with a new coupled atmosphere-ocean model GENMOM. Geosci. Model Dev. 4, 69–83. doi:10.5194/gmd-4-69-2011

Alvarez, M.J., Pérez, D.E., 2016. Gerontic intraspecific variation in the Antarctic bivalve *Retrotapes antarcticus*. Ameghiniana 53, 485–494. doi:10.5710/amgh.05.12.2015.2947

Anagnostou, E., John, E.H., Edgar, K.M., Foster, G.L., Ridgwell, A., Inglis, G.N., Pancost, R.D., Lunt, D.J., Pearson, P.N., 2016. Changing atmospheric CO 2 concentration was the primary driver of early Cenozoic climate. Nature 533, 380–384. doi:10.1038/nature17423

Barker, P.F., Filippelli, G.M., Florindo, F., Martin, E.E., Scher, H.D., 2007. Onset and role of the Antarctic Circumpolar Current. Deep. Res. Part II Top. Stud. Oceanogr. 54, 2388–2398. doi:10.1016/j.dsr2.2007.07.028

Bijl, P.K., Bendle, J.A.P., Bohaty, S.M., Pross, J., Schouten, S., Tauxe, L., Stickley, C.E., McKay, R.M., Rohl, U., Olney, M., Sluijs, A., Escutia, C., Brinkhuis, H., Klaus, A., Fehr, A., Williams, T., Carr, S.A., Dunbar, R.B., Gonzalez, J.J., Hayden, T.G., Iwai, M., Jimenez-Espejo, F.J., Katsuki, K., Kong, G.S., Nakai, M., Passchier, S., Pekar, S.F., Riesselman, C., Sakai, T., Shrivastava, P.K., Sugisaki, S., Tuo, S., van de Flierdt, T., Welsh, K., Yamane, M., 2013. Eocene cooling linked to early flow across the Tasmanian Gateway. Proc. Natl. Acad. Sci. 110, 9645–9650. doi:10.1073/pnas.1220872110

Bijl, P.K., Schouten, S., Sluijs, A., Reichart, G.-J., Zachos, J.C., Brinkhuis, H., 2009. Early Palaeogene temperature evolution of the southwest Pacific Ocean. Nature 461, 776–779. doi:10.1038/nature08399

Buick, D.P., Ivany, L.C., 2004. 100 years in the dark: Extreme longevity of Eocene bivalves from Antarctica. Geology 32, 921–924. doi:10.1130/G20796.1

Burgess, C.E., Pearson, P.N., Lear, C.H., Morgans, H.E.G., Handley, L., Pancost, R.D., Schouten, S., 2008. Middle Eocene climate cyclicity in the southern Pacific: Implications for global ice volume. Geology 36, 651. doi:10.1130/G24762A.1

Carter, A., Riley, T.R., Hillenbrand, C.D., Rittner, M., 2017. Widespread Antarctic glaciation during the Late Eocene. Earth Planet. Sci. Lett. 458, 49–57. doi:10.1016/j.epsl.2016.10.045

Cione, A.L., Reguero, M.A., Acosta Hospitaleche, C., 2007. Did the continent and sea have different temperatures in the Northern Antarctic Peninsula during the Middle Eocene? Rev. la Asoc. Geol. Argentina 62, 586–596.

Coxall, H.K., Wilson, P. a, Pälike, H., Lear, C.H., Backman, J., 2005. Rapid stepwise onset of Antarctic glaciation and deeper calcite compensation in the Pacific Ocean. Nature 433, 53–57. doi:10.1038/nature03135

Cramwinckel, M.J., Huber, M., Kocken, I.J., Agnini, C., Bijl, P.K., Bohaty, S.M., Frieling, J., Goldner, A., Hilgen, F.J., Kip, E.L., Peterse, F., Van Der Ploeg, R., Röhl, U., Schouten, S., Sluijs, A., 2018. Synchronous tropical and polar temperature evolution in the Eocene letter. Nature 559, 382–386. doi:10.1038/s41586-018-0272-2

Creech, J.B., Baker, J.A., Hollis, C.J., Morgans, H.E.G., Smith, E.G.C., 2010. Eocene sea temperatures for the mid-latitude southwest Pacific from Mg/Ca ratios in planktonic and benthic foraminifera. Earth Planet. Sci. Lett. 299, 483–495. doi:10.1016/j.epsl.2010.09.039

Deconto, R.M., Pollard, D., 2003. Rapid Cenozoic glaciation of Antarctica induced by declining atmospheric CO2. Nature 421, 245–249.

Dettman, D., Reische, A.K., Lohmann, K.C., 1999. Controls on the stable isotope composition of seasonal growth bands in aragonitic fresh-water bivalves (unionidae). Geochim. Cosmochim. Acta 63, 1049–1057.

Dingle, R. V., Marenssi, S.A., Lavelle, M., 1998. High latitude Eocene climate deterioration: Evidence from the northern Antarctic Peninsula. J. South Am. Earth Sci. 11, 571–579. doi:10.1016/S0895-9811(98)00035-2

Douglas, P.M.J., Affek, H.P., Ivany, L.C., Houben, A.J.P., Sijp, W.P., Sluijs, A., Schouten, S., Pagani, M., 2014. Pronounced zonal heterogeneity in Eocene southern high-latitude sea surface temperatures. Proc. Natl. Acad. Sci. U. S. A. 111, 1–6. doi:10.1073/pnas.1321441111

Dutton, A.L., Lohmann, K.C., Zinsmeister, W.J., 2002. Stable isotope and minor element proxies for Eocene climate of Seymour Island, Antarctica. Paleoceanography 17, 6-1-6–13. doi:10.1029/2000PA000593

Eldrett, J.S., Greenwood, D.R., Harding, I.C., Huber, M., 2009. Increased seasonality through the Eocene to Oligocene transition in northern high latitudes. Nature 459, 969–973. doi:10.1038/nature08069

Elliot, D.H., Trautman, T.A., 1982. Lower Tertiary strata on Seymour Island, Antarctic Peninsula, in: Craddock, C. (Ed.), Antarctic Geosciences. University of Wisconsin Press, pp. 287–297.

Evans, D., Sagoo, N., Renema, W., Cotton, L.J., Müller, W., Todd, J.A., Saraswati, P.K., Stassen, P., Ziegler, M., Pearson, P.N., Valdes, P.J., Affek, H.P., 2018. Eocene greenhouse climate revealed by coupled clumped isotope-Mg/Ca thermometry. Proc. Natl. Acad. Sci. 115, 1174–1179. doi:10.1073/pnas.1714744115

Feakins, S.J., Warny, S., Deconto, R.M., 2014. Snapshot of cooling and drying before onset of Antarctic Glaciation. Earth Planet. Sci. Lett. 404, 154–166. doi:10.1016/j.epsl.2014.07.032

Galeotti, S., DeConto, R., Naish, T., Stocchi, P., Florindo, F., Pagani, M., Barrett, P., Bohaty, S.M., Lanci, L., Pollard, D., Sandroni, S., Talarico, F.M., Zachos, J.C., 2016. Antarctic Ice Sheet variability across the Eocene-Oligocene boundary climate transition. Science (80-.). 352, 76–80. doi:10.1126/science.aab0669

Gasson, E., Lunt, D.J., Deconto, R., Goldner, A., Heinemann, M., Huber, M., Legrande, A.N., Pollard, D., Sagoo, N., Siddall, M., Winguth, A., Valdes, P.J., 2014. Uncertainties in the modelled CO2 threshold for Antarctic glaciation. Clim. Past 10, 451–466. doi:10.5194/cp-10-451-2014

Gill, A.E., Niller, P.P., 1973. The theory of the seasonal variability in the ocean. Deep. Res. Oceanogr. Abstr. 20, 141–177. doi:10.1016/0011-7471(73)90049-1

Glorioso, P.D., 1987. Temperature distribution related to shelf-sea fronts on the Patagonian Shelf. Cont. Shelf Res. 7, 27–34. doi:10.1016/0278-4343(87)90061-6

Grossman, E.L., Ku, T.L., 1986. Oxygen and carbon isotope fractionation in biogenic aragonite: temperature effects. Chem. Geol. 59, 59–74.

Gulick, S.P.S., Shevenell, A.E., Montelli, A., Fernandez, R., Smith, C., Warny, S., Bohaty, S.M., Sjunneskog, C., Leventer, A., Frederick, B., Blankenship, D.D., 2017. Initiation and long-term instability of the East Antarctic Ice Sheet. Nature 552, 225–229. doi:10.1038/nature25026

Hansen, J., Fung, I., Lacis, A., Rind, D., Lebedeff, S., Ruedy, R., Russell, G., Stone, P., 1988. Global climate changes as forecast by Goddard Institute for Space Studies three-dimensional model. J. Geophys. Res. 93, 9341. doi:10.1029/JD093iD08p09341

Hansen, J., Sato, M., Ruedy, R., 2012. Perception of climate change. Proc. Natl. Acad. Sci. 109, E2415–E2423. doi:10.1073/pnas.1205276109

Henkes, G.A., Passey, B.H., Grossman, E.L., Shenton, B.J., Pérez-Huerta, A., Yancey, T.E., 2014. Temperature limits for preservation of primary calcite clumped isotope paleotemperatures. Geochim. Cosmochim. Acta 139, 362–382. doi:10.1016/j.gca.2014.04.040

Hines, B.R., Hollis, C.J., Atkins, C.B., Baker, J.A., Morgans, H.E.G., Strong, P.C., 2017. Reduction of oceanic temperature gradients in the early Eocene Southwest Pacific Ocean. Palaeogeogr. Palaeoclimatol. Palaeoecol. 475, 41–54. doi:10.1016/j.palaeo.2017.02.037

Hirahara, S., Ishii, M., Fukuda, Y., 2014. Centennial-scale sea surface temperature analysis and its uncertainty. J. Clim. 27, 57–75. doi:10.1175/JCLI-D-12-00837.1

Hollis, C.J., Handley, L., Crouch, E.M., Morgans, H.E.G., Baker, J.A., Creech, J., Collins, K.S., Gibbs, S.J., Huber, M., Schouten, S., Zachos, J.C., Pancost, R.D., 2009. Tropical sea temperatures in the high-latitude South Pacific during the Eocene. Geology 37, 99–102. doi:10.1130/G25200A.1

Hollis, C.J., Taylor, K.W.R., Handley, L., Pancost, R.D., Huber, M., Creech, J.B., Hines, B.R., Crouch, E.M., Morgans, H.E.G., Crampton, J.S., Gibbs, S., Pearson, P.N., Zachos, J.C., 2012. Early Paleogene temperature history of the Southwest Pacific Ocean: Reconciling proxies and models. Earth Planet. Sci. Lett. 349–350, 53–66. doi:10.1016/j.epsl.2012.06.024

Houben, A.J.P., Bijl, P.K., Sluijs, A., Schouten, S., Brinkhuis, H., 2019. Late Eocene Southern Ocean Cooling and Invigoration of Circulation Preconditioned Antarctica for Full-Scale

Glaciation. Geochemistry, Geophys. Geosystems 20, 2214–2234. doi:10.1029/2019GC008182

Huber, M., Brinkhuis, H., Stickley, C.E., Döös, K., Sluijs, A., Warnaar, J., Schellenberg, S.A., Williams, G.L., 2004. Eocene circulation of the Southern Ocean: Was Antarctica kept warm by subtropical waters? Paleoceanography 19, n/a-n/a. doi:10.1029/2004PA001014

Inglis, G.N., Farnsworth, A., Lunt, D., Foster, G.L., Hollis, C.J., Pagani, M., Jardine, P.E., Pearson, P.N., Markwick, P., Galsworthy, A.M.J., Raynham, L., Taylor, K.W.R., Pancost, R.D., 2015. Descent toward the Icehouse: Eocene sea surface cooling inferred from GDGT distributions. Paleoceanography 30, 1000–1020. doi:10.1002/2014PA002723

Ivany, L.C., Lohmann, K.C., Hasiuk, F., Blake, D.B., Glass, A., Aronson, R.B., Moody, R.M., 2008. Eocene climate record of a high southern latitude continental shelf: Seymour Island, Antarctica. Geol. Soc. Am. Bull. 120, 659–678. doi:10.1130/B26269.1

Ivany, L.C., Patterson, W.P., Lohmann, K.C., 2000. Cooler winters as a possible cause of mass extinctions at the Eocene/Oligocene boundary. Nature 407, 887–890. doi:10.1038/35038044

Jadwiszczak, P., 2010. Penguin response to the Eocene climate and ecosystem change in the northern Antarctic Peninsula region. Polar Sci. 4, 229–235. doi:10.1016/j.polar.2010.03.001

Jagniecki, E.A., Lowenstein, T.K.T.K., Jenkins, D.M., Demicco, R. V., 2015. Eocene atmospheric CO2 from the nahcolite proxy. Geology 43, 1075–1078. doi:10.1130/G36886.1

Judd, E.J., Ivany, L.C., DeConto, R.M., Halberstadt, A.R.W., Miklus, N.M., Junium, C.K., Uveges, B.T., 2019. Seasonally resolved proxy data from the Antarctic Peninsula support a heterogeneous middle Eocene Southern Ocean. Paleoceanogr. Paleoclimatology 2019PA003581. doi:10.1029/2019PA003581

Judd, E.J., Wilkinson, B.H., Ivany, L.C., 2017. The life and time of clams: Derivation of intra-annual growth rates from high-resolution oxygen isotope profiles. Palaeogeogr. Palaeoclimatol. Palaeoecol. 490, 70–83. doi:10.1016/j.palaeo.2017.09.034

Kaplan, J.O., 2003. Climate change and Arctic ecosystems: 2. Modeling, paleodata-model comparisons, and future projections. J. Geophys. Res. 108, 8171. doi:10.1029/2002JD002559

Keating-Bitonti, C.R., Ivany, L.C., Affek, H.P., Douglas, P., Samson, S.D., 2011. Warm, not super-hot, temperatures in the early Eocene subtropics. Geology 39, 771–774. doi:10.1130/G32054.1

Kennett, J.P., 1977. Cenozoic evolution of Antarctic glaciation, the circum-Antarctic Ocean, and their impact on global paleoceanography. J. Geophys. Res. 82, 3843–3860. doi:10.1029/JC082i027p03843

Kobashi, T., Grossman, E.L., Yancey, T.E., Dockery, D.T., 2001. Reevaluation of conflicting Eocene tropical temperature estimates: Molluskan oxygen isotope evidence for warm low latitudes. Geology 29, 983–986. doi:10.1130/0091-7613(2001)029<0983:ROCETT>2.0.CO

Lear, C.H., Elderfield, H., Wilson, P.A., 2000. Cenozoic Deep-Sea Temperatures and Global Ice Volumes from Mg/Ca in Benthic Foraminiferal Calcite. Science (80-.). 287, 269–272. doi:10.1126/science.287.5451.269

Liu, Z., Pagani, M., Zinniker, D., DeConto, R., Huber, M., Brinkhuis, H., Shah, S.R., Leckie, R.M., Pearson, A., 2009. Global cooling during the eocene-oligocene climate transition. Science (80-.). 323, 1187–1190. doi:10.1126/science.1166368

Marenssi, S.A., Net, L.I., Santillana, S.N., 2002. Provenance, environmental and paleogeographic controls on sandstone composition in an incised-valley system: The Eocene La Meseta Formation, Seymour Island, Antarctica. Sediment. Geol. 150, 301–321. doi:10.1016/S0037-0738(01)00201-9

Marshall, G.J., Orr, A., van Lipzig, N.P.M., King, J.C., 2006. The impact of a changing Southern Hemisphere Annular Mode on Antarctic Peninsula summer temperatures. J. Clim. 19, 5388–5404. doi:10.1175/JCLI3844.1

McKay, R.M., Barrett, P.J., Levy, R.S., Naish, T.R., Golledge, N.R., Pyne, A., 2016. Antarctic Cenozoic climate history from sedimentary records: ANDRILL and beyond. Philos. Trans. R. Soc. London A Math. Phys. Eng. Sci. 374. doi:10.1098/rsta.2014.0301

Miklus, N.M., 2008. The high-latitude response of temperature seasonality to global Eocene cooling. Syracuse University.

Morrison, J.O., Brand, U., 1986. Paleoscene# 5. Geochemistry of recent marine invertebrates. Geosci. Canada 13.

Pagani, M., Huber, M., Liu, Z., Bohaty, S.M., Henderiks, J., Sijp, W., Krishnan, S., DeConto, R.M., 2011. The role of carbon dioxide during the onset of antarctic glaciation. Science (80-.). 334, 1261–1264. doi:10.1126/science.1203909

Pearson, P.N., van Dongen, B.E., Nicholas, C.J., Pancost, R.D., Schouten, S., Singano, J.M., Wade, B.S., 2007. Stable warm tropical climate through the Eocene Epoch. Geology 35, 211–214. doi:10.1130/G23175A.1

Petersen, S. V., Schrag, D.P., 2015. Antarctic ice growth before and after the Eocene-Oligocene transition: New estimates from clumped isotope paleothermometry. Paleoceanography 30, 1305–1317. doi:10.1002/2014PA002769

Pfuhl, H.A., McCave, I.N., 2005. Evidence for late Oligocene establishment of the Antarctic Circumpolar Current. Earth Planet. Sci. Lett. 235, 715–728. doi:10.1016/j.epsl.2005.04.025

Porebski, S.J., 1995. Facies architecture in a tectonically-controlled incised-valley estuary: La Meseta Formation (Eocene) of Seymour Island, Antarctic Peninsula. Stud. Geol. Pol.

Porębski, S.J., 2000. Shelf-valley compound fill produced by fault subsidence and eustatic sea-level changes, Eocene La Meseta Formation, Seymour Island, Antarctica. Geology 28, 147–150. doi:10.1130/0091-7613(2000)28<147:SCFPBF>2.0.CO;2

Prandle, D., Lane, A., 1995. The annual temperature cycle in shelf seas. Cont. Shelf Res. 15, 681–704. doi:10.1016/0278-4343(94)E0029-L

Raymo, M.E., Ruddiman, W.F., 1992. Tectonic forcing of late Cenozoic climate. Nature 359, 117–122. doi:10.1038/359117a0

Sadler, P.M., 1988. Geometry and stratification of uppermost Cretaceous and Paleogene units on Seymour Island, northern Antarctic Peninsula, in: Feldmann, R.M., Woodburne, M.O. (Eds.), Geology and Paleontology of Seymour Island, Antarctic Peninsula. Geological Society of America Memoir 169, pp. 303–320.

Sarkar, S., Basak, C., Frank, M., Berndt, C., Huuse, M., Badhani, S., Bialas, J., 2019. Late Eocene onset of the Proto-Antarctic Circumpolar Current. Sci. Rep. 9, 1–10. doi:10.1038/s41598-019-46253-1

Scher, H.D., Bohaty, S.M., Smith, B.W., Munn, G.H., 2014. Isotopic interrogation of a suspected late Eocene glaciation. Paleoceanography 29, 628–644. doi:10.1002/2014PA002648

Scher, H.D., Martin, E.E., 2006. Timing and climatic consequences of the opening of Drake Passage. Science (80-.). 312, 428–430. doi:10.1126/science.1120044

Scher, H.D., Martin, E.E., 2004. Circulation in the Southern Ocean during the Paleogene inferred from neodymium isotopes. Earth Planet. Sci. Lett. 228, 391–405. doi:10.1016/j.epsl.2004.10.016

Scher, H.D., Whittaker, J.M., Williams, S.E., Latimer, J.C., Kordesch, W.E.C., Delaney, M.L., 2015. Onset of Antarctic Circumpolar Current 30 million years ago as Tasmanian Gateway aligned with westerlies. Nature 523, 580.

Sluijs, A., Bijl, P.K., Schouten, S., Röhl, U., Reichart, G.J., Brinkhuis, H., 2011. Southern ocean warming, sea level and hydrological change during the Paleocene-Eocene thermal maximum. Clim. Past 7, 47–61. doi:10.5194/cp-7-47-2011

Sluijs, A., Schouten, S., Pagani, M., Woltering, M., Brinkhuis, H., Sinninghe Damsté, J.S., Dickens, G.R., Huber, M., Reichart, G.-J., Stein, R., Matthiessen, J., Lourens, L.J., Pedentchouk, N., Backman, J., Moran, K., the Expedition, S., 2006. Subtropical Arctic Ocean temperatures during the Palaeocene/Eocene thermal maximum. Nature 441, 610–613. doi:10.1038/nature04668

Steinthorsdottir, M., Vajda, V., Pole, M., Holdgate, G., 2019. Moderate levels of Eocene pCO2 indicated by Southern Hemisphere fossil plant stomata. Geology 47, 914–918. doi:10.1130/g46274.1

Tierney, J.E., 2013. Biomarker-Based Inferences of Past Climate: The TEX86 Paleotemperature Proxy, 2nd ed, Treatise on Geochemistry: Second Edition. Elsevier Ltd. doi:10.1016/B978-0-08-095975-7.01032-9

Tierney, J.E., Tingley, M.P., 2015. A TEX 86 surface sediment database and extended Bayesian calibration. Sci. Data 2, 1–10. doi:10.1038/sdata.2015.29

Tremblin, M., Hermoso, M., Minoletti, F., 2016. Equatorial heat accumulation as a long-term trigger of permanent Antarctic ice sheets during the Cenozoic. Proc. Natl. Acad. Sci. 113, 11782–11787. doi:10.1073/pnas.1608100113

Turner, J., Colwell, S.R., Marshall, G.J., Lachlan-Cope, T.A., Carleton, A.M., Jones, P.D., Lagun, V., Reid, P.A., Iagovkina, S., 2005. Antarctic climate change during the last 50 years. Int. J. Climatol. 25, 279–294. doi:10.1002/joc.1130

Wilkinson, B.H., Ivany, L.C., 2002. Paleoclimatic inference from stable isotope profiles of accretionary biogenic hardparts - A quantitative approach to the evaluation of incomplete data. Palaeogeogr. Palaeoclimatol. Palaeoecol. 185, 95–114. doi:10.1016/S0031-0182(02)00279-1

Zachos, J.C., Dickens, G.R., Zeebe, R.E., 2008. An early Cenozoic perspective on greenhouse warming and carbon-cycle dynamics. Nature 451, 279–283. doi:10.1038/nature06588

Zanazzi, A., Judd, E., Fletcher, A., Bryant, H., Kohn, M.J., 2015. Eocene-Oligocene latitudinal climate gradients in North America inferred from stable isotope ratios in perissodactyl tooth enamel. Palaeogeogr. Palaeoclimatol. Palaeoecol. 417, 561–568. doi:10.1016/j.palaeo.2014.10.024

Zhang, Y.G., Pagani, M., Liu, Z., Bohaty, S.M., Deconto, R., 2013. A 40-million-year history of atmospheric CO 2. Phil Trans R Soc A A 40-million-year history of atmospheric CO 2. doi:10.1098/rsta.2013.0096

Emily J. Judd

Curriculum Vitae

EDUCATION

Anticipated 2020	Ph.D., Earth Sciences, Syracuse University *Syracuse, NY*
2013	B.S., Geology, minor in Philosophy, Utah Valley University *Orem, UT*

APPOINTMENTS

Present	Research Assistant, *Syracuse University Department of Earth Sciences*
2019	Summer Dissertation Fellow, *Syracuse University*
2018- 2019	Research Assistant, *Syracuse University Department of Earth Sciences*
2018	Instructor of Record, EAR210: History of Life and Earth, *Syracuse University Department of Earth Sciences*
2016-2017	Research Assistant, *Syracuse University Department of Earth Sciences*
2014-2016	Teaching Assistant, *Syracuse University Department of Earth Sciences*

HONORS, AWARDS, AND GRANTS

2019	INTERN Grant *National Science Foundation, $41,537*
2018, 2019	Student Publication Award *Syracuse University Department of Earth Sciences*
2018	Urbino Summer School in Paleoclimatology Scholarship *National Science Foundation*
2017	Outstanding Teaching Assistant Award *National Association of Geoscience Teachers*
2017	Newton E. Chute Award for Graduate Excellence *Syracuse University Department of Earth Sciences*
2017	Chairman's Award *Syracuse University Department of Earth Sciences*
2016	Graduate Student Research Grant; *Outstanding Mention* *Geological Society of America; $2,500*
2016	Outstanding Teaching Assistant Award *Syracuse University*
2016	Patricia H. Kelley Student Poster Award *Paleontological Research Institute Summer Symposium*

2015	Grant-in-Aid of Research *Sigma Xi*; *$1,000*
2015	Research Grant *Syracuse University Department of Earth Sciences; $2,500*
2013	Scholarly Activities Committee Grant *Utah Valley University College of Science and Health; $4,000*
2013	Robert and Anne Peper Endowed Physical Science Scholarship *Privately funded tuition scholarship*
2013	Field Camp Scholarship *Utah Geological Association*

PUBLICATIONS

Judd, E.J., Bhattacharya, T, and Ivany, L.C. (*submitted*). A modern perspective on ancient sea surface temperatures.

Muirhead, J.D., Fischer, T.P., Laizer A., Oliva, S.J., **Judd, E.J.**, Lee, H, Kazimoto, H., Ebinger, C.J., Sano, Y., Takahata, N., Tiberi, C., van Wijk, J., Dufek, J., Foley, S.F., Currie, C.A., and Reiss, M.C. (*in revision*). Displacement of cratonic mantle and lithospheric channeling concentrates deep carbon during continental rifting. *Nature*.

Jimenez, M.Y., Ivany, L.C., **Judd, E.J.**, Henkes, G. (2019). Low and seasonally variable salinity in the Pennsylvanian equatorial Appalachian Basin. *Earth and Planetary Science Letters*. https://doi.org/10.1016/j.epsl.2019.04.051

Judd, E.J., Ivany, L.C., DeConto, R.M., Halberstadt, A.R.W., Miklus, N.M., Junium, C.K., Uveges, B.T. (2019). Seasonally resolved proxy data from the Antarctic Peninsula support a heterogeneous middle Eocene Southern Ocean. *Paleoceanography and Paleoclimatology*. https://doi.org/10.1029/2019PA003581

Judd, E.J., Wilkinson, B.H., Ivany, L.C. (2018). The life and time of clams: Derivation of intra-annual growth rates from high-resolution oxygen isotope profiles. *Palaeogeography, Palaeoclimatology, Palaeoecology*, vol. 490. https://doi.org/10.1016/j.palaeo.2017.09.034

Moss, D.K., Ivany, L.C., **Judd, E.J.**, Cummings, P.W., Bearden, C.E., Kim, W., Artruc, E.G., Driscoll, J.R. (2016). Lifespan, growth rate, and body size across latitude in marine Bivalvia with implications for Phanerozoic evolution. *Proceedings of the Royal Society B: Biological Sciences*, vol. 283 (1836). https://doi.org/10.1098/rspb.2016.1364

Zanazzi, A., **Judd, E.**, Fletcher, A., Bryant, H., Kohn, M.J. (2015). Eocene-Oligocene latitudinal climate gradients in North America inferred from stable isotope ratios in perissodactyl tooth enamel. *Palaeogeography, Palaeoclimatology, Palaeoecology*, vol. 417. https://doi.org/10.1016/j.palaeo.2014.10.024

CONFERENCE ABSTRACTS *(five most recent first author)*

Judd, E.J., Bhattacharya, T, and Ivany, L.C. (2019). Dynamic controls on zonal variability of sea surface temperatures and implications for paleoclimate reconstruction. American Geophysical Union Fall Meeting.

Judd, E.J., Ivany, L.C., Bhattacharya, T. (2018). A statistical model to better understand the heterogeneous global distribution of seasonal temperature ranges in the modern world. American Geophysical Union Fall Meeting.

Judd, E.J., Ivany, L.C., DeConto, R.M., Halberstadt, A.R.W., Miklus, N.M., Junium, C.K., Uveges, B.T. (2018). Middle Eocene seasonality: Insights from the geochemistry of fossil bivalves and driftwood. Goldschmidt Conference.

Judd, E.J., Ivany, L.C., Miklus, N.M., Uveges, B.T., Junium, C.K., Halberstadt, A.R.W, DeConto, R.M. (2017). Eocene Antarctic seasonality inferred from high-resolution stable isotope profiles of fossil bivalves and driftwood. American Geophysical Union Fall Meeting.

Judd, E.J., Ivany, L.C., Miklus, N.M. (2017). Late Eocene reduction in Antarctic seasonality as inferred from the isotopic composition of nearshore marine bivalves. Climate and Biotic Events of the Paleogene.

(20 published conference abstracts from the Geological Society of America Fall Meeting, American Geophysical Union Fall Meeting, Goldschmidt Conference, Climatic and Biotic Events of the Paleogene 2017, and 4th International Sclerochronology Meeting; 10 first-author, 10 co-authored.)

TEACHING EXPERIENCE

SYRACUSE UNIVERSITY

2017, 2019	BIO400: Isotopic Approaches and Global Change, Guest Lecturer *two 90-minute lectures*
2018	EAR210: History of Life and Earth, Instructor of Record *three 1-hour lectures weekly*
2015-2016	EAR105: Earth Science, Teaching Assistant Coordinator *four 1-hour recitations weekly, two semesters*
2014-2015	EAR105: Earth Science, Teaching Assistant *five 1-hour recitations weekly, two semesters*

UTAH VALLEY UNIVERSITY

2013	GEO3080: Earth Materials, Teaching Assistant *one 3-hour lab weekly*

INVITED TALKS

2019	Marine Palynology and Paleoceanography Group, Utrecht University *'Using the spatial variability of modern sea surface temperatures to better understand ancient climates'*
2017	Earth Science Seminar Series, Utah Valley University *'Variations in seasonality across large-scale climate transitions: Insights from stable isotope profiles of Eocene Antarctic bivalves'*

2017	Technology Alliance of Central New York Junior Café Scientifique, Museum of Science and Technology *'Stranger than fiction: A journey through the history of life'*
2016, 2017	Frontiers of Science, Earth Science Session *'Past and current climate change'*
2016	Syracuse University Project Advance *'High latitude seasonality in a changing climate'*

OUTREACH AND SERVICE

2017 – Present	PaleoX weekly seminar, *coordinator* Syracuse University Department of Earth Sciences
2017-2018	Quaternary paleoclimate new hire search committee, *non-voting member* Syracuse University Department of Earth Sciences
2015-2018	Frontiers of Science, *student coordinator* Syracuse University Department of Science Teaching
2014 - 2015	Geology Graduate Organization, *Faculty Representative, Officer* Syracuse University Department of Earth Sciences
2014-2015	*Student Representative* Utah Valley University Department of Earth Science

Reviewer of manuscripts for: *Climate of the Past; Global and Planetary Change; Palaeogeography, Palaeoclimatology, Palaeoecology; Canadian Journal of Zoology.*

Undergraduate mentoring: Lindsay Moon ('19), Alaina Hickey ('17), Claire Bearden ('15).

SUMMARY OF GRADUATE COURSEWORK

Geochemistry
Geochemical patterns
Chemical oceanography
Advanced plate tectonics
Isotope geochemistry (I, II)
Earth's organic processes
Probability and statistics
Global change through the geologic record
Stable isotope geochemistry
Writings of Stephen J. Gould
Numerical methods in geosciences